ARCHIVES OF ACOUSTICS
17, 1, 3–5 (1992)

Oswald Leroy – the h.c. doctor of the Gdańsk University

Photo: Piet Hellin, Kortrijk

The University of Gdańsk conferred the degree of doctor honoris causa on Oswald Leroy, the professor of mathematics and physics at the Catholic University in Leuven –the Kortrijk Campus (Belgium), a well-known specialist in the world and the authority especially in acousto-optics.

The solemn promotion was held on 8th February, 1991. Professor Antoni Śliwiński, who was the promotor, presented in his laudation the person and the scientific achievements of Professor Leroy, particularly emphasizing the theory of light and two-beam ultrasonic interaction. This theory was developed for a wide range of frequencies, intensities and phase shifts. As a result of twenty years co-operation with the University of Gdańsk, the theory was verified experimentally by acousto-optical group at the Institute of Experimental Physics (P. Kwiek, A. Markiewicz, A. Śliwiński).

The most important and well-known in the world achievements of Professor Leroy in acousto-optics are following:

– elaboration of the theory of light diffraction on complex systems of ultrasonic beams,

– explanation of the interaction mechanisms between light and ultrasounds, taking into account phase and amplitude relations,

– determination of symmetry conditions of acousto-optical spectra in various systems of the interaction between light and ultrasounds,

– determination of light intensity modulation by ultrasounds depending on evenness and oddness of the interacting components in two-beam systems,

– application of acousto-optical interactions for the determination of reflectivity and loss coefficients on boundary surfaces of real media. Professor Leroy has also great achievements in theoretical physics. His activity in this field is concerned with: examination of symmetry problems in physics, proofs of the existence of solutions to the problem of heavy particles movement in the field of the Earth, construction of self-coupling Hill operators having periodic eigen functions, new approach to the propagation of electromagnetic and elastic waves in non-homogeneous media, behaviour of waves on a statistically non-uniform liquid solid boundary, mechanism of bend wave reflection. Professor Leroy published more then eighty papers, which were several times cited by eminent research workers, and were also introduced to monographies and books. From among these papers, twelve were published in co-operation with the authors from the Gdańsk University.

Professor Leroy is a member of many Societies and Scientific Committees not only in Belgium but also abroad. He was a lecturer not only at European universities but in the USA and Japan as well.

Concluding, Professor Śliwiński emphasized that Polish physicists particularly those dealing with acousto-optics, greatly appreciated Professor Leroy's authority, scientific achievement and also his friendly attitude towards Poland.

In his speech, Professor Leroy thanked the Rector of the University of Gdańsk – Professor Grzonka, Senate and promotor – Professor Śliwiński for conferring on him the h.c. doctor of the University of Gdańsk. He also thanked the Rector of his university – Monseigneur Maertend, who was also present, for all his efforts in supporting the co-operation with the University of Gdańsk. He emphasized that during his each visit in acousto-optical laboratory at the University of Gdańsk he was surprised with the state of development of laboratory because certain investments were made in the proper apparatus, and the theory was not only for the first time experimentally verified here

but also he was inspired to further theoretical work.

He said: "After solving the diffraction problem, which took us about twenty years, now we are researching the inwerse problem. We want to 'see' ultrasound; in particular, we want to look at the ultrasound reflected and transmitted through an unknown medium. In general. I could say that we are researching image techniques based on acousto-optical interaction."

He also mentioned the relationship between Poland and Flanders, their similar cultural roots and way to freedom. In conclusion he said that he admired a great satisfaction because of the titule of the h.c. doctor of the Gdańsk University.

Stanisław Zachara

ARCHIVES OF ACOUSTICS
17, 1, 7–17 (1992)

DISTRIBUTION OF PHONATION AND PAUSE DURATIONS IN FLUENT SPEECH AND STUTTERERS SPEECH

W. KUNISZYK-JÓŹKOWIAK

Institute of Physics, Maria Curie-Skłodowska University
(20-031 Lublin)

This work is a fragment of investigations into an objective method of evaluation of speech fluency. The paper presents statistical distributions of phonation and pause durations in utterances of stutterers speaking with a simultaneous auditory feedback and synchronously with an echo and in utterances of fluently speaking subjects. It is shown that the speech envelope can be a source of information about both speech velocity and the degree of speech non-fluency. The most probable phonation and pause durations have been found to exist and a correlation between these durations and the duration of one syllable has been revealed. This make makes a speech velocity evaluation possible on the basis of statistical distributions of phonation and pause durations. Distributions of phonation and pause durations in fluent and non-fluent speech have been compared. Non-fluent speech contains shorter phonations than fluent speech. Total phonation durations have been determined in utterances of stutterers and fluently speaking subjects. They are much shorter in non-fluent utterances than in fluent ones. The total phonation distribution can be an important parameter in an evaluation of speech fluency.

1. Introduction

The main parameters in an evaluation of results of a therapeutic influence on the speech process in stutterers are: speech velocity and stuttering intensity [2, 3, 5 – 8]. At present, they are measured by auditory methods. The speech velocity is determined by measuring fluently pronounced syllables and the time period they take. In the case of stutterers these fluent sections are short and the measurements are subject to a significant error. The stuttering intensity is determined by a number of errors characteristic of stuttering, such as: repetitions, insertions, blockades etc. per 100 fluently pronounced syllables.

The aim of the research reported in this paper is to develop an objective method of evaluating non-fluency of speaking in stutterers.

It is strictly connected with the answer to the question, what exactly is stuttering. According to some authors [4, 9], stuttering is a disturbance at the beginning of speech sounds, resulting in a wrong duration and accent of the motoric units they precede. The

greater vocal effort at the beginning and pronunciation of speech sounds leads to disturbances in time relations between periods of activity (phonations) and periods of rest (pauses) of articulators.

Distributions of phonation and pause durations in fluent and non-fluent speech are the subject of this work.

2. Apparatus and measurement procedure

Speech signals from a tape-recorder (*1*) were put through an analogue detector of envelopes (*2*), converted to digital signals (*A/D* converter – (*3*) and memorized (*4*) on

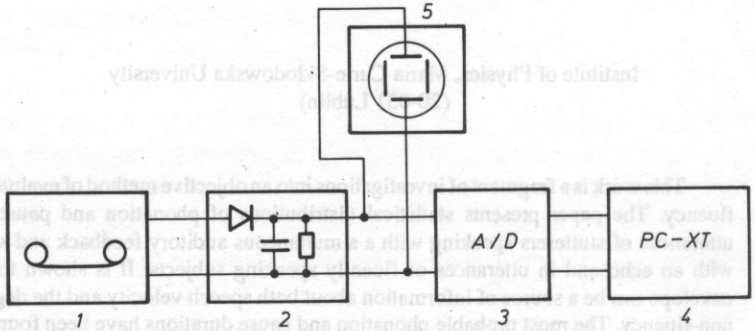

FIG. 1. Block diagram of the set-up for measuring phonation and pause durations.

floppy disks (Fig. 1). The maximum levels of analogue signals fed to the converter were monitored at a CRT (*5*). An exemplary shape of a speech envelope is presented in Fig. 2. The dynamic range of analogue signals was 40 dB. The conversion time of the analog-to-digital converter was 5 ms. 100 second records were made for 30 stutterers speaking: a) with a simultaneous auditory feedback, b) synchronously with an echo [1], and for 30 fluently speaking subjects.

The computer procedure were developed:

1) measurement of phonation and pause durations resulting in a statistical distribution of these parameters at an arbitrary width of the time interval,

2) measurement of the total phonation time during an utterance.

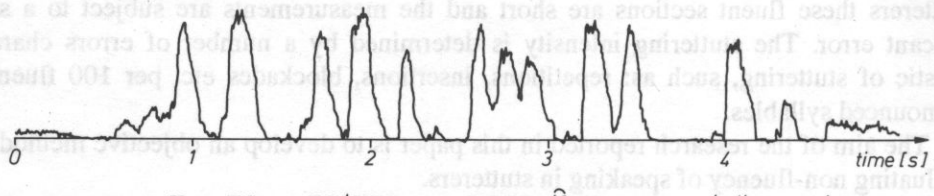

FIG. 2. Exemplary shape of a speech envelope.

3. Description of persons to speech analysis

3.1. Stutterers

The group of stutterers subjected to speech analysis comprised 23 men and 7 women. Their age ranged from 11 to 21 years. The stuttering intensity defined as a number of errors per 100 syllables ranged from 1 to 38 (the average value was 16 errors per 100 syllables). The speech velocity when speaking with a simultaneous auditory feedback was from 2.3 to 5.1 syllables per second (average: 4.0 syl/s), while with echo it was from 0.7 to 2.5 syl/s (average: 1.8 syl/s). The stuttering intensity when speaking with an echo decreased to a lower value ranging from 0 to 7.4 errors per 100 syllables in individual stutterers (average: 1.7 errors per 100 syllables). The subjects described simple pictures.

3.2. Fluently speaking persons

The group of fluent speakers included 15 students who described the same pictures as the stutterers did. The examinations included 100 second fragments of official speeches of 15 members of Parliament recorded from the radio.

Note that the subjects were intentionally not selected for their age or for their sex. This rule applied both to fluently speaking subjects and to stutterers. This follows from the fact that it is the aim of the research to reveal features which differentiate the speech of stutterers from that of fluently speaking subjects, no matter what their age or sex.

4. Relationship between statistical distributions of phonation and pause durations and speech velocity

Examples of statistical distributions of phonation and pause durations (in the range of 1 s) in utterances of stutterers speaking (a) with simultaneous auditory feedback (unaided speaking) and synchronously with an echo are shown in Fig. 3.

Pronounced maxima in numbers of phonations and pauses distributions can be observed. Their locations change with speech velocity (which was 3.5 syl/s in the case of utterances shown in Fig. 3 a and 2.4 syl/s in Fig. 3 b). Figure 4 shows a dependence of the most frequent values of phonation durations t_{ph} and the most frequent values of pause durations t_p and their sum $t_{ph} + t_p$ on an average time of pronunciation of one syllable (the reciprocal of speech velocity – t_s). The most frequent values of phonation durations increase with the duration of one syllable duration. This relationship is approximately described by

$$t_{ph} = 0.86\, t_s - 0.04\ [s]. \tag{1}$$

Pause durations increase only slightly with the duration of one syllable

$$t_p = 0.18\, t_s + 0.02\ [s]. \tag{2}$$

The best correlation can be observed between the sum $t_{ph} + t_p$ and the average duration of one syllable

$$t_{ph} + t_p = 1.04\, t_s - 0.02\ [s]. \tag{3}$$

This leads to the next conclusion that the reciprocal of the sum $t_{ph} + t_p$ is correlated with the speech velocity (Fig. 5)

$$V_{ph+p} = 0.99\, V_s + 0.06$$

$$\left(V_{ph+p} = \frac{1}{t_{ph} + t_p},\ V_s = \frac{1}{t_s} \right). \tag{4}$$

5. Differences in statistical distributions of phonation and pause durations observed in fluent and non-fluent speech

The distributions of phonation and pause durations in stutterers speaking with a simultaneous auditory feedback (non-fluent speech) are different from the distributions obtained when speaking with an echo (almost fluent speech). In order to visualize these

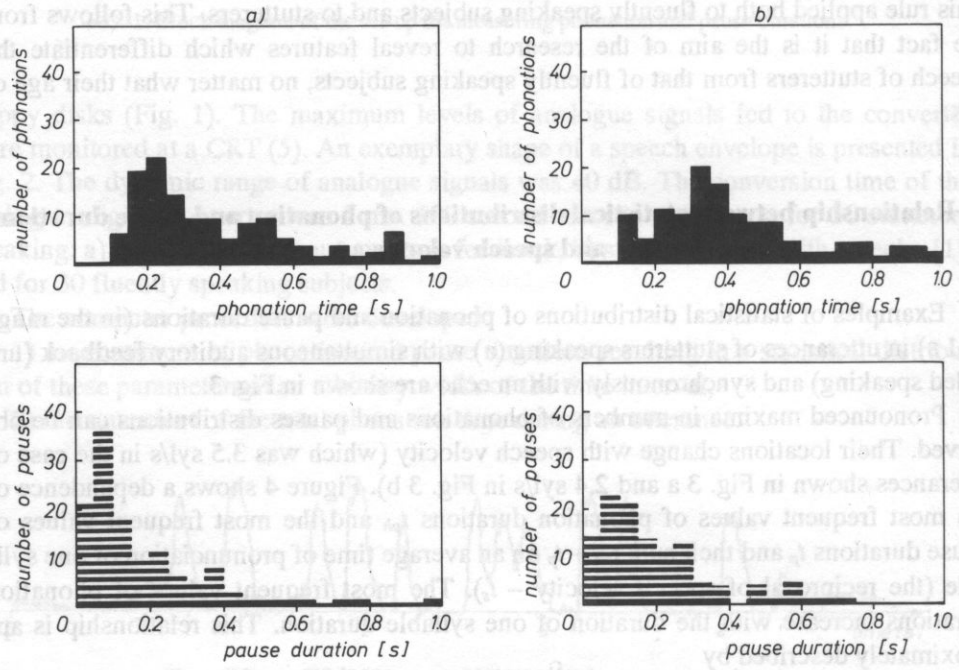

FIG. 3. Statistical distributions of phonation and pause durations in speech of stutterers speaking a) with a simultaneous auditory feedback, b) synchronously with an echo.

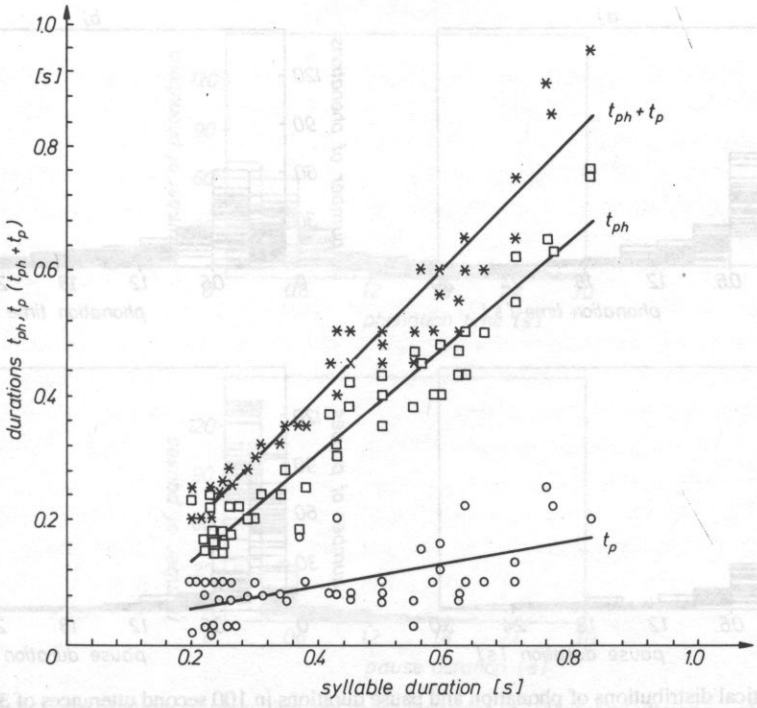

FIG. 4. Dependence of phonation durations corresponding to maxima (t_{ph}), pause durations corresponding to maxima (t_p) and their sum $t_{ph} + t_p$ on an average time of pronunciation of one syllable (the reciprocal of speech velocity).

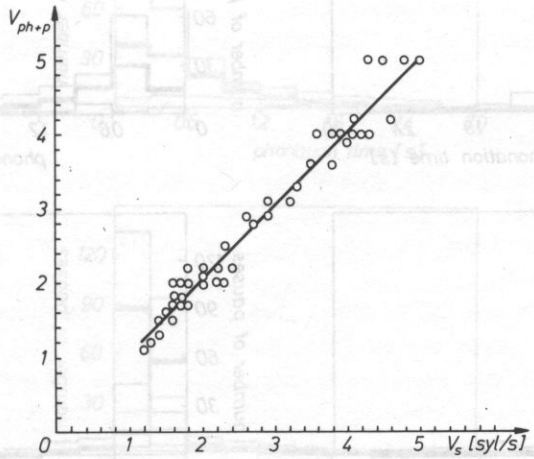

FIG. 5. Correlation between $V = \dfrac{1}{t_{ph} + t_p}$ and V_s determined by a number of syllables pronounced during one second.

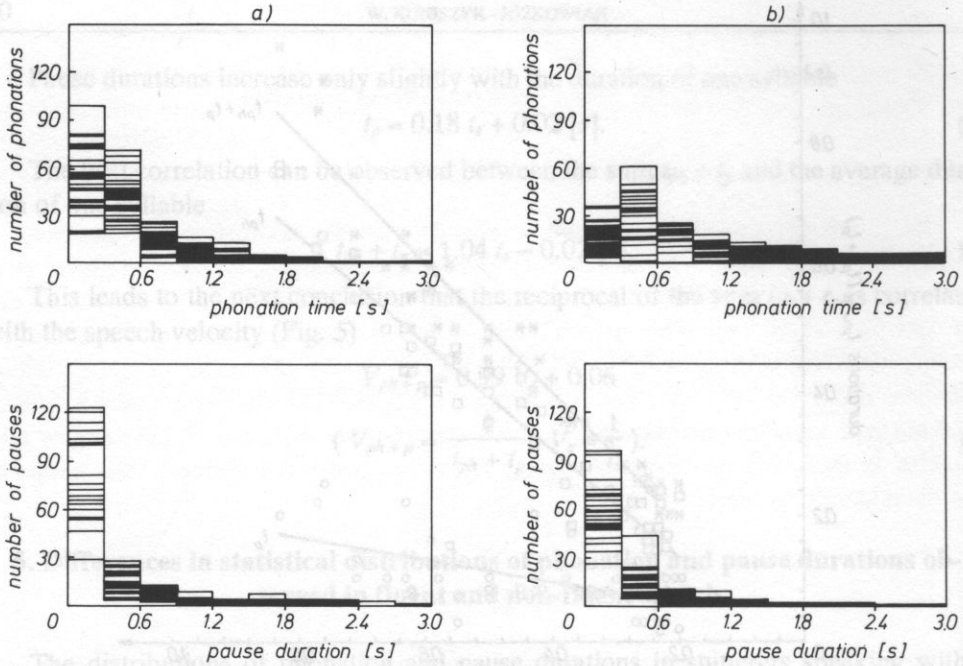

FIG. 6. Statistical distributions of phonation and pause durations in 100 second utterances of 30 stutterers speaking a) with a simultaneous auditory feedback, b) with an echo.

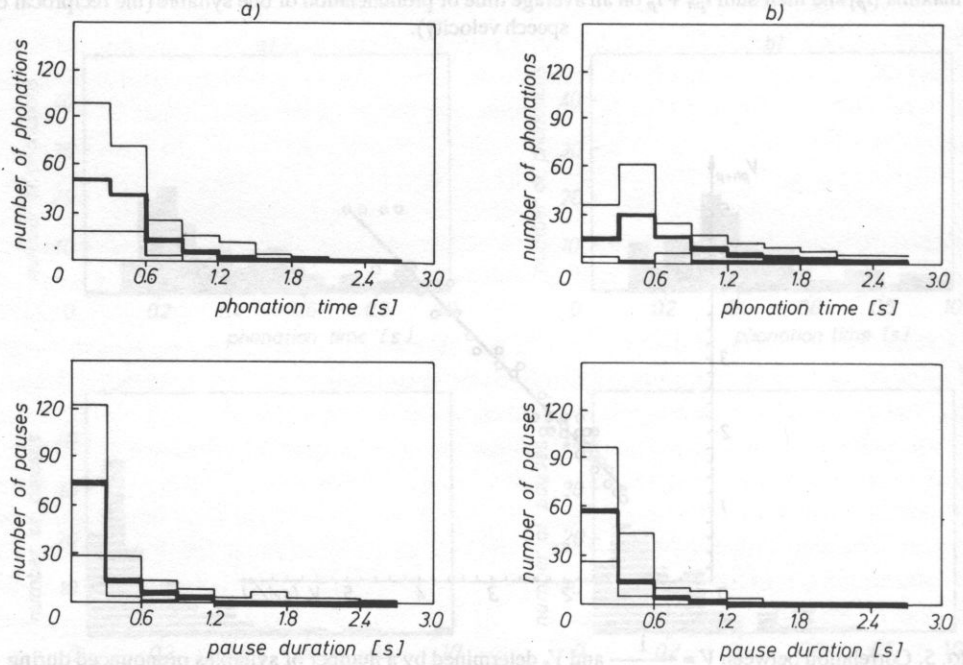

FIG. 7. Average (heavy line), maximum and minimum occurrences of phonation and pause durations in relevant time intervals calculated from utterances of 30 stutterers speaking a) with a simultaneous auditory feedback, b) with an echo.

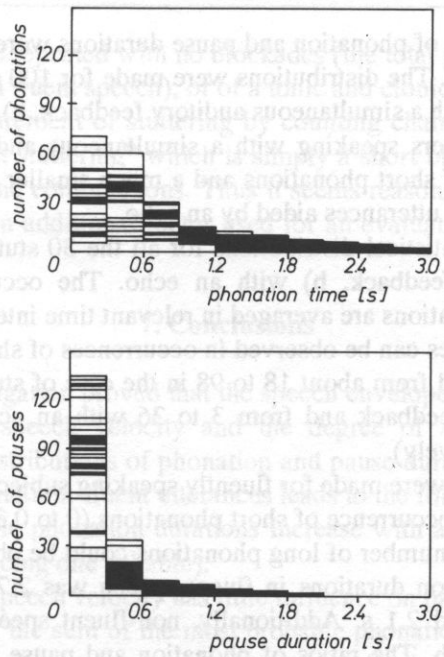

FIG. 8. Statistical distributions of phonation and pause durations in 100 second utterances of 30 fluently speaking subjects.

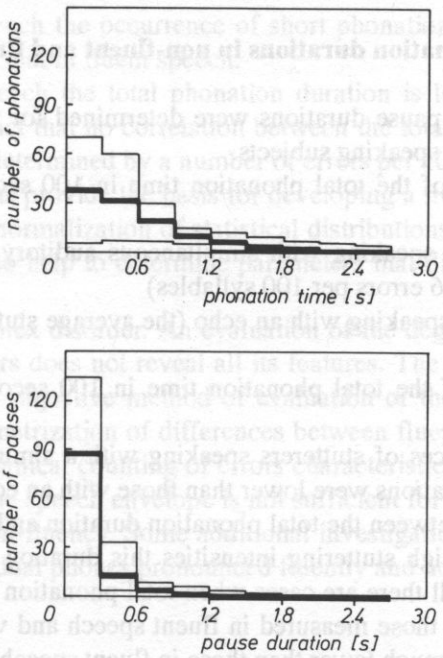

FIG. 9. Average, maximum and minimum occurrences of phonation and pause durations in relevant time intervals calculated from utterances of 30 fluently speaking subjects.

differences, distributions of phonation and pause durations were prepared assuming the time interval width 0.3 s. The distributions were made for 100 second utterances of 30 stutterers speaking a) with a simultaneous auditory feedback, b) with an echo.

Utterances of stutterers speaking with a simultaneous auditory feedback show a much greated number of short phonations and a much smaller number of long phonations in comparison with utterances aided by an echo.

Figure 6 presents statistical distributions for all the 30 stutterers speaking a) with simultaneous auditory feedback, b) with an echo. The occurrences of indivudual phonation and pause durations are averaged in relevant time intervals (Fig. 7).

Significant differences can be observed in occurrences of short phonation durations (0 to 0.3 s) which ranged from about 18 to 98 in the case of stutterers speaking with a simultaneous auditory feedback and from 3 to 36 with an echo (the average values were 49 and 15, respectively).

Similar distributions were made for fluently speaking subjects (Figs. 8 and 9).

In fluent speech the occurrence of short phonations (0 to 0.3 s) ranged from 4 to 70 (average: 37). A greater number of long phonations could be observed here. The range of uninterrupted phonation durations in fluent speech was 2.7 s, while in non-fluent speech it did not exceed 2.1 s. Additionally, non-fluent speech contains more long pauses that fluent speech. The ratios of phonation and pause durations in fluent and non-fluent speech were determined by a measurement of total phonation durations.

6. Total phonation durations in non-fluent and fluent speech

Total phonation and pause durations were determined for utterances of all the 30 stutterers and 30 fluently speaking subjects.

The average values of the total phonation time in 100 second utterances of stutterers were:

a) 55 seconds when speaking with simultaneous auditory feedback (the average stuttering intensity was 16 errors per 100 syllables)

b) 72 seconds when speaking with an echo (the average stuttering intensity was 1.7 errors per 100 syllables).

An average value of the total phonation time in 100 second utterances of fluent speakers was 72 seconds.

In almost all utterances of stutterers speaking with a simultaneous auditory feedback, total phonation durations were lower than those with an echo. However, no correlation can be observed between the total phonation duration and the stuttering intensity. Though in the case of high stuttering intensities this duration is significantly smaller than in fluent speech, still there are cases when total phonation durations at high levels of stuttering are close to those measured in fluent speech and vice versa, at low levels of stuttering they can be much lower than those in fluent speech. This is connected with the various forms stuttering can assume. It can be of a tonic nature, i.e., with a predomination of blockades (then the total phonation time will be small); of a clonic nature,

when speech sounds are repeated with no blockades (the total phonation time would be close to that observed in fluent speech); or of a tonic and clonic nature.

The auditory measurement of stuttering by counting characteristic errors does not reveal so-called "hidden stuttering" which is simply a short blockade or an intentional avoidance of some phone combinations. Thus it seems reasonable to measure the total phonation duration as an additional factor used for an evaluation of speech fluency or therapeutic results.

7. Conclusions

The reported investigation proved that the speech envelope could be a source of information about both speech velocity and the degree of speech non-fluency. An analysis of statistical distributions of phonation and pause durations and a total phonation duration in fluent and non-fluent utterances leads to the following conclusions:

1. The most probable phonation durations increase with a drop in speech velocity (longer time of pronouncing one syllable).

2. A slow-down in speech velocity has little influence on pause durations.

3. The reciprocal of the sum of the most probable phonation duration and the most probable pause duration is correlated with speech velocity defined as a number of syllables pronounces during 1 second. The relationship can be used for speech velocity measurements.

4. In non-fluent speech the occurrence of short phonations (shorter than 0.3 s) is significantly lower than that in fluent speech.

5. In non-fluent speech the total phonation duration is lower than that in fluent speech in spite of the fact that no correlation between the total phonation duration and the stuttering intensity determined by a number of errors per 100 syllables.

The presented results provide the basis for developing a method of speech velocity evaluation through the normalization of statistical distributions of phonation and pause durations. They will also help to determine parameters that differentiate fluent speech from that of stutterers.

Stuttering is a complex disorder. An evaluation of the degree of this disorder by a simple counting of errors does not reveal all its features. The aim of the presented research is to develop an objective method of evaluation of the degree of speech non-fluency through a parametrization of differences between fluent and non-fluent speech and not through a mechanical counting of errors characteristic of stuttering. The information obtained from the speech envelope is not sufficient for an explicit evaluation of the degree of speech non-fluency. Some additional investigation into the differences in characteristics of individual phones pronounced fluently and not fluently will follow.

Acknowledgement

I wish to thank Prof. Bogdan ADAMCZYK for his valuable remarks and discussion.

The work reported in this paper is part of a research series supported by Program CPBP 02.03.9.4.

References

[1] B. ADAMCZYK, W. KUNISZYK-JÓŹKOWIAK, E. SMOŁKA, *Correction effect in chorus speaking by stuttering people*, XVIth International Congress of Logopedics and Phoniatrics, Interlaken 2–6 (1976).

[2] B. ADAMCZYK, W. KUNISZYK-JÓŹKOWIAK, E. SMOŁKA, *Influence of echo and reverberation on the speech process*, Folia Phoniatrica **31**, 70–81 (1979).

[3] B. ADAMCZYK, W. KUNISZYK-JÓŹKOWIAK, *Effect of echo and reverberation of a restricted capacity on the speech process*, Folia Phoniatrica, **39**, 9–17 (1987).

[4] J. AGNELLO, *Voice onset and termination features of stutterers*, in: L. M. Webster and L. Furst (eds.), Vocal tract dynamics and dysfluency, New York: Speech and Hearing Institute, 1975, 40–70.

[5] W. KUNISZYK-JÓŹKOWIAK, B. ADAMCZYK, *Effect of filtered echo and reverberation on speech velocity* (in Polish), Archiwum Akustyki, **18**, 3, 280–294 (1980).

[6] W. KUNISZYK-JÓŹKOWIAK, B. ADAMCZYK, *Effect of auditory and tactile echo and reverberation on stuttering*, Proceedings XV Congress Union European Phoniatricians, Erlangen 1988, 103–105 (1988).

[7] W. KUNISZYK-JÓŹKOWIAK, B. ADAMCZYK, *Correlations between speech velocity decrease and speech fluency in stutterers under echo and reverberation*, XXIst Congress of the "International Association of Logopedics and Phoniatrics, Prague, 152–154 (1989).

[8] W. KUNISZYK-JÓŹKOWIAK, B. ADAMCZYK, *Effect of tactile echo and tactile reverberation on the speech fluency of stutterers*, International Journal of Rehabilitation Research, **12**, 3, 312–317 (1989).

[9] H. F. M. PETERS, L. BOVES, C. H. INEKE VAN DIELEN, *Perceptual judgement of abruptness of voice onset in vowels as a function of the amplitude envelope*, Journal of Speech and Hearing Disorders, **51**, 299–308 (1986).

Received on November 20, 1990

ARCHIVES OF ACOUSTCS
17, 1, 17–30 (1992)

TIMBRE, TONE COLOR, AND SOUND QUALITY : CONCEPTS AND DEFINITIONS

T. ŁĘTOWSKI

Department of Communication Disorders
The Pennsylvania State University
University Park, PA 16802

Timbre is a magic word used by composers, musicians, sound engineers, and other audio and hearing professionals to describe all auditory sensations other than pitch, loudness, and perceived duration. The concept of timbre is widely used and has a long tradition. However, the meaning of timbre is fuzzy and encompasses an enormous variety of phenomena. The formal definition of timbre, as accepted by the American Standards Association, is very limited and impractical and there is little consistency in its interpretation. There also is general confusion regarding relations among timbre, tone color, and sound quality, which are frequently treated as synonymous terms. In addition, a multidimensional character of timbre is not supported by a practical system of well-defined and clearly linked dimensions. To develop such a system one needs to clarify the meaning of timbre and to reexamine its current definition.

1. Introduction

Music and speech, together with visual information, are two of the most important elements of human communication and artistic expression. Changes in loudness, pitch, timbre, tempo, and rhythmic pattern of mutually related sounds efficiently convey various moods, impressions, desires and intellectual arousal. Through the centuries humanity has developed large numbers of spoken languages and very sophisticated musical systems. It also has enlarged substantially musical instrumentarium. The technical means to produce, transmit, and reproduce sound-based information has been also improved significantly, especially during the last thirty years. In this context it is alarming that our ability to communicate with words about sound is still very limited and does not match our abilities to manipulate the sound.

The area that especially lacks uniform and clear terminology is the area of sound quality (Pol. jakość dźwięku), tone color (Pol. brzmienie), and timbre (Pol, barwa dźwięku). Despite some standardized definitions and many attempts to discover underlying elements of these terms, the meaning and range of them are still unclear. There is

also a multitude of other terms that appear to have identical or very similar meaning with terms listed above. A selected list of such terms is presented in Table 1.

Table 1. The most common terms with meanings synonymous with or very similar to timbre which have appeared in selected publications on speech and music perception, psychoacoustics, and audiology

GENERAL:	sound quality
	tone quality
	sound color
	tone color
	spectral timbre
	spectral color
	timbral color
	timbral quality
MUSIC:	musical quality
	musical color
	musical timbre
	instrumental color
	instrumental timbre
SPEECH:	voice quality
	vocal quality
	vowel quality
	vowel color
	vocal color

The lack of precision and stability of terminology has led to enormous richness of terms used by both professionals and general public in describing changes in sound. The large number of terms used in sound description is a blessing for artistic freedom of expression, but it is a source of problems when it comes to communication among people. Effective communication requires a formalized system of terms where all denotations are clearly defined and linked together in both the vertical and the horizontal structures.

Despite the richness of vocabulary used by professionals in describing the sound, or maybe rather due to it, the average person has little or no vocabulary for explaining his perceptual and emotional reactions to sound. There are several reasons why public illiteracy in sound description has developed at a time when so much effort has been given to enrich our musical perception and to develop "true-to-nature" sound reproduction. Among them are (1) overemphasis of visual communication in public education, (2) "loud is good" philosophy in audio entertainment, (3) traditional, counterproductive competition between "engineering" and "musical" description of sound, (4) myth of the "golden ears" created by some professional reviewers of sound- and audio-related pro-

ducts, and (5) problems with effective translation of sound-related terminology from one language into another. In addition, the meaning of some words changes as a function of profession (musician, sound engineer, audiologist, acoustic consultant, speech therapist), region, age, and cultural background. Some words also become suddenly more fashionable, and this temporarily broadens their meanings beyond the more-or-less established ones. Some researchers in the field also contributed to the present state of the art in public sound education by overemphasizing the need for experimental testing of specific hypothesis concerning the mechanisms underlying sound perception while neglecting the need for clear definitions of terms being tested. As a result there have appeared many publications on sound quality and timbre in which the conclusions contradict rather than complement each other. They help neither to understand the phenomena underlying timbral perception nor to improve our communication about sound.

An additional important source of difficulties in communicating about auditory sensations is misinterpretation or lack of understanding of the conceptual model underlying the adopted system of terms. In many cases one terminological system is as good as another, yet they cannot be mixed together without the risk of increasing the confusion. A typical logical error is assuming that (a) loudness, pitch and timbre are independent dimensions of perception and (b) different pure tones produce different timbre sensations. The nature of this error becomes more obvious later.

The purpose of this article is to discuss and clarify the meaning of the three basic terms used in the global description of sound: timbre, tone color, and sound quality. The article presents some of the author's concepts and offers suggestions on possible links between main psychoacoustical terms in an effort to make our communication easier and less ambiguous. The specific goal of this article is to advocate more general interpretation of timbre than has been found in the majority of the textbooks on musical acoustics and psychoacoustics and to differentiate between the connotations of timbre, tone color, and sound quality. The author also hopes that this article will invigorate discussion on timbre terminology that will ultimately become clear and logically structured.

2. The concept of timbre

Physical sounds stimulating our ears result in various auditory images that evolve in our perceptual space [22]. McAdams [23] defined auditory image as a "psychological representation of a sound exhibiting an internal coherence in its acoustical behavior". The stress on coherence is important, since different acoustical components are combined in the auditory space into a single percept representing a physically meaningful entity. Such a percept is a weighted sum of various underlying sensations and can be described in terms of their values. A single auditory image can be perceptually analyzed by the listener by focusing his attention on individual sensations or details of the image, and/or by making changes to his actual frame-of-reference [12]. Several coexisting images can also be merged together to create a more generalized picture of the acoustical environment surrounding the listener. This picture is the sound that we hear.

An auditory image is commonly described in terms of loudness, pitch, (perceived) duration, spaciousness, and timbre. While loudness, pitch, and perceived duration can be considered as one-dimensional magnitudes, both spaciousness and timbre clearly have a complex (multidimensional) character.

Loudness is that attribute of an auditory image that reflects the listener's impression of the amount of sound energy which reaches the ear. A loudness scale orders sounds from soft to loud.

Pitch is that attribute of an auditory image that reflects the listener's impression of the location of the dominant spectral component along the frequency scale. A scale of pitch orders sounds from low to high.

Perceived duration is that attribute of an auditory image that reflects the listener's impression of the physical duration of a stimulus. A scale of perceived (apparent) duration orders sounds from short to long.

All three above-defined parameters are widely recognized as the universal attributes of auditory images. This means that, in general, they are neither source nor process specific. This cannot be said about the other two attributes, especially timbre, which first and foremost carries information about a source of sound and/or characteristics of sound transmission.

Timbre has been defined by the American Standard Association (ASA) [1] as "that attribute of ausitory sensation in terms of which a listener can judge that two sounds similarly presented and having the same loudness and pitch are dissimilar". This definition is supplemented by a note stating that "timbre depends primarily upon the spectrum of the stimulus, but it also depends upon the waveform, the sound pressure, the frequency location of the spectrum, and the temporal characteristics of the stimulus."

The ASA definition follows in its concept the original definition of timbre (Klangfarbe) formulated by HELMHOLTZ [11]. The phrase "similarly presented" refers foremost to sound duration and spatial presentation. In a similar definition offered by PLOMP [28], loudness and pitch are supplemented by apparent duration.

Timbre, understood in the above way, encompasses a vast variety of phenomena, yet its formal definition is very limited and does not permit one to compare timbres of two arbitrary sounds. In an important attempt to clarify the meaning of timbre, PRATT and DOAK [30] revised ASA and Plomp's definitions to the form given below.

Timbre is that attribute of auditory sensation whereby a listener can judge that two [similarly presented] sounds are dissimilar using any criteria other than pitch, loudness or duration.

Pratt and Doak's intention was to free the timbre definition from the impression that judgement of timbre must take place under conditions of equal loudness, pitch, and duration. Their timbre definition is also more suitable for atonal (undefined-pitch) sounds.

In its narrow interpretation timbre depends on the spectrum of the stimulus and can be interpreted as the perceived spectrum, i.e. the listener's reaction to the distribution of sound energy along the frequency scale. Such reaction involves both the spectral envelope and the spectral distribution of sound components. This narrow interpretation of

timbre, however, is only applicable to steady state sounds (static timbre). Timbre of sounds varying in time (dynamic timbre) depends additionally upon the waveform envelope and the temporal characteristics of the stimulus. These two aspects of timbre have been called "musical quality" and "sound quality", respectively, by HELMHOLTZ [11].

It is generally accepted that the same sound reaching our ear with different sound intensities causes different timbre sensations. There is no consensus, however, whether the same musical note played on the same musical instrument with two different dynamic levels invokes identical or different timbre sensations. And if we can recognize that two sounds were played on the same musical instrument, does it mean that they have produced identical timbre sensations? Answers to such questions cannot be given on the basis of the existing definition of timbre.

The authors of the ASA definition of timbre seem to accept the existence of a certain, three-dimensional auditory space with two of the dimensions labeled as loudness and pitch. What they have not specified clearly enough is whether the sensation of timbre is or is not independent of sensations of loudness and pitch. In other words, they did not specify if pitch and loudness were dimensions of timbre, or if all three of them were orthogonal dimensions of something else. A good analogy to such ambiguity is the description of an elongated cube (perpendicular parallelepiped) either with the help of its three basic dimensions (a, b, c) or by its volume (V) and two of its basic dimensions. Since $V = abc$, both descriptions are correct and satisfactory, yet as long as all the components of the equation are not identified, we do not know whether we talk about three linear variables or two linear plus one global variable.

3. Hearing-vision analogy

In many instances drawing an analogy between two similar systems helps to understand the inner workings of one of them. In the case of the auditory system such a reference is usually the visual system. A visual image has two main attributes: color and form. Perception of color is called color vision, and perception of form is called spatial vision. Color vision refers to the perception of light, while spatial vision refers to the perception of patterns and details in the visual world. These two types of vision closely resemble two types of hearing: spectral hearing and spatial hearing.

Color, like beauty, is in the eye of beholder [4]. The sensation of color derives from intensity, dominant wavelength, and composition (purity) of light. These three elements have their perceptual counterparts in brightness (sometimes calles lightness), hue, and saturation.

Brightness (lightness) is the aspect of color sensation that comes from the amount of energy of light waves. However, the phenomenal brightness of light depends not only on energy but also on frequencies involved. This dependency is a close analog to the mechanisms underlying the sensation of loudness.

Hue (chroma) is the sensation reported by an observer with normal color vision exposed to monochromatic light, i.e. to a single electromagnetic wavelength falling be-

tween approximately 420 (violet) and 740 (red) nanometers. Hues are numbered from 1 to 24 and traditionally represented on a color circle, called the Oswald circle. Distances between two successive hues along the circle correspond to just noticeable differences and therefore differ in the size of intervals along the frequency scale. Such a scale resembles the Bark (critical band) scale of pitch sensation [34, 46].

Saturation (strength of hue) refers to the purity (dominance) of a particular wavelength contributing to color sensation. The narrower the band of wavelengths, the more highly saturated is the resulting color sensation. Two different hues combined together produce another hue but with lower saturation than would be produced by the monochromatic light of corresponding frequency. If the number of hues added to the sensation becomes large enough the resulting sensation approaches gray. Several scales of saturation have been developed to describe the change in sensation resulting from an increase in the number of hues. The most widely known scale has been developed by INDOW and STEVENS [13] and is based on a unit called "chrome".

The above description of color vision indicates a strong analogy between loudness of sound and brightness of color and between pitch of sound and hue of color. According to CHRISTMAN [4] and KIMBLE and GARMEZY [15], there is also an analogy between saturation of color and timbre of sound. Such sets of analogies would speak of the close relationship between the organization of visual and auditory spaces. However, the last analogy seems to be superficial since saturation of color is a unidimensional phenomenon while timbre of sound has a multidimensional character. To this author the auditory analog of the saturation of color is the strength of pitch (timbral tonality, tonal clarity, or width of sound [18]) rather than the complex timbre sensation.

4. The timbre confusion

On the basis of the information provided it is logical to assume, as PRATT and DOAK [30] seem to have assumed, that the American Standard Association intended to define timbre as a dimension orthogonal to loudness and pitch. Such a definition of timbre, disguised sometimes as quality or tone color, can be found in several dictionaries, lexicons, and research papers (e.g. [16, 31, 44]). However, since the definition of timbre itself is not unequivocal, global interpretation of timbre also is possible. Interestingly, such an interpretation is directly expressed, or can be inferred from positions taken toward timbre, by BLADON and LINDBLOM [2], CLARK and MILNER [5], NAKATANI and MERMELSTEIN [26], PORGES [29], SCHÖNBERG [35], TIFFANY and CARRELL [42], WINCKEL [45], and others.

Arnold SCHÖNBERG [35, pp. 503–504], as cited by WINCKEL [45, p. 118)), says, "I cannot accept the distinction between tone color and pitch as it generally is stated. I find that tone makes itself noticed through color, one dimension of which is pitch. Tone color is therefore the large area, of which pitch is one division." The concept of pitch as an attribute of timbre agrees also in essence with the concept of frequency-based timbre solfege [20], where timbre recognition is based on perceptual monitoring

of loudness density distribution along the pitch scale. Contemporary speech research also seems to accept the notion that timbre (quality) of vowel depends primarily on the combination of pitches given by prominent spectral peaks of physical sound.

A strong argument for loudness and pitch as dimensions of timbre comes from research on brightness (density) and volume sensations produced by pure and complex tones [3, 10, 17, 39, 41]. Results of these studies indicate that brightness and volume (a) are independent (orthogonal) of each other, and (b) can be unequivocally described in terms of loudness and pitch. In other words, they constitute a pair of new (rotated) coordinates in the loudness-pitch plane. Therefore, all those who accept Stevens' concept of volume and brightness and also assume that these dimensions are dimensions of timbre (as many people do) should also accept both pitch and loudness as timbre dimensions.

EISLER [7], GABRIELSSON and SJÖGREN [9], MCDERMOTT [25], SONE, KIDO, and NEMURA [38], and several other researchers who investigated timbre (quality, tone color) by means of factorial analysis of semantic differential also have found that loudness and/or pitch are dimensions of timbre. Such a result is hardly surprising since (a) loudness and pitch were included into a set of initial scales, (b) loudness and pitch are dominating perceptual attributes of sound, and (c) listeners probably had much more experience in judging loudness than most of the other attributes. Inclusion of loudness and/or pitch as initial scales of judgement in the above studies also means that the authors of those studies might consider loudness and/or pitch as attributes of timbre.

The above described ambiguity in the definition of timbre also contributes to the confusion about whether all pure tones produce different or identical timbre sensations (or have any timbre at all). If the meaning of timbre encompasses pitch and loudness, the answer should be affirmative, but if its meaning is independent of them, the answer should be negative. The psychoacoustical literature is divided on this subject and one can find statements supporting the former [40, 45] as well as the latter [28, 33, 43] view.

The facts and discussion presented above have led this author to the conclusion that timbre, as defined by ASA and understood as a sensation independent of pitch and loudness, is not the same "general timbre" to which we usually refer when talking about music and auditory sensations. Such "general timbre" clearly embraces both loudness and pitch. Therefore, one may conclude that we need two different terms to describe these two separate connotations. But then, which of these two connotations should still be labeled "timbre"? And how should the other term be labeled to clarify the issue rather than to deepen existing confusion? Finally, one has to realize that any attempt to redefine the "fuzzy" meaning of timbre may likely result in a massive opposition by one or another group of the society. SLAWSON [37] warns that since timbre "is already used widely in many different senses by scientists, music theorists, and composers, it would be hopeless to try to reach agreement on a single meaning." This is certainly true when the "new" meaning of timbre is a relatively narrow one. However, the present author believes that a single but at the same time clear and sufficiently broad meaning of timbre, which embraces many various "denominations of timbre", will help us to

communicate and will earn a general acceptance.

In this content it should be noted that the idea to supplement "timbre" by another auxiliary term is not a new one. In a frustrating attempt to answer the question whether two different sounds played on the same musical instrument produce or do not produce the same timbre sensation, KITAMURA [16] suggested replacing timbre by two separate timbre-related terms: (a) sound impression produced by characteristic properties of the sound source (sound color), and (b) "sound impression expressed by descriptive adjectives of sound color" (quality of sound color). Similar frustration seems to have led SLAWSON [37, p. 20] to introduce the term "sound color" to denote an abstract, i.e. having no reference to a specific mode of sound production, representation of the timbre. One may wonder, however, whether the proposed distinctions are practical and if they do not clutter even more the differentiation between the phenomena of sensation and perception.

5. The expanded concept of timbre

The concept of timbre presented in this paper is built directly upon the ambiguity of the ASA definition that permits interpretation of timbre as a global dimension embracing both pitch and loudness. According to this concept, timbre is a global sensation embracing all other sensations reflecting the spectral, but not the spatial, character of sound. Such sensations include but are not limited to loudness, pitch, perceived duration, brightness, roughness, annoyance, etc. Thus, timbre is, first and foremost, an N-dimensional spectral sensation. It can be viewed in different frames-of-reference, analyzed along various scales of attributes, or judged as a whole according to one of the designated criteria of timbre (pleasantness, naturalness, or fidelity) [19]. Therefore, two sounds which produce the same sensation of loudness but sound different, produce different timbre sensations observed in $(N - 1)$ – dimensional space. When both loudness and pitch are identical the timbre difference is confined to $N - 2$ dimensions. Every comparative judgment involving the perceived spectra of two or more sounds can therefore be viewed as a timbre judgment in a limited timbral subspace.

The above generalized concept of timbre is practical and seems to be intuitively adopted in many studies in music, psychoacoustics, and quality assessment of audio transmission. Its main advantages are:

(1) it captures well the popular meaning of timbre and permits elimination of the "ambiguity and awkwardness" [42] of the current definition of timbre;

(2) it applies to both the comparative and the absolute assessment of sound; comparison of timbre of a particular sound to our preconceptions does not seem to involve a conscious adjustment in pitch and/or loudness;

(3) it can be successfully applied in perceptual comparison among sounds having only either equal loudness or pitch;

(4) it embraces both tonal and atonal sounds; and

(5) it permits treatment of correlated scales of annoyance and loudness as two di-

mensions of timbral space (the classical interpretation of timbre separates loudness from timbre).

According to the above concept of timbre both the ASA definition and the PRATT and DOAK'S definition [30] of timbre are acceptable and valid as long as loudness, pitch, and perceived duration of all compared sounds are kept constant. These definitions, however, do not reflect an assumed generality of timbre connotation. Such a general definition should be formulated as, or in a manner similar to, the definition given below.

Timbre is that multidimensional attribute of an auditory image in terms of which the listener judges the spectral character of sound. Timbral differences observed among a group of sounds are meaningful only as long as they refer to the same conditions of comparison.

A complementary definition of spaciousness can be formulated as follows.

Spaciousness is that multidimensional attribute of an auditory image in terms of which the listener identifies the size and locations of various sound sources and the size of acoustical space. Spatial differences observed among a group of sounds are meaningful only as long as they refer to the same conditions of comparison.

If differences along one dimension of timbre, such as loudness, dominate overall perception of sound and are not a desired object of assessment, such differences can be equalized; i.e., the said dimension can be excluded from assessment. After such a dimension is excluded from consideration, the auditory images are projected to $(N-1)$ – dimensional space, and the differences among the images along the remaining dimensions of perceptual space become more pronounced. This operation can be extended on more than one dimension. The resulting $(N-k)$ – dimensional space, where k is the number of dimensions removed from consideration, may be called a "residual space" or "residual dimension". Many such spaces can be created with different dimensions removed (equalized). They need, however, to be clearly labeled for future identification. For example, one needs to know whether data obtained in two different studies on timbre refer to the same timbral space.

The above concept of "residual dimension" is not new and for many decades we have subscribed to the concept of timbre as a "residual dimension" representing the remaining differences in sensation when differences in loudness and pitch had been equalized. This particular residual dimension is very convenient in a variety of application. For example, normalized loudness and pitch are basic requirements for comparative assessment of musical instruments and sound reproduction systems. In some other cases, however, normalized loudness is all that is needed (e.g. selection of radio announcers, evaluation of pathological voices). Surprisingly, although timbre has been assigned as a residuum for both loudness and pitch together, we have not established similar residual dimensions for either loudness or pitch alone. Therefore, it seemms justified, and even beneficial, to accept a more general connotation of timbre and talk, when we need to, about loudness-equalized timbre (L – timbre), pitch-equalized timbre (P – timbre), loudness/pitch-equalized timbre (LP – timbre), and so on. Such a system of timbral sub-

spaces may be called the X – timbre system. A basic descriptive model of an auditory image that utilizes the X – timbre system of labels is shown in Fig. 1.

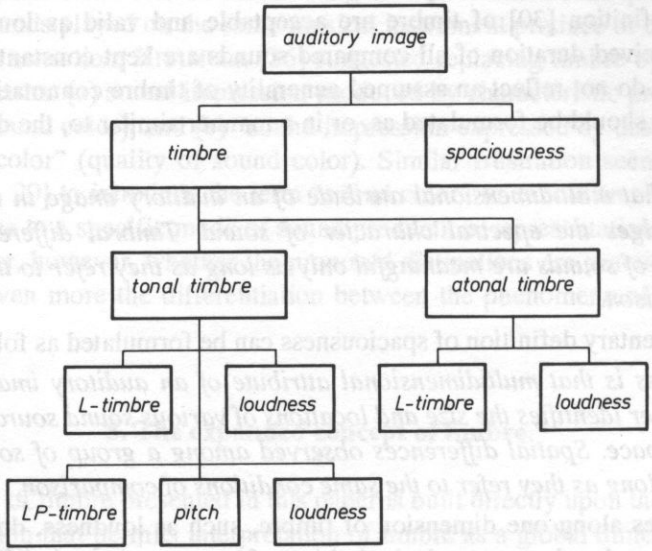

FIG. 1. Basic elements of a hierarchical model of the auditory image based on the concept of "residual dimensions" (X – timbre).

The X – timbre method of labeling the timbral subspaces is very flexible and cannot be outgrown. It constitutes a solid frame of reference needed for the future development of more specific attributes of auditory image which are necessary for parametric sound assessment [21]. Those among the readers who feel appalled by the "technical" character of X – timbre terms may always assign and define one or more "operational" labels and use them instead of X – timbre terminology. Such operational labels may be especially useful when particular timbral subspaces are widely and frequently used; e.g. LP – timbre subspace. In the case of LP – timbre, such a term might be "spectral timbre" or the "spectral color", which has already appeared in that context in the literature [24, 42]. In fact, as long as the concept of timbre presented in this study is used, the actual labels of timbral subspaces are of secondary importance providing they are clearly defined and generally acceptable. The readers are invited to help in developing such operational labels for frequently used subspaces.

6. Timbre vs. tone color

Most dictionaries and professional publications on music and acoustics are in agreement that timbre and tone color are two synonymous terms. Usually a third term, sound quality, also is added to this list. The term tone by itself, however, refers to a sound

which has a particular and usually well-defined pitch [31, 44]. Tone color, therefore, implies the tonal property of sound and should be used within such limits. Thus, it should only denote the timbre of a sound that has a defined pitch (tonal timbre).

According to the above interpretation, the sound having tone color always possesses timbre but the reverse statement is not always true. Therefore, tone color should be regarded as a timbral subspace rather than as a synonym of timbre.

Tone color is that attribute of an auditory image that reflects the listener's impression of the spectral character of a defined-pitch (tonal) sound and its changes under defined listening conditions.

Such a meaning of tone color is broader than the connotations given to "musical timbre" and "instrumental timbre" in music (e.g., [11, 36]) since it embraces defined-pitch noises and impulse sounds. The presented concept of tone color is also different from that of PLOMP [28], who suggested the possibility of using tone color to refer to the perceptual differences between steady-state complex tones.

7. Timbre vs. sound quality

As noted before, timbre, sound quality, and tone color, are traditionally regarded as synonymous terms [6, 11, 14, 32, 33]. The Random House Dictionary [31] refers to acoustic quality as "the texture of a tone, dependent on its overtone content, that distinguishes it from others of the same pitch and loudness", and to phonetic quality as "the tonal color, or timbre, that characterizes a particular vowel sound." Not everybody, however, follows such a concept. OLSON [27], for example, described timbre as "an instantaneous cross-section of the tone quality." FISHBURN [8] defined timbre as "tone quality plus tone color," and ŁĘTOWSKI [19, 21] described sound quality as the emotional aspect of timbre.

In general, quality may be broadly defined as a set of properties (features, characteristics) of a given object that determine the object's capacity to fulfill a particular need. The term quality refers, therefore, to both the designated character of an object and to the merit of its superiority. In the domain of psychoacoustics, the first of these meanings is parallel to the connotation of timbre while the second meaning is a unique one. Sound quality, therefore, can either imply timbre or a rating or emotional assessment and, in such cases, cannot be viewed as an equivalent to timbre which is emotionally neutral and simply represents differences among auditory images. One timbre is no better than another unless we set up a target (reference point) and judge the excellence of fit or superiority of one fit over another. Therefore, it seems logical to differentiate between timbre (perceptual attribute) and quality (emotional attribute) of sound. This permits timbre to reflect sound categories while sound quality reflects superiority, fit, and the listener's level of appreciation. Such a differentiation reflects well in the types of scales used for multidimensional (parametric) assessment. Timbre constituents are those which are assessed on the dominance or similarity scales, while quality components are assessed on the preference scales [19].

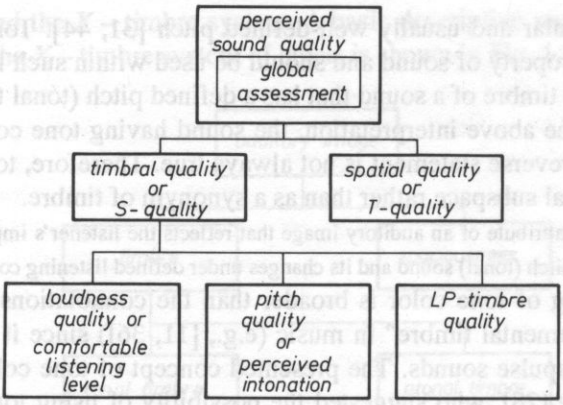

FIG. 2. General outline of a hierarchical model of sound quality assessment.

There is one more practical reason to differentiate between timbre and sound quality. Sound quality frequently extends beyond timbre and incorporates an impression of spaciousness. In such cases one may talk about timbral as well as spatial quality of sound. These two qualities merge together in the overall quality of sound. Sound quality, therefore, should be defined generally enough to embrace all of these meanings. Such a definition is proposed below.

Sound quality is that attribute of an auditory image in terms of which the listener can express his/her satisfaction or dissatisfaction with that image. Sound quality can be judged by comparing images produced by several external stimuli or by referencing a perceived image to the concept residing in the listener's memory.

Similarly as for timbre, we can differentiate between various "residual" subspaces of sound quality and label them correspondingly. For example, we can single out the spatial quality (timbre-equalized quality, or T – quality), loudness-equalized quality (L – quality), or loudness/pitch-equalized quality (LP – quality). The basic elements constituting the general frame of the timbral quality assessment are shown in Fig. 2. The terms displayed in Fig. 2. are designed to be used when the precise information about conditions of quality judgments is essential. In everyday human communication, when such information is not sought, the general term "sound quality" may be sufficiently descriptive.

8. Conclusions

The discussion presented above outlined certain implications resulting from various interpretations and/or understandings of timbre, tone color, and sound quality. The author's definitions of timbre, tone color and sound quality clearly differentiate between the denotations of these three terms. The author advocates a more general interpretation of timbre, than it is found in majority of textbooks on musical acoustics and psychoacoustics. His definition of timbre embraces both loudness and pitch as timbral dimensions. His concept of X-timbre extends the meaning of timbre also to smaller,

($N - k$) – dimensional, perceptual spaces ($k = 0, 1, 2, ..., N$). According to the author's belief, such a generalized concept of timbre and separation of timbre from tone color and sound quality, clear the way toward effective parametric description of auditory images.

Ideas presented in this paper are intended to make psychoacoustical terminology less ambiguous and more practical. The author hopes that his suggestions clarify rather than just modify existing terminology. Nevertheless, the concepts and suggestions presented in this article are only propositions and an invitation to join the efforts in making sound description and assessment clearer and more meaningful.

References

[1] American National Standards Institute. *USA Standard Acoustical Terminology*, S1.1-1960 (1960).

[2] R.A.W. BLADON, B. LINDBLOM, *Modeling the judgment of vowel quality differences*, J. Acoust. Soc. Am., **69**, 1414–1422 (1981).

[3] E.G. BORING, S.S. STEVENS, *The nature of tonal brightness*, Proc. Nat. Acad. Sci., 2, 514–521 (1936).

[4] R.J. CHRISTMAN, *Sensory experience*, Scranton, PA: Intext Educational Publishers, 1971.

[5] M. CLARK, P. MILNER, *Dependence of timbre on the total loudness produced by musical instruments*, J. Audio Eng. Soc. **12**, 29–33 (1964).

[6] C.A. CULVER, *Musical acoustics*, (4th edition), New York, NY: The Blakiston Co., 1956.

[7] H. EISLER, *Measurement of perceived acoustic quality of sound-reproducing systems by means of factor analysis*, J. Acoust. Soc. Am., **39**, 484–492 (1966).

[8] H. FISHBURN, *Fundamentals of music appreciation*, New York, NY: Longmans, Green, & Co., 1955.

[9] A. GABRIELSSON, H. SJÖGREN, *Perceived sound quality of sound-reproducing systems*, J. Acoust. Soc. Am., **65**, 1919–1933 (1979).

[10] M. GUIRAO, S.S. STEVENS, *Measurement of auditory density*, J. Acoust. Soc. Am., **36**, pp. 1176–1182 (1964).

[11] H.L.F. HELMHOLTZ, *On the sensation of tone*, (second English edition). London: Longmans & Co., 1885.

[12] R.C. HEYSER, *Geometrical considerations of subjective audio*, J. Audio Eng. Soc., **22**, 674–682 (1974).

[13] T. INDOW, S.S. STEVENS, *Scaling of saturation and hue*, Percept. Psychophys., **1**, 253–271 (1966).

[14] J.J. JOSEPHS, *The physics of musical sound*, Princeton, NJ: D. van Nostrand Co., Inc., 1967.

[15] G.A. KIMBLE, N. GARMEZY, *Principles of general psychology*, New York, NY: Ronald Press Co, 1968.

[16] O. KITAMURA, *The content of "timbre"*, The 2nd Joint Meeting of ASA and ASJ (paper SS21), November 1988.

[17] E. KÖTTER, *Der Einfluss ubertragungstechnischer Faktoren auf als Musikhören*, Koln: Arno Volk Verlag, 1968.

[18] T. ŁĘTOWSKI, *Pitch strength vs. subjective width of sound*, Prace Naukowe ITA, 43, 255–258 (1979). (in Polish with English abstract).

[19] T. ŁĘTOWSKI, *Auditory assessment of signals and their sources*, Warsaw: Warsaw Music Academy, 1984. (in Polish).

[20] T. ŁĘTOWSKI, *Development of technical listening skills: Timbre Solfeggio*, J. Audio Eng. Soc., **33**, 240–244 (1985).

[21] T. ŁĘTOWSKI, *Sound quality assessment: concepts and criteria*, The 87th AES Convention (preprint 1825), New York, 1989.

[22] T. ŁĘTOWSKI, W. MAKOWSKI, *Properties of auditory images*, Technika Radia TV, 1977, 1, 16–21 (in Polish).
[23] S. MCADAMS, *Spectral fusion, spectral parsing and the formation of auditory images*, Stanford, CA: Stanford University, Department of Music, Report STAN–M–22, 1984.
[24] S. MCADAMS, K. SAARIAHO, *Qualities and functions of musical timbre*, Vancouver: Proceedings of the International Computer Music Conference, 1985.
[25] B.J. MCDERMOTT, *Multidimensional analyses of circuit quality judgments*, J. Acoust. Soc. Am., **45**, 774–781 (1969).
[26] M. NAKATANI, P. MERMELSTEIN, *Subjective speech-to-noise ratio as a measure of speech quality for digital waveform coders*, J. Acoust. Soc. Am., **72**, 1136–1144 (1982).
[27] H. OLSON, *Music, physics, and engineering*, New York, NY: Dover, 1967.
[28] R. PLOMP, *Timbre as a multidimensional attribute of complex tones*, In *Frequency analysis and periodicity detection in hearing*, R. Plomp and F.G. Smoorenburd (Eds.). Leiden: Suithoff, 1970.
[29] G. PORGES, *Applied acoustics*, Los Altos, CA: Penninsula Publishing, 1977, p. 48.
[30] R. PRATT, P. DOAK, *A subjective rating scale for timbre*, J. Sound Vib., 45, 317–328 (1976).
[31] *Random House Dictionary of the English Language, The* (second edition, unabridged), New York, NY: Random House, 1987.
[32] J.G. ROEDERER, *Introduction to the physics and psychophysics of music*, New York, NY: Springer-Verlag, 1974.
[33] T. ROSSING, *The science of sound*, Reading, MA: Addison-Wesley Publishing Co., 1982.
[34] B. SCHARF, *Critical bands*, In: *Foundations of modern auditory theory*, Vol. 1, J.V. Tobias, Ed., pp. 157–202. New York, NY: Academic Press, 1970.
[35] A. SCHÖNBERG, *Harmonielehre*, Vienna: Universal Edition, 1922, (Quoted in Winckel, 1967).
[36] A.W. SLAWSON, *Vowel quality and musical timbre as functions of spectrum envelope and fundamental frequency*, J. Acoust. Soc. Am., **43**, 87–101 (1968).
[37] A.W. SLAWSON, *Sound color*, Berkeley, CA: University of California Press, 1985.
[38] T. SONE, K. KIDO, T. NEMURA, *Factor analysis of descriptive adjectives for the evaluation of sounds*, J. Acoust. Soc. Japan., **18**, 320–326 (1962). (in Japanese with English abstract).
[39] S.S. STEVENS, *Tonal density*, J. Exper. Psychol., 17, 585–592 (1934).
[40] S.S. STEVENS, *Hearing: its psychology and physiology* (second printing), New York, NY: American Institute of Physics, 1983, (original edition: 1937).
[41] S.S. STEVENS, M. GUIRAO, A.W. SLAWSON, *Loudness a product of volume times density*, J. Exper. Psychol., 69, 503–518 (1965).
[42] W.R. TIFFANY, J. CARRELL, *Phonetics: Theory and application*, New York: McGraw-Hill Book Co., 1977.
[43] W.D. WARD, *Musical perception*, In: *Foundations of modern auditory theory*, vol. 1, J. V. Tobias, Ed. New York, NY: Academic Press, 1970.
[44] D.W. WHITE, *The audio dictionary*, Seattle, WA: University of Washington Press, 1987.
[45] F. WINCKEL: *Music, sound, and sensation*, New York, NY: Dover, 1967.
[46] E. ZWICKER, *Subdivision of the audible frequency range into critical bands* (Frequenzgruppen), J. Acoust. Soc. Am., **33**, 248 (1961).

Received on October 30, 1990

ARCHIVES OF ACOUSTICS
17, 1, 31–41 (1992)

NOISE GENERATED BY A MOVING LINE SOURCE IN A DISSIPATIVE ATMOSPHERE

R. MAKAREWICZ

Institute of Acoustics, A. Mickiewicz University
(60-769 Poznań, ul. Matejki 48)

It is the purpose of this paper to present the resultant effect of geometrical spreading, air absorption, Doppler frequency shift and the distortion of the sound field due to the motion of a line source. It is assumed that the source is moving slowly along a straight line. The results obtained can be used for prediction of the A– weighed sound pressure level of railway noise.

Introduction

The sound field of any moving source is affected by the Doppler effect and convection effect. To give more accurate description, one has to take into account air absorption as well.

This paper will attempt to describe the combined effect of all these phenomena for a continuous line of dipole sources.

Well-known relations for a motionless line source have been used as the starting point (Section 1). Under the assumption of a low Mach number, explicit functions for mean-square sound pressure and its spectral density have been derived in Section 2, for both nondissipative and dissipative mediuma.

The results presented in this paper can be employed for railway noise prediction.

1. Source at rest

Some sources of noise, among them train noise, can be modeled by a continuous line of incoherent dipole sources. Hence the spectral density of the mean square sound pressure produced by a unit length is

$$\tilde{p}^2 = \frac{N(f)\cos^2\phi\rho c}{r^2}\exp\{-2\alpha(f)r\}, \tag{1}$$

where the characteristic impedance of air, ρc, equals 415 rayls (speed of sound

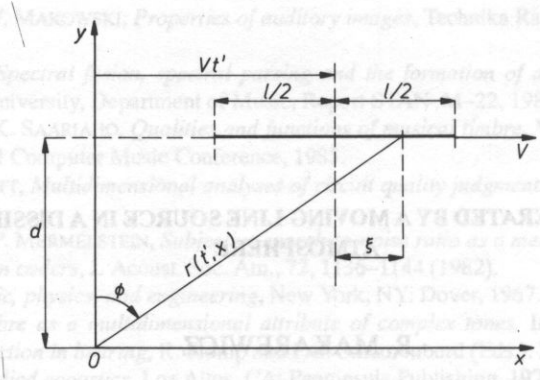

FIG. 1. Geometry of the moving line source with respect to the point of observation 0.

$c = 343$ m/s, air density $\rho = 1.21$ kg/m^3). The distance r and the angle ϕ are defined in Fig. 1.

Spectral characteristic

$N(f)$ in the above equation expresses the spectral characteristic of a source. There are many real sources for which $N(f)$ has one absolute maximum. Such a spectrum can be approximated by the function

$$N(f) = N^{(0)} f^m \exp(-\mu f), \quad m \geq 0. \tag{2}$$

The integration of this equation from $f = 0$ to $f = \infty$ gives (Ref. [1], integral 3.351.3):

$$N = N^{(0)} m!\, \mu^{-(m+1)}. \tag{3}$$

The spectrum described by Eq. (2) peaks at $f_{\max} = m/\mu$ and its maximal value is

$$N(f_{\max}) = \frac{N^{(0)}\mu}{m!}\left(\frac{m}{e}\right)^m. \tag{4}$$

The set of sources of the same value of N and with $m = 0, 1, 2, \ldots$ can be described by the following equation, as illustrated in Fig. 2:

$$N(f) = \frac{N}{m!}\,\mu^{m+1} f^m \exp(-\mu f). \tag{5}$$

For a large value of μ low frequencies predominate. If the parameter μ decreases, then $N(f_{\max})$ (Eq. 4) declines and $f_{\max} = m/\mu$ shifts toward high frequencies.

The results of measurements of the sound pressure level with banpass filtres can be converted to the spectrum level. Then, making use of regression analysis, the numerical values of the parameters $N^{(0)}$, m and μ can be found. For example, the A– frequency weighed railroad noise can be characterized by $N^{(0)} \approx 10^{-12}$, $m = 3$, $\mu = 2 \cdot 10^{-3}$

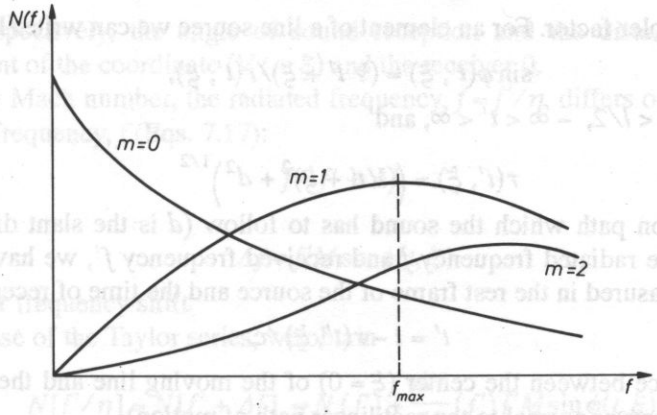

FIG. 2. Spectral characteristic of source (Eq. 2).

Atmospheric absorption

The absorption coefficient $\alpha(f)$ (Eq. 1) depends strongly on the frequency (f), and relative humidity (h_r), and less strongly on temperature (T). It also depends slightly on the ambient pressure. The explicit form of the function $\alpha(f, h_r, t)$ is rather complicated [2]. Under some conditions [3] the absorption coefficient α can be approximated by a linear function of frequency

$$\alpha(f, h_r, T) = \beta(h_r, T)f, \tag{6}$$

where

$$\beta = \alpha(f^*_{\max}, h_r, T)/f^*_{\max}.$$

Frequency f^* depends on the power spectrum of the source [3]. The numerical values of $\alpha(f^*, h_r, T)$ are given in international standards such as ANSI S1.26 or ISO 3891–1978 E.

2. Moving source

In this paper we restrict our attention to a line source of length l which moves with constant speed, V much smaller than the speed of sound c (Mach number $M = V/c << 1$), along a straight line at slant distance $d >> l/2$ (Fig. 1).

Due to the motion of the dipole, its radiation field, i.e., the spectral density $p^2(f')$ and the received frequency, f', become different from that produced when the source is at rest, $\tilde{p}^2(f)$, and f (Eq. 1). The convection and the Doppler effects are given by [4,5]:

$$\tilde{p}^2 = p^2\eta^4, \quad f' = f\eta, \tag{7}$$

where

$$\eta(t', \xi) = (1 + M\sin\phi(t', \xi))^{-1} \tag{8}$$

denotes the Doppler factor. For an element of a line source we can write (Fig. 1)

$$\sin\phi(t', \xi) = (V t' + \xi)/r(t', \xi), \tag{9}$$

where $-l/2 < \xi < l/2$, $-\infty < t' < \infty$, and

$$r(t', \xi) = \left((Vt' + \xi)^2 + d^2\right)^{1/2} \tag{10}$$

is the propagation path which the sound has to follow (d is the slant distance). Corresponding to the radiated frequency f and received frequency f', we have the time of emission (t') measured in the rest frame of the source and the time of reception (t) :

$$t' = t - r(t', \xi)/c. \tag{11}$$

Vt' is the distance between the center ($\xi = 0$) of the moving line and the y – axis (the line from the observer normal to the rectilinear path of motion).

From Eqs. (10) and (11), we get

$$Vt' = \left\{ Vt - M^2\xi - M\left[(Vt)^2 + (1 - M^2)d^2 + (ct + M\xi)^2 - (ct)^2\right]^{1/2} \right\}/(1 - M^2). \tag{12}$$

2.A. Nondissipative medium

A.1. Spectral density of mean square sound pressure. For a nondissipative medium we set $\alpha = 0$ and Eqs. (1,7) yield the spectral density of mean square sound pressure produced by a unit length:

$$p^2(f', \xi) = \frac{N(f'/\eta(\xi))d^2\rho c}{r^4(\xi)}\eta^4(\xi). \tag{13}$$

The total spectral density of mean square sound pressure is obtained by integration over the length of the line source (Eq. 13):

$$p^2(f') = d^2\rho c \int_{-l/2}^{l/2} \frac{N(f'/\eta(t', \xi))\eta^4(t', \xi)}{r^4(t', \xi)} d\xi. \tag{14}$$

where $\eta(t', x)$ and $r(t', \xi)$ are defined as above (Eqs. 8–10).

To get some insight into the physics of sound generation and propagation, we approximate the integral (14) under the assumption of a low Mach number: $M << 1$ and $l/2 << d$. Thus we can write (Eqs. 8–10, 12).

$$Vt' = Vt - Mr(t, 0), \tag{15}$$

$$r(t', \xi) = r(t, \xi)\left[1 - M\sin\phi(t, \xi)\frac{r(t, 0)}{r(t, \xi)}\right], \tag{16}$$

$$\eta(t', \xi) = 1 - M\sin\phi(t, \xi), \tag{17}$$

where

$$\sin\phi(t, \xi) = \frac{Vt + \xi}{r(t, \xi)} \quad \text{and} \quad r(t, \xi) = \left\{(Vt + \xi)^2 + d^2\right\}^{1/2} \tag{18}$$

represent, respectively, the angle of sound reception and the distance between the source element of the coordinate $(V t + \xi)$ and the receiver 0.

For a low Mach number, the radiated frequency, $f = f'/\eta$, differs only slightly from the received frequency, f (Eqs. 7.17):

$$f \approx f' + \Delta f, \tag{19}$$

where

$$\Delta f = f' M \sin \phi(t, \xi)$$

is the Doppler frequency shift.

Making use of the Taylor series, we obtain

$$N[f'/\eta] = N[f' + \Delta f] \approx N(f') + \frac{dN}{df'}(f') f' M \sin \phi(t, \xi). \tag{20}$$

Finally the expressions (14–17, 20) give the total spectral density of mean square sound pressure:

$$p^2(f', t) = p_S^2(f', t) + p_D^2(f', t) + p_C^2(f', t), \tag{21}$$

where

$$p_S^2(f', t) = d^2 \rho c N(f') \int_{-l/2}^{l/2} \frac{d\xi}{r^4(t, \xi)} \tag{22}$$

corresponds to a "quasi-stationary" source,

$$p_D^2(f', t) = M d^2 \rho c \frac{dN}{df'}(f') f' \int_{-l/2}^{l/2} \frac{\sin \phi(t, \xi)}{r^4(t, \xi)} d\xi \tag{23}$$

describes the influence of the Doppler effect, and

$$p_C^2(f', t) = 4 M d^2 \rho c N(f') \int_{-l/2}^{l/2} \left[\frac{r(t, 0)}{r(t, \xi)} - 1 \right] \frac{\sin \phi(t, \xi)}{r^4(t, \xi)} d\xi, \tag{24}$$

can be related to the convection effect.

The influence of both effects (p_D^2, p_C^2) is proportional to the Mach number. However, we have assumed $M << 1$; therefore the quasi-stationary source $(p_S{}^2)$ tends to dominate.

Making use of a table of integrals [1], we get the formulas (Eqs. 18, 22–24):

$$p_S^2(f', t) = \frac{1}{2} \frac{\rho c}{d} N(f') F_S(t), \tag{25}$$

$$p_D^2(f', t) = \frac{1}{3} M \frac{\rho c}{d} f' \frac{dN}{df'}(f') F_D(t), \tag{26}$$

$$p_C^2(f', t) = \frac{1}{3} M \frac{\rho c}{d} N(f') F_C(t), \tag{27}$$

with the time functions

$$F_S(t) = \sin\phi_2\cos\phi_2 - \sin\phi_1\cos\phi_1 + \phi_2 - \phi_1, \tag{28}$$

$$F_D(t) = \cos^3\phi_1 - \cos^3\phi_2, \tag{29}$$

$$F_C(t) = 3[1 + (Vt/d)^2]^{1/2}(\cos^4\phi_1 - \cos^4\phi_2) - 4(\cos^3\phi_1 - \cos^3\phi_2), \tag{30}$$

where the angles ϕ_2 and ϕ_1 are associated with the leading and trailing edge of the line source:

$$\sin\phi_2 = \frac{Vt + l/2}{\left((Vt + l/2)^2 + d^2\right)^{1/2}}, \quad \sin\phi_1 = \frac{Vt - l/2}{\left((Vt - l/2)^2 + d^2\right)^{1/2}}, \tag{31}$$

$$\cos\phi_2 = \frac{d}{\left((Vt + l/2)^2 + d^2\right)^{1/2}}, \quad \cos\phi_1 = \frac{d}{\left((Vt - l/2)^2 + d^2\right)^{1/2}}.$$

At $t = 0$, when the center of the line source ($\xi = 0$) is opposite to the point of observation, the above expressions yield: $p_D^2(f, 0) = 0$ and $p_C^2(f, 0) = 0$. Hence the contributions of the Doppler and convection effects vanish at the moment of passing by.

A.2. Time history of mean square sound pressure. The relation between the mean square sound pressure and its spectral density is

$$p^2(t) = \int_0^\infty p^2(f', t)\, df', \tag{32}$$

where f' is the observed frequency.

Thus (Eqs. 21, 25–27, 32)

$$p^2(t) = p_S^2(t) + p_D^2(t) + p_C^2(t), \tag{33}$$

where the contributions of the "quasi-stationary" source, Doppler effects, and the convection effect are given by

$$p_S^2(t) = \frac{N\rho c F_S(t)}{2d}, \tag{34}$$

$$p_D^2(t) = M\frac{P\rho c F_D(t)}{3d}, \tag{35}$$

$$p_C^2(t) = M\frac{N\rho c F_C(t)}{3d}. \tag{36}$$

Here, parameters N and P are related to the power spectral density of a line source:

$$N = \int_0^\infty N(f')\, df', \quad P = \int_0^\infty \frac{dN}{df'}(f') f'\, df'. \tag{37}$$

Assuming that $N(f')$ has the form given by Eq. (2), we obtain N from Eq. (3) and $P = -N$ [1]. Thus Eqs. (33–36) combine to yield

$$p^2(t) = \frac{N\rho c}{2d}\left\{F_S(t) - \frac{2}{3}M[F_D(t) - F_C(t)]\right\}, \tag{38}$$

with $F_S(t)$, $F_D(t)$, and $F_C(t)$ defined by Eqs. (28–31).

Equation (38) described the time variations of the mean-square sound pressure for a line source in motion.

Expression (28) shows that the function $F_S(t)$ is even: $F_S(-t) = F_S(t)$. In contrast $F_D(-t) = -F_D(t)$ and $F_C(-t) = -F_C(t)$, i.e., both functions are odd. Thus, introducing the measure of $p^2(t)$ asymmetry (Fig. 3)

$$\Delta p^2 = p^2(t^*) - p^2(-t^*),$$

one gets (Eq. 38):

$$\Delta p^2(t^*) = -\frac{2N\rho c}{3d}M[F_D(t^*) - F_C(t^*)]. \tag{39}$$

It follows that the asymmetry of the mean square sound pressure is proportional to the Mach number and decreases with the slant distance (d),

2B. Dissipative medium.

B.1. Spectral density of mean square sound pressure. Including air absorption, one obtains more general expressions for the mean square sound pressure, p^2, and its spectral density, $p^2(f)$.

From Eqs. (1,14) and Fig. 1, we get

$$p^2(f') = d^2\rho c\int_{-l/2}^{l/2} N\frac{[f'/\eta]\,\eta^4}{r^4(t',\xi)}\exp(-2\alpha(f')r(t',\xi))\,d\xi, \tag{40}$$

where $r(t', \xi)$ and $\eta(t', \xi)$ are determined by Eqs. (8–10).

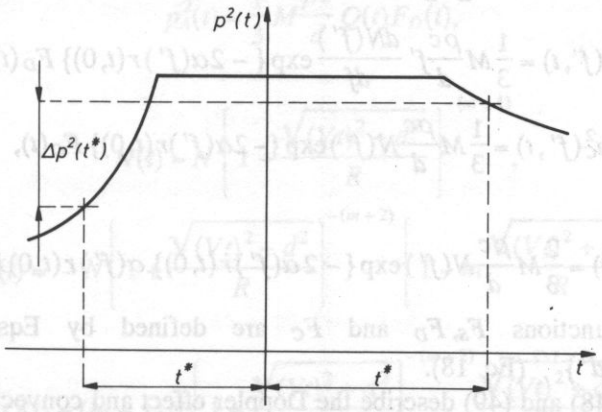

FIG. 3. Measure of $p^2(t)$ asymmetry, $\Delta p^2(t^*)$ (Eq. 39).

To evaluate the above integral, the analysis can be carried out (with $M << 1$) in a manner quite parallel to that in Section A2. The final result is

$$p^2(f',t) = p_S^2(f',t) + p_D^2(f',t) + p_C^2(f',t) + p_A^2(f',t), \tag{41}$$

where

$$p_S^2(f',t) = d^2\rho cN \int_{-l/2}^{l/2} \frac{\exp(-2\alpha r(t,\xi))}{r^4(t,\xi)}\, d\xi, \tag{42}$$

$$p_D^2(f',t) = Md^2\rho cf' \frac{dN}{df'} \int_{-l/2}^{l/2} \frac{\sin\phi \exp(-2\alpha r(t,\xi))}{r^4(t,\xi)}\, d\xi, \tag{43}$$

$$p_C^2(f',t) = 4Md^2\rho cN \int_{-l/2}^{l/2} \left[\frac{r(t,0)}{r(t,\xi)} - 1\right] \frac{\sin\phi \exp(-2\alpha r(t,\xi))}{r^4(t,\xi)}\, d\xi, \tag{44}$$

and

$$p_A^2(f',t) = 2Md^2\rho cN\alpha r(t,0) \int_{-l/2}^{l/2} \frac{\sin\phi \exp(-2\alpha r(t,\xi))}{r^4(t,\xi)}\, d\xi, \tag{45}$$

where the absorption coefficient α and the characteristic N depend on the observed frequency f' (Eqs. 2,6). The distance $r(t,0)$ and $r(t,\xi)$ are determined by Eq. 18. When $l/2 << d$, then the distances between the point of observation and both edges of a line source, $r(t,-l/2)$, $r(t,l/2)$, are almost the same as the distance between the point of observation and the center of a line source, $r(t,0)$, (see Fig. 4), i.e.,

$$\frac{r(t,l/2) - r(t,0)}{r(t,0)} << 1, \quad \frac{r(t,-l/2) - r(t,0)}{r(t,0)} << 1, \tag{46}$$

Thus Eqs. (42–45) can be approximated by

$$p_S^2(f',t) = \frac{1}{2}\frac{\rho c}{d} N(f') \exp\{-2\alpha(f')r(t,0)\} F_S(t), \tag{47}$$

$$p_D^2(f',t) = \frac{1}{3} M \frac{\rho c}{d} f' \frac{dN(f')}{df} \exp\{-2\alpha(f')r(t,0)\} F_D(t), \tag{48}$$

$$p_C^2(f',t) = \frac{1}{3} M \frac{\rho c}{d} N(f') \exp\{-2\alpha(f')r(t,0)\} F_C(t), \tag{49}$$

and

$$p_A^2(f',t) = \frac{2}{3} M \frac{\rho c}{d} N(f') \exp\{-2\alpha(f')r(t,0)\}\, \alpha(f')r(t,0) F_D(t). \tag{50}$$

The time functions F_S, F_D and F_C are defined by Eqs. (28–30) and $r(t,0) = \{(Vt)^2 + d^2\}^{1/2}$ (Eq. 18).

Expressions (48) and (49) describe the Doppler effect and convection effect modified by air absorption. To find the physical meaning of Eq. (50), let us note that $F_D(t)$ is

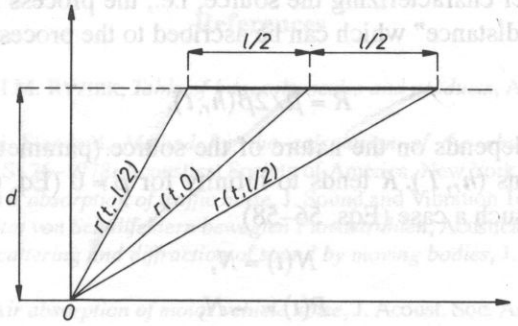

FIG. 4. Definition of the distances $r(t, -l/2)$, $r(t, l/2)$, and $r(t, 0)$ (Eqs. 46).

negative for $t < 0$ and positive for $t > 0$ (Eqs. 29,31). Thus, we have $p_A^2 < 0$ and $p_A^2 > 0$ for $t < 0$ and $t > 0$ respectively. Such an increase of the mean square sound pressure can be explained by the decrease of air absorption caused by the Doppler frequency shift.

B.2. Time history of mean square sound pressure. From Eqs. (32, 47–50) we can obtain the mean square sound pressure as follows:

$$p^2(t) = p_S^2(t) + p_D^2(t) + p_C^2(t) + p_A^2(t), \tag{51}$$

where

$$p_S^2(t) = \frac{1}{2}\frac{\rho c}{d} N(t) F_S(t), \tag{52}$$

$$p_D^2(t) = \frac{1}{3} M \frac{\rho c}{d} P(t) F_D(t), \tag{53}$$

$$p_C^2(t) = \frac{1}{3} M \frac{\rho c}{d} N(t) F_C(t), \tag{54}$$

$$p_A^2(t) = \frac{1}{3} M \frac{\rho c}{d} Q(t) F_D(t), \tag{55}$$

with

$$N(t) = N\left\{1 + \frac{\sqrt{(Vt)^2 + d^2}}{R}\right\}^{-(m+1)}, \tag{56}$$

$$P(t) = -N\left\{1 + \frac{\sqrt{(Vt)^2 + d^2}}{R}\right\}^{-(m+2)} \cdot \left\{1 - m\frac{\sqrt{(Vt)^2 + d^2}}{R}\right\}, \tag{57}$$

and

$$Q(t) = (m+1)N\left\{1 + \frac{\sqrt{(Vt)^2 + d^2}}{R}\right\}^{-(m+2)} \cdot \frac{\sqrt{(Vt)^2 + d^2}}{R}. \tag{58}$$

N is the parameter characterizing the source, i.e., the process of generation (Eq. 3) and R is the "critical distance" which can be ascribed to the process of propagation, i.e., air absorption [6]:

$$R = \mu/2\beta(h_r, t). \tag{59}$$

Its numerical value depends on the nature of the source (parameter μ, see Eq. 2) and the weather conditions (h_r, T). R tends to infinity for $\beta = 0$ (Eq. 6), i.e., for a nondissipative medium. In such a case (Eqs. 56–58)

$$\begin{aligned} N(t) &= N, \\ P(t) &= -N, \\ Q(t) &= 0, \end{aligned} \tag{60}$$

and the expression (52–54) simplifies to the form given by Eqs. (34–36) with $P = -N$.

3. Conclusions

The final result of geometrical spreading, air absorption, Doppler, and convection effects due to the motion of a line source have been described in terms of means square sound pressure (p^2). Making use of the definition, $L_p = 10 \lg (p^2/p_0^2)$ one can predict the sound pressure $(p_0 = 2 \times 10^{-5}\ \mathrm{N/m^2})$. The spectrum of a line source, frequency-weighed or not, is characterized by the function $N(f)$ (Eq. 2). In the case of A-frequency weighing, $N = N_A(f)$ we are able to calculate the A-weighed sound pressure level, $L_{pA} = 10 \lg (p_A^2/p_0^2)$, of noise generated, e.g., by a train.

The formulae have been derived under the assumption that the noise is generated by a continuous line of dipole sources.

The most general expressions (Eqs. 51–55) hold true for $M << 1$, linear dependence of the absorption coefficient on frequency (Section 1.B), and the condition determined by the inequality $l/2 << d$.

Air absorption can be neglected and one can use a simpler expression (38), when $r(t, 0) << R$, i.e. (Eqs. 51–59)

$$|t| << \frac{1}{V}\sqrt{[\mu/2\beta(h_r, T)]^2 - d^2}\,. \tag{61}$$

Numerical values of β can be found for any relative humidity (h_r) and air temperature (T) (Eq. 6).

Acknowledgement

This work was supported by the grant CPBP 02.03 from the Polish Academy of Sciences.

References

[1] I.S. GRADSHTEYN, I.M. RYZHIK, *Table of integrals, series and products*, Academic Press, New York 1980.

[2] American National Standard, *Method for the calculation of the absorption of sound by the atmosphere*, ANSI SI.26–1978, Acoustical Society of America, New York 1978.

[3] R. MAKAREWICZ, *Air absorption of traffic noise*, J. Sound and Vibration **160** (1993) in press.

[4] G. WITTEK, *Intensitat von Schallfeldern bewegten Punktstrahlen*, Acustica, **45**, 316–321 (1980).

[5] D.G. CRIGHTON, *Scattering and diffraction of sound by moving bodies*, J. Fluid Mech. **72**, 209–228 (1975).

[6] R. MAKAREWICZ, *Air absorption of motor vehicle noise*, J. Acoust. Soc. Am. **80**, 561–568 (1986).

Received on December, 4, 1990

ARCHIVES OF ACOUSTICS
17, 1, 43–50 (1992)

ACOUSTIC RELAXATION NEAR THE ISOTROPIC LIQUID-NEMATIC PHASE TRANSITION IN THE NEMATIC PHASE IN p-n-OCTYLOXY p'CYANOBIPHENYL

A. DRZYMAŁA, M. CIEŚLAK, H. HERBA and J. MICHALSKI

Chair of Physics, Technical University
(35-959 Rzeszów, ul. W. Pola 2)

The paper presents the results of the completation measurements on p-n-octyloxy p'cyanobiphenyl [1] of the absorption and the ultrasonic velocity in the smectic-nematic phase for a frequency range varying from. 2.5 MHz to 60 MHz.

In the nematic phase near the isotropic liquid-nematic transition, the contributions to the quantities $\alpha\lambda$ and α/f^2 the critical slowing down of the order parameter, the fluctuations of the order parameter and the director fluctuations were analyzed. Each ultrasonic absorption mechanism was characterized by an appropriate relaxation time near the phase transition.

1. Introduction

The classical theories [2, 3] fail to explain ultrasonic absorption in liquid crystals. The disagreements observed can be explained with the aid of the relaxation theory of absorption which takes into account both the molecular relaxation and the critical molecular relaxation associated with present phase transitions. Near the phase transition temperature, an increase of absorption (decrease of velocity) is observed. However, during the phase transition the maximum of absorption and minimum (or strong change) are observed. Now it has generally been agreed that the interaction of ultrasonic with the order parameter fluctuation [2, 3, 4, 5] is the main mechanism of absorption in the isotropic liquid crystal.

Near the phase transition in the nematic phase three [3, 4] absorption processes are present:

1. Coupling of the sound wave and director fluctuations.
2. Coupling of the sound wave and order parameter fluctuations,
3. Coupling of the sound wave and critical slowing down of the order parameter.

The absorption coefficient

$$\alpha = \alpha_n + \alpha_{\delta s} + \alpha_s + \alpha_v \tag{1}$$

is given by components associated with the appropriate absorption mechanism where: α_n – described the director fluctuations, $\alpha_{\delta s}$ – describes the order parameter fluctuations, α_s – described the slowing down of the order parameter, α_v – described the absorption which is not related to any relaxation process.

According to the results of NAGAI [4], we obtained the following forms for the absorption coefficients referred to the wave length:

$$\alpha_n \lambda(f) = D\frac{f}{f_0}\left\{1 - \frac{f}{4\sqrt{2}f_0}\left(\ln\left|\frac{1+\sqrt{\frac{2f}{f_0}}+\frac{f}{f_0}}{1-\sqrt{\frac{2f}{f_0}}+\frac{f}{f_0}}\right| + 2\,\mathrm{arctg}\,\frac{\sqrt{2ff_0}}{f-f_0}\right)\right\} \tag{2}$$

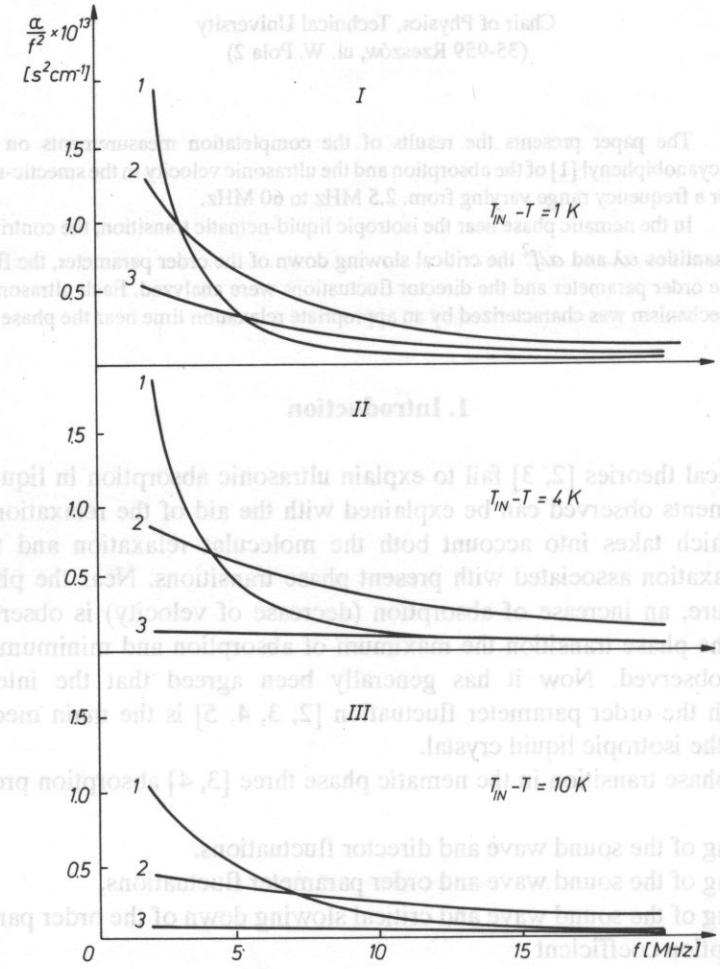

FIG. 1. Contribution of different absorption mechanism in α/f^2 for the mesomorphic nematic phase [5].

$$\alpha_{\delta s}\,\lambda(f) = E\sqrt{\frac{1}{f}}\left(\sqrt{\frac{f_0'}{f} + \sqrt{\left(\frac{f_0'}{f}\right)^2 + 1}} - \sqrt{\frac{2f_0'}{f}}\right), \tag{3}$$

$$\alpha_s\lambda(f) = F\frac{\frac{f}{f_R}}{1+\left(\frac{f}{f_R}\right)^2}, \tag{4}$$

$$\alpha_v\lambda(f) = Qf, \tag{5}$$

where f_0, f_0', f_R are the relaxation frequencies of the director fluctuation, the order parameter fluctuation and the critical slowing down of the order parameter, respectively. All D, E, F and Q are free parameters which require to be adjusted. MANDELSTAMM and LEONTOWICH [6] explained the observed "above Stokes" part of absorption in terms of losses induced by the volume viscosity. It appears during the volume change in space where the substance is condensed. Starting from the theoretical results [5] obtained for the ultrasonic absorption in the nematic liquid crystals phase near the isotropic liquid-nematic transition, we can write [4, 7, 8]:

$$\frac{\alpha}{f^2} = \frac{2\Pi^2}{\rho V^3}\left(\eta_v^{(s)}(f) + \eta_v^{(\delta s)}(f) + \eta_v^{(n)}(f)\right) + G\alpha_4, \tag{6}$$

where: ρ – liquid crystal density, V – ultrasonic velocity, $\eta_v^{(s)}$, $\eta_v^{(\delta s)}$, $\eta_v^{(n)}$ denote the contribution of the critical slowing down of the order parameter, the order parameter fluctuating and the director fluctuations in volume viscosity, respectively. $G\alpha_4$ denotes the regulator part of the absorption [9]. The components of volume viscosity related to given processes assisting in the critical ultrasonic absorption are given by

$$\eta_v^{(a)}(f) = \frac{A}{1+\left(\frac{f}{f_R}\right)^2}, \tag{7}$$

$$\eta_v^{(\delta s)}(f) = \frac{B}{\sqrt{(2\pi f)^3}}\left[\sqrt{\sqrt{\left(\frac{2f_0'}{f}\right)^2 + 1} + \frac{2f_0'}{f}} - \sqrt{\left(\frac{4f_0'}{f}\right)}\right], \tag{8}$$

$$\eta_v^{(n)}(f) = \frac{C}{2\pi f_0}\left\{1 - \frac{1}{2}\sqrt{\frac{f}{2f_0}}\left[\frac{1}{2}\ln\frac{\frac{f}{f_0} + \sqrt{\frac{2f}{f_0}} + 1}{\frac{f}{f_0} - \sqrt{\frac{2f}{f_0}} + 1} + \right.\right.$$

$$\left.\left. + \operatorname{arctg}\left(\sqrt{\frac{2f_0}{f}} + 1\right) + \operatorname{arctg}\left(\sqrt{\frac{2f_0}{f}} - 1\right)\right]\right\}. \tag{9}$$

Here A, B, C, G are constants which can be calculated from numerical calculations under the experimental results of α/f^2. Starting from the measured quantities $\alpha\lambda$ and α/f^2, one should determine the concentration of particular mechanisms near the phase transition so as to fit the experimental curves to the theoretical ones given by Eqs. (2)–(6). The dependence of different absorption mechanisms on the quantity α/f^2 in the mesomorphic nematic phase is plotted in Fig. 1 [5].

2. Experiment and examined material

The p-n-octyloxy-p′-cyanobiphenyl $C_8H_{17}O-<\overline{O}>-<\overline{O}>-CN$ liquid crystal processes the smectic mesophase and the nematic phase. The temperatures of the phase transitions were determined under the behaviour of the absorption and the velocity during the cooling process (Fig. 2) and the value of enthalpy by the DSC method at the M. Luther University Halle. The obtained results are solid state $\frac{326.35\ \mathrm{K}}{29.3\ \mathrm{KJ/mol}}$ smectic A $\frac{341.45\ \mathrm{K}}{62.5\ \mathrm{J/mol}}$ nematic $\frac{348.55\ \mathrm{K}}{754\ \mathrm{J/mol}}$ isotropic liquid.

The ultrasonic set US-6 (made at the IFTR in Warsaw) was used for absorption measurements which make possible research of liquid crystals (in the frequency range (9.8–60) MHz [10] or in a modified version in the frequency range: (2.5–7.5) MHz.

3. Experimental results, calculations and discussion

The experimental results of the wave propagation velocity for p-n-octyloxy p′-cyanobiphenyl [1] and calculations of $\alpha\lambda$ for five temperatures near the isotropic liquid-nematic transition (this temperature range contains the mesomorphic nematic phase) and formulas (2)–(4) allow us to find the characteristic relaxation frequencies for appropriate mechanisms for a given frequency range. The description of the main absorption processes near the phase transition formulas (1)–(5) requires the need to fit the set of parameters f_0, D, f_0', E, f_R, F and Q for the appropriate. The χ^2 test was used to estimate the quality of fitting with χ^2given by

$$\chi^2 = \sum_f \chi^2(f) = \sum_f \left(\frac{\alpha\lambda_{\exp}^{(f)} - \alpha\lambda_{\mathrm{th}}^{(f)}}{\Delta\alpha\lambda(f)} \right)^2 ,$$

Here $\alpha\lambda_{exp}^{(f)}$ and $\alpha\lambda_{th}^{(f)}$ describe the experimental and theoretical values of the absorption coefficient referred to the wavelength respectively. The experimental error to $\alpha\lambda_{exp}^{(f)}$ described $\Delta[\alpha\lambda_{exp}^{(f)}]$. The parameters were determined from the minimum condition for χ^2. The values of the absorption components associated with particular

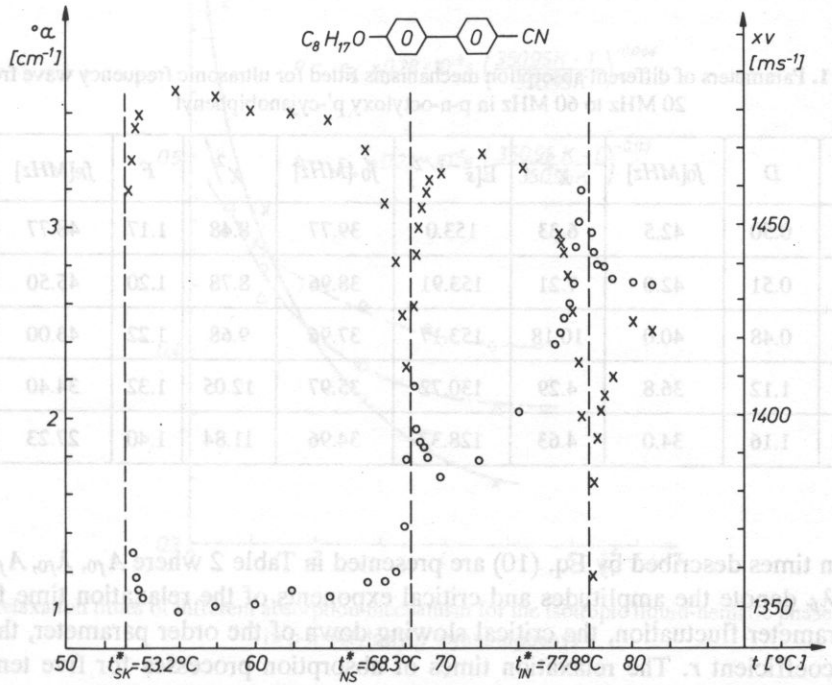

FIG. 2. Absorption and velocity of ultrasonic wave for a frequency equal to 2.5 MHz in p-n-octyloxy p'-cyanobiphenyl.

mechanisms were calculated with the help of the results presented in [4] and [5] (for a frequency range of the ultrasonic wave from 20 MHz to 60 MHz). The estimated parameters describing the absorption referred to the wave length for particular cases are presented in Table 1. Let T_{IN}^* express the temperature for the $N-I$ phase transition which is the minimal temperature for the (metastable) isotropic phase ($T_{IN}^* < T_{IN}$) to exist and is very close to T_{IN} the so-called hypothetical second kind phase transition temperature [11, 12]. Next, the behaviour of the relaxation times ($\tau_{rel} = 1/2\pi f_{rel}$) for absorption mechanisms are described by the Fisher function [13]:

$$\tau = A\left(\frac{T_{IN}^* - T}{T_{IN}^*}\right)^{\lambda}. \tag{10}$$

Here λ is the critical exponent, the amplitude A is constant and T is the absolute temperature. The temperature T_{IN}^{*} and T_{IN} satisfy the inequality $|T_{IN} - T_{IN}^{*}| \leq 1$ K. The critical exponents were determined by least square analysis. The correlation coefficients r was obtained and was in agreement with the Keller criterion [15] with its limit values $|r|$ depending on the measurements data number. The obtained values of the

Table 1. Parameters of different absorption mechanisms fitted for ultrasonic frequency wave from 20 MHz to 60 MHz in p-n-octyloxy p'-cyjanobiphenyl

$T[K]$	D	$f_0[MHz]$	χ^2	$E[s^{-1/2}]$	f_0' $[MHz]$	χ^2	F	$f_R[MHz]$	χ^2
346.15	0.50	42.5	6.33	153.0	39.77	8.48	1.17	48.77	0.31
347.15	0.51	42.0	7.21	153.91	38.96	8.78	1.20	45.50	0.56
348.15	0.48	40.0	10.18	153.17	37.96	9.68	1.22	43.00	0.65
349.75	1.12	36.8	4.29	130.72	35.97	12.05	1.32	34.40	3.43
350.35	1.16	34.0	4.63	128.37	34.96	11.84	1.40	27.23	9.36

relaxation times described by Eq. (10) are presented in Table 2 where A_{f0}, λ_{f0}, $A_{f'0}$, $\lambda_{f'0}$ and A_{fr}, λ_{fr} denote the amplitudes and critical exponents of the relaxation time for the order parameter fluctuation, the critical slowing down of the order parameter, the correlation coefficient r. The relaxation times of absorption processes for five temperatures are shown in Fig. 3.

We analyzed the variation of α and v with temperature for the constant value of the ultrasonic incidence frequency (Fig. 3). The results indicate that we are dealing with a

Table 2. Quantities of p-n-octyloxy p'-cyjanobiphenyl describing the relaxation times for different absorption mechanisms

$T_{IN}^{*}[K]$	$A_{f0} \cdot 10^{-8}[s]$	λ_{f0}	r
350.95	0.23	-0.113 ± 0.002	0.991
$T_{IN}^{*}[K]$	$A_{f0}' \cdot 10^{-8}[s]$	λ_{f0}'	r
350.95	0.28	-0.086 ± 0.003	0.994
$T_{IN}^{*}[K]$	$A_{fR} \cdot 10^{-8}[s]$	λ_{fR}	r
350.95	0.12	-0.234 ± 0.004	0.995

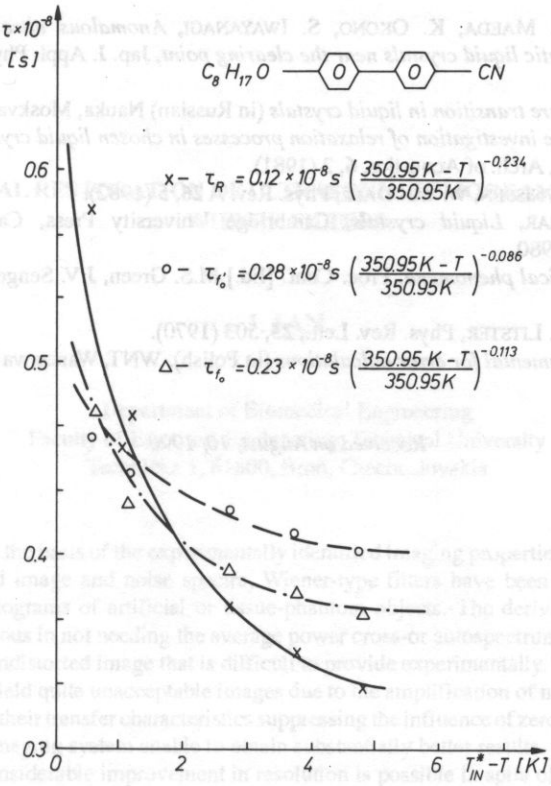

FIG. 3. Relaxation times of different absorption mechanism for the isotropic liquid-nematic phase transition in p-n-octyloxy p'-cyanobiphenyl

relaxation process which is conditioned by the character of the phase transition. The calculated characteristic relaxation times for the critical slowing down of the order parameter and the director fluctuation mechanisms are characteristic qualities near the phase transition.

References

[1] A. DRZYMAŁA ET AL. Raport CPBP 02.03, II.2.8, 1987, 1988 (not published).

[2] H.E. STANLEY, *Introduction to phase transition and critical phenomena*, Clavendon Press, Oxford 1981.

[3] A.P. KAPUSTIN, C.A. KAPUSTINA, *Acoustics of liquid crystals, (in Russian)*, Nauka, Moskva 1986.

[4] S. NAGAI, *A new interpretation of critical ultrasonic absorption in the nematic phase of liquid crystals*, Jap. J. of Appl. Phys., **18**, 5, 903–908 (1979).

[5] N.I. ALEKSIEJEW, W.P. ROMANOW, S.W. ULJANOW, *Acoustic absorption in liquid crystals near the isotropic liquid-nematic phase transition*, (in Russian), J. of Acoustics, **14**, 3, 398–407 (1988).

[6] L. MALDELSTAM, M. LEONTOWICH, J. Exp. Theor. Phys. USSR, **7**, 438–449 (1937).

[7] H. IMURA, K. OKONO, *Theory of anomalous ultrasonic absorption and dyspersion of nematic liquid crystals just above the clearing point,* Chem. Phys. Lett., **19**, 3, 387–390 (1973).

[8] Y. KAVAMURA, Y. MAEDA, K. OKONO, S. IWAYANAGI, *Anomalous ultrasonic absorption and dispersion of nematic liquid crystals near the clearing point*, Jap. J. Appl. Phys., **12**, 10, 1510–1524 (1973).
[9] A.S. PIKIN, *Structure transition in liquid crystals* (in Russian) Nauka, Moskva 1981 p. 336.
[10] A. DRZYMAŁA, *The investigation of relaxation processes in chosen liquid crystals by ultrasonic and dielectric methods*, Arch. of Acoustics, **6**, 2 (1981).
[11] I. THOEN, H. MARYNISSEN, W. VAN DAEL, Phys. Rev. A **26**, 5 (1982).
[12] S. CHANDRASEKHAR, *Liquid crystals*, Cambridge University Press, Cambridge-London-New York-Melbourne 1980.
[13] M.E. FISHER, *Critical phenomena*, Proc. Conf. [Ed.] M.S. Green, J.V. Sengers, N.B.S. Misc. Publ. **273**, 21 (1965).
[14] T.W. STINSON, I.D. LITSTER, Phys. Rev. Lett., **25**, 503 (1970).
[15] H. HANSEL, *Fundamental for error calculations* (in Polish), WNT, Warszawa 1968.

Received on August, 10, 1990

ARCHIVES OF ACOUSTICS
17, 1, 51–66 (1992)

EXPERIMENTAL RESTORATION OF ULTRASONIC TOMOGRAMS BY MODIFIED WIENER FILTERS

J. JAN

Department of Biomedical Engineering
Faculty of Electrical Engineering, Technical University
Technicka 1, 61600, Brno, Czechoslovakia

On the basis of the experimentally identified imaging properties, esp. point-spread-function and image and noise spectra, Wiener-type filters have been designed and applied to ultrasonograms of artificial or tissue-phantom objects. The derived type of filters are advantageous in not needing the average power cross-or autospectrum involving the properties of the undistorted image that is difficult to provide experimentally. It has been found that the filters yield quite unacceptable images due to the amplification of noise but simple modifications of their transfer characteristics suppressing the influence of zeroes in the transfer function of the imaging system enable to obtain substantially better results.

Considerable improvement in resolution is possible in spite of the strong nonlinearities involved in the image forming process. Suppressing speckle textures on the basis of differences between average power spectrum of the noise and of the useful image structures has shown only a modest success possibly due to rather small extend of the used image-and spectra matrices and also because of low extent of data not providing good spectral estimates.

1. Introduction

The principle of echo-ultrasonography does not allow for very high resolution in the resulting images. Especially lateral resolution is rather low which is a consequence of wide directional characteristics of ultrasonic transducers. Although there is a lot of improvement in providing sharper images thanks to better and more sophisticated transducers (fixed and dynamic focusing), still it seems worth to consider digital post-processing of the resulting images to sharpen them. Many attempts in this direction have been published, e.g. [1, 2]. The basic obstacle is the nonlinearity of the imaging process, caused primarily by wave interference of echoes followed by strongly non-linear signal envelope detection and also by logarithmic characteristics of the signal processing chain on the receiving side. In principle, it is possible to process radio frequency signals before the envelope detection, but it is technically very demanding and at the same time the reported results e.g. [3, 4] are not substantially better.

The present contribution deals with the video-(envelope detected) signals, but in their original form as provided by a typical wobbling crystal sector scanner, e.g. in polar coordinates. It seems that using this form of non-format-converted data is one of the conditions for restoration; it has been experimentally shown [8] that imaging process can be considered practically isoplanar on most of the image area if using this form of data.

The problem of noise, inherent in every restoration, is especially difficult with ultrasonography due to presence of s.c. speckles that are specific textures caused by interference of echoes from elementary microscopic reflectors or scatterers that are insonified coherently. As these textures are influenced primarily by the properties of the imaging system and only in a less extend by the tissue characteristics, it would be mostly desirable to remove them from the image. Unfortunately, the spectral components of the noise occupy frequency areas common with the components of the useful structures so that linear filtering can only limit but not remove them completely. Another possibility how to suppress speckles is to average several images (tomograms) depicting the same useful structures but with diversified speckles. As such a diversification based on special technical means [5, 6] is again quite demanding, a simple approach, based on diversification by small scanhead displacements, has been tried [11] with certain promising results. It seems that combination of averaging (or preliminary median filtering [7]) and Wiener filtering could suppress the speckles in a practically interesting extend.

The paper is directed towards deriving a simple form of the Wiener filter which could be designed on the basis of knowledge available from identification of imaging properties of an ultrasonic scanner, as published elsewhere [8–10]. Several questions should be answered: if there is a possibility to deconvolve the responses to "point" targets in spite of the effect of interference and nonlinearity which substantially change the image in comparison with purely additive image, how to modify the theoretical inverse filter in order to improve its originally not acceptable performance and finally to evaluate the performance of s.c. correcting filter which should take into account the influence of noise. Also for this filter a modification will be needed.

2. Modified filters for restoration

Supposed model of the image distortion has the general form

$$g(\bar{r}) = N\left[\int_{-\infty}^{\infty}\int_{-\infty}^{\infty} h(\bar{r}-\bar{r}')\cdot f(\bar{r}')\,dx'dy' + n(\bar{r})\right] \qquad (1)$$

where g means the distorted image, f is the original image, h is the point spread function of the imaging system and n is the noise component; $\bar{r} = (x, y)$. The linearly distorted image as described by the expression in square brackets is subject to a nonlinear transform N. The problem to solve the equation (1) for f is not an elementary one for

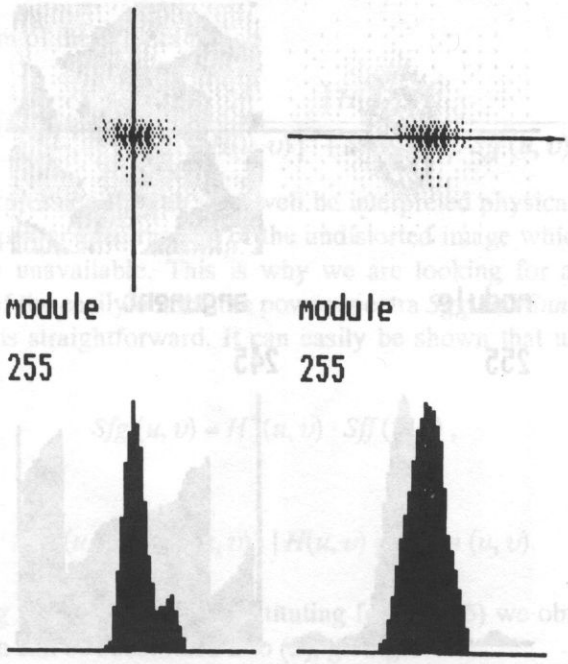

FIG. 1. Experimentally determined average point spread function of typical sector scanner.

two reasons: the noise n is not known explicitly-only some of its statistical characteristics can be experimentally determined – and the equation itself is "stiff", being too sensitive to small changes in its components. Also the nonlinearity complicates substantially the situation.

As for the nonlinearity, it can either be taken into account by an inverse transform N^{-1} which linearizes the problem – this leads to a homomorphic filter, or in some cases it can be neglected and linear restoration algorithm used directly. It has been shown experimentally several times that even this simplified approach can give acceptable results unless the nonlinearity is too severe.

The linearized version of (1) can be regarded as a family of equations where g, f and n are random fields while only h is a deterministic function; the solution $\hat{f}$ is then sought as an estimate minimizing on average the error function

$$e^2(\bar{r}) = E[(f(\bar{r}) - \hat{f}(\bar{r}))^2]$$

for a given g and a known statistics of n. The general solution, as well known, is then the conditional expectation of f given g but this is a complicated nonlinear function of g which depends on the joint probability density over the fields f and g that is practically impossible to obtain. This is why a simplified solution in the linear superposition form

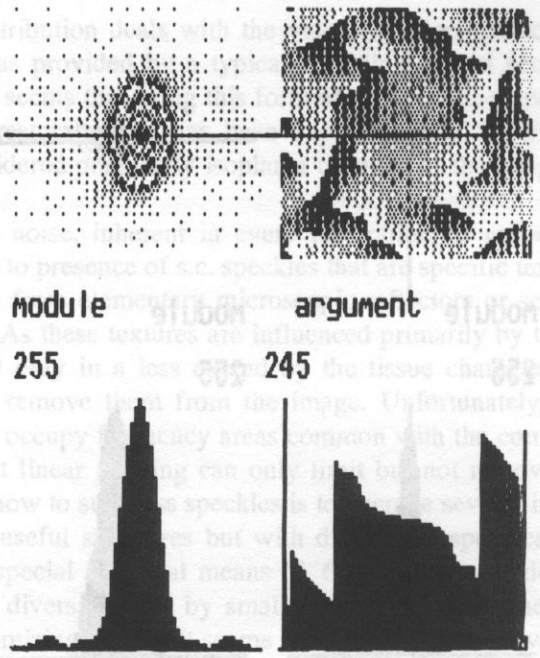

FIG. 2. Average transfer function of the sector scanner.

$$\hat{f}(\bar{r}) = \int_{-\infty}^{\infty}\int_{-\infty}^{\infty} m(\bar{r},\bar{r}') \cdot g(\bar{r}')\, dS(\bar{r}'), \quad dS(\bar{r}') = dx'\, dy',$$

is looked for, which under the condition that the fields are homogeneous turns into convolution integral

$$\hat{f}(r) = \int_{-\infty}^{\infty}\int_{-\infty}^{\infty} m(\bar{r}-\bar{r}') \cdot g(\bar{r}')\, dS(\bar{r}'). \tag{2}$$

where $m(\bar{r}-\bar{r}')$ can be regarded as a point spread function of a linear two-dimensional filter. Thus, linear filtering is used as the estimation procedure and the problem reduces into determining its frequency transfer function $M(u, v)$. The classical Wiener solution is

$$M(u,v) = Sfg(u,v)/Sgg(u,v), \tag{3}$$

where Sfg is power cross-spectrum of the fields f and g and Sgg is the auto power spectrum of g. Unfortunately, while Sgg can relatively easily be estimated by averaging spectra of individual realizations of g, the cross spectrum is very difficult, and in many cases impossible, to obtain.

This obstacle can be circumvented under the condition that f and n are uncorrelated and that at least one of them (usually noise) has zero mean. Then we arrive to the most

commonly used form of the Wiener filter

$$M(u,v) = \frac{1}{H(u,v)} \cdot \frac{|H(u,v)|^2}{|H(u,v)|^2 + Snn(u,v)/Sff(u,v)}. \quad (4)$$

Although the expression (4) can very well be interpreted physically, it relies on the knowledge of auto power spectrum *Sff* of the undistorted image which in certain cases (as in ours) is also unavailable. This is why we are looking for a form expressing $M(u, v)$ by means of the easily obtainable power spectra *Sgg* and *Snn*.

The derivation is straightforward. It can easily be shown that under given conditions,

$$Sfg(u,v) = H^*(u,v) \cdot Sff(u,v), \quad (5)$$

and

$$Sgg(u,v) = Sff(u,v) \cdot |H(u,v)|^2 + Snn(u,v). \quad (6)$$

Then expressing *Sff* from (6) and substituting for it in (5) we obtain an expression for *Sfg* which in turn can be substituted into (3), giving

$$M(u,v) = \frac{H^*(u,v)}{|H(u,v)|^2} \cdot \frac{Sgg - Snn}{Sgg}. \quad (7)$$

This rather unusual form of the Wiener filter can be interpreted as cascade of two filters: the first one is the direct inverse filter while the second is a correction of the noise influence which is obviously unimportant in those areas of the frequency domain where *Snn* is negligible in comparison with *Sgg*.

When experimenting with a given class of images (with a common point spread function *h* and fixed statistical properties of noise) we can, using the form (7), benefit on dividing the problem into two parts: the first part being PSF identification and derivation of a direct inverse filter and the second one the estimation of the statistical properties of the distorted image and separate noise and derivation of the correcting filter. This is especially advantageous if there exists a possibility of providing almost noiseless images with "point", "line" or "edge" objects enabling to identify the PSF of the imaging process on one hand and pure noise images (or at least image areas) from which the noise power spectrum can be estimated on the other. There are usually no problems with providing good estimate of the spectrum of the distorted image class.

3. Modified inverse filter

The scanner average point spread function as determined experimentally [8] is depicted on Fig. 1, its spectrum on Fig. 2. The exact inverse of it (Fig. 3),

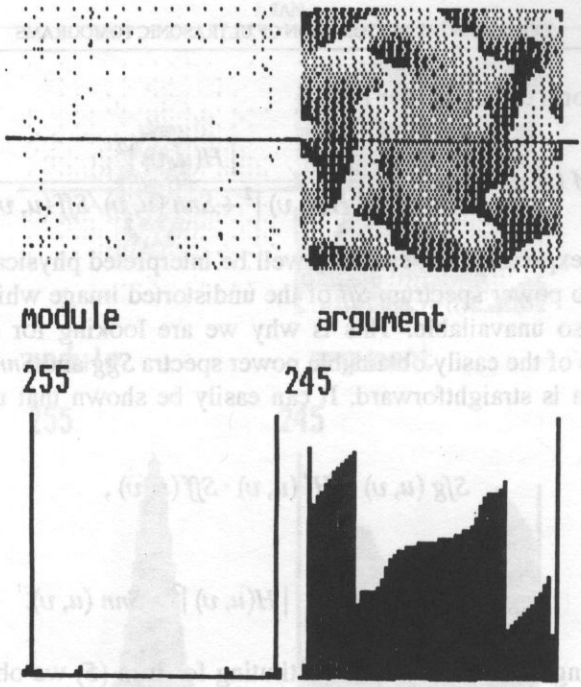

FIG. 3. Transfer function of the inverse filter.

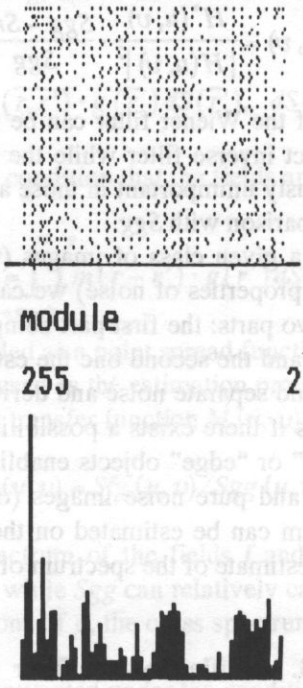

FIG. 4. Point spread function of the inverse filter.

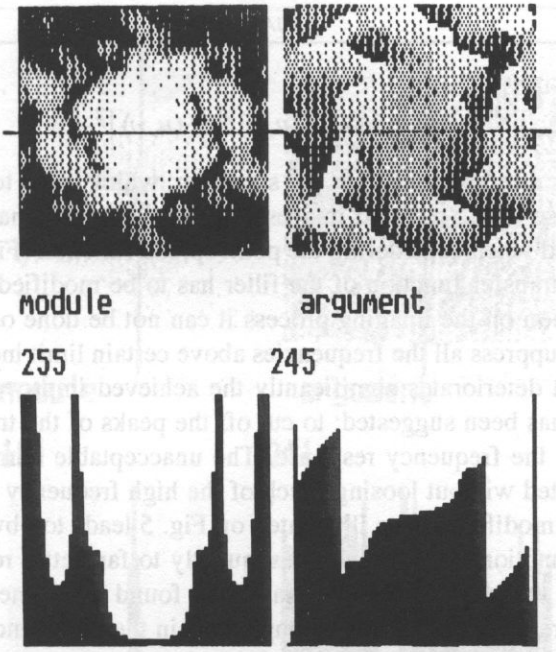

FIG. 5. Transfer function of the modified inverse filter.

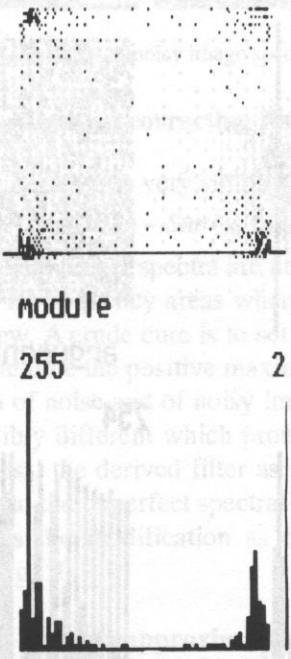

FIG. 6. Point spread function of the modified inverse filter.

$$M_1(u, v) = H^*(u, v)/|H(u, v)|^2 \tag{8}$$

has very high peaks due to "zeroes" in the spectrum, which leads to unacceptable level of narrow-band noise in the restored images even when the original noise is quite low. This can be expected when considering the point spread function (Fig. 4) of the filter.

Obviously, the transfer function of the filter has to be modified but due to the lack of precise information on the imaging process it can not be done on formal bases. The usual approach-to suppress all the frequencies above certain limit including the peaks-in not acceptable as it deteriorates significantly the achieved improvement in resolution. Another approach has been suggested: to cut off the peaks of the transfer function thus partially equalizing the frequency response. The unacceptable narrow-band amplification is then eliminated without loosing much of the high frequency bands important for the resolution. The modification as illustrated on Fig. 5 leads to obviously much smoother point spread function (Fig. 6) and consequently to far better restored images. The threshold value for the transfer function has to be found experimentally as a compromise between suppressing the spurious components in the result and preserving a significant extent of sharpening effect; the rule of thumb being to set the limit to only a few percent of the original maximum.

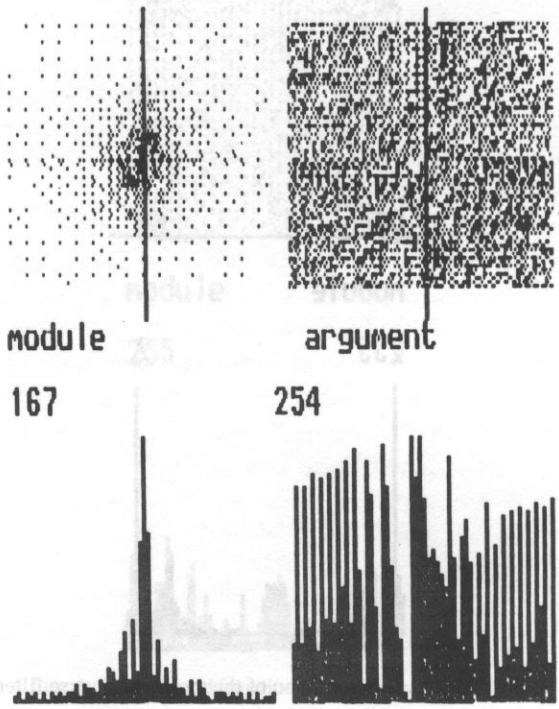

FIG. 7. Example of speckle noise spectrum.

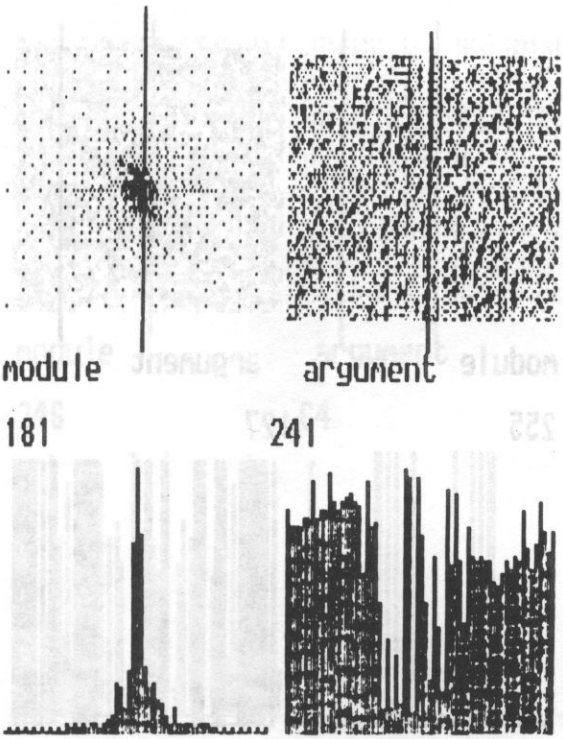

FIG. 8. Example of noisy image spectrum.

4. Modified correcting filter

The theoretical correcting filter has the very simple form

$$M_2(u, v) = [Sgg(u, v) - Snn(u, v)]/Sgg(u, v) \quad (9)$$

in which good estimates of the auto power spectra are needed. It may happen that due to imperfect estimates, there will be frequency areas where $Snn > Sgg$ which is obviously false from physical point of view. A crude cure is to set the numerator in (9) to zero for frequencies, limiting at the same time the positive maxima of $M(u, v)$ to a certain value. Examples of individual spectra of noise and of noisy image are on Fig. 7 and 8, respectively. The two spectra are visibly different which promises the possibility of deriving the correcting filter. Nevertheless, the derived filter as shown on Fig. 9 does not seem very reasonable, obviously due to the imperfect spectral estimates based on the averages of several power spectra. Thus the modification as described above was necessary yielding the filter depicted on Fig. 10.

5. Discrete approximations

The frequency domain procedures as described above have to be practically realized by discrete approximations, e.g. using discrete Fourier transform (DFT) instead of the

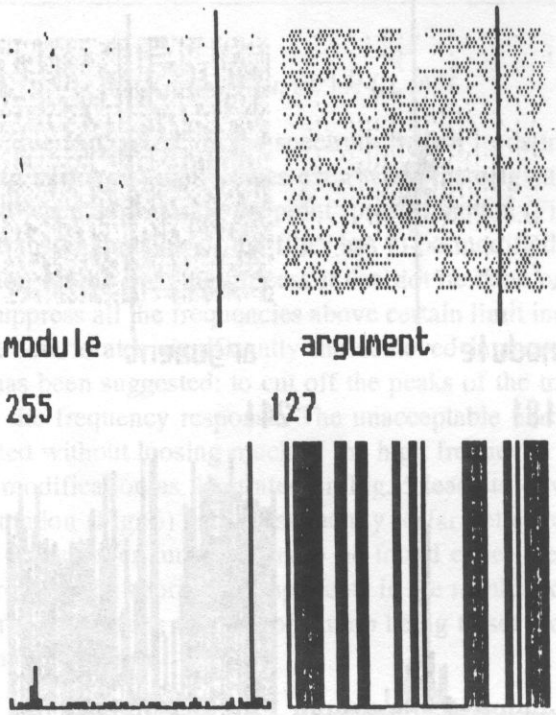

FIG. 9. Transfer function of the theoretical correcting filter.

continuous one. To prevent undesirable effects of circular convolution that consequently replaces the linear one, substantially bigger matrices then just necessary for keeping the needed amount of image and spectral data must be used which increases the computational and memory demands to the equipment used. Though it is obvious that the size of spectral matrices in case of providing convolution via frequency domain must be four times bigger then the image data and PSF matrices in order to enable appropriate padding by zeroes, the extent of the PSF of the restoration filter is a priori unknown and may well be bigger than the available size of matrices. When working with rather small matrices, it must be realized that the marginal effects caused by circular convolution may influence substantial part of the resulting image.

The presented figures have been derived using original image matrices of the size 32 × 32 ; frequency domain operations were carried out in matrices 64 × 64 big. While this seems to be quite sufficient for deriving the direct inverse filter as the extent of the original point spread function is rather small, the inverse filtering itself should have been done in bigger matrices, at least 96 × 96, as the PSF of the filter has in principal size 64 × 64. Also, such small matrices can describe the content of the distorted images or even of image noise only very roughly. This is probably one of the reasons of not very good estimates of the power spectra and consequently of obviously imprecise correcting filter (Fig. 9).

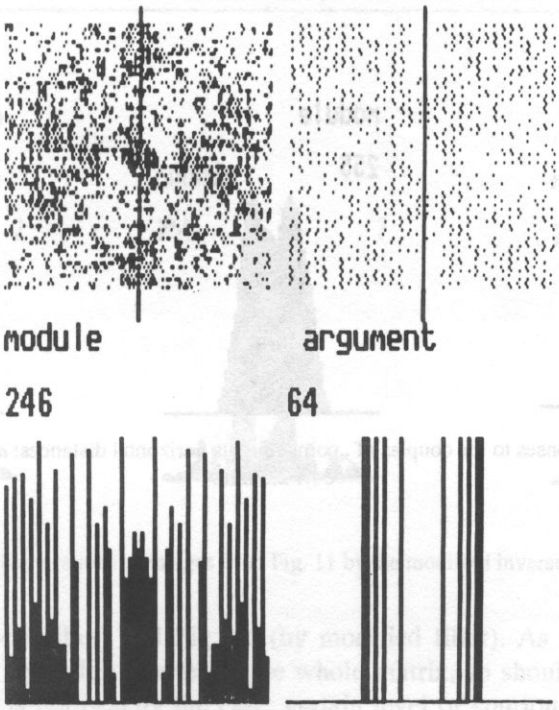

FIG. 10. Transfer function of the modified correcting filter

6. Discussion of results

First part of the results consists of restorations of images of couples of "point" targets that were provided by using the modified direct inverse filter ($M_1(u, v)$). The first example (Fig. 11) (a) depicts the response to a couple with negligible distance of the targets, the second (b) corresponds to the case of a distance just at the limit of resolution and the third one (c) is a case under the resolution limit of the imaging system. Fig. 12 a, b, c shows the restorations by the unmodified filter while on Fig. 13 we see the same objects but restored by the heavily modified filter. Obviously the simple modification of the filter removed most of the spurious signals in the restored images. On the other hand, the sharpness of the peaks visible on line profiles, which corresponds to obtainable resolution is practically the same in Fig. 12 as in Fig. 11. This is rather surprising as the high frequency peaks in the original filter have been suppressed in the modification as much as to only 2 per cent of their original value. The example (c) proves that substantial resolution improvement is possible and preserved even by using a heavily modified filter.

The second part of the results concerns the use of the correcting filter ($M_2(u, v)$). An example of the input image data with marked area for further processing is shown in Fig. 14. Clearly, the used areas are very small. The results of restoration are shown on

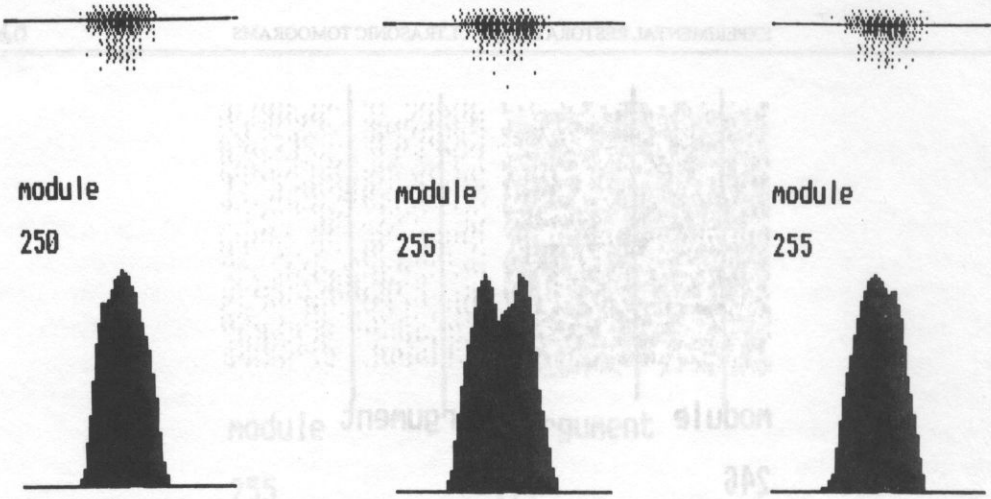

FIG. 11. Original responses to the couples of „point" targets horizontal distances: *a* ...0 mm, *b* ... 3.9 mm, *c* ... 2.3 mm.

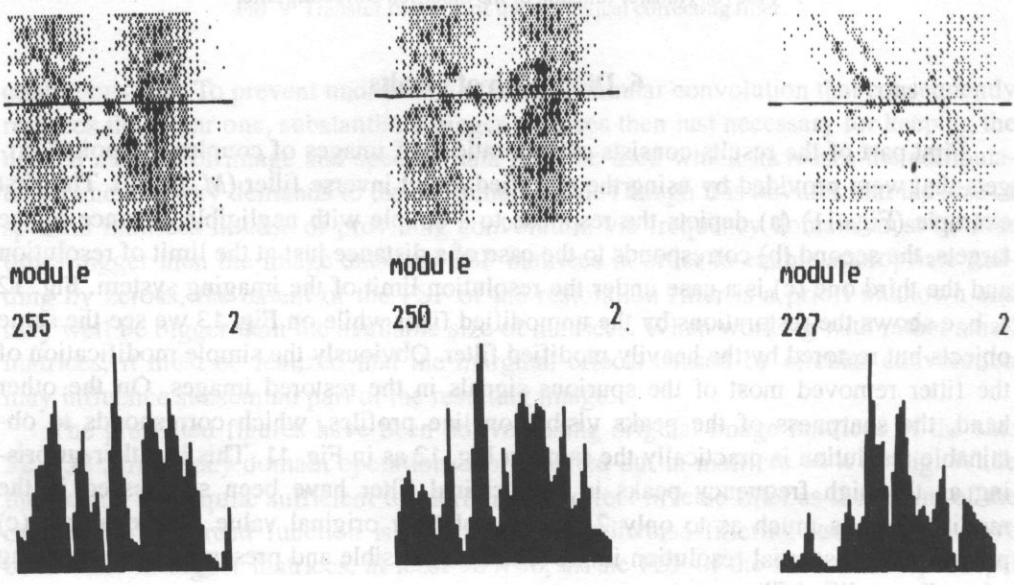

FIG. 12. Restorations of images from Fig. 11 by the theoretical inverse filter.

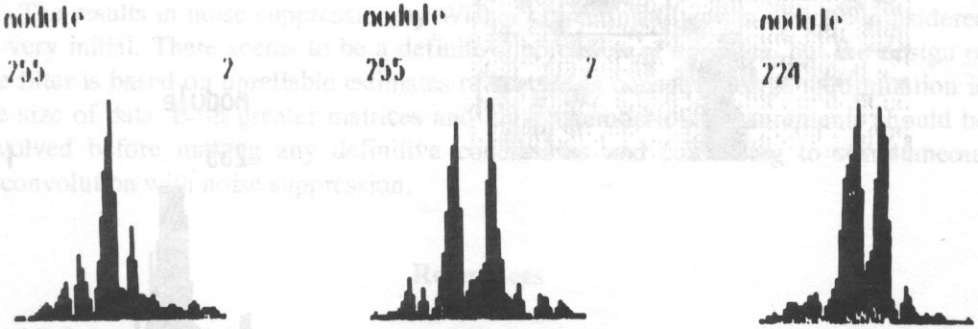

FIG. 13. Restorations of images from Fig. 11 by the modified inverse filter.

Fig. 15 (by theoretical filter) and Fig. 16 (by modified filter). As the original image matrices filled only upper left quarter of the whole matrix, so should do even the restored images which is not exactly the case; certain level of spurious signals (different from speckles) fills the whole image area. Anyway it seems that the original speckles have been removed though it is difficult to determine the extent of improvement in signal to noise ratio. Also, the distortion of useful structures is definitely present.

A comment should be inserted on the attempts to linearize the problem by homomorphic transform, inverse to the average nonlinearity of the imaging process as derived experimentally in [9, 10]. The rectifying transform strongly emphasizes the high level components of the image thus suppressing the noise components including speckles. The unwanted textures are practically invisible in the transformed images so that no further improvement could have been found in the images filtered by a filter based on the average spectra of the rectified images.

7. Conclusions

The form (7) of the Wiener filter seems to be a good tool for experimenting with restoration of ultrasonic tomograms because it enables to separate the problem of pure deconvolution and the connected problem of identification of transfer function of the imaging system from the other problem of suppressing the noise and designing the corresponding filter by determining the statistical properties of average image and average noise. It also removes the necessity to determine the average statistics of the unavailable undistorted image as needed for the common form (4).

The results for the deconvolution problem are rather promising: in spite of the non-additive character of the responses the resolution can be significantly improved even in

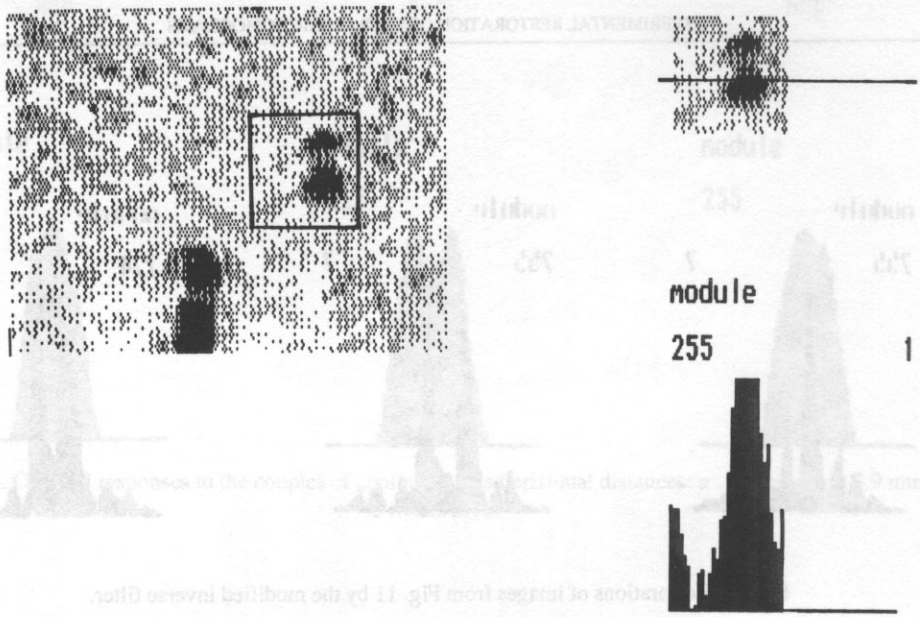

FIG. 14. Part of original image data with marked area to be restored.

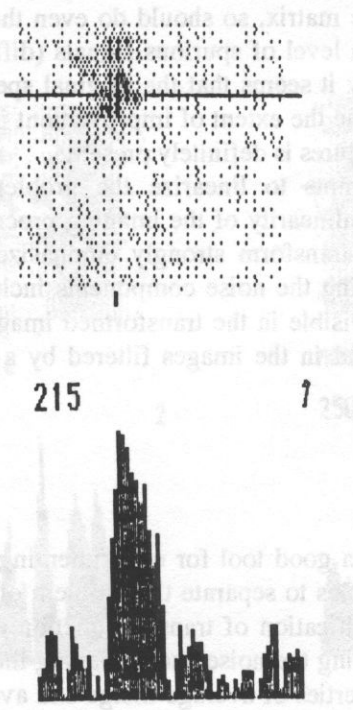

FIG. 15. Noisy image area from Fig. 14 processed by theoretical correcting filter.

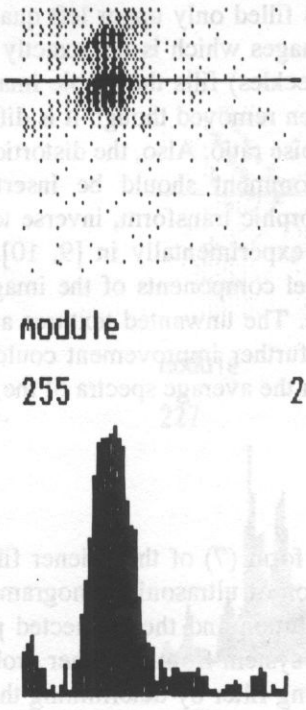

FIG. 16. Noisy image area from Fig. 14 processed by modified correcting filter.

cases of responses seriously damaged by wave interference. An important condition contributing to the positive results is probably working with the non-format-converted data. Any success of the deconvolution is of course dependent on the possibilities of noise suppression, either by filtering or by other means, as averaging.

The results in noise suppression by Wiener correcting filter can only be considered as very initial. There seems to be a definite suppression of speckles, but the design of the filter is based on unreliable estimates of spectra in consequence of the limitation in the size of data. Both greater matrices and higher number of measurements should be involved before making any definitive conclusions and continuing to simultaneous deconvolution with noise suppression.

References

[1] D.E. ROBINSON, H. WING, *Lateral deconvolution of ultrasonic beams*, Ultrasonic Imaging, **6**, 1–12 (1984).

[2] G. DEMOMENT, R. REYNAUD and A. HERMENT, *Rangle resolution improvement by a fast deconvolution method*, Ultrasonic Imaging, **6**, 435–451 (1984).

[3] J.P. ARDOUIN, *A model for an ultrasonic phased-array restoration*, MSc thesis, University of Toronto, 1985.

[4] T.J.M. JEURENS, J.C. SOMER, F.A.M. SMEETS and A.P.G. HOEKS, *The practical significance of two-dimensional deconvolution in echography*, Ultrasonic Imaging, **9**, 106–116 (1987).

[5] S.M. GEHLBACH, F.G. SOMMER, *Frequency diversity speckle processing*, Ultrasonic Imaging, **9**, 2, 92–105 (1987).

[6] S.W. SMITH, O.T. v. RAMM, *The Maltese cross processor: speckle reduction for circular transducers*, Ultrasonic Imaging, **10**, 153-170 (1988).

[7] T. LOUPAS, W.N. MC DICKEN, P.L. ALLAN, *An adaptive weighted median filter for speckle suppression in medical ultrasonic images*, IEEE Trans. CS, **36**, 1, 129–136 (1989).

[8] J. JAN, R. KUBAK, M. KNOTEK, *Point spread function of a typical sector ultrasonic scanner*, Proc. of Biocybernetics and biomedical engineering conf., Cracow, Poland 1987.

[9] J. JAN, *Degree of nonlinearity in ultrasonographic image forming*, Proc. VIIIth IEEE-EMBS Conference, 1043–1046, Dallas-Fort Worth USA 1986.

[10] J. JAN, R. KUBAK, M. KNOTEK, *Identification of average nonlinear properties of a typical ultrasound real time sector scanner under more realistic conditions*. In: E. Carson et al. Eds. Advances in Biomedical Measurements, 121–125, Plenum Publ., New York–London 1987.

[11] J. JAN, R. KUBAK, *Speckle suppression by averaging of parallel ultrasonograms*, Proc. of EUROSON'90, 7 th congress of EFSUMB, Jerusalem Israel 1990.

[12] J. JAN, *Frequency domain deconvolution of ultrasonic tomograms*, Proc. BIOENG'90 Aveiro Portugal 1990.

Received on September 26, 1990

ARCHIVES OF ACOUSTICS
17, 1, 67–76 (1992)

THE EFFECT OF STRUCTURE AND SWELLING OF CONCRETE ON THE FREQUENCY OF ACOUSTIC EMISSION SIGNALS

W. KOŁTOŃSKI

Institute of Fundamental Technological Research Polish Academy of Sciences
(00-049 Warszawa, Świętokrzyska 21)

In this paper results of experimental studies on the relationship between fundamental frequency of acoustic emission signals and time of water percolation into cement as well as its structure, are presented and discussed. Possibilities of practical application of this relationship for use in the building industry have been indicated.

1. Introduction

Experiments described in the first and second issue of Archives of Acoustics in 1990 [3] have proved that the process of water percolation into cement is accompanied by acoustic emission AE within a wide frequency range. It was initially stated that this effect can be used for remote signalling of water leaks through bad sealings of concrete prefabricated products, controlled at the experimental stand. However, further studies including various parameters have disclosed new possibilities of its application. One of these is interesting from the cognitive and practical point of view. It concerns the relationship between fundamental frequency of AE signals, and structure and swelling of moist concrete. This is the object of this paper.

2. Description of performed studies

Rectangular blocks of lightweight and dense concrete with 240 × 240 base and 150 or 450 mm height were tested. Every block had a metal rod inserted in a suitable place, to which the AE signals receiver (accelerometer was attached).

Every experiment started with the measurement of the natural level of AE in the concrete block prepared for measurement and placed on its base in a dry laboratory tank. This level was compensated by an adequate setting of the sensitivity threshold of the apparatus. Then the controlled flow of water (0.5 l per hour) into the bottom of the tank was turned on. Fundamental frequency f_p of received AE signals was measured in

1 min intervals, while their total energy E_s and number (event rate N_e') was measured in 10 s intervals. The purpose of simultaneous measurement of these three parameters is explained further on in this paper.

Experimental results indicate the existence of AE signals with frequency ranging from a few kHz to about 100 kHz in moist concrete. Hence, the overall frequency response of apparatus was equal 5 kHz –150 kHz. A rather low lower limit frequency did not allow total elimination of acoustic noise from the surroundings. Therefore, investigations had to be performed at low ambient noise.

In order to check the effect of the path length of an AE signal on its fundamental frequency f_p, measurements were made in blocks from identical concrete but with different heights 0.15 m and 0.45 m. This way AE signals travelling along a shorter and longer path were received. In accordance with previously made observations it was assumed that for water flow to the base of the concrete block equal to 0.5 l / h, AE sources are only created in the moist zone which reaches to about 2 cm above the base of the block during 2 hours [2].

Figure 1 presents the block diagram of the used measurement system, where: *1* – KD 91 accelerometer, *2* – investigated concrete block, *3* – laboratory tank, *4* – preamplifier of AE signals type 233–5, *5* – 232 B band amplifier, *6* – digital storage oscilloscope 2230, *7* – 1210 printer, *8* – EA-3, apparatus for AE parameter measurement designed by the author, *9* – B72BP two-channel analogue *X* – *Y* plotter.

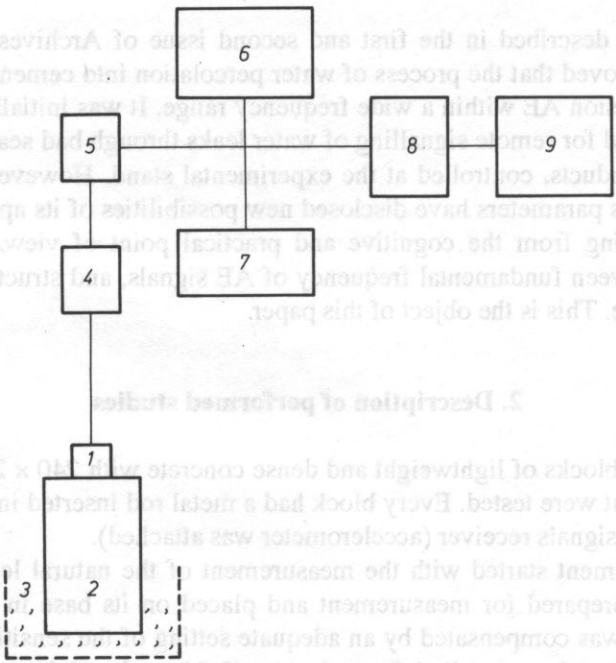

FIG. 1. Block diagram of measuring system.

Event rate, N_e', and energy, E_s, was measured with the AE-3 apparatus and results were recorded by the plotter. The fundamental frequency f_p, of AE signals was read off the digital display of an oscilloscope and printed. Mean f_p values for successive 10 – minute periods were calculated. Owing to this $f_p = f(t)$ diagrams became more readable and could be more easily interpreted. Above mentioned measurements were performed in individual concrete blocks during 2.6 – 3 hours. After this time the process of concrete swelling terminated and an increased stream of water would be necessary to initiate the process again. But this would change the conditions of the experiment, which should be constant [6].

3. Research results and their discussion

Fundamental frequency measurements of AE signals as a function of time were made in 21 concrete blocks. Examples of typical results for lightweight concrete and AE sources situated about 0.15 m from the signal receivers are presented in Figs. 2, 3, 4, 5. While results for greater distances travelled by AE signals – up to about 0.45 m – are shown in Figs. 6, 7, 8.

An increase of path length of AE signals from 0.15 to 0.45 m in dense concrete only slightly influenced frequency f_p and, thus, it was messured only in concrete blocks with 0.15 m height. Figures 9, 10, 11 present examples of results obtained from this measurement.

It is characteristic of results of $f_p = f(t)$ measurements in lightweight concrete blocks with 0.15 m height that increases and decreases of AE signal frequency are noted alternately. The range of these variations decreases with time and the f_p value decreases at the same time (see Figs. 2, 3, 4, 5).

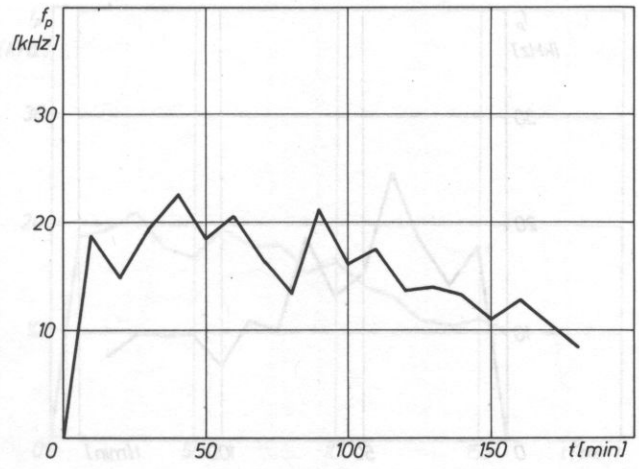

FIG. 2. Example of changes $f_p = f(t)$ in lightweight concrete with length 0.15 m.

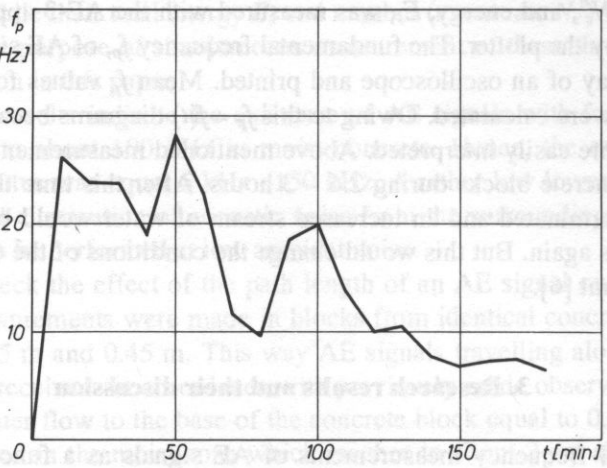

FIG. 3. Example of changes $f_p = f(t)$ in lightweight concrete with length 0.15.

The dimension of the source of acoustic emission is the fundamental factor conditioning the fundamental frequency of the signal. If a crack in the material is such a source (as e.g. in case of concrete swelling) then f_p is inversely proportional to the crack's length. Taking this into consideration one might expect f_p changes in diagrams to illustrate deformations in concrete due to its dampness. Initial small cracks in binding material (accompanied by higher frequency AE signals) cause it to expand and shift (lower frequency AE signals). This is promoted by the porous and weak structure of the material. This process repeats in cycles with decreasing intensity as the concrete becomes saturated with water. In the final stage of the experiment, deformations generating low frequency AE signals dominate. These can be bigger cracks (bigger than those

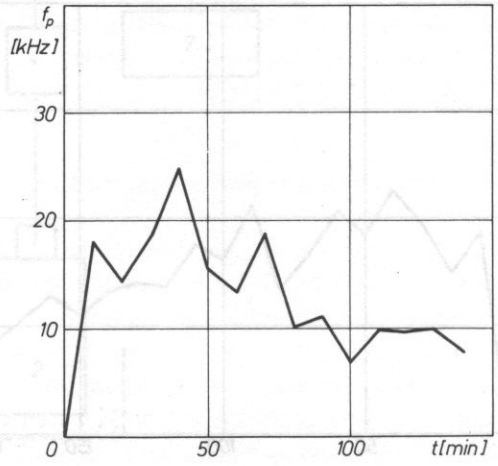

FIG. 4. Example of changes $f_p = f(t)$ in lightweight concrete with length 0.15 m.

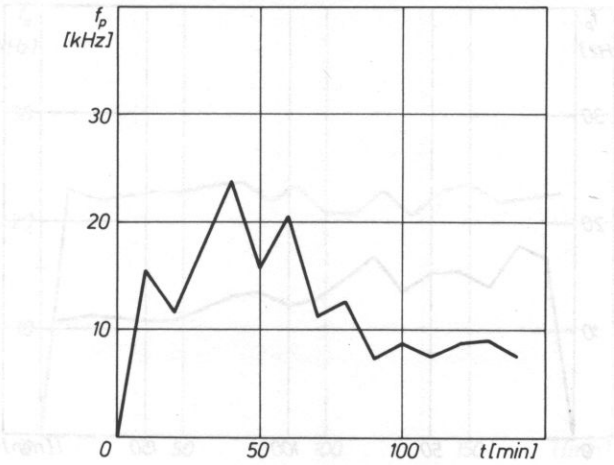

FIG. 5. Example of changes $f_p = f(t)$ in lightweight concrete with length 0.15 m.

in the binding material) created by releasing of energy, cumulated locally in the concrete body due to prolonged expanding action caused by material swelling.

When the path of AE signals in lightweight concrete legthens out up to about 0.45 m, then higher frequencies are attenuated much more strongly than lower ones. Hence, the measured range of f_p values is relatively small, but the downward tendency in f_p values is observed as in previous experiments with lightweight concrete blocks with 0.15 m height (see Figs. 6, 7, 8).

In dense concrete f_p value fluctuations are small and they oscillate around the same average level (see Figs. 9, 10, 11) even for a short path of AE signals (about 0.15 m). This indicates a different process of material deformation than for lightweight concrete. Low porosity, high compaction and rigidity of dense concrete structure promotes the

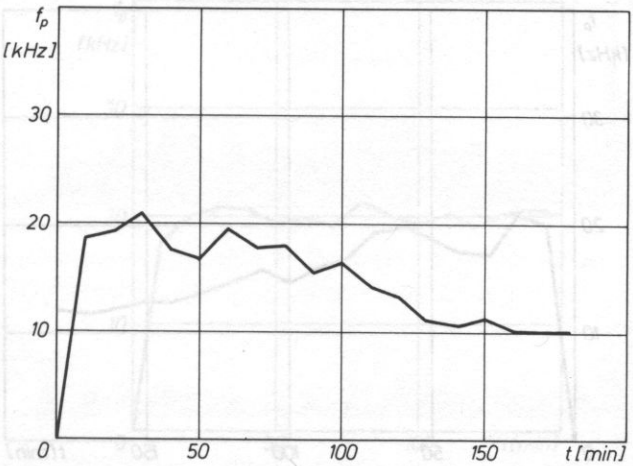

FIG. 6. Example of changes $f_p = f(t)$ in lightweight concrete with length 0.45 m.

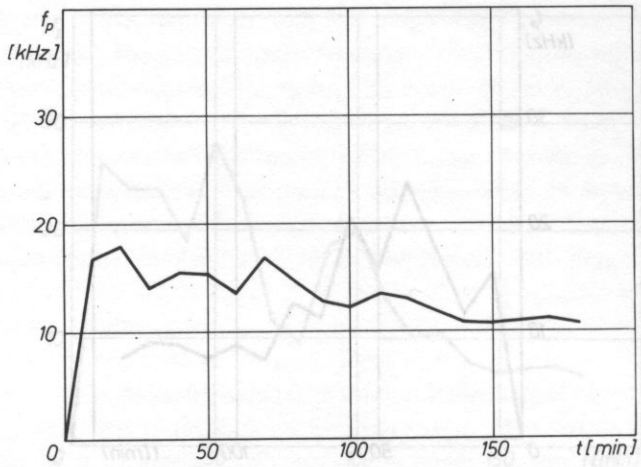

FIG. 7. example of changes $f_p = f(t)$ in lightweight concrete with length 0.45 m.

formation of rather small cracks and at the same time it resists the displacement of swelling binding material. This can surely explain the process of rather stable deformation of dense concrete due to moisture. It finds confirmation in results of $f_p = f(t)$ measurements.

Independently of the type of tested concrete, AE signals with fundamental frequency equal to about 100 kHz were observed in the final stage of most experiments. A supposition arises here that after a longer period of water percolation some eroded aggregate grains undergo swelling. However, these grains are harder and more resistant to compression than concrete binder. This creates conditions for the formation of microcracks in these grains, which can be sources of high frequency AE signals.

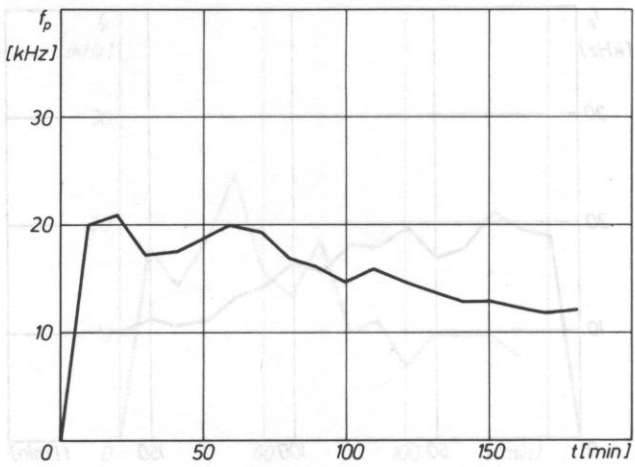

FIG. 8. Example of changes $fp = f(t)$ in lightweight concrete with length 0.45 m.

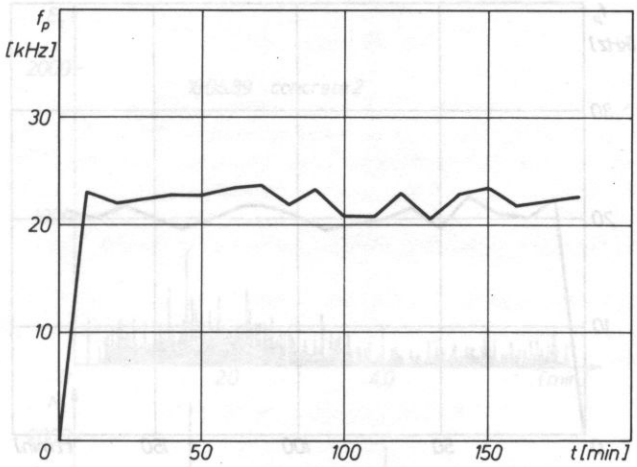

FIG. 9. Example of changes $f_p = f(t)$ in dense concrete with length 0.15 m.

For the last several years the AE signals energy to event rate ratio has been considered as an important source of information about the type of material deformation. High values of this ratio indicate the formation of big but not numerous cracks. whereas for low E_s/N_e' values numerous, small cracks are formed.

Figure 12 presents an example of measurement results of E_s energy of AE signals and event rate N_e' versus time for lightweight concrete. In Fig. 13 we have the same relation for dense concrete. Comparing these results we can find that in most 10-second intervals $E_s/N_e' > 1$ in lightweight concrete and $E_s/N_e' < 1$ in dense concrete Similar results were achieved in experiments with other concrete blocks.

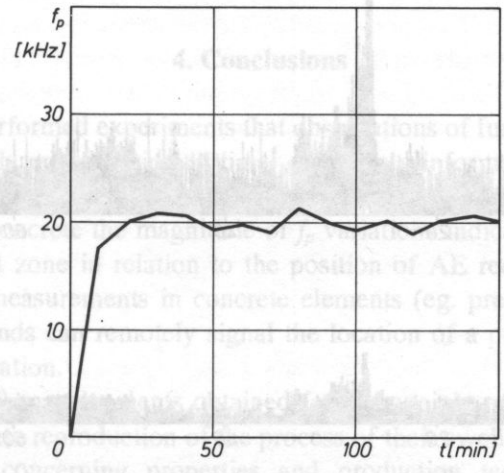

FIG. 10. Example of changes $f_p = f(t)$ in dense concrete with length 0.15 m.

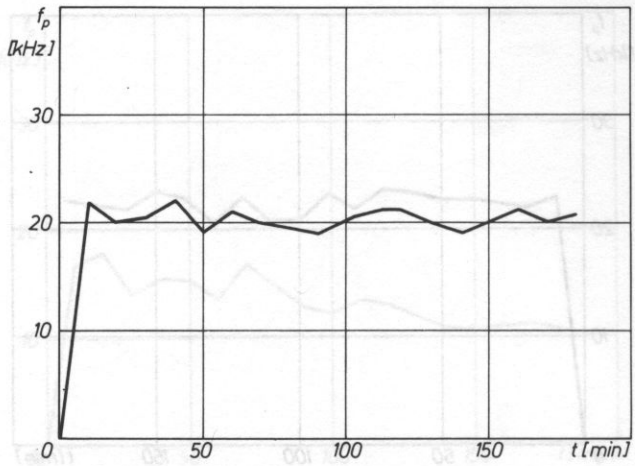

FIG. 11. Example of changes $f_p = f(t)$ in dense concrete with length 0.15 m.

All E_s and N_e' measurements were performed in the same conditions. Hence, we can pressume on the basis of given above dependences that moisture generates bigger cracks in light weight concrete than in dense concrete. This conclusion agrees with results of f_p measurements.

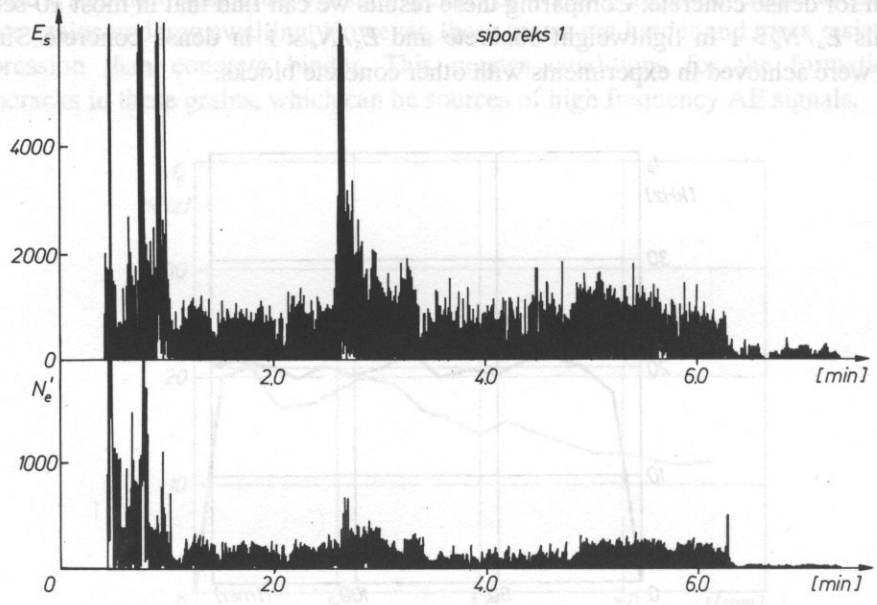

FIG. 12. Typical example of experimental results of E_s, $N_e' = f(t)$ in lightweight concrete.

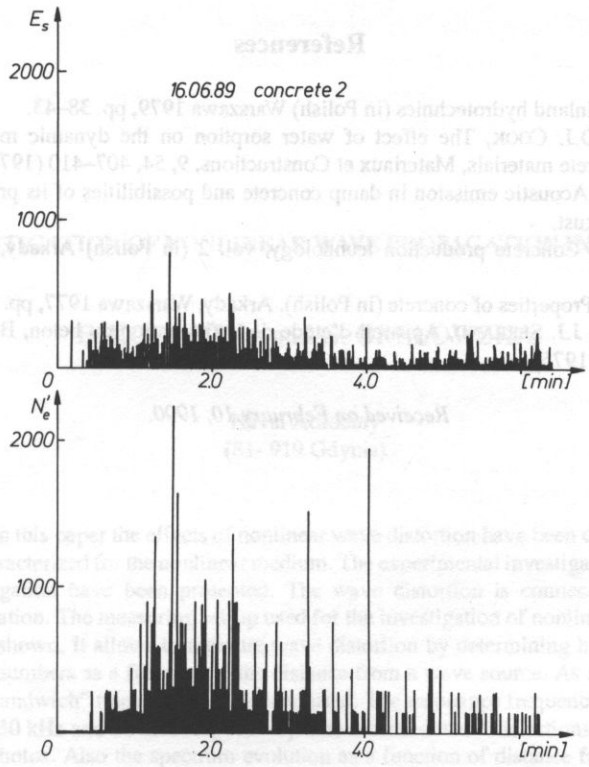

FIG. 13. Typical example of experimental results of E_s, $N'_e = f(t)$ in dense concrete.

4. Conclusions

It results from performed experiments that observations of fundamental frequency f_p changes of AE signals as a function of time, can supply information about the type of concrete into which water begins to permeate and about the swelling process itself. In case of lightweight concrete the magnitude of f_p variations indicates approximately the location of the moist zone in relation to the position of AE receiver. In practice this means that $f_p = f(t)$ measurements in concrete elements (eg. prefabricated joints) controlled on testing stands can remotely signal the location of a possible water leak and approximately its duration.

Results of $f_p = f(t)$ measurements obtained for lightweight and dense concrete also lead to a more accurate reproduction of the process of their swelling (see p. 3) than that found in literature concerning properties and production technology of concrete [1, 4, 5].

References

[1] W. BALCERSKI, Inland hydrotechnics (in Polish) Warszawa 1979, pp. 38–43.
[2] M.N. HAQUE, D.J. COOK, The effect of water sorption on the dynamic modulus of elasticy of desiccated concrete materials, Materiaux et Constructions, **9**, 54, 407–410 (1976).
[3] W. KOŁTOŃSKI, Acoustic emission in damp concrete and possibilities of its practical application (in Polish) Arch. Akust.
[4] W. KUCZYŃSKI, Concrete production technology, vol. 2 (in Polish) Arkady, Warszawa 1972, pp. 575–583.
[5] A.M. NEVILLE, Properties of concrete (in Polish). Arkady, Warszawa 1977, pp. 259–272, 307–312.
[6] A.M. PAILLERE, J.J. SERRANO, Appareil d'etude de la fissuration du beton, Bull. Liaison Lab. P. et Ch., **83**, 29–38 (1976).

Received on February 10, 1990.

ARCHIVES OF ACOUSTICS
17, 1, 77–87 (1992)

INVESTIGATION OF NONLINEAR WAVE PROPAGATION IN WATER

E. KOZACZKA and G. GRELOWSKA

Naval Academy
(81- 919 Gdynia)

In this paper the effects of nonlinear wave distortion have been described. This problem is characterized for the nonlinear medium. The experimental investigation results of nonlinear propagation have been presented. The wave distortion is connected with the harmonic generation. The measuring set-up used for the investigation of nonlinear wave distortion has been shown. It allows to measure wave distortion by determining harmonic amplitude and their numbers as a function of the distance from a wave source. As a primary wave source, the "sandwich" transducers have been used. The resonance frequencies of these transducers were 30 kHz and 81 kHz respectively. The recorded wave distortions are shown in diagrams and photos. Also the spectrum evolution as a function of distance from the wave source is shown. The investigation results are connected with the weak nonlinear wave distortion.

1. Finite amplitude wave propagation in nonlinear medium

The description of dynamical effects is carried out by means of equations of continuity, motion and state that characterize this phenomenon. The system of equations of continuity, motion, entropy and state makes it possible to obtain the nonlinear equation. This equation describes wave propagation with finite amplitude [2].

The assumption that the acoustic Mach number has small values in hydroacoustics is correct. This means that relative changes of density and pressure are small. Thanks to these facts, one can describe the nonlinear equation of acoustics as follows [3]:

$$\Delta p' - \frac{1}{c_0^2}\frac{\partial^2 p'}{\partial t^2} + \frac{b}{c_0^2 \rho_0}\frac{\partial}{\partial t}\Delta p' = -Q \tag{1}$$

where

$$Q = \frac{1}{c_0^4 \rho_0}\left(\frac{\partial p'}{\partial t}\right)^2 + \frac{\varepsilon - 1}{c_0^4 \rho_0}\frac{\partial^2 p'}{\partial t^2} + \frac{\rho_0}{2}\Delta v^2 + \rho_0 v \Delta v \tag{1a}$$

$p' = p - p_0$ – acoustic pressure, c_0 – speed of sound wave, ρ_0 – medium density ar rest, b – attenuation factor, t – time, ε – nonlinearity parameter factor, v – vibration velocity.

The solution of Eq. (1) has not been found till now, but a few methods of its simplification are used. Sometimes the perturbation method is used. It gives good results in the case when the nonlinear effects are relatively small. This method takes into account the spare assumptions: the wave is a plane wave and the attentuation factor is equal to zero.

The other form of the known method which allows to solve Eq. (1) is connected with the quasi-optical assumption. It is assumed that the wave distortion is very small on the path equal to the wave length and the form of energy flux can change not only in the direction of wave propagation but in the transverse one, too. The transverse changes are larger than the longitudal ones because of the diffraction effect. By fixing a coordinate system in the zero phase of the wave that propagates with c_0 speed, one can transform Eq. (1) to the following form [7]:

$$\frac{\partial}{\partial\tau}\left[\frac{\partial p'}{\partial z}-\frac{\varepsilon}{c_0^3\rho_0}p'\frac{\partial p'}{\partial\tau}-\frac{b}{2c_0^3\rho_0}\frac{\partial^2 p'}{\partial\tau^2}\right]=\frac{c_0}{2}\left(\frac{\partial^2 p'}{\partial x^2}+\frac{\partial^2 p'}{\partial y^2}\right) \tag{2}$$

where: $\tau = t - z/c_0$ – time in the Lagrange description, z – wave propagation direction, x, y – axis orthogonal to z. This equation is called the Chochlov-Zabolotska-Kuznetsov equation. The above presented equation has no solution. When the right side of the equation equals zero, then one obtains the Burgers equation [7]:

$$\frac{\partial p'}{\partial z}-\frac{\varepsilon}{\rho_0 c_0^3}p'\frac{\partial p'}{\partial\tau}-\frac{b}{2\rho_0 c_0^3}\frac{\partial^2 p'}{\partial\tau^2}=0\,. \tag{3}$$

It is a nonlinear equation that can be solved. The solution of Eq. (3) is very useful in analizing the nonlinear effects occurring on the energy flux axis. Unfortunately, it does not take into account the diffraction phenomenon because of one dimension of Burger's equation. Its solution describes the plane waves. Another advantage of this solution is the lack of any limits of acoustic Reynolds number values determined by [5]

$$\mathrm{Re}_a=\frac{\rho_0 c_0 v}{b\omega} \tag{4}$$

where $\omega = 2\pi f$, f – frequency.

Burgers' equation can be solved for the two main cases, that is for a small Reynolds number and for a large one. The first case is strictly connected with the large dissipative effects and the second one when the nonlinear effects are dominating.

The effect of nonlinear distortion in water is similar to the phenomenon which takes place during shock wave propagation in air. In air the finite amplitude wave distortion takes place due to the difference of phase velocity. In the compression area the phase velocity is higher than in the rest area as well as in the expansion one. Finally this phenomenon causes a wave distortion from sine form to a saw-tooth one. The wave distortion is strictly connected with harmonic generation whose numbers and amplitudes are a function of the distortion degree.

The effect of wave shape change can be observed on the basis of Riemman's solution of an equation that describes the plane finite amplitude wave in an idealized fluid.

The Lagrange description is used. The particle velocity v can be described in the form [4]:

$$v(z,\tau) = v_0 \sin\omega(\tau - \frac{z\varepsilon v}{c_0^2}) \tag{5}$$

where v_0 – source vibration velocity.

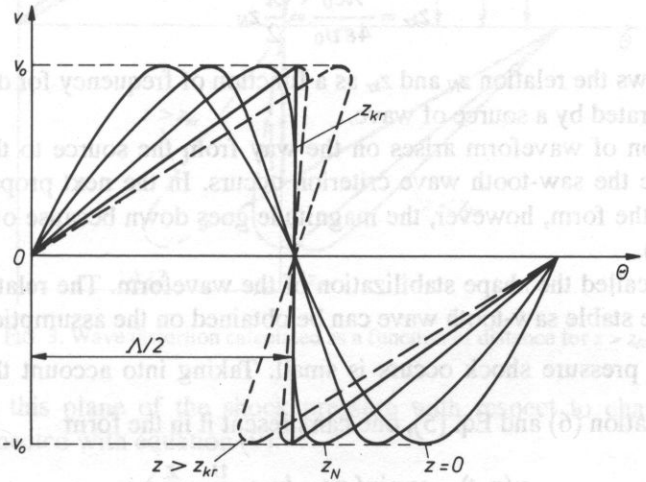

FIG. 1. Wave distortion calculated as a function of distances for $z \leq z_{kr}$.

According to Eq. (5), the waveform changes the shape (see Fig. 1) step by step up to the point where it reaches the range $z = z_N$. The value z_N is a boundary value of a coordinate z for which the functional described by the relation (5) is single-valued function. This value can be determined by means of the following formula [4]:

$$z_N = \frac{c_0^2}{\omega\varepsilon v_0} = \frac{c_0\lambda}{2\pi\varepsilon v_0}. \tag{6}$$

At the range from the source $z > z_N$, the solution of Eq. (5) is not a single-valued function. This range is sometimes called the distance of loss of solution continuity or simply the discontinuity distance. The loss of a continuity of waveform description takes place only in mathematical formalism because it takes into account the wave propagation in the idealized fluid. In the case of sound propagation in the real medium, that is water, with the increase of distortion the loss of wave energy increases, too. As a result of these interactions, the harmonic wave becomes saw-tooth shaped at some distance from the source. This distance is called the critical distance. This distance can be determined on the basis of the following approach. The finite amplitude were speed can be taken apart as the sum of two components of speed. The first one is a sound speed in the rest medium and the second component is connected with the rise of the total speed as a result of the medium nonlinearity [5]:

$$c = c_0 + \varepsilon v(z, \tau). \tag{7}$$

To create the saw-tooth wave, the top of the wave must overcome the way $\lambda/4$ (λ – wavelength) with the speed εv_0 at the same time as the distance $z = z_{kr}$ is overcome with c_0 speed. Assuming that these times are equal, one can obtain the following relation [5]:

$$z_{kr} = \frac{\lambda c_0}{4\varepsilon v_0} = \frac{\pi}{2} z_N \tag{8}$$

Figure 2 shows the relation z_N and z_{kr} as a function of frequency for different values of pressure generated by a source of wave.

The distortion of waveform arises on the way from the source to the critical distance (z_{kr}) where the saw-tooth wave criterion occurs. In the next propagation region the wave keeps the form, however, the magnitude goes down because of the nonlinear damping (Fig. 3).

This area is called the shape stabilization of the waveform. The relation describing the motion of the stable saw-tooth wave can be obtained on the assumption that the distance where the pressure shock occurs is small. Taking into account that $\tau = t - \frac{z}{c_0}$, $k = \omega/c_0$, the relation (6) and Eq. (5), one can present it in the form

$$v(z, t) = v_0 \sin(\omega t - kz + \frac{v}{v_0} \cdot \frac{z}{z_N}). \tag{9}$$

The plane where the pressure shock occurs moves in the space with phase speed c_0 and during time t it overcomes the way from a transmitter equal to $z = c_0 t$. The position of this plane is described by means of the phase equation $\omega t - kz = 0$. The condition of

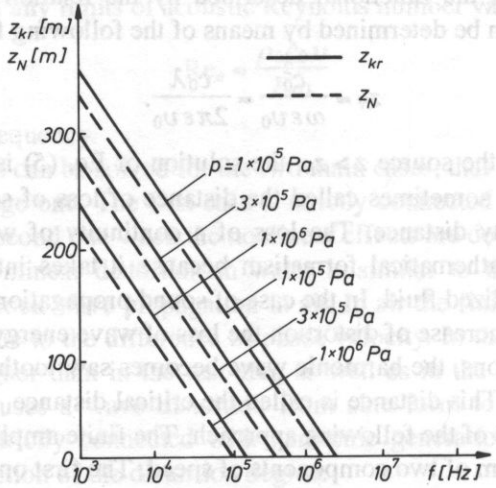

FIG. 2. The dependence of the distances z_N and z_{kr} on the frequency calculated for different values of pressure generated by the wave source.

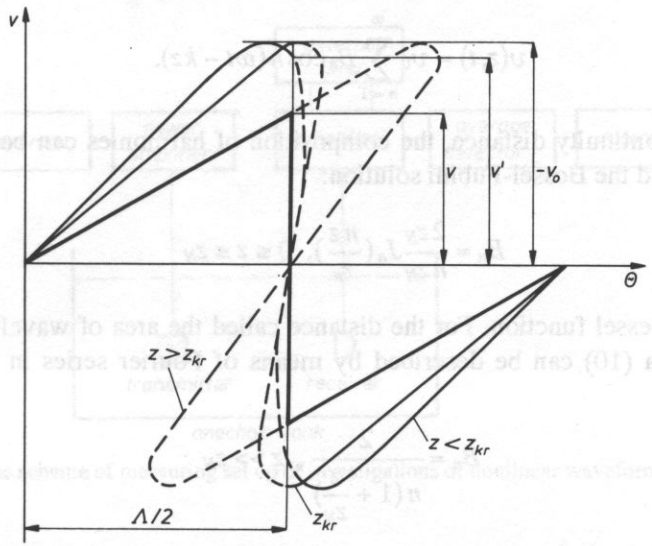

FIG. 3. Wave distortion calculated as a function of distance for $z > z_{kr}$

occurrence on this plane of the shock pressure with respect to changes of particle velocity is connected with equation (9):

$$v = v_0 \sin\left(\frac{v}{v_0} \cdot \frac{z}{z_N}\right) \tag{10}$$

where $z > z_{kr}$ and v is the magnitude of the saw-tooth wave. In the distance of $z/z_N >> 1$, the expression $\sin\left(\frac{v}{v_0} \cdot \frac{z}{z_N}\right)$ can be represented by a Taylors' series expansion close to point π, allowing the formula (10) to show in the simpler form

$$v = v_0 \frac{\pi}{1 + \frac{z}{z_N}} \tag{11}$$

that describing the decrease of the wave magnitude.

At the large distance from the transmitter, as a result of dissipation of wave energy, the nonlinear distortion falls down and the wave-front changes. The shape of the wave goes to the harmonic wave.

2. Finite amplitude plane wave spectrum

The change of the shape of the finite amplitude harmonic wave during propagation in nonlinear medium is connected at the same time with a change of wave spectrum.

The evolution of the wave spectrum can be shown using the Fourier series of the solution of Burgers' equation for large Reynolds numbers [1]:

$$v(z,t) = v_0 \sum_{n=1}^{\infty} B_n \cos n(\omega t - kz). \tag{12}$$

For the discontinuity distance, the composition of harmonics can be shown in the form that is called the Bessel-Fubini solution:

$$B_n = \frac{2z_N}{n z_N} J_n\left(\frac{nz}{z_n}\right), \quad 0 \le z \le z_N \tag{13}$$

where $J_n(\cdot)$ – Bessel function. For the distance called the area of waveform stabilization, the formula (10) can be described by means of Fourier series in the following form:

$$B_n = \frac{2}{n\left(1 + \frac{z}{z_N}\right)}, \quad z >> z_N \tag{14}$$

Distortion of the harmonic wave is connected with the phenomenon of pumping of the primary wave energy to harmonics. The nonlinear distortion can be characterized by a change of the wave spectrum. The spectrum of a radiated wave at the transmitter ($z = 0$) has only spike whose value equals v_0. In the area $0 < z \le z_{kr}$ the number of spectrum spikes related to higher harmonics increases and their amplitudes increase too, but the amplitude of primary wave decreases. In the distance of the stabilizing waveform, the loss of energy is due to nonlinear attenuation. The value of the differential attenuation coefficient is not a function of frequency. With regard to this fact, the number of harmonics is constant but the values of their amplitudes decrease. At a large distance from the transmitter $z >> z_{kr}$, the spectral spikes related to higher harmonics slowly decay. Taking into account the above data one can notice that for investigation of large intensity waveform distortion the method of measuring harmonics amplitudes is very useful.

3. The Measuring system

The observation of nonlinear distortion of waveform during its propagation in water was carried out by measuring the harmonic amplitudes. The measure were carried out by means of a set up that is shown in Fig. 4.

Piezoelectric transducers in "sandwich" form are used as transmitters with the frequency 30 kHz and 81 kHz, respectively. In both cases the wave intensity was limited by cavitation phenomena [6].

The measurements of harmonic amplitudes were carried out on the axis of the transmitters' beams. The receiving signal from the receiving transducers was amplifield by means of a measuring amplifier with a set of band pass filters allowing to measure and register the value of harmonic amplitudes.

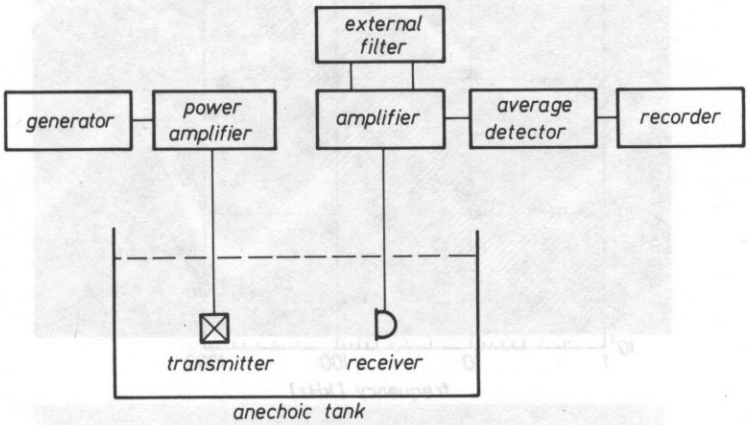

FIG. 4. The scheme of measuring set up of investigations of nonlinear waveform distortions.

4. Investigation results

Our investigations consisted in observing primary wave distortion and the creation of harmonics. In Fig. 6 the change of primary waveform shape (frequency 30 kHz and value of Reynolds number $Re_a = 8.5$) in water at the distance of $12\,R_0$ is shown. R_0 is the Rayleigh length $R_0 = S/\lambda$, S – area of transmitter. Figure 7 shows the primary wave shape, the first harmonic and the second one at the distance of $6\,R_0$ from the transmitter. The primary wave distortion ($f = 81$ kHz, $Re_a = 14.2$) is shown in Fig. 8. During investigation, time histories are recorded by means of a digital oscilloscope. One can notice the distortion of waveform shape and the first harmonic. On the second line of the oscilloscope view, the reference signal that is put into the transmitter is shown.

The distortion of wave shapes shown in the figures and photos are not too large. However, one can notice the differences between the length of the increase and decrease slopes.

The study carried out allows to observe the changes of wave spectrums during propagation in water. The wave's spectrum of the primary wave with frequency equal to 81 kHz ($Re_a = 14.2$) at the range $15\,R_0$ from the transmitter (Fig. 8) is shown in Fig. 9.

The measuring results of the harmonic components of the 30 kHz primary wave ($Re_a = 8.5$) as a function of the range from the transmitter is presented in Fig. 10. The correction factor connected with the spherical spreading of the waveform outside the Rayleighs area ($z > R_0$) is taken into account.

The registered nonlinear distortion are relatively small as a result of the limitation of the wave intensity due to the occurrence of a cavitation in both cases. The increase of the cavitation threshold for the same frequency can be obtained following the increase of the static pressures or by increasing the localization of the depth of the transmitting transducer. A similar result can be achieved by using cleaned and degased water.

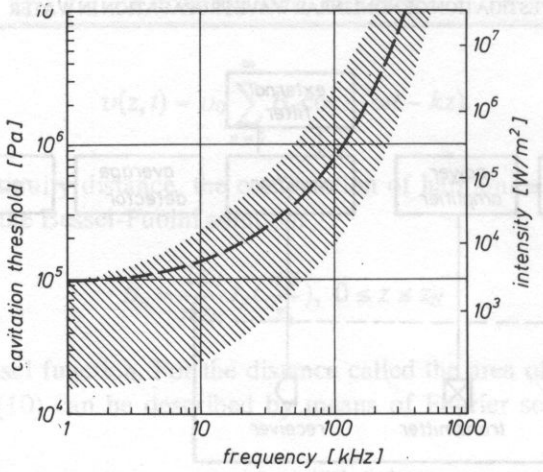

FIG. 5. The dependence of the cavitation threshold on the frequency [6].

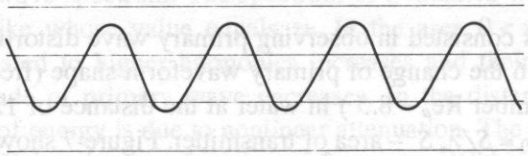

FIG. 6. The shape of the wave (frequency 30 kHz) measured at the distance of 12 R_0 from the transmitter.

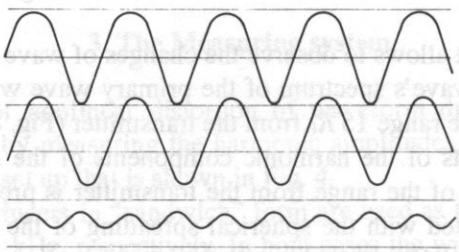

FIG. 7. The shape of the wave frequency 30 kHz and the first and the second harmonics measured at the distance of 6 R_0 from the transmitter; $\mathrm{Re}_a = 8.5$.

a)

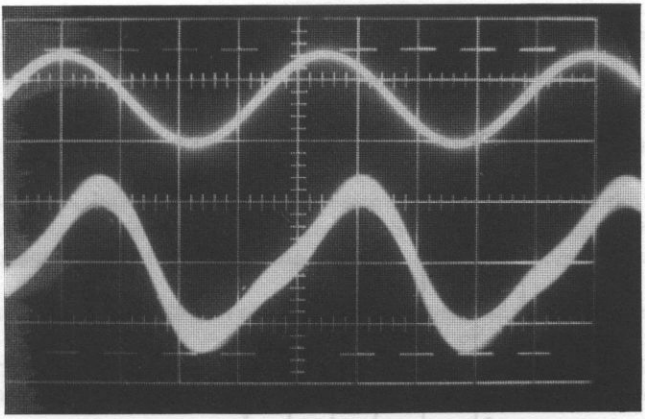

b)

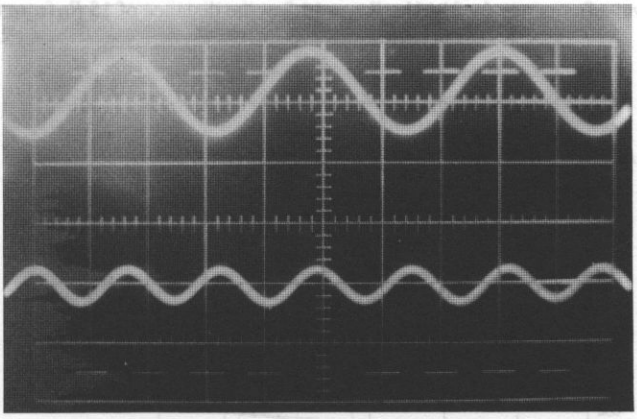

c)

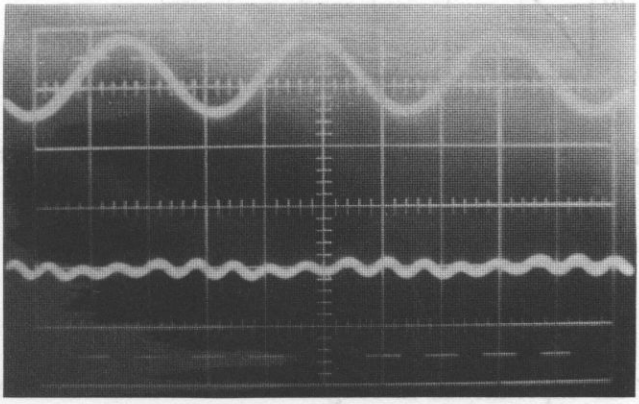

FIG. 8. The distortion of the wave shape (frequency 81 kHz) (a), the second harmonic (b) and the fifth one (c).

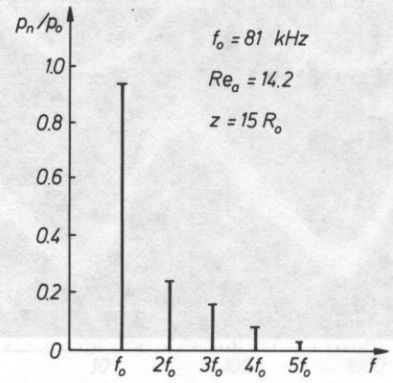

FIG. 9. Spectrum of wave frequency $f = 81$ kHz, $Re_a = 14.2$ at the distance of 15 R_0 from the transmitting transducer.

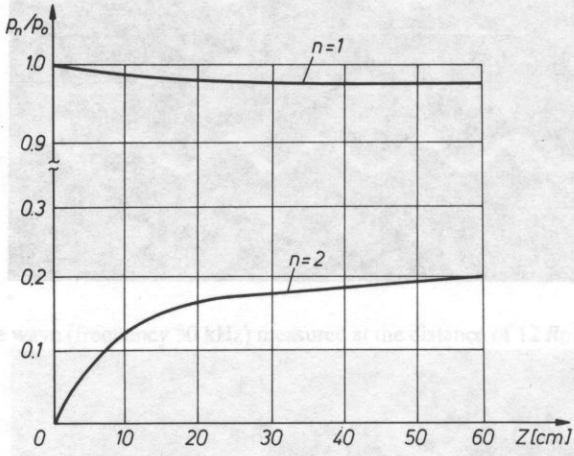

FIG. 10. The first and the second harmonic measurements as a function of the range from the primary wave transmitter $f = 30$ kHz .

5. Conclusions

The results of the experimental investigation of the nonlinear wave propagation presented above allows to determine the wave distortion. The method based on measurements of harmonics amplitudes and their numbers as a function of the range from the wave source is effective in the case of a weak nonlinear interaction, too.

In particular, changes of the second harmonic amplitude can be used to determine the nonlinearity parameter B/A.

References

[1] D.T. BLACKSTOCK, *Connection between the Fay and Fubini solutions for plane sound waves of finite amplitude*, J. Acoust. Soc., Am., **39**, 6, 1019–1016 (1966).

[2] P.M. MORSE, U.K. INGRAD, *Theoretical acoustics*, McGraw–Hill, New York 1968.

[3] B.K. NOVIKOV et al., *Nonlinearity hydroacoustics*, Sudostroene, Leningrad 1981.

[4] D.V. RUDENKO, S.I. SOLUAN, *A theoretical introduction to nonlinearity acoustics*, Nauka, Moscow 1975.

[5] V.A. SCHUTILOV, *An introduction to physics of ultrasound*, Leningrad University Press, Leningrad 1980.

[6] R.J. URICK, *Principles of underwater sound*, McGraw–Hill Book Company 1975.

[7] L.K. ZAREMBO, V.I. TIMOSCHENKO, *Nonlinearity acoustics*, Moscow University Press, Moscow 1984.

Received on September 14, 1990

ARCHIVES OF ACOUSTICS
17, 1, 89–102 (1992)

ULTRASONIC WAVES IN SOME BIOLOGICAL SUSPENSIONS AND EMULSIONS

J. LEWANDOWSKI

Institute of Fundamental Technological Research Polish Academy of Sciences
00-049 Warszawa, Świętokrzyska 21

The frequency dependence is established for the propagation velocity and attenuation coefficient of ultrasonic waves in dilute suspensions and emulsions and digital computations are performed for the aqueous emulsion of sunflower oil. The results show that the measurements of the propagation velocity of ultrasonic waves enable us to estimate the volume fraction of the suspended particles of both dilute and highly concentrated suspensions and emulsions.

Keywords: suspensions; emulsions; ultrasonic waves; propagation velocity; attenuation coefficient.

1. Introduction

In many areas of research such as cloud physics, underwater acoustics, medicine and in engineering application such as rocket propulsion, lubrication and so on are of interest the effective dynamic properties of some types of suspensions and emulsions. These properties are related to the acoustic wave velocities in the materials under study and their structure. Therefore some properties and structure parameters of suspensions and emulsions can be estimated on the basis of ultrasonic measurements.

In this paper, the two-component media are described using Truesdell's concept of replacing the noncontinuous components by fictitious continuous constituents [1]. The basic phenomenon responsible for attenuation and dispersion is, in the approach presented, relaxation of the phases (components) due to the velocity difference between them. In other words, attenuation and dispersion are caused by the inability of the phases to follow each other in the changes of the mechanical state, the changes being induced by the ultrasonic waves. The frequency dependence of the wave velocity and attenuation is evaluated by using a secular equation which, in turn, is obtained from hydrodynamic considerations.

2. Equations of continuity and balance of linear momentum

As previously mentioned we consider a two-component medium with a Newtonian fluid as one of the components (phases). Throughout the paper this fluid is called the f – phase and all the quantities concerning this phase are denoted by abbreviations with the subscript or superscript f. The other phase is called the s – phase and is taken to have the form of an elastic skeleton with a statistical distribution of interconnected pores or a set of particles with arbitrary shape and size. The particles are assumed to be made up of a solid material or of another Newtonian fluid which is immiscible in the first one (f – phase) and chemically non-reacting with that. Throughout the paper every abbreviation with the subscript or superscript s denotes a quantity referred to the s – phase.

If $\rho_{(\alpha)}$ denotes the density of the phase component occupying the set of disjoint domains V_α of the Lebesgue measure $m[V_\alpha]$ and b_α is its volume fraction, then ρ_α defined as

$$\rho_\alpha = b_\alpha \rho_{(\alpha)}, \quad b_\alpha = \frac{m[V_\alpha]}{m[V]}, \quad \alpha = s, f \tag{2.1}$$

represents the mass of the α-th component per unit volume, and the formula

$$\rho = \sum_\alpha \rho_\alpha \tag{2.2}$$

defines the density of the medium occupying the domain V of the Lebesgue measure (volume) $m[V]$. The formulae (2.1) can be regarded as the definitions of the density ρ_α of the α-th fictitious constituent and its volume fraction with the constituent considered to be present in every point of the domain V.

Such a concept of treating an n – phase medium ($n = 2, 3, 4...$) as a mixture of n fictitious continuous constituents was proposed by TRUESDELL [1] and is employed throughout the paper. Equations (2.1) define the volume fraction of the α-th constituent and density to be set functions $b_\alpha(V)$ and $\rho_\alpha(V)$, respectively. However, for making the mathematical analysis methods suitable, all the scalar, vector and tensor fields considered in this paper are required to be point functions of the vector $\mathbf{r} = (x_1, x_2, x_3)$ of the position in the heterogeneous medium under consideration. The Radon-Nikodym theorem enables a wide class of set functions, $F(V)$, to be converted into point functions, as it was explained in the paper [2] by converting $b_\alpha(V)$ in the form given by the formula (2.1) into $b_\alpha(\mathbf{r})$. Use was made of the fact that $m[V_\alpha] = 0$ whenever $m[V] = 0$, where one can conclude that the additive set function $m[V_\alpha]$ is absolutely continuous with respect to Lebesgue measure. Hence, on the strength of the Radon-Nikodym theorem, there exists a point function $b_\alpha(\mathbf{r})$ such that [2]

$$m[V_\alpha] = b_\alpha(V) m[V] = \int_V b_\alpha(\mathbf{r})\, d^3\mathbf{r}, \quad \mathbf{r} \in V \tag{2.3}$$

or, equivalently

$$b_\alpha(\mathbf{r}) = \lim_{m[V]\to 0} \frac{m[V_\alpha]}{m[V]}. \tag{2.4}$$

Now consider the ith, $i = 1, 2, 3$, component of the displacement on the α-th component during the unit time. Let $Q_i^\alpha(V)$ and $q_i^\alpha(V)$ denote the volumes sweeped out due to this movement by the α-th component contained in the whole volume of the domain V and in its unit volume element, respectively. Therefore we can write

$$Q_i^\alpha(V) = q_i^\alpha(V)\, m[V], \; i = 1, 2, 3. \tag{2.5}$$

In such a way we define the volume flux $q_i^\alpha(V)$ to be a set function. It can be converted to a point function, $q_i^\alpha(\mathbf{r})$, $\mathbf{r} \in V$, by employing the fact that $Q_i^\alpha(V) = 0$ whevener $m[V] = 0$. Hence we conclude that the additive set function $Q_i^\alpha(V)$ is absolutely continuous with respect to Lebesgue measure. Thus, by the Radon-Nikodym theorem, there exists a function $q_i^\alpha(r)$ such that

$$Q_i^\alpha(V) = q_i^\alpha(V)\, m[V] = \int_V q_i^\alpha(\mathbf{r})\, d^3\mathbf{r}, \; \mathbf{r} \in V \tag{2.6}$$

Equivalently, one may write

$$q_i^\alpha(\mathbf{r}) = \lim_{m[V]\to 0} \frac{Q_i^\alpha(V)}{m[V]}. \tag{2.7}$$

On defining the volume flux as a point function $q_i^\alpha(r)$, we can write

$$q_i^\alpha(\mathbf{r}) = s_0\, v_i^\alpha(\mathbf{r}); \quad v_i^\alpha(\mathbf{r}) = b_\alpha(\mathbf{r}) v_i^{(\alpha)}(\mathbf{r}), \quad i = 1, 2, 3. \tag{2.8}$$

s_0 denotes the unit surface. Equations (2.6) and (2.8) or, equivalently (2.7) and (2.8) define the velocities $v_i^{(\alpha)}(\mathbf{r})$ and $v_i^\alpha(\mathbf{r})$ of the α-th component and fictitious continuous constituent, respectively, as point functions.

After defining the point functions $b_\alpha(\mathbf{r})$ and, consequently, $\rho_\alpha(\mathbf{r})$, and $v^\alpha(\mathbf{r})$, the equations of continuity and balance of linear momentum can be derived in the usual way (see, e.g. [2]) for the two-component medium under consideration. In this way we arrive at the following continuity equations:

$$\frac{\partial \rho_\alpha}{\partial t} + \operatorname{div}(\rho_{(\alpha)} \mathbf{v}_\alpha) = 0, \quad \alpha = s, f \tag{2.9}$$

which express the laws of mass conservation on the α-th continuous constituent, $\alpha = s, f$. If we add Eqs. (2.9) to each other and next if we add and subtract the expression $\operatorname{div}(\rho_f \mathbf{v}^s)$ to and from the resulting equation then we arrive at the following equation, after some manipulation:

$$\frac{\partial \rho}{\partial t} + \operatorname{div}(\rho\, \mathbf{v}^{(s)} - \rho_f \mathbf{u}) = 0 \tag{2.10}$$

where the so-called diffusion velocity, $\mathbf{u}$, is defined as follows $\mathbf{u} = \mathbf{v}^{(s)} - \mathbf{v}^{(f)}$.

To obtain Eqs. (2.9) and, consequently, Eq. (2.10) by following [2], a volume $V(t)$ has been considered which is allowed to change with increasing time, t, due to progressing flow so that the mass, m, of the mixture contained remains constant. Then the changes in the momentum of the mass m can be equated to the sum of the forces acting on the medium occupying the volume $V(t)$. These forces can be divided into forces $\mathbf{F}_S$ acting on the surface $S(t)$ of $V(t)$, and body forces $\mathbf{F}_V$ which act upon the heterogeneous medium occupying every infinitesimal element $dV(t)$ of the volume $V(t)$. Moreover, the phases s and f act on each other but the forces of the phase interaction cancel out each other during summation over $\alpha = s, f$. Therefore, if we neglect the body forces the exterior forces due to gravity, etc. and represent the forces acting on the surface $dS(t)$ of the volume $dV(t)$ by the so-called effective stress tensor, σ, then, following [2, 3] we arrive at the equations

$$\rho_f \frac{\partial \mathbf{v}^{(f)}}{\partial t} + \rho_s \frac{\partial \mathbf{v}^{(s)}}{\partial t} + \rho_f (\mathbf{u}^{(f)} \cdot \operatorname{grad}) \mathbf{v}^{(f)} + \rho_s (\mathbf{v}^{(s)} \cdot \operatorname{grad}) \mathbf{v}^{(s)} = \operatorname{div} \sigma \tag{2.11}$$

σ denotes the stress acting in the medium as a whole.

In the remainder of this paper, we confine ourselves to flows in which the momentum transferred from the continuum f to the continuum s depends linearly on the velocities $\mathbf{v}^{(f)}$, $\mathbf{u}$, and the pressure p_f in the continuum f. Accordingly, we can write

$$\rho_s \frac{d\mathbf{v}^{(s)}}{dt} = \hat{P}\mathbf{u} + \hat{Q}\mathbf{v}^{(f)} + \hat{S}p_f \tag{2.12}$$

$\hat{P}$, $\hat{Q}$ and $\hat{S}$ denote operators which should be determined for every particular model of the medium and flow under study.

To define the pressure p in the medium as a whole, consider the mean internal compression δF_c exerted by the surrounding medium on the surface δS of a small volume δV. If δV can be treated as a good approximation of an infinitesimal volume element dV, then p is to be thought as the ratio of δF_c to δS and its value is supposed to be equal approximately to the mean value between the pressures inside the components occupying the volume δV, i.e.,

$$p = b_f p_{(f)} + b_s p_{(s)} := p_f + p_s \tag{2.13}$$

where $p_{(\alpha)}$, $\alpha = s, f$, stands for the pressure inside the α-th component.

In a similar way, if the s – component is also a Newtonian fluid, we define the dynamic viscosity η, and the second viscosity ζ of the medium as

$$\eta = b_f \eta_{(f)} + b_s \eta_{(s)}, \quad \zeta = b_f \zeta_{(f)} + b_s \zeta_{(s)}. \tag{2.14}$$

$\eta_{(\alpha)}$ and $\zeta_{(\alpha)}$ denote the dynamic and the second viscosity of the α-th component, respectively.

3. Linearized acoustic equations of the solid-fluid heterogeneous media

The scalar, vector and tensor quantities which are involved in the system of Eqs. (2.9) – (2.12) as unknown functions, $F(\mathbf{r}, t)$ are assumed to be of the form

$$F(\mathbf{r}, t) = \bar{F} + \Delta F(\mathbf{r}, t), \quad \bar{F} = const. \tag{3.1}$$

$\Delta F(\mathbf{r}, t)$ denotes the local and instant fluctuation in a quantity $F(\mathbf{r}, t)$ about its equilibrium value which is denoted by the overbar. It is assumed that

$$\left| \frac{\Delta F(\mathbf{r}, t)}{\bar{F}} \right| << 1.$$

Henceforth the fluctuations $\Delta F(\mathbf{r}, t)$ only in the form of acoustic ultrasonic disturbances are of interest to us, simple harmonic time and position dependence being assumed, i.e.,

$$\Delta F(\mathbf{r}, t) = \Delta F_0 \exp\left[-i(\omega t - \mathbf{k} \cdot \mathbf{r})\right], \quad \mathbf{k} = \left(\frac{\omega}{c} + i\mu\right)\mathbf{e}_k, \quad i = (-1)^{1/2}, \quad \mathbf{e}_k = 1. \tag{3.3}$$

The expressions (3.3) describe an attenuated plane wave propagating in the direction $\mathbf{e}_k$ and with the velocity c through a medium with the attenuation coefficient μ. The abbreviation ΔF_0 stands for the amplitude of the fluctuation $\Delta F(\mathbf{r}, t)$. Therefore the acoustic disturbances under consideration are assumed to be the periodic fluctuations (3.3) in the density $\Delta\rho_\alpha(\mathbf{r}, t)$, pressure $\Delta p_\alpha(\mathbf{r}, t)$, and the velocity $\mathbf{v}^\alpha(\mathbf{r}, t)$ about the respective equilibrium values

$$\bar{\rho}_\alpha(\mathbf{r}, t) = \bar{\rho}_\alpha = \text{const}, \quad \bar{p}_\alpha(\mathbf{r}, t) = \bar{p}_\alpha = \text{const},$$

$$\overline{\mathbf{v}^{(\alpha)}}(\mathbf{r}, t) = 0, \quad p_\alpha = b_\alpha \rho_\alpha, \quad \alpha = s, f. \tag{3.4}$$

The acoustic disturbances are assumed to be adiabatic. Among others, this assumption implies the validity of the following equation:

$$\frac{dp_{(f)}(\mathbf{r}, t)}{dt} = \frac{c_{(f)}^2 d\rho_{(f)}(\mathbf{r}, t)}{dt} \Rightarrow c_{(f)}^2 = \frac{\Delta p_{(f)}}{\Delta \rho_{(f)}}. \tag{3.5}$$

$c_{(f)}$ denotes the velocity of the propagation of the wave given by the formulae (3.3) through the fluid f. If the following inequalities are assumed to be valid:

$$\left| \frac{d(b_f q_{(f)})}{dt} \right| >> q_{(f)} \frac{db_f}{dt}; \quad q_f = b_f q_{(f)}, \quad q = \rho, p \tag{3.6}$$

then

$$\frac{dq_{(f)}}{dt} \equiv \frac{d(q_f / b_f)}{dt} \approx \frac{1}{b_f} \frac{dq_f}{dt}. \tag{3.7}$$

On substituting the relations (3.7) into Eqs. (3.5), we obtain

$$\frac{dp_f(\mathbf{r}, t)}{dt} = c_{(f)}^2 \frac{d\rho_f(\mathbf{r}, t)}{dt} \Rightarrow c_{(f)}^2 = \frac{\Delta p_{(f)}}{\Delta \rho_{(f)}} = \frac{\Delta p_f}{\Delta \rho_f} = c_f^2. \tag{3.8}$$

Thus, if the inequalities (3.6) are fulfilled, the velocities of the adiabatic propagation of the wave considered through both the component (fluid) f and f-th continuous

constituent are equal to each other. Further in this paper, we will be interested only in this case.

Now the unknown functions $\rho_\alpha, p_\alpha, \mathbf{v}^{(\alpha)}$, $\alpha = s, f$ involved in Eqs. (2.9)–(2.12) are taken to be of the form given by the formulae (3.1). After such a substitution, only terms up to those linear in the acoustic disturbances $\Delta F(\mathbf{r}, t)$ are kept in these equations. This acoustic linearization of the flow equations yields, after some manipulation,

$$\frac{\partial(\Delta\rho_\alpha)}{\partial t} + \overline{\rho}_\alpha \operatorname{div} \mathbf{v}^{(\alpha)} = 0 \tag{3.9}$$

$$\frac{\partial(\Delta\rho)}{\partial t} + \overline{\rho} \operatorname{div} \mathbf{v}^{(s)} - \overline{\rho}_f \operatorname{div} \mathbf{u} = 0 \tag{3.10}$$

$$\overline{\rho} \frac{\partial \mathbf{v}^{(s)}}{\partial t} - \overline{\rho}_f \frac{\partial \mathbf{u}}{\partial t} = \operatorname{div} \sigma^L \tag{3.11}$$

$$\overline{\rho}_s \frac{\partial(\mathbf{u}^{(f)} + \mathbf{u})}{\partial t} - \hat{Q}\mathbf{u}^f - \mathbf{F}^s = 0. \tag{3.12}$$

$\mathbf{F}^s$ is the density of the viscous drag force experienced by the continuum s when it executes oscillations. $\hat{Q}\mathbf{v}^{(f)}$ is the external force produced by the sound field.

In this paper Eqs. (3.10)–(3.12) and one equation arbitrarily chosen from Eqs. (3.9) are treated as the system of equations describing the propagation of the acoustic disturbances through the media considered. For instance, if Eq. (3.9) for $\alpha = s$ is chosen, a system of 8 equations (3.9)–(3.12) is obtained with 10 unknown functions: $\Delta\rho_s, \Delta\rho_f, p_s, p_f, v_i^{(s)}, u_i$, $i = 1, 2, 3$. To equate the number of acoustic equations with that of the acoustic disturbances (unknown functions), we add to Eqs. (3.10)–(3.12) the relations expressing the assumption that both phases are disturbed adiabatically. Then the unknown functions can be sought for in the wave form given by the formulae (3.3). On substituting such forms of the disturbances into the set of acoustic equations, the set of algebraic linear and homogeneous equations is obtained for the disturbance amplitudes. The condition of the existence of the non-trivial solution to the system of linear homogeneous equations is obtained for the disturbance amplitudes. The condition of the existence of the non-trivial solution to the system of linear homogeneous equations leads to a secular (determinant) equation which enables the dispersion laws to be found for the medium considered. These dispersion laws express the frequency dependence of the propagation velocity and attenuation coefficient of acoustic waves which propagate through the two-component medium under study.

It should perhapes be stressed that it will be possible to establish the dispersion laws in the above way for every particular type of the two-component media under consideration if the respective forms are found for the effective stress tensor σ and operators $\hat{P}$ and $\hat{Q}$. In the next section such considerations are presented for dilute suspensions and emulsions.

4. Propagation velocity and attenuation of ultrasonic waves in dilute suspensions and emulsions

Basic assumptions

In this section dilute suspensions and emulsions are considered and use is made of the above described hydrodynamic approach to derive the dispersion laws for the media under study.

An emulsion is thought of as being a mixture of two chemically non-reacting and immiscible viscous fluids. One fluid called the f – phase is volumetrically dominant and the other called the s – phase is uniformly dispersed in the form of a large number of spherical particles with a radius R. The viscosities of both fluids are assumed to be independent of the disturbance frequency ω. The limit when the ratio $\eta_{(f)}/\eta_{(s)}$ is negligibly small as compared with a quantity of order unity, i.e.,

$$\frac{\eta_{(f)}}{\eta_{(s)}} << 1 \tag{4.1}$$

corresponds to the case when the considered mixture is a suspension of rigid spheres (s – phase) in a Newtonian fluid (f – phase).

The assumption that the considered suspensions and emulsions are dilute, i.e.,

$$b_s << 1 \tag{4.2}$$

allows us to neglect the forces with which the particles act on each other and take the divergence of the effective stress tensor to be

$$\operatorname{div}\sigma^L = \operatorname{grad}[-\Delta p + \eta_f \operatorname{grad} \mathbf{v}^{(f)} + (\frac{\eta_f}{3} + \zeta_f) \operatorname{div} \mathbf{v}^{(f)}]. \tag{4.3}$$

According to the formula (2.13), the pressure disturbance Δp, in the emulsion as a whole is thought of as being given by the formula

$$\Delta p = b_f \Delta p_{(f)} + b_s \Delta p_{(s)} := \Delta p_f + \Delta p_s \tag{4.4}$$

where Δp_α and $\Delta \rho_\alpha$ are related with each other by Eqs. (3.8), i.e.,

$$c_\alpha^2 = \frac{\Delta p_\alpha}{\Delta \rho_\alpha}, \quad \alpha = s, f \tag{4.5}$$

Calculation of $\mathbf{F}^s$

When an ultrasonic wave meets a particle, freely suspended in a viscous, compressible, non-heat-conducting fluid, both the wave and the particle are affected by the frequency-dependent force of the viscous interaction between the fluid and particle. The wave induces changes in the mixture and motion of the particle which, however, is un-

able to follow closely the changes in the environment. Therefore, the basic phenomenon responsible for attenuation and dispersion is relaxation of the dispersed phase due to the difference between the velocity of the suspended particles and the suspending fluid.

To calculate $\mathbf{F}^s$, it is necessary to consider the interaction $\mathbf{F}^s$ between a single particle oscillating with the velocity $\mathbf{v}^{(s)}$ and the fluid surrounding the particle closely and occupying an influence domain of the volume of order much less than $(2\pi\frac{c_f}{\omega})^3$. The fluid occupying the influence domain oscillates as a whole with the velocity $\mathbf{v}^{(f)}$ where $\mathbf{v}^{(f)}$ is here to be thought of as the velocity of the fluid f at the centre of the particle if it were absent. Before going on to calculate the interaction, we replace the finite influence region by an infinite one and assume that the interaction in the last fictitious case differs negligibly from that in the former real case. In such a model, the infinitely extended fluid oscillates as a whole with the velocity $\mathbf{v}^{(f)}$ and exert a surface force, $\mathbf{F}^s$, on the particle which oscillates with the velocity $\mathbf{v}^{(s)}$ In order to calculate the force $\mathbf{F}^s$, it is necessary to find the velocity and pressure fields $\mathbf{v}^{ex}(\mathbf{r}, t)$ and $p_{ex}(\mathbf{r}, t)$ in the fluid f at the boundary S of the particle (sphere).

Solving the auxiliary problem of determining $\mathbf{v}^{ex}$ and p_{ex}, both the fluids f and s are treated to be viscous and incompressible. Then the unknown quantities are involved in the following set of equations:

$$\frac{\partial \mathbf{v}^{(m)}}{\partial t} + (\mathbf{v}^{(m)} \cdot \operatorname{grad})\mathbf{v}^{(m)} = \frac{1}{\rho_{(m)}} \nabla(-p_{(m)} + \eta_{(m)} \operatorname{grad} \mathbf{v}^{(m)}) \tag{4.6}$$

$$\operatorname{div} \mathbf{v}^{(m)} = 0, \; m = \text{in, ex} \tag{4.7}$$

Throughout the considerations concerning the calculation of the force $\mathbf{F}^s$, every abbreviation with sub- or superscript "in" and "ex" denotes a quantity referred to the particle or surrounding fluid, respectively. Equations (4.6) and (4.7) are to be solved with the following conditions at the boundary S of the particle (sphere):

1) the normal components of velocity both inside and outside the particle vanish;

2) the tangential components of velocity and stress are continuous.

Moreover, every suspended particle is assumed to maintain its spherical shape due to surface tension. Therefore, calculating $\mathbf{F}^{(s)}$, we take into account the motions of the particle (sphere) as a whole, all shearing and frictional effects, but neglect the expansion and deformation effects.

Although the applied method of calculation of $\mathbf{F}^{(s)}$ follows to a wide extent AHUJA'S method [4], it is more general and the utility of their results is released from some limitations. Ahuja omitted the term with the time derivative in the Navier-Stokes equation describing the viscous and incompressible flow of the fluid inside an oscillating particle. In our calculation this term is not omitted but only the nonlinear (with respect to velocity) terms in Eqs. (4.6) are omitted. Introducing the respective dimensionless variables into Eqs. (4.6), one can verify that the nonlinear terms may be neglected if

$$\mathrm{St} = \frac{a}{R} << 1,\ \mathrm{Ru}_{(m)} = \frac{\bar{p}_{(m)}}{\rho_{(m)} a^2 \omega^2} << 1,\ \mathrm{Re}_{(m)} = \frac{\mathrm{Ra}\omega\bar{\rho}_{(m)}}{\eta_{(m)}} << 1. \tag{4.8}$$

a denotes the oscillation amplitude. The abbreviations St, $\mathrm{Ru}_{(m)}$, and $\mathrm{Re}_{(m)}$, m = in, ex, denotes the Strouhall, Ruark and Reynolds number, respectively. On finding the expressions for $\mathbf{v}^{ex}$ and p_{ex} from Eqs. (4.6) and (4.7) with their boundary conditions and conditions (4.8), we substitute the right hand-sides of $\mathbf{v}^{ex}$ and p^{ex} into the following well-known formula:

$$\mathbf{F}^{(s)} = \int_S (-p_{ex}\cos\theta + \sigma_{rr}^{ex}\cos\theta - \sigma_r^{ex}\sin\theta)\, ds \tag{4.9}$$

where the integration is to be performed over the surface of the spherical particle. The integrand of Eq. (4.9) is presented in the polar spherical coordinates with the polar axis parallel to **u**. After evaluating the integral (4.9), we get the drag force as

$$\mathbf{F}^{(s)} = -[4\pi(i\kappa + \kappa^2 R)\eta_{(f)} C_0 - \frac{2}{3} i\omega\bar{\rho}_{(f)} R^3]\mathbf{u} \tag{4.10}$$

$$\kappa = (1+i)\left[\frac{\omega\bar{\rho}_{(f)}}{2\eta_{(f)}}\right]^{1/2} \tag{4.11}$$

$$C_0 = \frac{3}{2}\frac{3\eta_{(s)} + 2\eta_{(f)} + 2\eta_{(s)}\Psi}{\frac{3}{R} i\kappa(\eta_{(f)} + \eta_{(s)}) + \eta_{(s)}\kappa^2 + \frac{2}{R} i\kappa\eta_{(s)}\Psi} \tag{4.12}$$

$$\Psi = \sum_{n=1}^{\infty} n(n+1)H_n \,/\, [1 + \sum_{n=1}^{\infty} (n+1)H_n] \tag{4.13}$$

$$H_n = (-i)^n \left[\frac{R^2\omega\bar{\rho}_{(s)}}{\eta_{(s)}}\right]^n \Big/ \prod_{k=1}^{n} (2k+2)(2k+5) \tag{4.14}$$

Now the density $\mathbf{F}^s$ of the viscous drag force experienced by the continuum s when it executes oscillations may be evaluated from the formula

$$F^s = \frac{3}{4} b_s \pi^{-1} R^{-3} F^{(s)}. \tag{4.15}$$

The last expression which is required to be found before going on to derive the secular equation is the operator $\hat{Q}$ which has been introduced into Eqs. (2.12) and (3.12), Making use of [5, Eq. (7)], we get the operator $\hat{Q}$ as

$$Q = \bar{\rho}_s B \frac{\partial}{\partial t},\quad B = \frac{b_s\bar{\rho}_f}{b_f\bar{\rho}_s} = \frac{\bar{\rho}_{(f)}}{\bar{\rho}_{(s)}}. \tag{4.16}$$

Secular equation

Upon substituting the expressions (3.8), (4.3), (4.15) and (4.16) into Eqs. (3.11) and (3.12), we obtain from Eqs. (3.9)–(3.11), after some manipulation

$$\frac{\partial(\Delta\rho)}{\partial t} + \overline{\rho}\operatorname{div}\mathbf{v}^{(f)} + \overline{\rho}_s \operatorname{div}\mathbf{u} = 0 \tag{4.17}$$

$$\frac{\partial(\Delta\rho_f)}{\partial t} + \overline{\rho}_f \operatorname{div}\mathbf{v}^{(f)} = 0 \tag{4.18}$$

$$\overline{\rho}\frac{\partial \mathbf{v}^{(f)}}{\partial t} + \overline{\rho}_s \frac{\partial \mathbf{u}}{\partial t} + c_f^2 \operatorname{grad}(\Delta\rho_f) - \eta_f \Delta \mathbf{v}^{(f)} - (\zeta_f + \frac{\eta_f}{3}) \operatorname{grad}\operatorname{div}\mathbf{v}^{(f)} = 0 \tag{4.19}$$

$$[\frac{\partial}{\partial t}(1 + \frac{1}{2}B) + D]\mathbf{u} + (1 - B)\frac{\partial \mathbf{v}^{(f)}}{\partial t} = 0; \tag{4.20}$$

$$D = 3B(\overline{\rho}_f)^{-1} R^{-2} (i\kappa R^{-1} + \kappa^2)\eta_f C_0. \tag{4.21}$$

Now let us suppose that the unit vector $\mathbf{e}_k$ in the formulae (3.3) is parallel to the unit vector $\mathbf{e}_1$ along the direction of the reference axis Ox_1. Then the substitution of the formulae (3.3) into Eqs. (4.17)–(4.20) leads us to the following secular equation:

$$\begin{vmatrix} -i\omega & 0 & ik\overline{\rho} & ik\overline{\rho}_s \\ 0 & -i\omega & ik\overline{\rho}_f & 0 \\ 0 & ic_f^2 k & [-i\omega\overline{\rho} + k^2(\frac{4}{3}\eta_f + \zeta_f)] & -i\omega\overline{\rho}_s \\ 0 & 0 & -Z & 1 \end{vmatrix} \tag{4.22}$$

where the successive column of the determinant correspond to the amplitudes of the disturbances $\Delta\rho$, $\Delta\rho_f$, $\mathbf{v}^{(f)}$ and $\mathbf{u}$, respectively.

In accordance with Eq. (4.20), Z is defined as

$$Z = i\omega(1 - B)[D - i\omega(1 + \tfrac{1}{2}B)]^{-1}. \tag{4.23}$$

Equation (4.22) leads to the following equation

$$\left(\frac{1}{c^*} + i\mu^*\right)^2 = [\overline{\rho}_f + \overline{\rho}_s(Z + 1)]c_f^2[\overline{\rho}_f c_f^2 - i\omega(\frac{4}{3}\eta_f + \zeta_f)]^{-1} \tag{4.24}$$

where the dimensionless propagation velocity c^* and attenuation coefficient μ^* of the two-component medium is defined as

$$c^* = \frac{c}{c_f}, \quad \mu^* = \frac{\mu c_f}{\omega}. \tag{4.25}$$

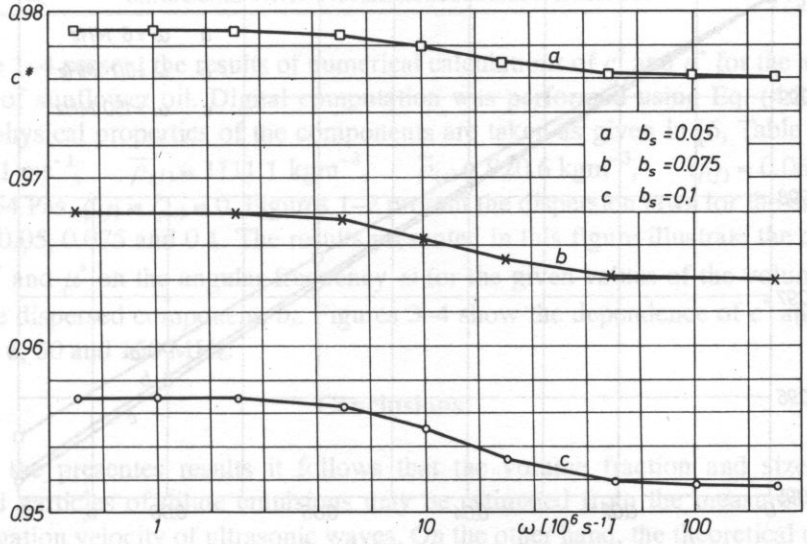

FIG. 1. The frequency dependence of the dimensionless propagation velocity c^* for $b_s = 0.05, 0.075, 0.1$ and $R = 2 \cdot 10^{-6}$m.

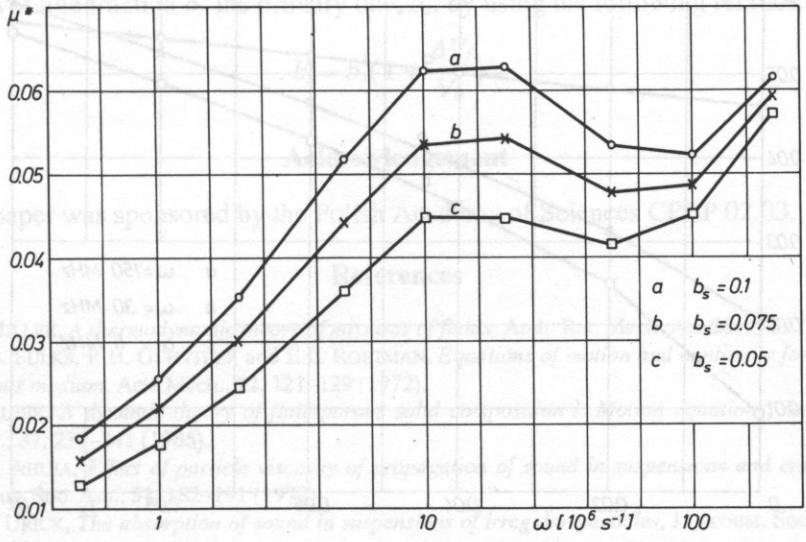

FIG. 2. The frequency dependence of the dimensionless attenuation coefficient μ^* for $b_s = 0.05, 0.75, 0.1$ and $R = 2 \cdot 10^{-6}$m.

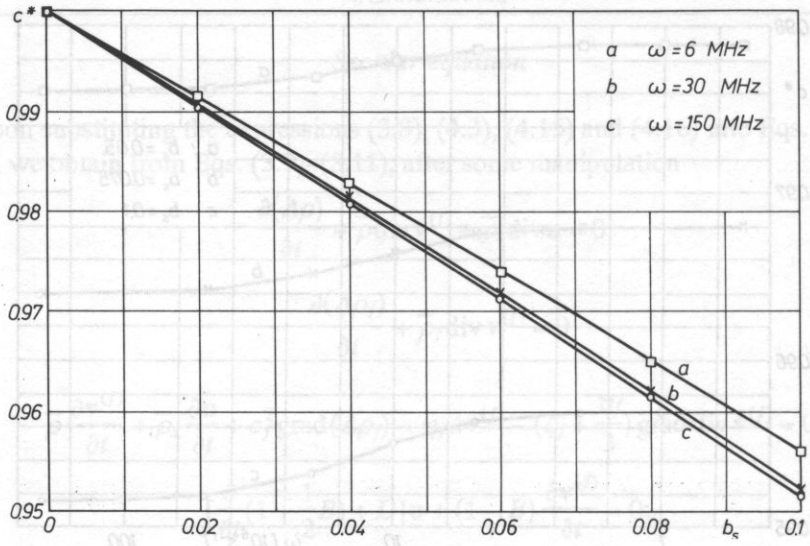

FIG. 3. The values of the dimensionless propagation velocity c^* as the function of the volume fraction b_s for $\omega = 6, 30, 150$ MHz and $R = 2 \cdot 10^{-6}$m.

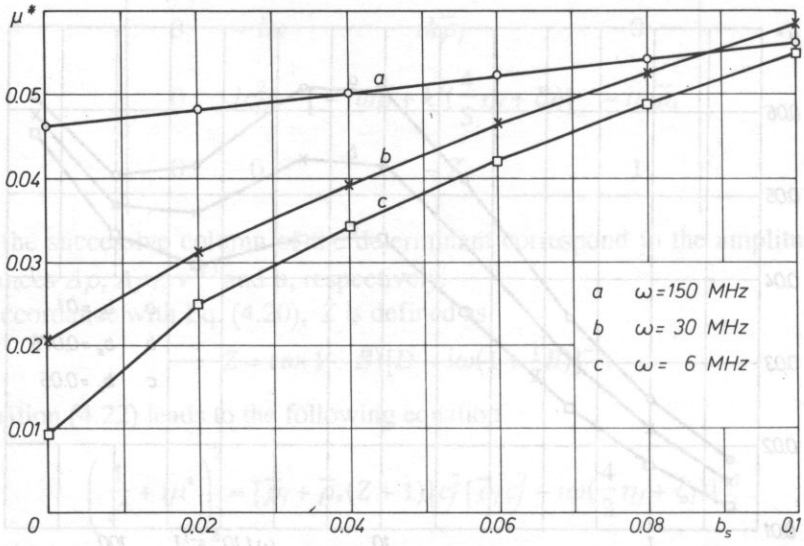

FIG. 4. The values of the dimensionless attenuation coefficient μ^* as the function of the volume fraction b_s for $\omega = 6, 30, 150$ MHz and $R = 2 \cdot 10^{-6}$m.

Figure 1–4 present the results of numerical calculations of c^* and μ^* for the aqueous emulsion of sunflower oil. Digital computation was performed using Eq. (4.24). The required physical properties of the components are taken as given in [6, Table 1], i.e., $c_f = 1604.1\ \mathrm{ms}^{-1}$, $\overline{\rho}_{(f)} = 1111.1\ \mathrm{kgm}^{-3}$, $\overline{\rho}_{(s)} = 920.6\ \mathrm{kgm}^{-3}$, $\eta_{(f)} = 0.0677$ Pas, $\eta_{(s)} = 0.054$ Pas, $\zeta_{(f)} = \zeta_{(s)} = 0$. Figures 1–2 present the dispersion laws for the emulsion with $b_s = 0.05$, 0.075 and 0.1. The results presented in this figure illustrate the dependence of c^* and μ^* on the angular frequency ω for the given values of the volume fraction of the dispersed component, b_s. Figures 3–4 show the dependence of c^* and μ^* on b_s for $\omega = 6$, 30 and 150 MHz.

Conclusions

From the presentes results it follows that the volume fraction and size of the suspended particles of dilute emulsions may be estimated from the measurements of the propagation velocity of ultrasonic waves. On the other hand, the theoretical description of ultrasonic wave propagation in dilute emulsions is rather simple as compared with that for highly concentrated emulsions. It should perhaps be stressed that this method of the estimation of b_s and R could be used not only for dilute suspensions and emulsions which have been considered above, but also for highly concentrated two-phase media. It follows from the fact that every highly concentrated two-phase medium of the primary volume V^0 may be converted into a dilute one by introducing an amount ΔV_f of the suspending fluid. If the volume ΔV_f is known, then we may evaluate from the final volume fraction b_s^1 the primary one, b_s^0, by using the following relation:

$$b_s^0 = b_s^1\left(1 + \frac{\Delta V_f}{V_0}\right).$$

Acknowledgement

The paper was sponsored by the Polish Academy of Sciences CPBP 02.03.

References

[1] L. MILLER, *A thermodynamic theory of mixtures of fluids*, Arch. Rat. Mech. An. **28**, 1–39 (1968).

[2] W.B. FULKS, R.B. GUENTHER and E.L. ROETMAN, *Equations of motion and continuity for fluid in a porous medium*, Acta Mech., **12**, 121–129 (1972).

[3] J. KUBIK, *A dynamic theory of fluid-porous solid composition I. Motion equations*, Arch. Mech. Stos., **37**, 231–341 (1985).

[4] A.S. AHUJA, *Effect of particle viscosity of propagation of sound in suspensions and emulsions*, J. Acous. Soc. Am., **51**, 182–191 (1972).

[5] R.J. URICK, *The absorption of sound in suspensions of irregular particles*, J. Acoust. Soc. Am., **20**, 283–289 (1948).

[6] D.J. MC CLEMENT, M.J.W. POWEY, M. JURRY and E. BETSANIS, *Ultrasonic characterization of a food emulsion*, Ultrasonics, **28**, 226–272 (1990).

Received on December 31, 1990

ARCHIVES OF ACOUSTICS
17, 1, 103–115 (1992)

WIDEBAND CHARACTERIZATION OF ULTRASOUND TRANSDUCERS AND MATERIALS USING TIME DELAY SPECTROMETRY

P.A. LEWIN

Department of Electrical and Computer Engineering and Biomedical Engineering and Science Institute
Drexel University, Philadelphia, PA 19104

M.A. SCHAFER

Sonic Technologies, 101 Gibraltar Road, Horsham, PA19044

This paper describes a procedure based on a swept frequency technique which provides wideband characterization of ultrasound transducers and materials. The procedure utilizes the Time Delay Spectrometry (TDS) principle and features significantly improved signal to noise ratio when compared to other conventional swept frequency systems. The experimental data illustrate the main advantages of the technique. In particular, they demonstrate the use of TDS to determine key parameters of acoustic transducers including transmitting and receiving frequency response, directivity patterns, and effective aperture. In addition, measurements of material acoustic attenuation are shown as a virtually continuous function of frequency.

1. Introduction

Several methods for evaluating ultrasonic transducer performance and measuring material acoustic parameters are currently in use [1–4]. Transducer performance evaluations are needed to provide quantitative data for any ultrasonic exposimetry related measurements. Such measurements require not only the knowledge of the absolute frequency response of the acoustic sources or receivers, but also information on their directivity patterns and associated effective apertures [5]. The desing and testing of transducers involves acoustic measurements on auxiliary materials. Those materials are used for instance as acoustic windows baffles, reflectors, and sound absorbers or anechoic coatings. In particular, development of mechanically scanned diagnostic ultrasound devices, involves the critical choice of the coupling liquid in which the transducer is immersed [6, 7]. Although it may first appear that a "lossless" liquid would be the best choice, it is often desirable to have some attenuation in order to reduce reverbera-

tion artifacts from multiple acoustic reflections within the probe assembly. Therefore, knowledge of liquid attenuation properties, especially over the entire diagnostic frequency range is of importance to transducer designers and manufacturers.

The techniques and procedures for transducer characterization are closely related to those used for evaluation of material acoustic parameters. In general, the characterization procedures are carried out either in the time of frequency domains. Since the goal of this paper is to discuss applications of a spectral analysis technique i.e. measurements carried out in the frequency domain, this is the primary technique discussed here. However, it may be appropriate to briefly point out the principle and potential problems associated with time domain measurements.

The standard procedure for characterizing an ultrasonic transducer in the time domain involves determining the transducer's impulse response. Two basic approached to the measurement of the impulse response can be distinguished. The first one is based on reflection and is known as the pulse-echo technique [2]; the second approach involves a small hydrophone probe [8], positioned at the desired point in the field of the acoustic source. Both approaches depend on the transmitter-receiver separation and off-axis location. The primary advantage of the pulse-echo technique is that it is relatively simple, however it is difficult to comprehensively characterize an ultrasonic transducer by the pulse-echo method alone. This is because the measurements combine the acoustic sources' transmitting and receiving characteristics. In addition, the results are modified due to the changes in the electrical load as a function of frequency. Time domain approaches also suffer from the fairly low signal to noise ratio inherent to a broadband measurement system, especially when the measurements are performed at relatively low acoustic pressure levels (0.1–1 kPa), such as those encountered during measurements of the off-axis field distribution. Many of these disadvantages may be overcome by using frequency domain measurements.

Quantitative measurements of transducer frequency characteristics require a free-field environment, which may be obtained by using an anechoic water tank with absorber lined side and bottom surfaces. However, if continuous wave (CW) excitation is used, the dimensions required of the water tank increase as the frequency decreases, making the anechoic water tank an impractically costly proposition. To overcome that limitation, the gated tone burst technique is widely used to facilitate the measurements in a relatively small water tank [9]. It is now possible (e.g. using a programmable function generator) to generate a tone burst of any desired frequency. However, in practice, at the biomedical ultrasonics range of frequencies, measurements are usually carried out at discrete frequencies, often separated by more than one megahertz. This is inadequate in several applications, in that it may overlook steep, critical variations in the frequency response [10]. To alleviate this problem, a unique swept frequency approach was employed that allowed free field measurements. The approach uses the Time Delay Spectrometry technique originally proposed by Heyser over two decades ago for the analysis of loudspeaker performance [11]. Subsequently, the technique gained attention for quantitative measurements of acoustic field parameters at medical ultrasonics frequencies [12–14]. In the following section the Time Delay Spectrometry princi-

ple is briefly reviewed, and the key acoustic parameters characterizing ultrasound transducers are introduced.

Section 3 presents details of the measurements approach, including measurement arrangement; the results of characterization of ultrasound transducers and acoustic materials are given in Section 4.

2. Time Delay Spectrometry and acoustic parameters

Time Delay Spectrometry (TDS) Principle

Time Delay Spectrometry (TDS) principle is illustrated in Fig. 1. The TDS concept is based on converting the given propagation time (here between the acoustic source and the receiver hydrophone probe) into a carefully controlled, prescribed frequency

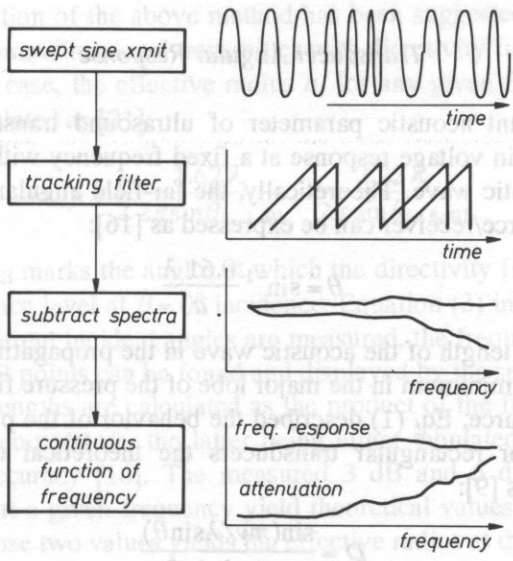

FIG. 1. Time Delay Spectrometry principle.

shift. This is accomplished by using a linearly swept sinusoidal signal to excite a wideband transducer, always maintaining a constant frequency sweep rate. By accounting for the time delay between the transmitter and the receiver, it is possible to isolate the direct acoustic path signal from any reflections from the sides and bottom of the water tank, through narrow band filtering. In this way, free-field measurements can be performed in an acoustically reflective environment. The signal measured is detected by a wideband, calibrated PVDF hydrophone probe and after appropriate processing, can be displayed in terms of frequency response, angular response, and attenuation spectrum. The most significant advantages of the technique are that the responses and measured

as a virtually continuous function of frequency, and since the receiver signal is narrow band filtered, TDS offers improved signal to noise ratio when compared with any other measurements technique.

Transducer Frequency Response

Free-field end-of-cable frequency response as a function of frequency is one of the key parameters characterizing ultrasound transducers [8 – 10, 15]. The receiving voltage response is defined as a ratio of the electrical output voltage measured at the terminals of the receiver (hydrophone) with a specified load, and the acoustic pressure at normal incidence acting on the receiver, expressed in units volts per micropascal. Free field transmitting voltage response is expressed in units dB re 1 μPa per volt at a given distance and describes the transducer properties as an acoustic source. Its magnitude denotes an acoustic pressure amplitude generated at a given axial distance by the piezoelectric source excited with one volt.

Transducer Angular Response

Another important acoustic parameter of ultrasound transmitters and receivers describes variations in voltage response at a fixed frequency with varying angle of incidence of the acoustic wave. Theoretically, the far-field angular response of a planar circular acoustic source/receiver can be expressed as [16]:

$$\theta = \sin^{-1} \frac{0.61\,\lambda}{a} \tag{1}$$

where λ is the wave length of the acoustic wave in the propagating medium, θ denotes the angle of the first minimum in the major lobe of the pressure field and a is the effective radius of the source. Eq. (1) described the behavior of the piston in a rigid planar buffle. Similarly, for rectangular transducers the theoretical expression describing directivity function is [9]:

$$D = \frac{\sin(\pi w/\lambda \sin\theta)}{\pi w/\lambda \sin\theta} \tag{2}$$

where w is the width of the piezoelectric element and angle θ is defined in Fig. 4.

There are two other physical models which predict the angular response. The soft (pressure-release) baffle model modifies the Eq. (1) by introducing a $\cos\theta$ term, (i.e. Eq. (1) and (2) are multiplied by this cosine term) [16]. It is worth noting that it has been reported that this term is needed in the case of a very narrow strip acoustic radiator (e.g. single element in an array system, with w of the order of 0.3 mm) to obtain an agreement with the experimentally determined angular responses [17]. Similarly, unrestricted piston model modifies the response given by Eq. (1) and (2) by multiplying them by a term $[(1 + \cos\theta)/2]$ [18]. In general, the effect of the cosine terms is to narrow the main lobe and force the response to be zero at 90° incidence angle.

Effective aperture size of ultrasonic transducers

It is well known that the area of transduction and the geometrical area ot the ultrasound transducer are seldom identical [15, 19]. The empirically determined area (usually termed the effective area) varies with frequency, and often differs markedly from the geometrical area of the sensor element [5, 15]. The importance of knowing the effective area of ultrasound sources and receivers is well recognized – this area is needed in order to determine (and correct, if possible) the error introduced by it in a measurement of the spatial and temporal intensity of the acoustic field radiated by an acoustic source [5, 20]. While there are several theoretical expressions (see previous subsection) on which the experimental determination of the effective area of circular transducers can be based, the most widely used one assumes that the angular response is sufficiently well approximated by Eq. (1). Once the angle corresponding to the first minimum in the major lobe of the pressure field is experimentally determined, calculation of the effective radius of the transducer at a given frequency can be carried out.

A slight modification of the above method has been suggested in [2]. It is valid in the case of a nearly omnidirectional transmitter with directivity function not exhibiting any minima. In such case, the effective radius a_e for any given frequency f_i can more conveniently be calculated as [21]:

$$a_e, f_i = \frac{1}{2}\frac{1.62\lambda_i}{2\pi\sin\theta_{[-3\text{dB}]}} + \frac{2.22\lambda_i}{2\pi\sin\theta_{[-6\text{dB}]}} \tag{3}$$

where $\theta_{-3\text{dB}}$ and $\theta_{-6\text{dB}}$ marks the angles at which the directivity function is 3 and 6 dB down from its reference level at $\theta = 0°$ incidence. Equation (3) indicates that if spectra corresponding to different incident angles are measured, the frequencies corresponding to – 3 dB and – 6 dB points can be found and displayed by the spectrum analyser. The corresponding wavelengths are calculated as the product of the frequencies and sound velocity at a given temperature, the latter being either tabulated or calculated to the desired degree of accuracy [16]. The measured 3 dB and 6 dB half angles of the transducer response at a given frequency yield theoretical values of the transducer radius. The mean of those two values yields the effective radius at this frequency.

3. Materials and methods

This section describes the measurement system used to determine the acoustic parameters of ultrasound transducers and to measure the attenuation of various materials.

Measurement Arrangement

The measurement arrangement is shown in Fig. 2. An HP 3585A spectrum analyser is used to drive (via ENI 240LF power amplifier) a purpose built wideband PVDF

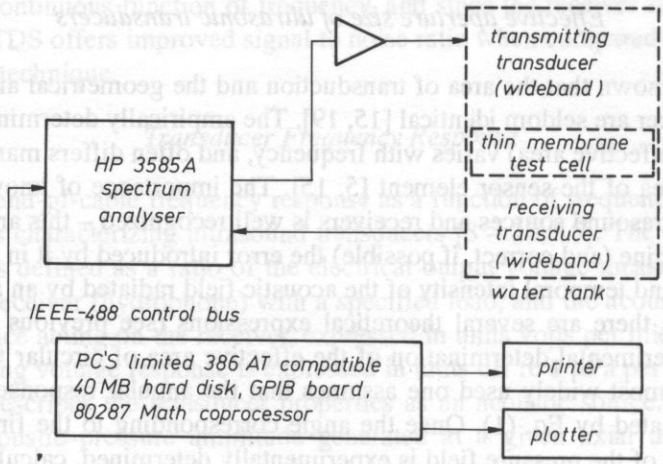

FIG. 2. Experimental setup.

transmitter [15]. This 10 mm diameter transmitter was designed to provide a wideband, uniform transmitting response. The acoustic signal is received by wideband PVDF hydrophone of needle-type design with a 0.6 mm diameter (Danish Institute of Biomedical Engineering, Copenhagen, Denmark) or by a 9 micron membrane type design with a 0.4 mm diameter (Sonic Technologies, Horsham, PA). Both probes exhibit smooth (to within ± 1.5 dB) frequency characteristics and predictible angular responses, and had been reciprocity calibrated. A review of the design and properties of hydrophones especially suited for ultrasound field measurements has been published [21]. The spectrum analyser is controlled by a 386–AT compatible computer over an IEEE-488 bus. A comprehensive description of the selection of appropriate TDS parameters such as sweep rate, resolution bandwidth, and sweep time is given in [14]. Further details of the scanning tank are given in section Attenuation Measurements.

Wideband Characterization of Ultrasound Transducers

Frequency response–hydrophone calibration technique. The primary wideband calibration of the hydrophone probes was carried out using a combined TDS and reciprocity technique [23, 24].

After detection by the reciprocity calibrated hydrophone probe, the signal was stored in one of the two built-in memories of the spectrum analyser and then displayed on its screen. Next, the calibrated hydrophone was replaced by the unknown hydrophone. Again, the signal detected by this hydrophone was stored in the spectrum analyser's second memory and both signals were transferred to the IBM PC computer which subtracted the two spectra, compared the result with the absolute frequency response of the reciprocity calibrated hydrophone probe and plotted a hard copy of the resulting free field, receiving frequency response of the unknown hydrophone.

Angular response. The angular responses or directivity patterns were determined in the following way. Relative spectra of the hydrophone probe (or acoustic source) as a function of acoustic pressure wave incidence angle were recorded, displayed on the screen of the spectrum analyser, and subsequently transferred to the IBM PC for a hard copy print out. The print outs were available as incidence angle versus frequency or as a more conventional representation in terms of polar diagrams [8].

Effective aperture size. The incidence angle versus frequency plot obtained during the assessement of the angular response was used to determine the effective aperture size of the differently shaped acoustic sources and hydrophone probes. The effective apertures were calculated based on the Eqs. (1) – (3) (Section 2).

To minimize possible errors, all measurements reported here were performed beyond the position of the last axial maximum on the acoustic axis of the wideband 10 mm diameter PVDF acoustic source [15]. The temperature of distilled, degassed water in the tank was temperature controlled ± 0.5 °C, partly to minimize the changes in the sound speed in the water and thus between the measurements taken over a period of time, and partly to minimize the variation in PVDF transducers with temperature. The uncertainty in the axial distance measurements as well as the uncertainty in the alignment of the hydrophones in the plane perpendicular to the acoustic axis of the transmitter, assuming constant propagation velocity in water, was estimated to be better than 0.15 mm. The deflection angle θ was controlled to within 0.2°C.

Attenuation Measurements using TDS

In order to measure the excess material attenuation as a function of frequency, the TDS technique described above (Section 2) was used in the following way: first, the wideband transmitter, hydrophone, and HP3585A spectrum analyzer were set up in water as they would be for frequency response calibration (see section above). The spectral data from the water measurement were transferred from the spectrum analyzer to the controlling computer. Then, the test cell with material to be tested (described in detail below) was placed in the direct acoustic path. The resultant spectrum was then subtracted from the stored, "water-only" spectrum to yield the relative attenuation of the tested material as a function of frequency. Figure 2 shows the measurement arrangement used; in practice the transmitter/hydrophone distance was about 19 cm. The measurements reported here were primarily carried out on liquids, however, the acoustic attenuation of a 6 mm thick plate made of Sorbothane TM was also tested.

It is important to realize that the attenuation results include the effects of both attenuation in the material, and reflection losses at the water/sample interface due to impedance mismatches. (The effect of membrane reflection in the test cell was minimal; this was confirmed using a test cell filled with water only). The reflection loss was accounted for using a separate measurement of the liquid's specific acoustic impedance, using the density and the sound speed determined from a modified differential distance technique [25]. Computer routines calculated and subtracted the reflection loss estimate

from the measured data, leaving only the attenuation component. Based on operator input as to the thickness of the test cell, the computer normalized the results to values of dB/cm.

Test Cell Design and Construction. The critical component in the attenuation measurement system is the test cell, which is designed to maintain the liquids as thin, uniform layers in the acoustic path. The eight centimeter square fluid area was large enough to be considered essentially of infinite extent when placed near the transmitting transducer. The key to the design of the test cell was the use of shrink-wrap plastic, which provided a thin yet strong membrane. The plastic film was held in place using 3 mm thick metal frames, and was sealed to the stiff Plexiglas shell structure using rubber cement. Then the membranes were carefully stretched taut using a heat gun. Caution was required, because overheating caused the membranes to rip open, requiring reassembly. The stretched membranes were about 18–20 μm thick, based on micrometer measurements of disassembled test cells. This 18 μm thickness could be considered negligible in comparison with the shortest wavelength of interest, approximately 100 μm at 15 MHz.

Once the membranes were sealed and stretched, the test cells were carefully filled with liquid through a fill hole using a hypodermic needle and syringe. In order to equalitze the hydrostatic pressure of the liquid against the membranes as the cell was filled, the cells were slowly dipped into the water tank during filling. This kept the membranes from bowing out; the fill hole was then sealed with a small set screw.

Several test cells were constructed with different thicknesses. In practice, there was a limit on the thickness of the test cells. Because the liquids used in the experiments had densities different from water, there was a tendency for the liquids to distort the test cells into a wedge shape when subjected to the hydrostatic pressure of the surrounding water. For example, if the liquid was denser than water, the test cells would sag. The thicker the test cell, the greated the hydrostatic effect and the greater wedge shaped distortion. Therefore, the thickest test cell used was 3 mm.

Scanning Tank Desing. The scanning tank had to meet certain specific requirements as to the geometry of the source, test cell, and receiver, and the alignment of the receiver with the plane of the acoustic source and test cells. The hydrophone probe was rigidly held in a machined slot using a set screw, thus ensuring that the probe was positioned perpendicular to the plane of the holder. In use, the holder was covered with a sound absorbing rubber to minimized reflections. The acoustic source (transmitter) holder was designed to permit the easy mounting of transmitters of different diameters and shapes. The acoustic axis of the transmitter could be aligned with the hydrophone, using a two-axis precision gymbal mount. (The alignment procedure is detailed below). With this gymbal mount, the angular position of the source was continuously adjustable over a ± 10° range with a resolution of 2 arc seconds. The transmitter assembly was moved perpendicularly to the receiver plane (along the Z – axis) using manually adjusted precision lead screw sliders. The test cell was mounted similarly to the transmitter, with a two-axis precision gymbal mount (± 6° angular range with 1 arc second resolution) on a manual Z – axis slider. The test cell and transmitter mounts were arranged

such that they could be positioned independently along the Z – axis without interfering with one another.

Alignment procedures. Since one possible influence on the measured attenuation was the alignment of the test cell with respect to the acoustic path, specific alignment procedures were developed to insure that the transmitter, the test cells, and the receiver were indeed aligned. First, the hydrophone assembly was positioned such that the flat Plexiglas portion of the holder was in front of the transmitter. The transmitter was connected to a Panametrics PR5052 pulser, set for pulse-echo mode. The transducer assembly was angled until the return echo from the hydrophone holder was maximized. To align the cell, the same pulse-echo techniques were used, only this time, the test cell was angled until the reflections from the membrane surfaces were maximized. These reflections were typically 25 dB lower than the Plexiglas echoes. The alignment accuracy was estimated to be better than 0.2° for the transmitter/receiver alignment, and 0.4° for the test cell alignment.

4. Results

Wideband ultrasound transducer characterization. The frequency response of the given hydrophone transmitter combination was compared to that obtained from TDS reciprocity calibration. Fig. 3 shows a typical plot of 9 micron, 0.4 mm diameter, membrane hydrophone sensitivity versus frequency from 1–15 MHz. This result is typical of the 9 micron thick films [15]. The hydrophones are expected to have uniform frequency response up to 40 MHz and 110 MHz for the 25 μm and 9 μm films, respectively [15]. The cable length of the membrane hydrophones was 75 cm, and the terminating load was 1 MΩ in parallel with 30 pF (input impedance of the HP 3585A analyser). The peak pressure amplitudes used for the TDS calibration procedure ranged from 10 kPa to approx. 100 kPa, and indicate the excellent signal to noise ratio obtainable with the TDS technique.

Figures 4 and 5 show an example of directivity patterns for two different acoustic radiators, the first being a 4 MHz, 14 mm nominal diameter focused bowl transducer,

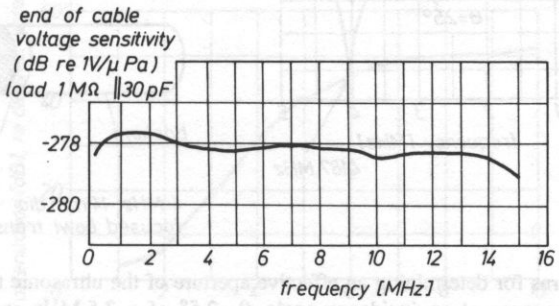

FIG. 3. Absolute, free-field, end of cable voltage frequency response of the 0.4 mm diameter, 9 μmm thick PDVF membrane hydrophone in water. For further details, see text.

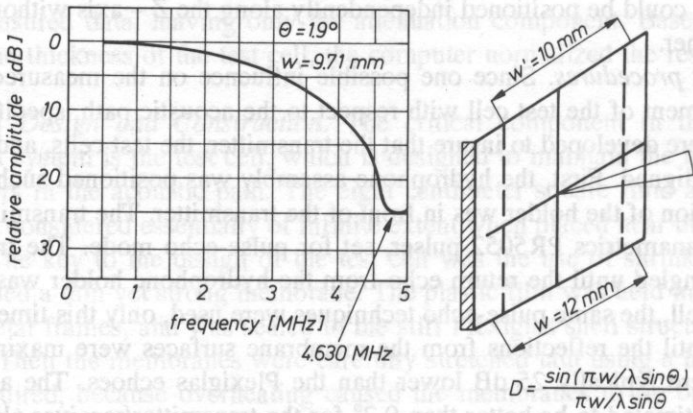

FIG. 4. Directivity patterns for determining an effective aperture of the ultrasonic transducer in water. As an example, angular response of a 4 MHz, 14 mm nominal diameter, focused bowl transducer at an incidence angle $\theta = 1.9°C$ is shown. Frequency corresponding to minimum is read-out from the spectrum analyser. See text for further details.

and the second being a rectangular 12 × 10 mm (nominal) radiator (electroded surfaces had dimensions 10 × 10 mm). From the directivity patterns, the effective diameter of the circular focused transducer was determined using Eq. (1) or (3). In the case of the focused transducer the effective radius was found to be 4.98 mm, indicating a significant difference from the nominal radius of 7 mm stated by the manufacturer. In practice, Eq. (3) is often more versatile and convenient to use than Eq. (1), particularly when the measured directivity pattern does not exhibit a sharp minimum and first lobe minimum angle is difficult to determine with adequate accuracy. The effective width of the

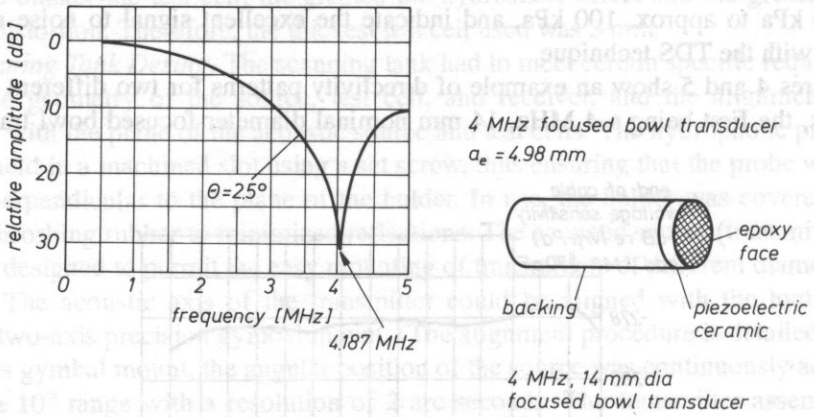

FIG. 5. Directivity patterns for determining an effective aperture of the ultrasonic transducers in water. As an example, angular response at an incidence angle $\theta = 2.5°$ of a 3.5 MHz rectangular (12 × 10 mm) transmitter is shown. Frequency corresponding to minimum is read-out from the spectrum analyser. See text for further details.

rectangular piezoelectric transmitter (9.71 mm) was calculated using Eq. (2) with the input data obtained from the measurements (Fig. 4 and 5). As mentioned previously, the effective aperture of ultrasonic transceivers is, in general, frequency dependent and when needed should be determined at the relevant frequency.

Attenuation measurements. Several different liquids were tested, based on previous experience with diagnostic medical equipment. The actual measurements took only a few seconds to complete; the majority of the time was spent on filling the test cells. Figure 6 shows results of tests on selected liquids, over the frequency range 1 to 15 Hz. Graphs show attenuation loss in dB/cm for 1.3 Butylene Glycol, and Polyethylene Glycol 400. Other tested liquids included glycols, silicone oils, and "natural" oils such as mineral oil and castor oil. Figure 7 shows relative overall attenuation loss in 6 mm thick Sorbothane™ material over the frequency range 1 – 10 MHz.

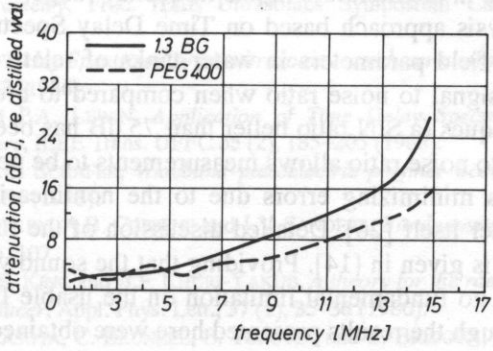

FIG. 6. Attenuation loss in dB/cm for 1.3 Butylene Glycol and Polyethylene Glycol 400.

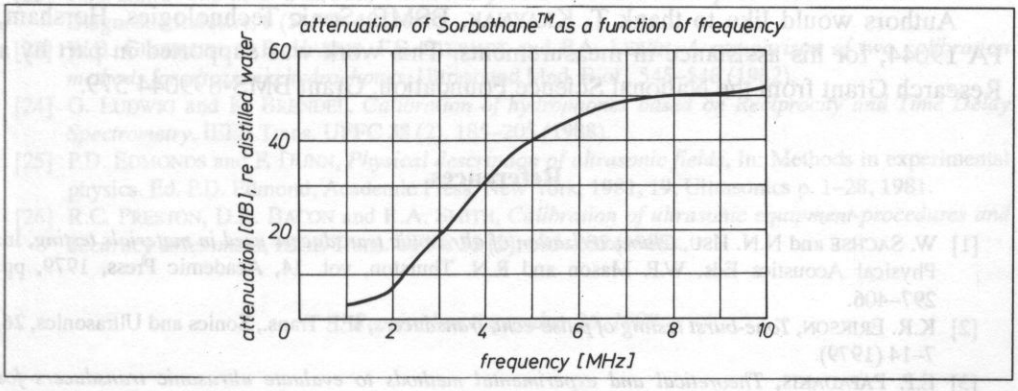

FIG. 7. Attenuation loss in dB/cm for 6 mm thick plate of the Sorbothane™ material.

Discussion and conclusions

Several applications of a spectral analysis technique based on the Time Delay Spectrometry principle have been illustrated in materials measurements and ultrasound transducer characterization. It has been shown that this technique provides a useful tool in determining essential acoustic parameters of ultrasound transmitters and receivers, and acoustic attenuation of different materials over wide range of frequencies. The results of attenuation measurements in liquids are in general agreement with those previously published [6] and show increasing attenuation with frequency, as is expected for viscous losses. The more viscous fluids generally showed higher levels of attenuation. Moreover, these parameters are available as a virtually continuous function of frequency. The results of attenuation measurements of 6 mm thick plate of absorbing material Sorbothane™ indicate 40 – 60 dB attenuation in comparison with water. No other data are available in the literature in this frequency range.

The spectral analysis approach based on Time Delay Spectrometry facilitates the determination of free-field parameters in water tanks of relatively small dimensions, and offers improved signal to noise ratio when compared to broadband time and frequency domain techniques (a S/N ratio better than 75 dB has been reported [12]). This relatively high signal to noise ratio allows measurements to be performed at low acoustic output levels, thus minimizing errors due to the nonlinearity of the propagation medium and transmitter itself [26]. Detailed discussion of the fundamental limitations of the TDS technique is given in [14]. Providing that the sound velocity is independent of frequency, there is no fundamental limitation on the usable frequency range of the TDS technique. Although the results presented here were obtained at the megahertz frequencies, the technique can be used at much lower frequencies. However, in practice, the low frequency limit of the measurements is restricted by the free space available (water tank dimensions).

Acknowledgements

Authors would like to thank T. KRAYNAK, BSME, Sonic Technologies, Horsham, PA 19044, for his assistance in measurements. This work was supported in part by a Research Grant from the National Science Foundation, Grant BMS-899044 579.

References

[1] W. SACHSE and N.N. HSU, *Characterization of ultrasonic transducers used in materials testing*, In: Physical Acoustics Eds. W.P. Mason and R.N. Thurston, vol. 14, Academic Press, 1979, pp. 297–406.

[2] K.R. ERIKSON, *Tone-burst testing of pulse-echo transducers*, IEE Trans., Sonics and Ultrasonics, **26**, 7–14 (1979).

[3] E.P. PAPADAKIS, *Theoretical and experimental methods to evaluate ultrasonic transducers for inspection and diagnostic applications*, IEEE Trans., Sonic and Ultrasonics, **26**, 155–26 (1979).

[4] N.G. PACE, *Impulse response of water loaded air-backed piezoelectric discs*, IEEE Trans. Sonics and Ultrasonics, **26**, 37–41 (1979).

[5] R.C. CHIVERS, L. BOSSELAR and P.A. FILMORE, *Effective area to be used in diffraction corrections*, J. Acoust. Soc. Am., 68, 80–84 (1980).

[6] A.R. SELFRIDGE, *Approximate material properties in isotropic materials*, IEEE Trans., EFFC **33** (3), 381–394 (1985).

[7] M.E. SCHAFER and P.A. LEWIN, *The influence of front-end hardware on digital ultrasonic imaging*, IEEE Trans., S-U 31 2, 295–306 (1984).

[8] P.A. LEWIN, *Miniature piezoelectric polymer ultrasonic hydrophone probes*, Ultrasonics, **16**, 213–216 (1981).

[9] R.J. BOBBER, *Underwater electroacoustic measurements*, Naval Research Laboratory, GPO, Washington, D.C. 1970.

[10] P.A. LEWIN, *Miniature ultrasonic probes for biomedical applications*, in Proc. of 1983 IEEE Ultrasonics Symposium, Atlanta October 1983, pp. 822–826.

[11] R.C. HEYSER, *Time Delay Spectrometry: an anthology of the works on measurement, analysis and perception*, AudioEngineering Society, 60 East 42 nd St.N.Y.10165, 1988.

[12] P.A. LEWIN, *Calibration and performances evaluation of miniature ultrasonic hydrophones using Time Delay Spectrometry*, Proc. IEEE Ultrasonics Symposium Chicago, Illinois, 1981, pp. 660–664.

[13] R.C. CHIVERS, *Time Delay Spectrometry for ultrasonic transducer characterization*, J. Phys. E: Sci. Instrum. **19**, 834–843 (1986).

[14] P.C. PEDERSEN and P.A. LEWIN, *Application of Time Delay Spectrometry for calibration of ultrasonic transducers*, IEEE Trans. UFFC **35** (2), 185–205 (1988).

[15] P.A. LEWIN and M.E. SCHAFER, *Wideband piezoelectric polymer acoustic sources*, IEEE Trans. UFFC, **35** (2) 175–184 (1988).

[16] L.E. KINSLER, A.R. FREY, A.B. COPPENS and J.V. SANDERS, *Fundamentals of acoustics*, 3rd edition John Wiley, 1982 pp. 107.

[17] A.R. SELFRIDGE, G.S. KINO and B.F. KHURI-YAKUB, *A theory for the radiation pattern for a narrow strip acoustic transducer*, Appl. Phys. Lett., **37** (1), 35–36 (1980).

[18] B. DELLANOY, H. LASOTA, C. BRUNEEL, E. TORQUET and E. BRIDOUX, Journal of Appl. Phys., **50**, 5189 (1979).

[19] P.A. LEWIN and R.C. CHIVERS, *Voltage sensitivity of miniature ultrasonic probes*, Ultrasonics, **21**, 282–283 (1983).

[20] G.R. HARRIS, *Hydrophone measurements in diagnostic ultrasound fields*, IEEE Trans. UFFC **35** (2), 87–101 (1988).

[21] Safety Standard for Diagnostic Sound Equipment, AIUM NEMA Standard Publication, No UL1–1981 (1981).

[22] P..A. LEWIN and M.E. SCHAFER, *Ultrasonic probes in measurement practice*, Medical Devices and Diagnostic Industry, **8** (5), 40–45 (1986).

[23] W.B. GLOERSEN, G.R. HARRIS, F.S. STEWART and P.A. LEWIN, *A comparison of two calibration methods for ultrasonic hydrophones*, Ultrasound Med. Biol., 545–548 (1982).

[24] G. LUDWIG and K. BRENDEL, *Calibration of hydrophones based on Reciprocity and Time Delay Spectrometry*, IEEE Trans. UFFC **35** (2), 185–205 (1988).

[25] P.D. EDMONDS and F. DUNN, *Physical description of ultrasonic fields*, In: Methods in experimental physics. Ed. P.D. Edmond, Academic Press, New York, 1981, 19, Ultrasonics p. 1–28, 1981.

[26] R.C. PRESTON, D.R. BACON and R.A. SMITH, *Calibration of ultrasonic equipment-procedures and accuracy assessment*, IEEE Trans. UFFC **35** (2), 185–205 (1988).

Received on September 26, 1990

ARCHIVES OF ACOUSTICS
17, 1, 117–131 (1992)

DESIGN PRINCIPLES OF TRANSDUCERS WITH MATCHING LAYERS BASED ON ADMITTANCE MEASUREMENTS

G. ŁYPACEWICZ and E. DURIASZ

Ultrasonic Department, Institute of Fundamental Technological Research,
Polish Academy of Sciences
(00-049 Warszawa, Świętokrzyska 21)

Basing on modified Mason's equivalent circuit of an acoustic probe the authors carried out the computation of admittances and pulses reflected from the ideal reflector immersed in water.

The relation between the admittance of a PZT transducer with acoustic layers (matching the acoustic impedance of the transducer to the acoustic impedance of the human body) and the thickness of the layer is given.

It is shown the optimal layer thickness should be determined as a quarter wave-length $\lambda_e/4$ (calculated for the electric resonance frequency). In such a case the admittance curve is symmetrical and reaches the minimum, and the reflected pulse is shortest. Small thickness changes of the layer causes more distinct changes of the admittance than of the reflected pulses.

The influence of the acoustic impedance of layers and electromechanical coupling coefficient k_t on the admittance curves is discussed.

The admittances of the transducer measured for different thicknesses of the acoustic matching layer are shown. The results are in good agreement with computations.

1. Introduction

The sensitivity of the ultrasonic diagnostic equipment depends on the ultrasonic probe construction. In order to increase the sensitivity of the probe, layers matching the acoustic impedance of the transducer to the human body are applied. As yet, the method of preparing the layers was very time consuming. To determine the optimal thickness of the layer the pulse reflected from a reflector immersed in water was observed. After each polishing of the layer surface the probe was connected to the measurement device, its position was corrected to obtain the maximum pulse amplitude. The polishing was finished when the reflected pulse ceased to increase.

Now we have devised a new method of determination of the optimal thickness of the layer. During polishing of the layer admittance of the probe immersed in water is

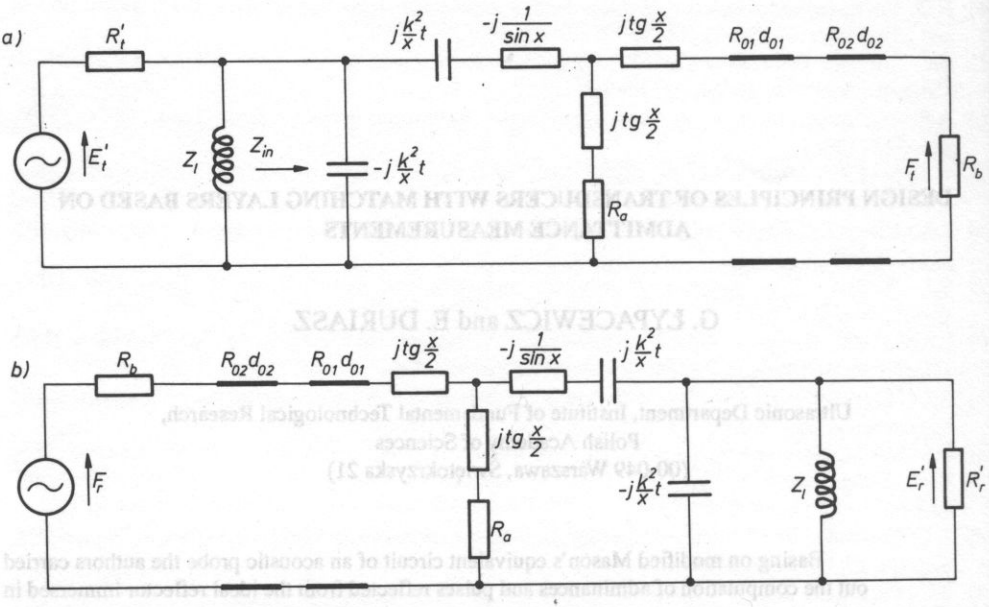

FIG. 1. Equivalent circuit of ultrasonic transducer with acoustic matching layers and parallel compensating inductance, a – transmitting, b – receiving.

measured automatically. Calculation are carried out, modified Mason's model described in [6] being assumed (Fig. 1).

All quantities describing the probe and the input transmitting-receiving system have been transferred to the mechanical side of the electromechanical transformer, and the corresponding relative values of parameters have been introduced:

– frequency $x = \pi f/f_m$;

– acoustic impedance of the transducer $R_p/R_p = 1$; where $R_p = A\,\rho_p c_p$;

– acoustic impedance of back load $R_a = A\,\rho_a c_a/R_p$,

– acoustic impedance of investigated medium $R_b = A\,\rho_b c_b/R_p$;

– acoustic impedance of matching layers

$$R_{01} = A\,\rho_{01} c_{01}/R_p,\quad R_{02} = A\,\rho_{02} c_{02}/R_p;$$

– thickness of matching layers – d_{01}, d_{02}, where $d_{01} = \lambda_m/n$, $d_{02} = \lambda_m/p$;

– impedance of parallel inductance $Z_l = k_t^2 x/\pi\, m^2$;

– voltage of transmitter $E'_t = E_t N$;

– voltage of pulse reflected from an ideal reflector $E'_r = E_r N$;

– resistance of transmitter $R'_t = R_t N^2/R_p$;

– resistance of receiver $R'_r = R_r N^2/R_p$; where f_m – frequency of transducer of the mechanical resonance, A – surface of transducer, $\rho_p c_p$, $\rho_a c_b$, $\rho_{01} c_{01}$, $\rho_{02} c_{02}$ – acoustic impedance of the transducer, back load, the investigated medium and the matching layers respectively; λ_m, λ_e – wavelength for the mechanical f_m and electric f_e transducer

resonance frequency; n, p are parameters of layer thickness (for instance for $n = 4$ thickness of layer $d_{01} = \lambda_m/4$, for $n = 4$ f_e/f_m the thickness $d_{01} = \lambda_e/4$), m is the parameter describing parallel inductance (for $m = 1$ inductance compensates the clamped capacity C_0 for frequency f_m, while for the electric resonance $m = f_e/f_m$); R_t, R_r – input resistances of the transmitter and receiver, $N^2 = 2\,k_t^2 f_m C_0 R_p$ – turns ratio of the electromechanical transformer, C_0 – clamped capacitance of the transducer, k_t – electromechanical coupling coefficient for the thickness vibration, E_t – voltage of the incident wave, E_r – voltage of the reflected wave.

In our work we assumed that transducer exhibits no mechanical and dielectric losses, the voltage exciting the transducer is the Dirac pulse – $E_t = \delta(t)$, $R_a = 0$, the ceramics is of PZT type ($\rho_p c_p = 34 \cdot 10^6$ kgm^2/s, $k_t = 0.4 - 0.7$ the investigated medium is water ($\rho_b c_b = 1.5 \cdot 10^6$ kgm^2/s), $R_t = 0.01\, Z_{in}(f_e)$, $R_r = 10\, Z_{in} f_e$ where Z_{in} – electrical impedance of the transducer.

2. Relation between layer thickness and admittance

The admittance of the transducer is distinctly dependent on the thickness of the matching layer. In Fig. 2 the admittance calculated for the PZT transducer ($\rho_p c_p = 34 \cdot 10^6$ kgm^2/s, $k_t = 0.5$) with matching layer of a different thickness is shown. The acoustic impedance of the layer was determined according to DE SILETS's formulae [7, 8].

As we can see, the value of admittance reaches its minimum when the thickness of the layer is equal to $(2k + 1)\lambda_e/4$ (Fig. 2a, g) (where $k = 0, 1, 2, ...k$), whereas for the layer thickness equal to $2k\lambda_e/4$ the admittance is close to that of the transducer without any layers, loaded by water (Fig. 2c, l).

It should be noticed that minimal admittance is obtained when the layer thickness is calculated not for mechanical, but the for electric resonance frequency $d_{01} = \lambda_e/4$ (Fig. 2g, h) [6].

It is obvious that the amplitude and shape of the reflected pulse depends on the matching layer. In Fig. 3 the reflected pulses calculated for the same layer thickness as in Fig. 2 are shown. As it could be expected, the optimal pulse is obtained for $d_{01} = \lambda_e/4$ (Fig. 3g).

Small changes (5%) of layer thickness do not noticeably influence the reflected pulse (Fig. 4), whereas we can see a distinct differences of admittance for the same changes of layer thickness (Fig. 5a, b, c). The acoustic impedance of matching layer was determined by the authors on the basis of various assumption. In this paper the impedance calculated according to CHEBYSHEFF [2], SUOQUET [9] and DE SILETS [7, 8] are taken into account.

For optimal thickness equal to $\lambda_e/4$, in all cases the corresponding curves approach symmetric form (Fig. 5b, e, h). It means that measurement of the admittance is a more sensitive method of the layer thickness than measurement of the reflected pulse.

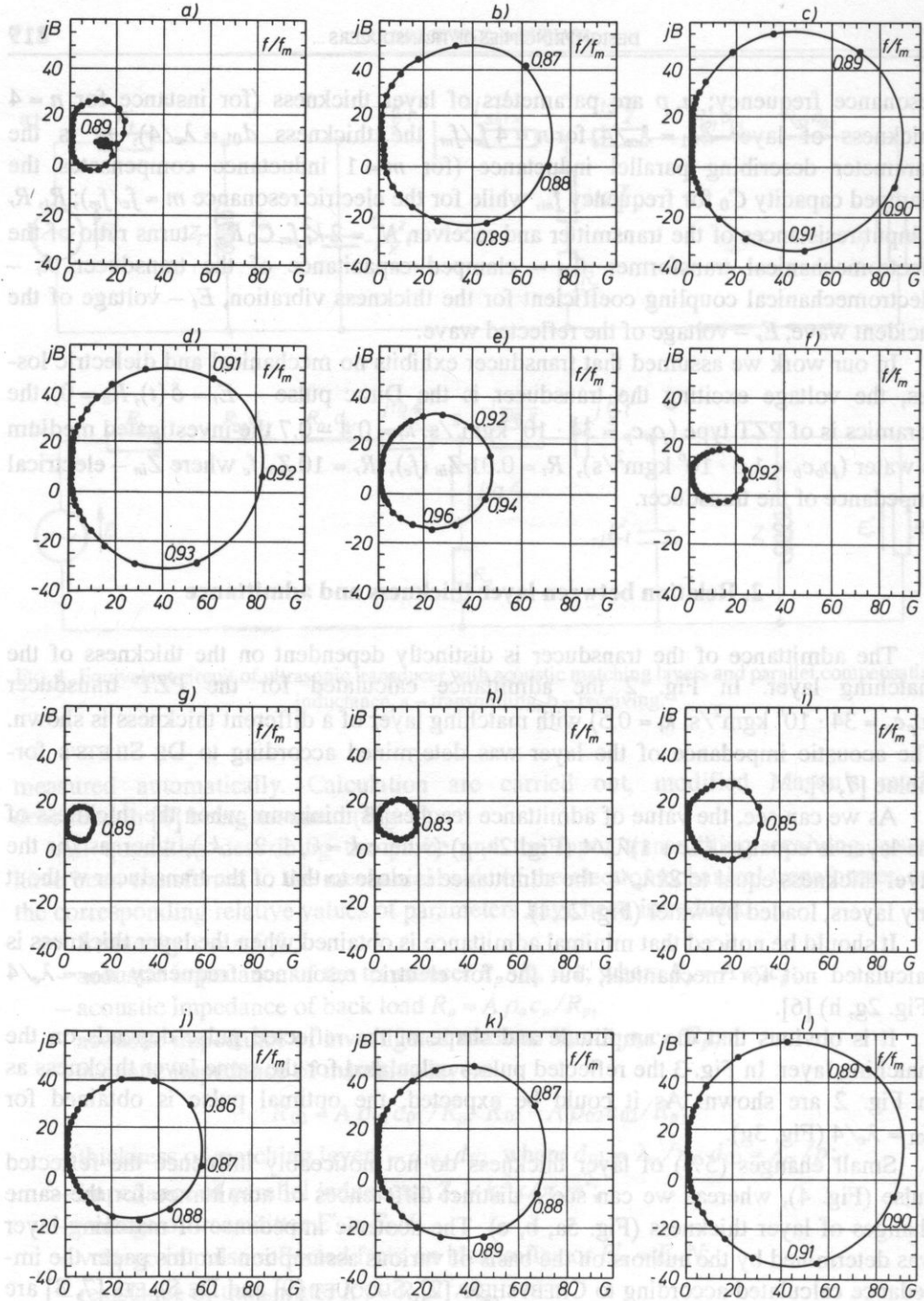

FIG. 2. Relative admittance calculated for PZT transducer ($k_t = 0.5$, $R_b = 0.044$) with acoustic matching layer calculated according to De Silet's formulae ($R_{01} = 0.122$) for different layer thicknesses.

a – $n = 1.2$ ($d_{01} = 3/4\ \lambda_e$) b – $n = 1.5$ c – $n = 1.78$ ($d_{01} = \lambda_e/2$)
d – $n = 2$ ($d_{01} = \lambda_m/2$) e – $n = 2.5$ f – $n = 3$
g – $n = 3.55$ ($d_{01} = \lambda_e/4$) h – $n = 4$ ($d_{01} = \lambda_m/4$) i – $n = 5$
j – $n = 7.5$ k – $n = 10$ l – without layer.

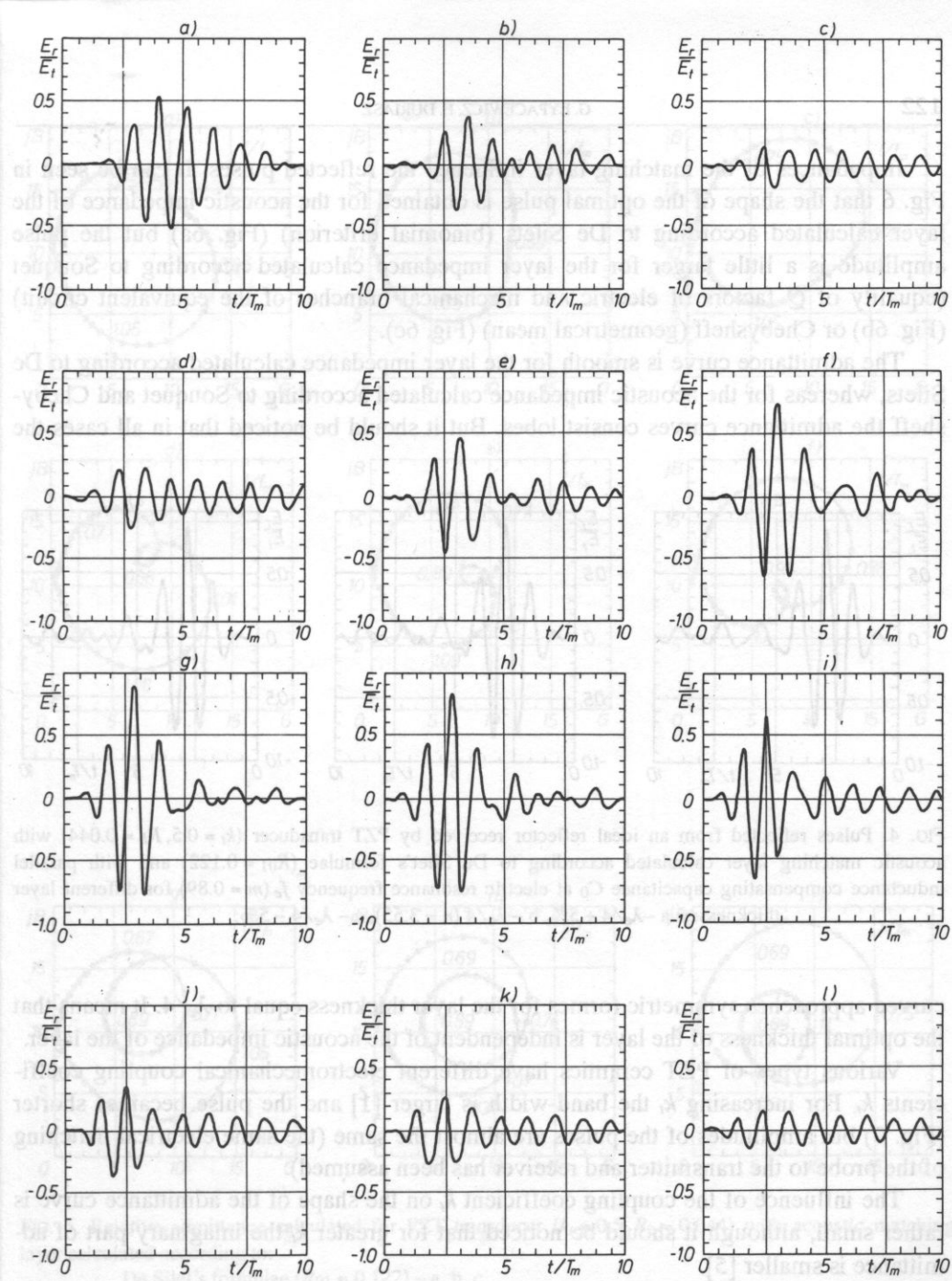

FIG. 3. Pulses reflected from an ideal reflector received by PZT transducer ($k_t = 0.5$, $R_b = 0.044$) with acoustic matching layer calculated according to De Silet's formulae ($R_{01} = 0.122$) and with parallel inductance compensating capacitance C_0 at electric resonanse frequency f_e ($m = 0.89$) for different layer thicknesses.

a – $n = 1.2$ ($d_{01} = \frac{3}{4}\lambda_e$) b – $n = 1.5$ c – $n = 1.78$ ($d_{01} = \lambda_e/2$)
d – $n = 2$ ($d_{01} = \lambda_m/2$) e – $n = 2.5$ f – $n = 3$
g – $n = 3.55$ ($d_{01} = \lambda_e/4$) h – $n = 4$ ($d_{01} = \lambda_m/4$) i – $n = 5$
j – $n = 7.5$ k – $n = 10$ l – without laye.r

Impedances of the matching layer influence the reflected pulses. It can be seen in Fig. 6 that the shape of the optimal pulse is obtained for the acoustic impedance of the layer calculated according to De Silets (binomial criterion) (Fig. 6a) but the pulse amplitude is a little larger for the layer impedance calculated according to Souquet (equality of Q factors of electric and mechanical branches of the equivalent circuit) (Fig. 6b) or Chebysheff (geometrical mean) (Fig. 6c).

The admittance curve is smooth for the layer impedance calculated according to De Silets, whereas for the acoustic impedance calculated according to Souquet and Chebysheff the admittance curves consist lobes. But it should be noticed that in all cases the

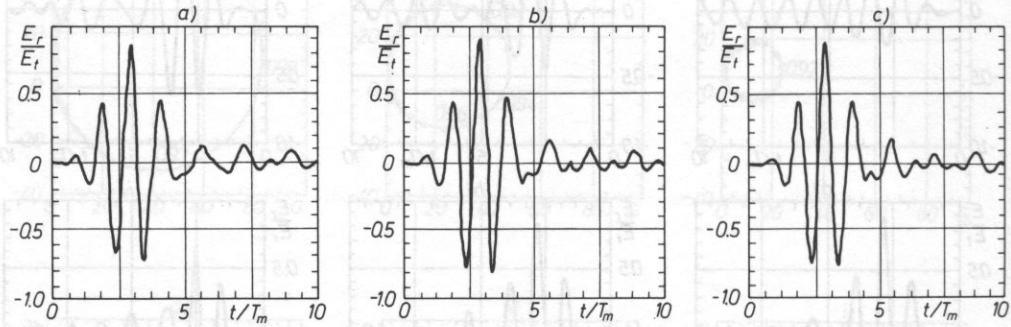

FIG. 4. Pulses reflected from an ideal reflector received by PZT transducer ($k_t = 0.5, R_b = 0.044$) with acoustic matching layer calculated according to De Silet's formulae ($R_{01} = 0.122$) and with parallel inductance compensating capacitance C_0 at electric resonance frequency f_e ($m = 0.89$) for different layer thicknesses: a $-\lambda_e/4 + 5\%$, b $-\lambda_e/4$ ($n = 3.55$), c $-\lambda_e/4 - 5\%$.

curved approaches symmetric formes for the layer thickness equal to $\lambda_e/4$. It means that the optimal thickness of the layer is independent of the acoustic impedance of the layer.

Various types of PZT ceramics have different electromechanical coupling coefficients k_t. For increasing k_t the band-width is larger [1] and the pulse becames shorter (Fig. 7) but amplitudes of the pulses are almost the same (the same electrical matching of the probe to the transmitter and receiver has been assumed).

The influence of the coupling coefficient k_t on the shape of the admittance curve is rather small, although it should be noticed that for greater k_t the imaginary part of admittance is smaller [5].

3. The second matching layer

Application of two matching layers increases the reflected the pulse (cf. Fig. 9a and c) and widens and flattens characteristics of the modulus and phase of the transducer impedances (cf. Fig. 9b and d).

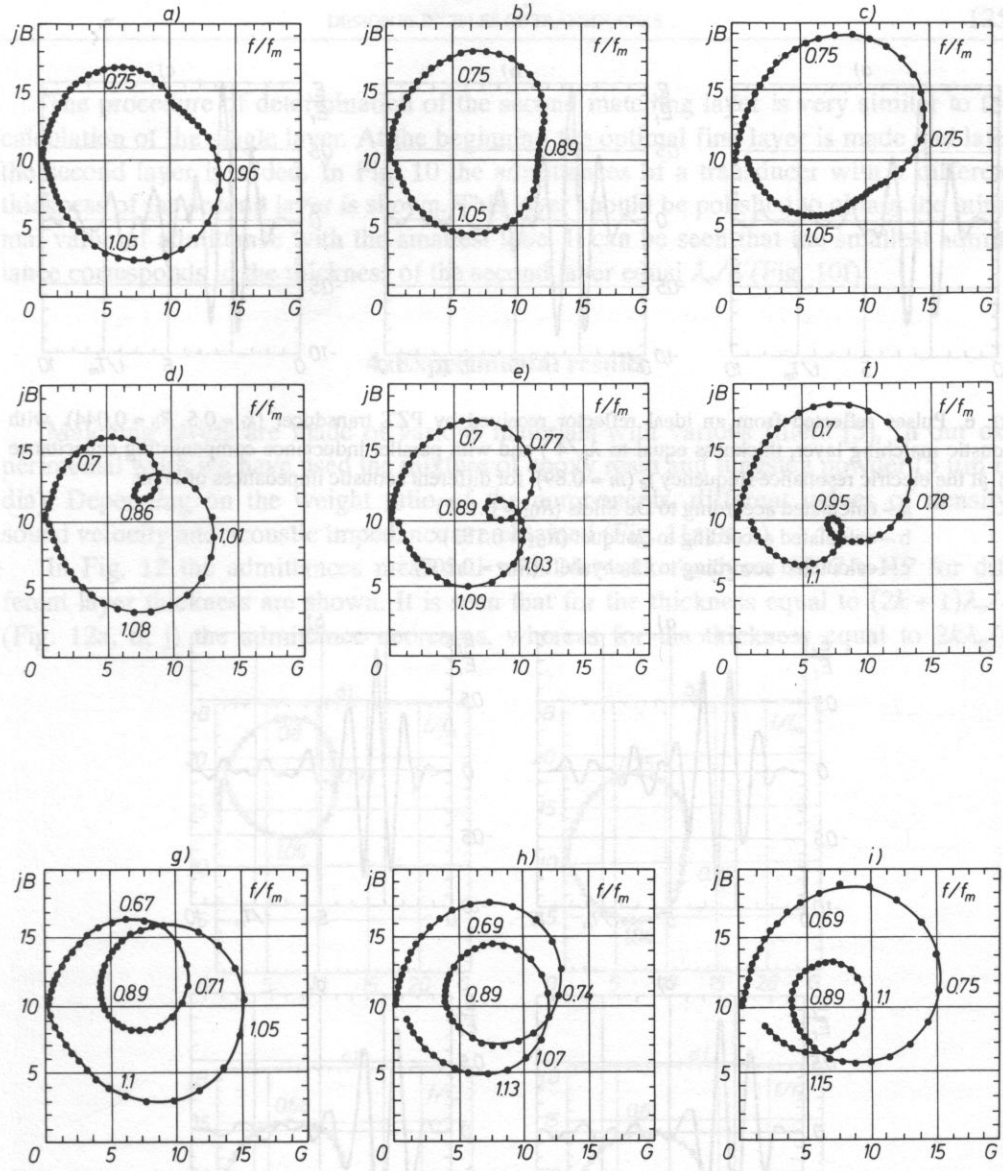

FIG. 5. Relative admittance calculated for PZT transducer ($k_t = 0.5, R_b = 0.044$) with acoustic matching layer calculated according to:

De Silet's formulae ($R_{01} = 0.122$) – a, b, c
Souquet's formulae ($R_{01} = 0.153$) – d, e, f
Chebysheff's formulae ($R_{01} = 0.207$) – g, h, i
for different layer thicknesses:

a, d, g – $\lambda_e/4 + 5\%$
b, e, h – $\lambda_e/4$ ($n = 3{,}55$)
c, f, i – $\lambda_e/4 - 5\%$.

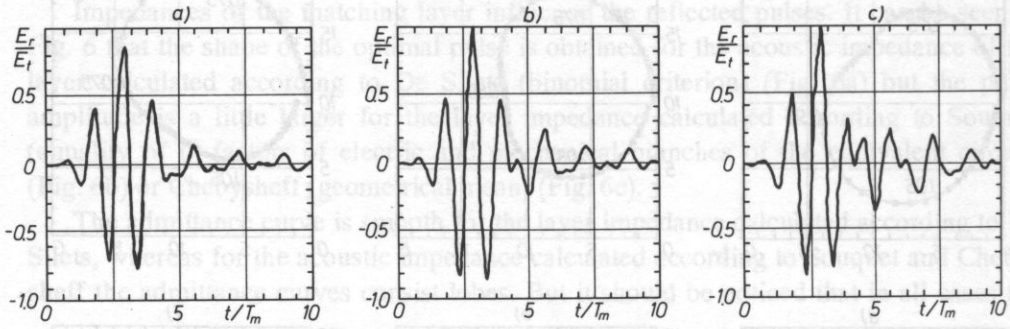

FIG. 6. Pulses reflected from an ideal reflector received by PZT transducer ($k_t = 0.5, R_b = 0.044$) with acoustic matching layer, thickness equal to $\lambda_e/4$) and with parallel inductance compensating capacitance C_0 at the electric resonance frequency f_e ($m = 0.89$) for different acoustic impedances of layer

a – calculated according to De Silets ($R_{01} = 0.122$)

b – calculated according to Souquet ($R_{01} = 0.153$)

c – calculated according to Chebysheff ($R_{01} = 0.207$).

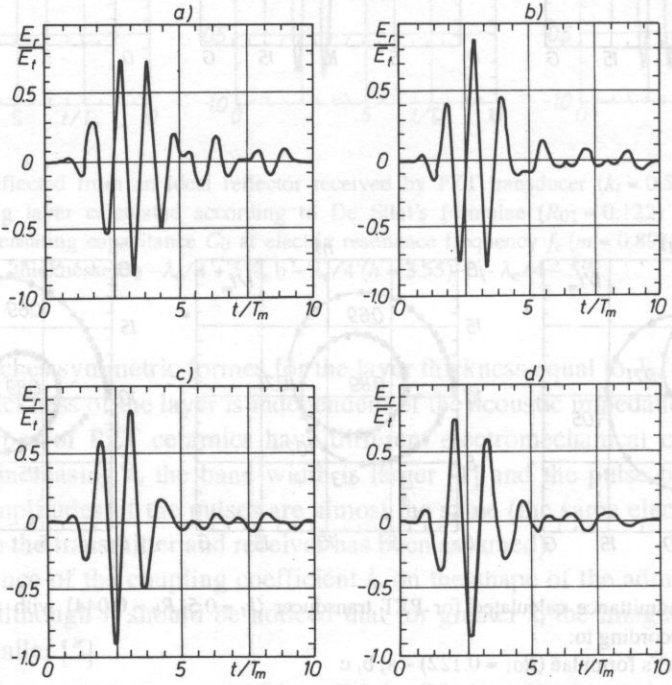

FIG. 7. Pulses reflected from an ideal reflector received by PZT transducer ($R_b = 0.044$) with different coupling coefficient k_t, with acoustic matching layer (impedance calculated according De Silets's formulae – $R_{01} = 0.122$, thickness equal to $\lambda_e/4$) and with parallel inductance compensating capacitance C_0 at electric resonance frequency f_e

a – $k_t = 0.4$ $n = 3.7$ $m = 0.93$ b– $k_t = 0.5$ $n = 3.55$ $m = 0.89$

c – $k_t = 0.6$ $n = 3.3$ $m = 0.82$ d – $k_t = 0.7$ $n = 3.0$ $m = 0.75$

The procedure of determination of the second matching layer is very similar to the calculation of the single layer. At the beginning the optimal first layer is made and later the second layer is added. In Fig. 10 the admittances of a transducer with a different thickness of the second layer is shown. This layer should be polished to obtain the minimal value of admittance with the smallest lobe. It can be seen that the smallest admittance corresponds to the thickness of the second layer equal $\lambda_e/4$ (Fig. 10f).

4. Experimental results

Matching layers are made of various materials with various fillers [5]. In our experimental work we have used the mixture of epoxy resin and tungsten powder (5 μm in dia). Depending on the weight ratio of the components, different values of density, sound velocity and acoustic impedance are obtained (Fig. 11a, b, c).

In Fig. 12 the admittances measured with Network Analyser 3577A–HP for different layer thickness are shown. It is seen that for the thickness equal to $(2k+1)\lambda_e/4$ (Fig. 12a, d, j) the admittance decreases, whereas for the thickness equal to $2k\lambda_e/4$

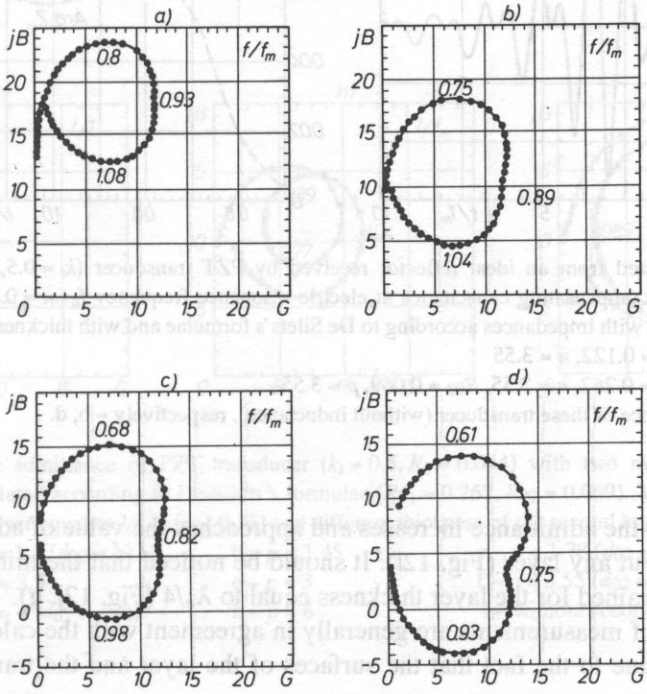

FIG. 8. Relative admittance calculated for PZT transducer ($R_b = 0.044$) with different coupling coefficient k_t, with acoustic matching layer (impedance calculated according to De Silets's formulae – $R_{01} = 0.122$, thickness equal to $\lambda_e/4$)

a – $k_t = 0.4, n = 3.7$ b – $k_t = 0.5, n = 3.55$

c – $k_t = 0.6, n = 3.3$ d – $k_t = 0.7, n = 3$.

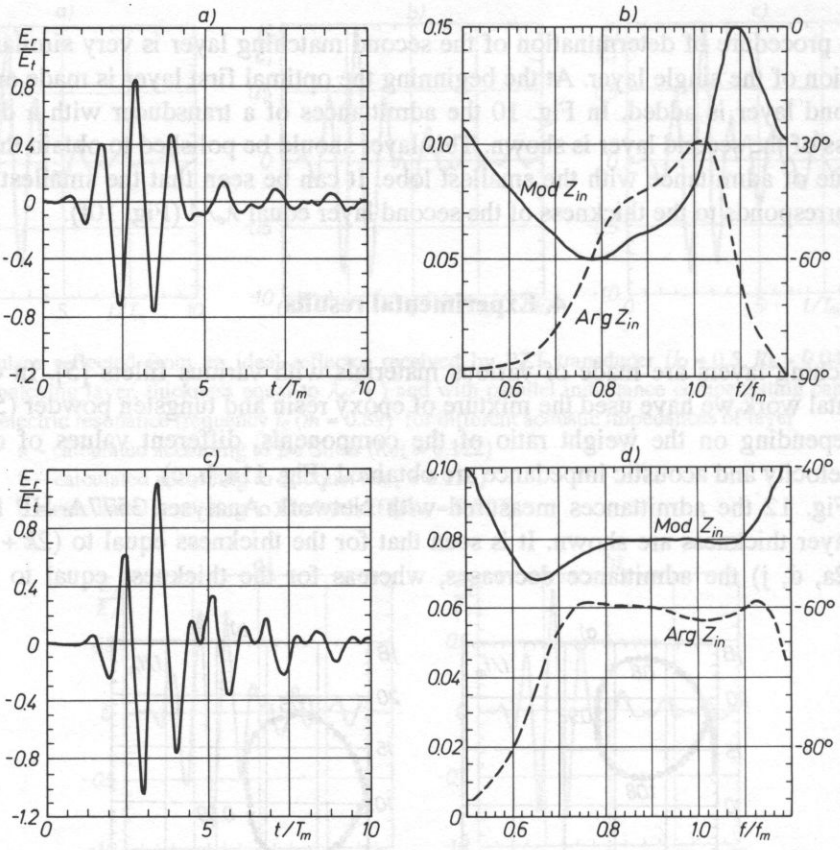

FIG. 9. Pulse reflected from an ideal reflector received by PZT transducer ($k_t = 0.5, R_b = 0.044$) with parallel inductance compensating capacitance at electric resonance frequency f_e ($m = 0.89$) with one and two matching layers with impedances according to De Silets's formulae and with thicknesses equal to $\lambda_e/4$

a – $R_{01} = 0.122$, $n = 3.55$

b – $R_{01} = 0.262$, $n = 3.55$, $R_{02} = 0.069$, $p = 3.55$

and relative impedance of these transducer (without inductance), respectively – b, d.

(Fig. 12b, g) the admittance increases and approaches the value of admittance of the transducer without any layer (Fig. 12l). It should be noticed that the minimum value of admittance is obtained for the layer thickness equal to $\lambda_e/4$ (Fig. 12j, g).

The results of measurements are generally in agreement with the calculations, some differences are due to the fact that the surfaces of the layer and the transducer are not ideally parallel.

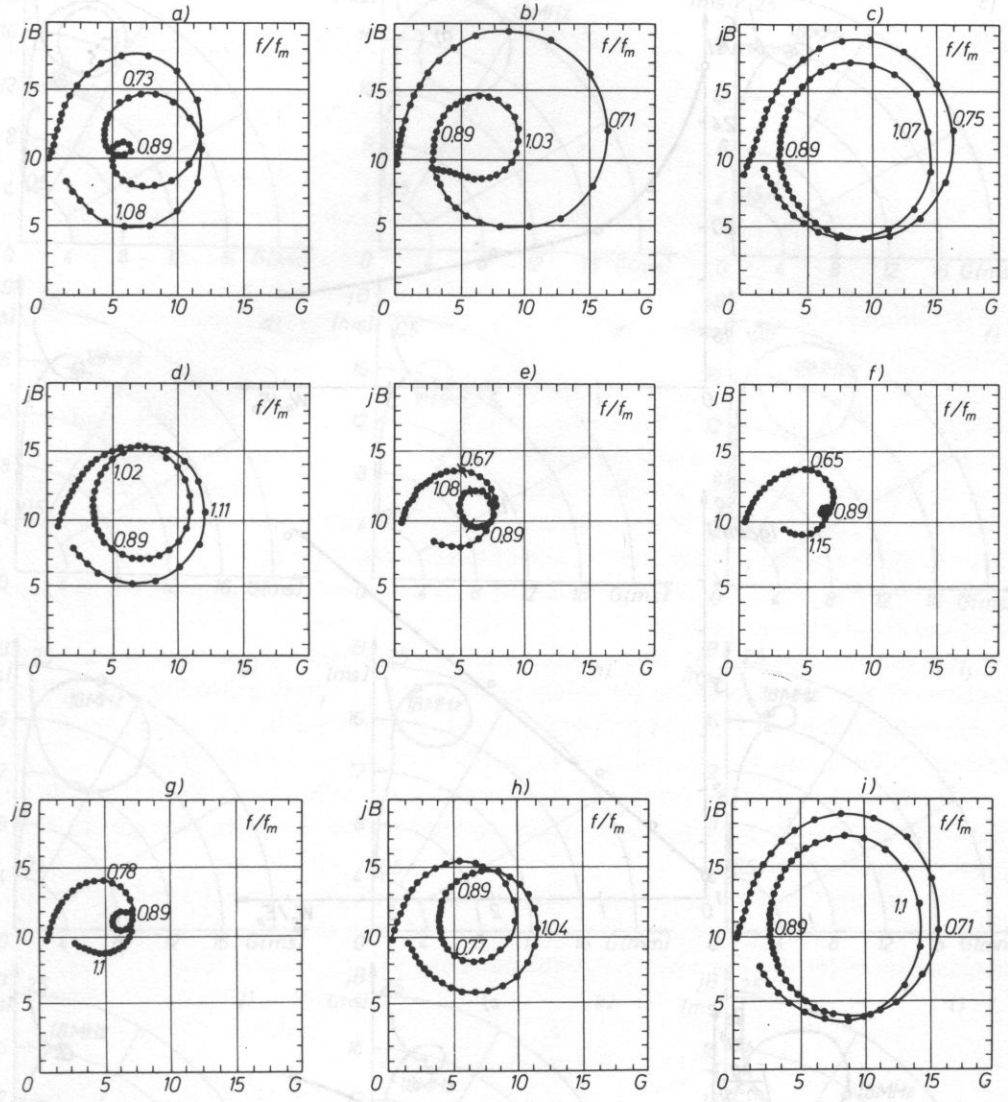

FIG. 10. Relative admittance of PZT transducer ($k_t = 0.5, R_b = 0.044$) with two matching layers with impedances calculated according to De Silets's formulae ($R_{01} = 0.262, R_{02} = 0.069$). Thickness of the first layer equal to ¼ λ_e ($n = 0.35$) and different thickness of the second layer.

a – $p = 1.2$ ($d_{02} = \frac{3}{4}\lambda_e$) b – $p = 1{,}45$ c – $p = 1.78$ ($d_{02} = \lambda_e/2$)
d – $p = 2.5$ e – $p = 3$ f – $p = 3.55$ ($d_{02} = \lambda_e/4$)
g – $p = 4$ ($d_{02} = \lambda_e/4$) h – $p = 6$ i – without second layer

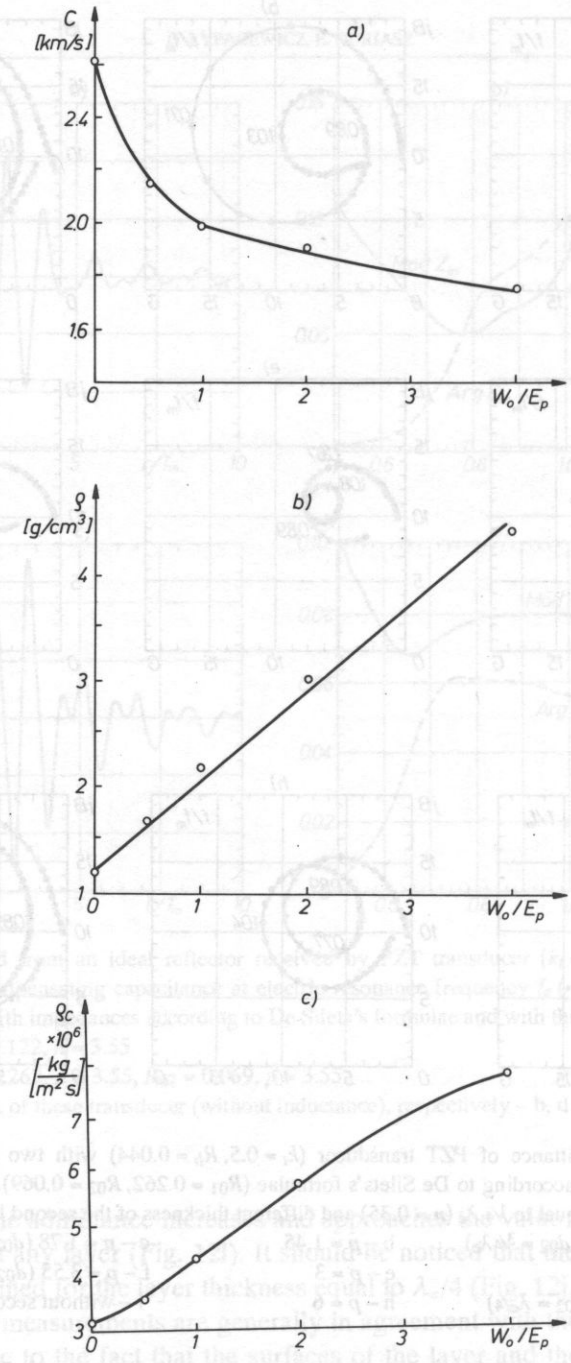

FIG. 11. Velocity of ultrasound wave (a) density (b) and acoustic impedances (c) as a function of weight ratio of tungsten-epoxy mixture (the samples were tested in vacuum).

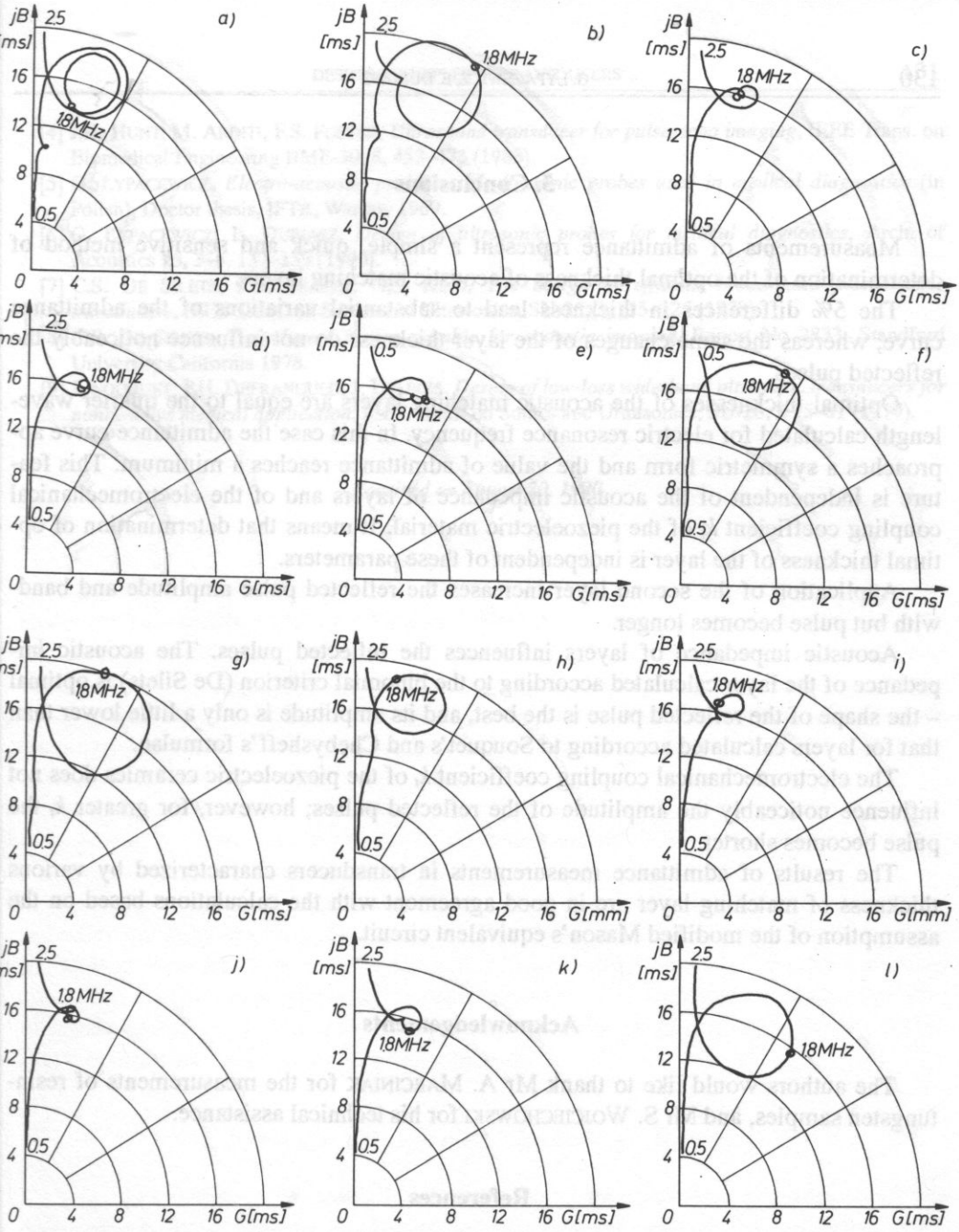

FIG. 12. Admittances of PZT transducer (CERAD PP-9) of 20 mm dia, with a matching layer made of tungsten-epoxy mixture (Wo: epoxy = 2.5), immersed in water measured for different thicnkesses of the layer

a – $d_{01} = 5/4\lambda_e$ b – $d_{01} = \lambda_e$ c – $d_{01} = 3/4\lambda_e + 5\%$

d – $d_{01} = 3/4\lambda_e$ e – $d_{01} = 3/4\lambda_e - 5\%$ f – $3/4\ \lambda_e > d_{01} > 1/2\ \lambda_e$

g – $d_{01} = 1/2\ \lambda_e$ h – $1/2\ \lambda_e > d_{01} > 1/4\ \lambda_e$ i – $d_{01} = 1/4\ \lambda_e + 5\%$

5. Conclusions

Measurements of admittance represent a simple, quick and sensitive method of determination of the optimal thickness of acoustic matching layers.

The 5% differences in thickness lead to substantial variations of the admittance curve, whereas the same changes of the layer thickness do not influence noticeably the reflected pulses.

Optimal thicknesses of the acoustic matching layers are equal to the quarter wavelength calculated for electric resonance frequency. In this case the admittance curve approaches a symmetric form and the value of admittance reaches a minimum. This feature is independent of the acoustic impedance of layers and of the electromechanical coupling coefficient k_t of the piezoelectric material. It means that determination of optimal thickness of the layer is independent of these parameters.

Application of the second layer increases the reflected pulse amplitude and bandwith but pulse becomes longer.

Acoustic impedance of layers influences the reflected pulses. The acoustic impedance of the layer calculated according to the binomial criterion (De Silets) is optimal – the shape of the reflected pulse is the best, and its amplitude is only a little lower than that for layers calculated according to Souquet's and Chebysheff's formulae.

The electromechanical coupling coefficient k_t of the piezoelectric ceramics does not influence noticeably the amplitude of the reflected pulses; however, for greater k_t the pulse becomes shorter.

The results of admittance measurements in transducers characterized by various thickness of matching layer are in good agreement with the calculations based on the assumption of the modified Mason's equivalent circuit.

Acknowledgements

The authors would like to thank Mr A. MARCINIAK for the measurements of resin-tungsten samples, and Mr S. WOJCIECHOWSKI for his technical assistance.

References

[1] L.F. FILIPCZYŃSKI, G. ŁYPACEWICZ, *Dependences between the Q-value of piezoelectric transducers loaded acoustically and the electromechanical coupling coefficient k* , Proc. Vibr. Probl., **10**, 2, 213–229 (1969).

[2] J.H. GOLL, *The design of broad-band fluid-loaded ultrasonic trancducers*, IEEE Trans. on Sonics and Ultrasonics, SU-26, 6, 385–395 (1979).

[3] M.G. GREWE, T.R. GURURAJA, T.R. SHROUT, R.E. NEWNHAM, *Acoustic properties of particle/polymer composites for ultrasonic transducer backing applications*, IEEE Trans. on Ultrasonics Ferroelectrics and Frequency Control, **37**, 6, 506–514 (1990)

[4] J.H. HUNT, M. ARDITI, F.S. FOSTER, *Ultrasound transducer for pulse-echo imaging*, IEEE Trans. on Biomedical Engineering BME-30, 8, 453–473 (1983).

[5] G. ŁYPACEWICZ, *Electro-acoustic problems of ultrasonic probes used in medical diagnostics* (in Polish), Doctor thesis, IFTR, Warsaw 1969.

[6] G. ŁYPACEWICZ, E. DURIASZ, *Design of ultrasonic probes for medical diagnostics*, Arch. of Acoustics **15**, 3–4, 137–159 (1990).

[7] C.S. DE SILETS, J.D. FRASER, G,S, KINO, *The design of efficient broad-band piezoelectric transducers*, IEEE Trans. on Sonics and Ultrasonics, SU-25, 3, 115–125 (1978).

[8] C.S. DE SILETS, *Transducers arrays suitable for acoustic imaging*, Report No 2833, Standford University California 1978.

[9] J. SOUQUET, P.H. DEFRANOULD, J. DESBOIS, *Desing of low-loss wide-band ultrasonic transducers for noninvasive medical application*, IEEE Trans. on Sonics and Ultrasonics, SU-26, 2 75–81 (1979).

Received on August 20, 1990

ARCHIVES OF ACOUSTICS
17, 1, 133–150 (1992)

PRINCIPLES OF PHASED-ARRAY IMAGING

J. SOMER

Limburg University, Maastricht, Netherlands

1. Introduction

A phased-array is a transducer which consists of a number of small transducer-elements each of which is individually accessible for excitation and reception (Fig. 1). In contrast to a linear array all elements always simultaneously contribute to the transmission of pulse or the reception of echoes.

Within certain limits, beams can be produced in any wanted direction, according to the Huygens' principle, by applying appropriate time-delays to the electrical signals to or from the elements.

Like for ordinary transducers the overall dimensions l_e (element-length) and l_a array-length in relation to the wave-length determine the beam-properties in terms of both near-field, far-field and beam-width.

Once the width of the elements w being chosen, the number of elements is determined by the array-length l_a. The necessary spaces between the elements should be kept as small as is technically realizable in order to have the maximum effective radiating area. This conflicts however with the requirement of sufficient acoustical isolation between the elements, so that here the first compromise has to be accepted. We will show that this is not the only one we have to cope with.

2. Principles of beam-steering and beam focussing

In order to realize either deviation or focussing of a sound-beam the elements of the array have to be excited by electrical signals which are delayed in a prescribed way with respect to each other, as illustrated in Fig. 2.

In Figure 2a the situation is represented for achieving beam-deviation only. The path-length differences, required to create a flat wave-front propagating in the direction Θ, are linearly dependent on the element-positions and so are the time-delays.

If now instead of a linearly varying time-delay a circular dependence is chosen we can achieve the forming of a circular wave-front rather than a flat one, as illustrated in

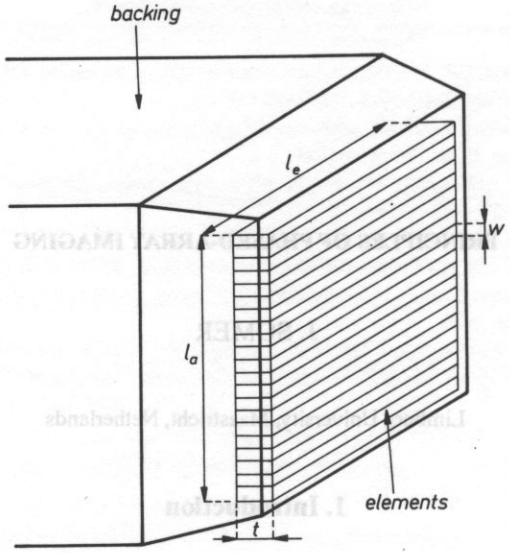

FIG. 1. Construction of a phased-array transducer. l_a = array-length, l_e = element-length, w-element-width, t = thickness (height).

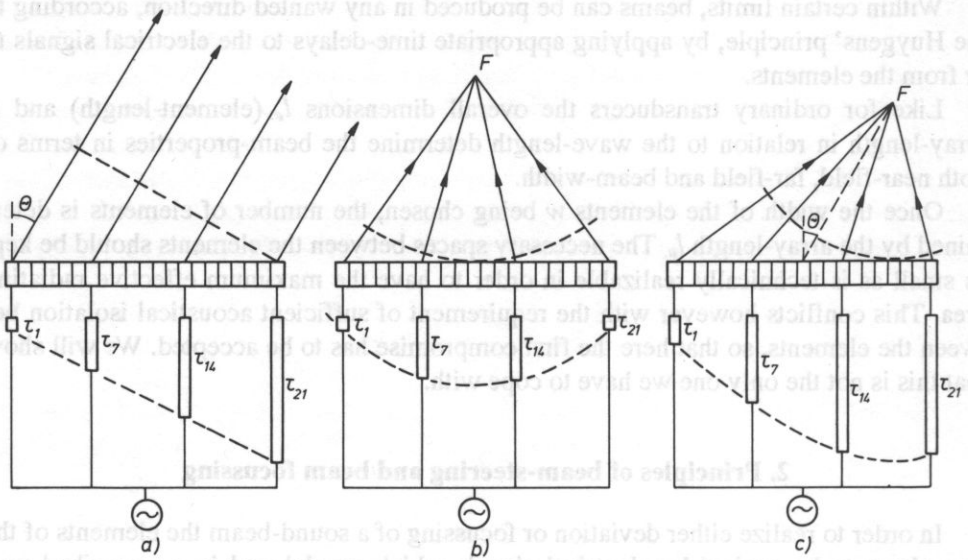

FIG. 2. Schematic presentation of three different transmission modes, together with the pertinent delay-line settings. For simplicity only 4 channels one shown

(a): unfocussed transmission at an off-axis angle Θ. Delay-time varies linearly with element position.

(b): focussed transmission in axial direction. Delay-time varies circularly with element-position.

(c): focussed transmission at angle Θ. Delay-time as function of element-position is a combination of (a) and (b).

Fig. 2b, and a focussed beam is obtained with the center of curvature F as its focal point. Finally, in Fig. 2c we show that the combination of a linear and a circular dependence of time-delay will result in the deviation of a focussed beam.

We mentioned earlier that the number of elements is determined by their widths and the overall array-length l_a (see Figure 1). From Fig. 2 and the pertinent description it is easy to comprehend that the complexity of the system and therefore costs increase proportionally with the number of channels. For this reason we are very keen on keeping the number of elements as low as possible, and the question is how far we can go in enlarging the widths of the elements, before any negative effects become unacceptable.

In order to illustrate the effects of changing any parameter like for instance the element width, we have to solve a tutorial problem. We have to find a useful way to describe sound-fields or beam-patterns in such a manner that significant features are not lost due to too much simplification.

Beam-characterization

In classical transducer theory the acoustic field formation is usually characterized in terms of directional patterns, in general measured or calculated for continuous sound. In Figure 3 a number of such patterns is shown for various source dimensions, calculated in this case for short pulses, rather than for continuous sound. Such a characterization, where the acoustical pressure-amplitude or intensity is plotted against the direction or lateral position, is only meaningful in the far-field because there the curve-shape is independent of range.

In modern echography, however, practically the whole range of interest is within the near-field. Here the field structure is rather complex, although much more for continuous sound than for short pulses involving wide frequency-spectra. This can be easily understood, if we realize that with continuous sound there will be interference between the circular continuous waves with amplitudes all varying between the same positive and negative values. There will be points of total summation and total cancelling; in other words, a rather wild pattern. In the case of pulses, however, it will be appreciated that the shorter the pulse-length, the more incomplete the interference will be, because the spatial extent over which the amplitude differs from zero will become shorter and shorter.

We hope to have explained now sufficiently that dealing with the near-field and at the same time using short pulses, forces us to find other ways of describing the mechanisms and the effects involved; other than just directional patterns.

Computer-generated beam-patterns

We will now set up a realistic model and calculate the field-patterns for different directions Θ different element-sizes, and for both non-focussed and focussed situations.

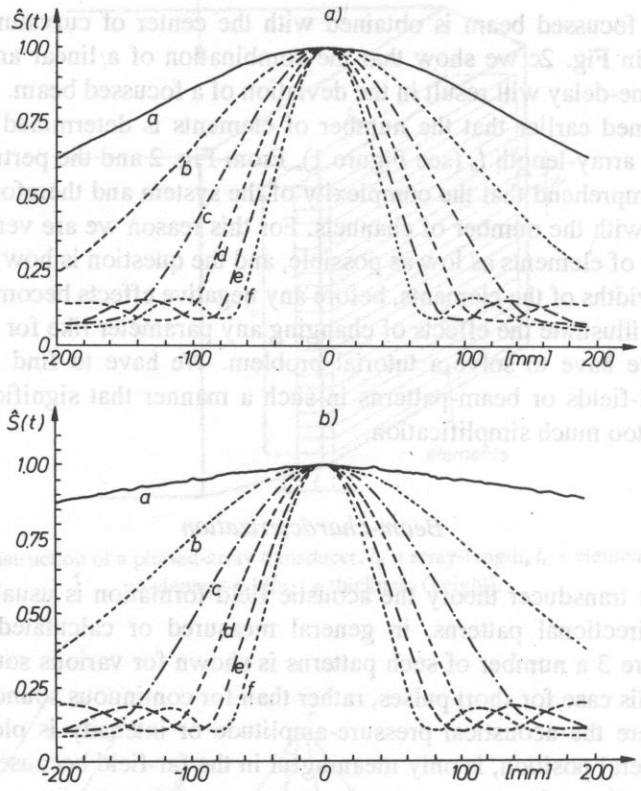

FIG. 3. Directional patterns of sound sources of different dimensions for both Case I in A and for Case II in B. (a): directional pattern of a 0.625 λ wide source (b) through (f): 2, 3, 4, 5 and 6 times source (a).

The array in our model has an overall length $l_a = 20$ mm and radiates pulses with a center-frequency of 3 MHz. Since the wave-length $\lambda = 0.5$ mm the total radiating aperture is 40 wave-lengths wide. The near-field length can be roughly calculated to be 200 mm, covering the whole range of interest.

We will consider the following cases:

Model A: elements of 0.625 $\lambda = 0.3125$ mm
total number of elements is 64
Model B: elements of 1.25 $\lambda = 0.625$ mm
total number of elements is 32.

For simplicity we neglect the isolating spaces between the elements. Since too many parameters affect the beam-patterns we will carry out calculations for two different cases. Case I concerns a line-array. This means that we disregard the second dimension of the elements l_e (see Figure 1) and thus reduce the model to a two-dimensional acoustical problem. Case II refers to an actual array where we have set l_e equal to l_a, that is 40 λ, or 20 mm at $f_c = 3$ MHz. All calculations are based on the same wave-form,

which is a signal with a cosine-squared envelope filled up with five periods of a cosine-function. At 3 MHz the total pulse-length is then 1.67 μsec.

Before we proceed with the field-calculations, we should investigate firstly the directional behaviour of the elements.

Figure 3A shows directional patterns in Case I for element-widths from $0.625 \times \lambda = 0.3125$ mm in curve (a), up to $6 \times 0.625 \times \lambda = 1.875$ mm in curve (f). We observe that the directional selectivity of a sound-source gradually increases with its width.

It is permitted to use directional patterns in these cases, since even for the largest width the near-field length is only 1.76 mm. We see then that curve (a) applies to what we adopted as Model A, and find that the radiated sound-pressure at the boundary-angles + 45° and – 45° has dropped from 1 to 0.72, which corresponds to 2.85 dB. We feel, more or less intuitively, that this could be acceptable for a practical system. In other words, it seems a good enough approximation of a point-source.

For Model B we assumed an element-width twice as large and this corresponds to curve (b) in Figure 3A. Here a drop from 1 to 0.55 can be noticed at the outer angles, which is 5.19 dB. This seems quite unacceptable, because, again intuitively, the summation of the contributions of all elements for these maximum angles will also be at least 5.2 dB lower than for $\Theta = 0°$. And if the elements radiate some spurious power in or near zero-direction, this will be strongly enhanced by the so much greater on-axis sensitivity. Let us see if our intuition is right.

For both models and for both cases field-patterns are calculated, using the pulse-shape as we described already. In a 3D-picture only three quantities can be mutually related. In this case these are the lateral displacement, the scanning-depth and the sound-pressure or the sound-intensity. We have to decide about the pulsatile signals we are dealing with. These are functions of time at each point in the plane considered and we have no means for taking up time as a fourth dimension. We recall, however, that in practical systems the signal-envelope, rather than the RF-signal, is displayed on the screen, and that the echo-brightness is determined mainly by the peak-value of it. We decided therefore to use also in our computer-model peak-detection of the signals. In the field-patterns as will be shown the variable characterizing the field-strength is thus the peak-value of the calculated sound-pulse in the field.

This variable, which we will call the peak-sound-pressure, is presented in the field patterns as the height of the curves above the "ground"- or zero-plane. It cannot be emphasized strongly enough that the exposed patterns do not represent the **beam-shape**, but the **sound-amplitude**. What the **brightness** is the Schlieren-pictures, is the **vertical deflection** or **"height"** in the shown field-patterns.

Case I

We now come to the discussion of the computer-generated field-patterns for both the Model A in Fig. 4 and the Model B in Fig. 5 in Case I. The left column shows the

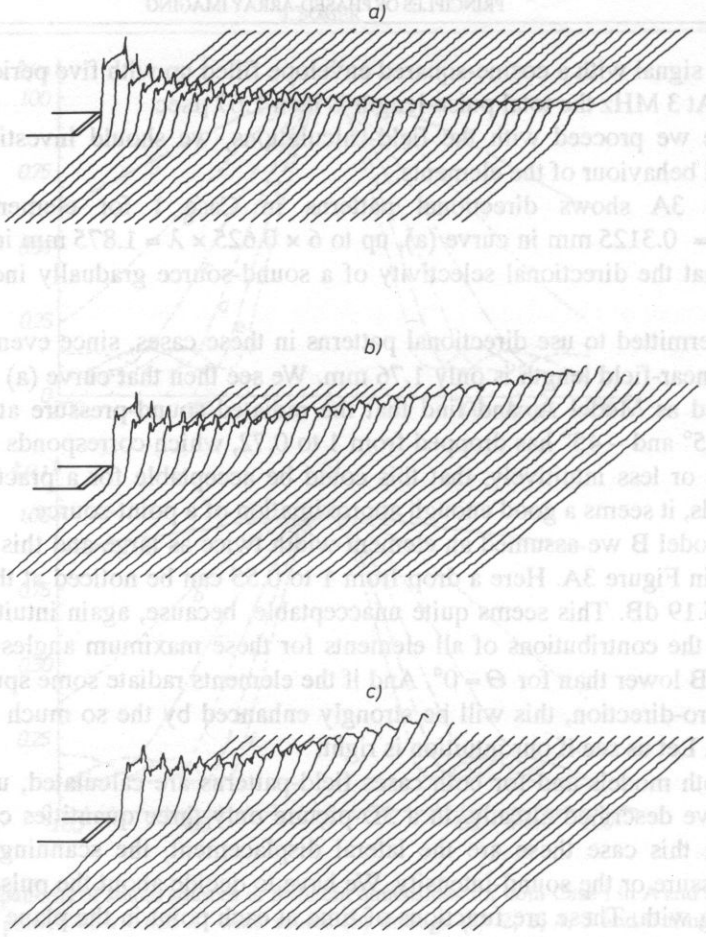
a)
b)
c)

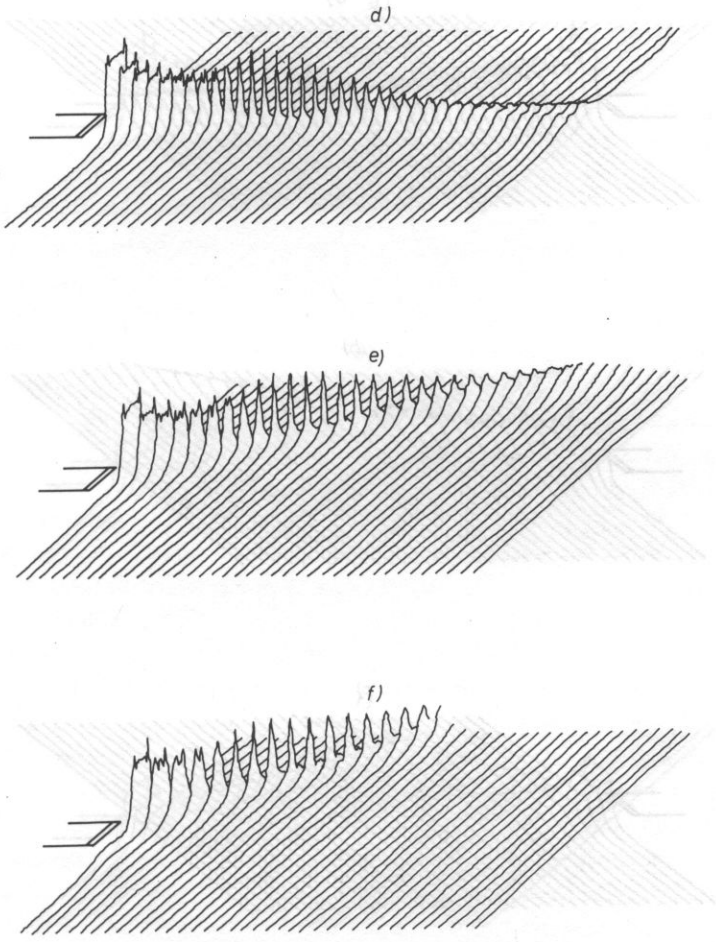

FIG. 4. Beam-patterns as calculated for a 40 λ wide line-array with 64 elements, each 0.625 λ wide
(a), (b) and (c): unfocussed beams at 0°, 30° and 45° respectively
(d), (e) and (f): beams focussed at 160 λ for the same angles.

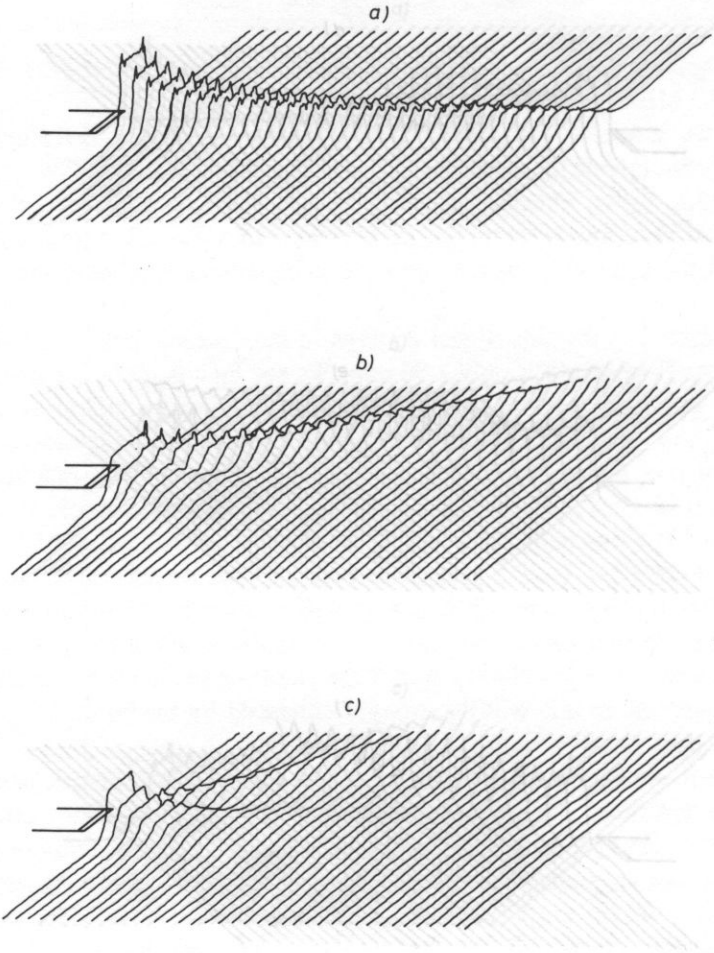
a)
b)
c)

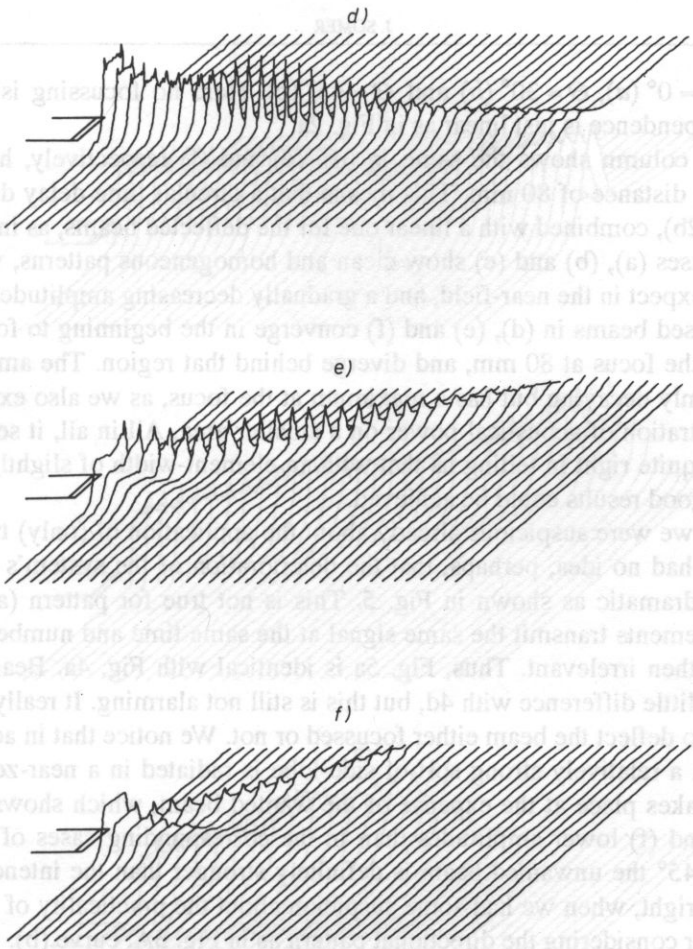

FIG. 5. Beam-patterns as calculated for a 40 λ wide line-array with 32 elements, each 1.25 λ wide. Specifications of (a) through similar to Fig. 4.

results for $\Theta = 0°$ (*a*), $\Theta = 30°$ (*b*) and $\Theta = 45°$ (*c*). Here no focussing is applied; the time-delay dependence is just linear as in Fig. 2a.

The right column shows the same in (d), (e) and (f) respectively, however with focussing at a distance of 80 mm. This means that a circular time-delay dependence is applied (Fig. 2b), combined with a linear one for the deflected beams, as in Fig. 2c. The unfocussed cases (a), (b) and (c) show clean and homogeneous patterns, with uniform width, as we expect in the near-field, and a gradually decreasing amplitude.

The focussed beams in (d), (e) and (f) converge in the beginning to form a narrow region about the focus at 80 mm, and diverge behind that region. The amplitude is no longer uniformly decaying but has a maximum at the focus, as we also expect because of the concentration of acoustical power on a smaller area. All in all, it seems that our intuition was quite right in telling us that with an element-width of slightly over half a wave-length good results could be achieved.

Although we were suspicious already about the application of (only) twice as wide elements, we had no idea, perhaps, that the deterioration of the system's performance would be so dramatic as shown in Fig. 5. This is not true for pattern (a), of course, because all elements transmit the same signal at the same time and number and size of elements are then irrelevant. Thus, Fig. 5a is identical with Fig. 4a. Beam-pattern 5d shows a very little difference with 4d, but this is still not alarming. It really goes wrong when we try to deflect the beam either focussed or not. We notice that in addition to the wanted beam, a relatively strong sort of side-lobe is radiated in a near-zero direction. This clearly takes place at the expense of the wanted beam, which shows in all cases (b), (c), (e) and (f) lower amplitudes than in the corresponding cases of Fig. 4. At a deflection of 45° the unwanted beam is definitely stronger than the intended one. Our intuition was right, when we had some suspicion about the practicality of double-sized elements, after considering the directional pattern as in Fig. 3A, curve (b).

In discussions about array-transducers often the term "aliasing" is used. This is a common expression in signal-theory and is used to characterize the effects of under-sampling of a signal. If we make the element-spacing too large, the sampling of the spatial signal is then too coarse. This applies only when there are frequency-components in the lateral direction, which means for deflected beams only. The reader may feel somewhat confused, since "sampling spatial signals" suggests that we are referring to reception of signals rather than to transmission. Then it may now be the right moment to emphasize that transmission and reception are fully reciprocal. The calculated patterns for transmission can as well be considered to represent reception sensitivity.

Case II

Showing the results of a line-array first has the advantage that any near-field effects due to the element-length l_e are eliminated and cannot obscure the particular effects of the lateral configuration. We can state now, roughly, that the differences between Fig. 6 and 7, representing Case II, and Fig. 4 and 5, referring to Case I, are due to the ele-

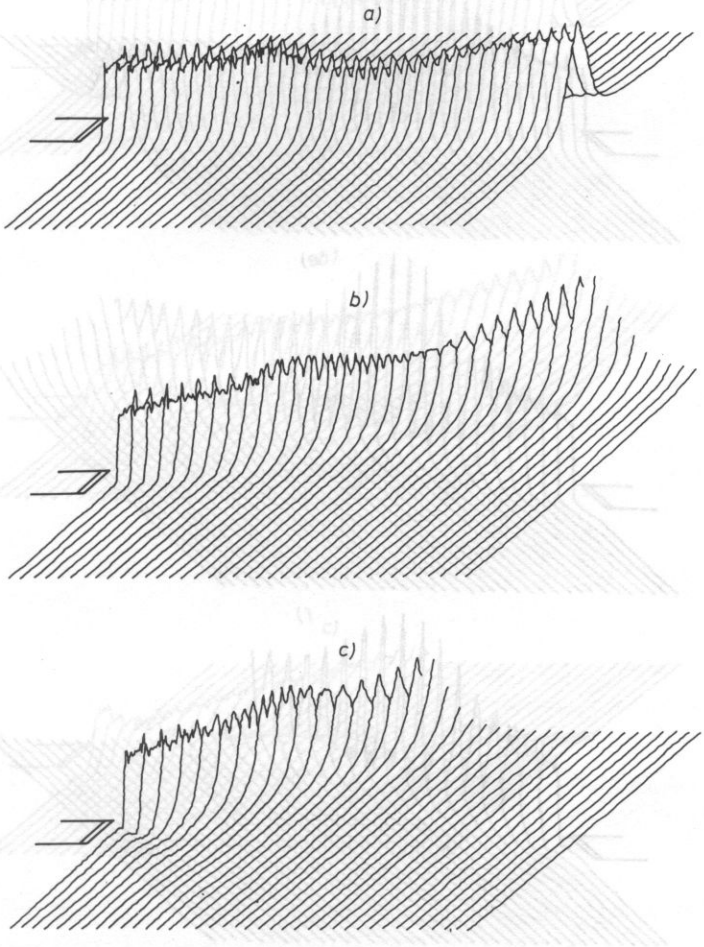
a)
b)
c)

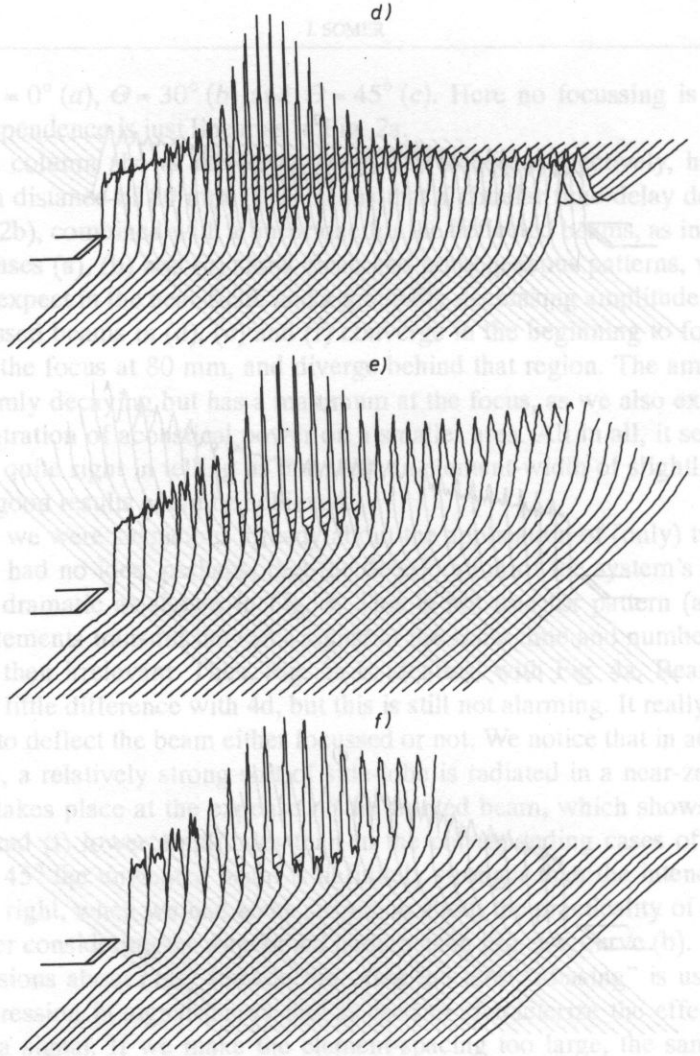

FIG. 6. Beam-patterns as calculated for a 40 λ wide rectangular-array with 64 elements, each 0.625 λ wide and 40 λ long
Specifications of (a) through (f) similar to Fig. 4.

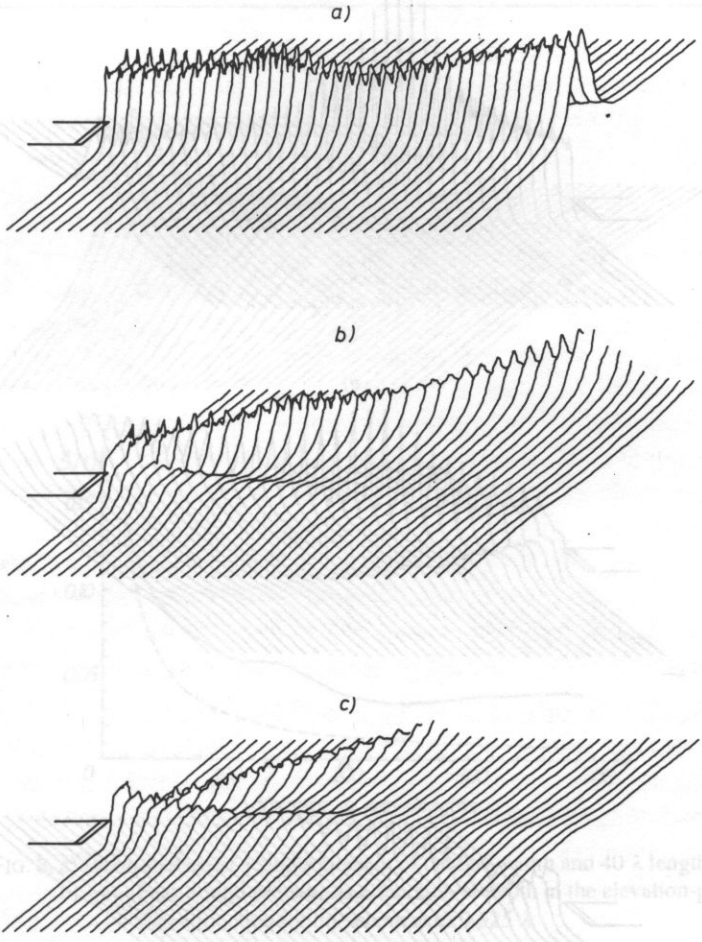
a)
b)
c)

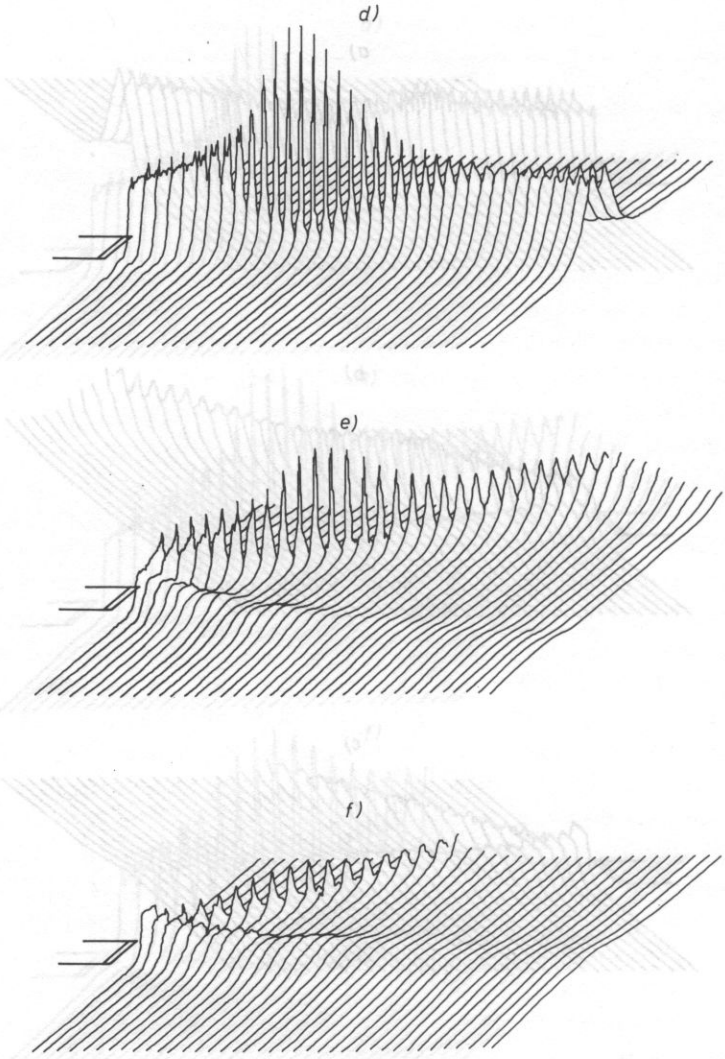

FIG. 7. Beam-patterns as calculated for a 40 λ wide rectangular-array with 32 elements, each 1.25 λ wide and 40 λ long.
Specifications of (a) through (f) similar to Fig. 4.

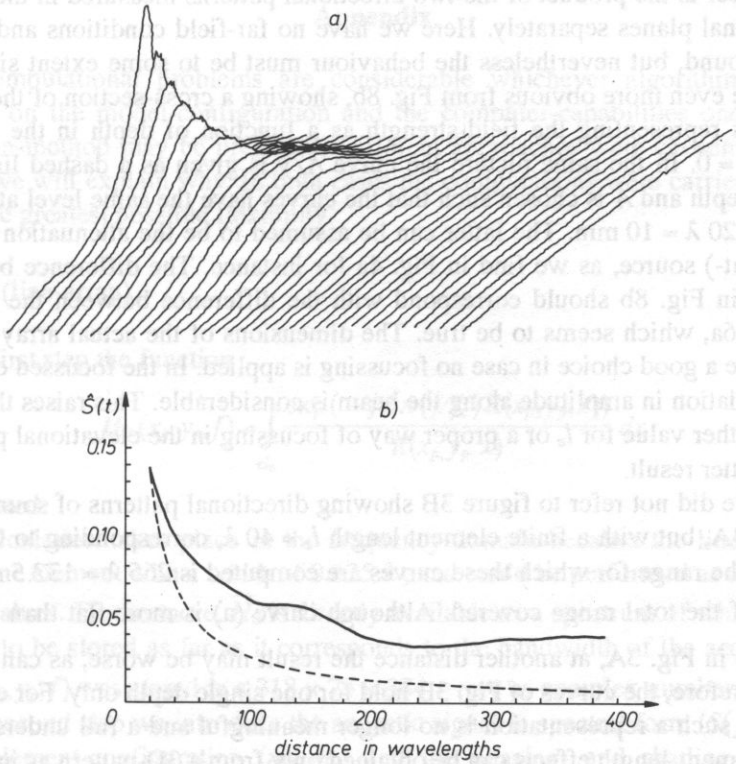

FIG. 8. a) Beam-pattern of a single element of 0.625 λ width and 40 λ length
b) —— Peak-sound pressure as a function of depth in the elevation-plane at $\Theta = 0$
------ Same function for line-element of 0.625 λ.

ment-length l_e. It may therefore be appreciated that changing l_e will yield different results, as will any (fixed) focussing applied in the elevation-plane.

Comparing Figures 5 and 7 shows that also for an actual array element-widths considerably greater than $\frac{1}{2}\lambda$ are out of the question because of the aliasing effects. We can thus restrict ourselves to comparing Figs. 4 and 6, which is quite revealing.

In Figure 6a, b and c we observe a more or less uniform level, whereas in the corresponding patterns of Figs. 4a, b and c a monotonous decrease with depth can be noticed. This means that there is an enhancement,effect obviously due to the directional-pattern in the elevation-plane.

This enhancement-effect is even more striking in the focussed-beams of Fig. 6d, e and f, as compared to the corresponding ones of Fig. 4.

In order to illustrate this further the beam-pattern was computed for just one element of 0.625 λ width and 40 λ length. The result is shown in Fig. 8a and reveals nicely the enhancement-effect over almost the whole range of interest. In the far-field and for continuous sine-waves there is a rule that the total 3-dimensional directional pattern

of a transducer is the product of the two directional patterns measured in the azimuthal and elevational planes separately. Here we have no far-field conditions and no mono-frequency sound, but nevertheless the behaviour must be to some extent similar. This may become even more obvious from Fig. 8b, showing a cross-section of the pattern in 8a, and thus representing the field-strength as a function of depth in the elevational plane for $\Theta = 0$. In the same picture the curve A/y is given as a dashed line where y represents depth and A is chosen such that the curves have the same level at the begin-point at $y = 20\ \lambda = 10$ mm. The latter can be assumed to be the attenuation curve of a line-(or point-) source, as we find in Fig. 4a for instance. The difference between the two curves in Fig. 8b should correspond with the difference between the patterns in Fig. 4a and 6a, which seems to be true. The dimensions of the actual array of Case II turn out to be a good choice in case no focussing is applied. In the focussed cases, however, the variation in amplitude along the beam is considerable. This raises the question whether another value for l_e or a proper way of focussing in the elevational plane could yield any better result.

So far we did not refer to figure 3B showing directional patterns of sources similar to those of 3A, but with a finite element length $l_e = 40\ \lambda$, corresponding to Case II. As in Fig. 3A, the range for which these curves are computed is $265\ \lambda = 132.5$ mm, which is about $\frac{2}{3}$ of the total range covered. Although curve (a) is more flat than the corresponding one in Fig. 3A, at another distance the result may be worse, as can be seen in Fig. 8a. Therefore, the curves of Fig. 3B hold for one single depth only. For elements of finite length such a representation is no longer meaningful and a full understanding of the finite element-length effects can be obtained only from a 3D-pattern as in Fig. 8a.

In the Appendix a brief account is given of the computational aspects, by which the results presented above, are achieved.

3. Conclusions

Since modern phased-array systems operate entirely in the near-field a new approach is necessary to describe their performance.

Investigation of computer-models has shown that increasing the element-width leads progressively to deterioration of the produced beams. The element width should not exceed $\frac{1}{2}\ \lambda$ too far. With $0.625\ \lambda$ a reasonable performance seems to be possible.

The element-length has a great influence on the overall beam intensity. It is likely that it can be used in the desing for shaping the beam in the azimuth-plane. Also focussing in the elevational plane may affect the overall beam-shape in the azimuth-plane. Of course, the beam contours in the elevation-plane are important too. It requires further research to acquire more knowledge about this aspect. Also the influence of the applied wave-form is not yet fully understood. All in all, as compared to far-field problems and mono-frequency sound, the complexity of the near-field problem and pulsatile signals is considerable.

Appendix

The computational problems are considerable whichever algorithm is chosen. Depending on the model-configuration and the computer-capabilities one or another computation-method may be preferred. Different approaches were chosen for the two cases and we will explain why. In both cases the computations were carried out in two steps for the greatest possible flexibility.

Case I (line-array)

In the first step the function

$$\overline{H}_0(x_p, y_p, f) = \int_{el_0} \frac{\exp(-j2\pi(f/f_c)R(x_p, y_p, x))}{R(x_p, y_p, x)}\, dx \tag{1}$$

was calculated.

The calculation takes place in the frequency-domain because the line integration was over one element with a width of 0.625 λ, and could be performed as a summation of only 5 values. Furthermore, $\overline{H}_0$ is directly available as a spectrum of which only that part needs to be stored as far as it corresponds to the bandwidth of the acoustic signal $\overline{S}(f)$. $\overline{H}_0(x_p, y_p, f)$ was stored in a 318 × 75 × 384 – rray as complex numbers.

In the second step we introduce the acoustic signal in spectral form ($S(f)$), together with the element-configuration (m_1, m_2) and the phasing- and shading-information ($\overline{w}_i(f)$).

Then

$$s_t(x_p, y_p) = \max\left|F^{-1}\left[\overline{S}(f) \sum_{i=m_1}^{m_2} \overline{w}_i(f) \cdot \overline{H}_0(x_p - i\Delta e, y_p, f)\right]\right| \tag{2}$$

Case II (rectangular array)

A similar approach as in Case I would now involve a surface-integral of a complexity depending on the element length l_e. Such a surface-integral can be avoided by applying the so-called impulse-response method [1]. The whole computation is then carried out in the time-domain. Instead of performing a surface-integral, the impulse-response $h_0(t)$ can directly be derived as a function of time. Considering the possibility of fast-fourier transforming this function leads to the conclusion that the bandwidth of $h_0(t)$ is too large. The huge number of points needed for the FFT, in order to avoid aliasing effects, would lead to much too high CPU-times. Fourier-transforming the $h_0(t)$ function analytically seems quite a formidable task.

Choosing the time-domain approach, however, requires the performing of a convolution-integral, which needs a lot of care to insure that a sufficient accuracy is obtained.

The first step to be carried out is now

$$p_0(x_p, y_p, t) = h_0(x_p, y_p, t) \otimes s(t) \quad \text{with } h_0(x_p, y_p, t) = \Theta_2(x_p, y_p, t) - \Theta_1(x_p, y_p, t), \tag{3}$$

where the Θ's are given as arcsine- and arccosine-functions.

Again, the field information for only one central element is calculated. Some flexibility, however, is lost since we have to introduce the wave-form in the first step already. The required storage is now half as much because of real numbers, rather than complex ones.

The second step requires the remaining information about element-configuration (m_1, m_2), phasing (t_{di}) and shading (w_i).

$$\hat{s}_t(x_p, y_p) = \max \left| \sum_{i=m_1}^{m_2} w_i p_0(x_p - i\Delta e, y_p, t + t_{di}) \right| \tag{4}$$

References

[1] P. R. STEPANISHEN, *Transient radiation from pistons in an infinite planar baffle*, Journ. Ac. Soc. America, **49**, 1629–1638 (1971).

Received on September 26, 1990

ARCHIVES OF ACOUSTICS
17, 1, 151–165 (1992)

NOVEL SURFACE-ACOUSTIC WAVE TRANSDUCERS

R.C. WOODS

Department of Electronic & Electrical Engineering,
University of Sheffield, Mappin Street, Sheffield, S1 3JD, England.

The conventional means of launching a Surface Acoustic Wave on a piezoelectric substrate is by using an inter-digital transducer. A modified structure using multilayer deposition, but only a single critical photolithography stage, is proposed in this paper. The potential advantages of this structure include greater ease of manufacture and/or access to higher frequencies. Several variants of the basic principle are possible, and these are analysed using a simple equivalent circuit model. Experimental results for several fabricated devices, including apodised (weighted) transducers, are presented. These results show that the technique is a viable method of launching surface acoustic waves and that the flexibility of the concept should approach that of the conventional type of transducer, with much scope for future development of more advanced versions.

1. Introduction

Surface-acoustic wave (SAW) devices have found wide applications in areas requiring filters (e.g. television IF strips), delay lines (e.g. radar installations) or convolvers (e.g. communications equipment). In many cases the system design has been influenced by the smallest feature size which can be fabricated, which governs the maximum frequency of operation of the interdigital transducers (IDTs) used. A method of increasing the maximum usable frequency of an IDT (without increasing the photolithography requirements over those for conventional IDTs) would be useful because this would allow access to frequency bands previously outside the capability of SAW devices, as well as potentially making available increased bandwidth for information transfer. In addition, further applications, formerly precluded because of considerations of maximum frequency and photolithography linewidth, could be contemplated. Alternatively, cost reductions over devices made using existing techniques, achieved through relaxed photolithography requirements, would also be extremely advantageous.

Direct-writing by electron-beam-lithography (EBL) is a commonly-quoted route to high frequencies, but this technique is best suited to very low volume applications where low throughput in the fabrication process is acceptable; its consequent relatively

high cost prevents its use in all but the most specialised applications. A means of reaching high frequencies using, as far as possible, *conventional* microelectronics fabrication technology would have wide application, by extending the useful range of SAW components into L – band. At present, components with fundamental operating frequencies in excess of ~ 700 MHz are exceptional. For example, filters covering the cellular radio bands around 900 MHz are extremely difficult to manufacture with good yield if a reasonable specification is to be satisfied; most SAW oscillators operating at L – band do so using harmonics or frequency multiplication, both of which degrade their performance. The devices described in this paper have the potential of enabling efficient manufacture of miniaturised filtering and delay functions at these frequencies.

Conventional SAW devices employ IDTs having the structure shown in Fig. 1, or variations of it [1]. These launch (or receive) SAW in two opposing directions on the surface of a piezo-electric crystal. To launch a SAW with wavelength λ using a synchronics transducer, it is normally necessary to be able to fabricate reliably lines with a width $\lambda/4$, so that if the linewidth limit is W and the SAW velocity is v, the maximum synchronous frequency (or "centre-frequency", for a symmetrical bandpass filter) that can be used is $v/4W = f_0$ (assuming for simplicity the usual 50:50 mark:space ratio when fabricating fine metal lines). If very fine lines are used, then the resistivity of the "fingers" becomes an additional, important, cause of loss in the IDT. Variants on this basic transducer design are also used, such as the use of multiple electrodes within each acoustic wavelength or the use of harmonic operation, but in all cases the high-frequency limit in the device design is set by the photolithography linewidth achievable.

A type of transducer structure has recently been independently developed [2] in which the gaps between the "finger" electrodes are very narrow (and are defined by a layer of deposited anodic oxide). The linewidth requirement is only $\lambda/2$ for this "narrow gap" structure, so that the "narrow gap" transducer has the potential of increasing

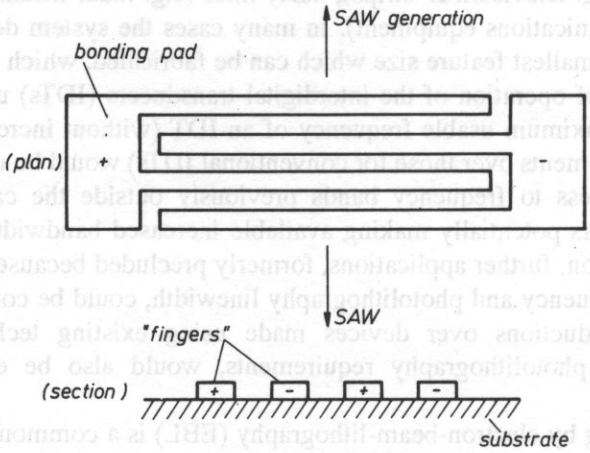

FIG. 1. Conventional SAW IDT. The electrodes are typically aluminium or gold thin films; the substrate is typically $LiNbO_3$, Quartz or GaAs .

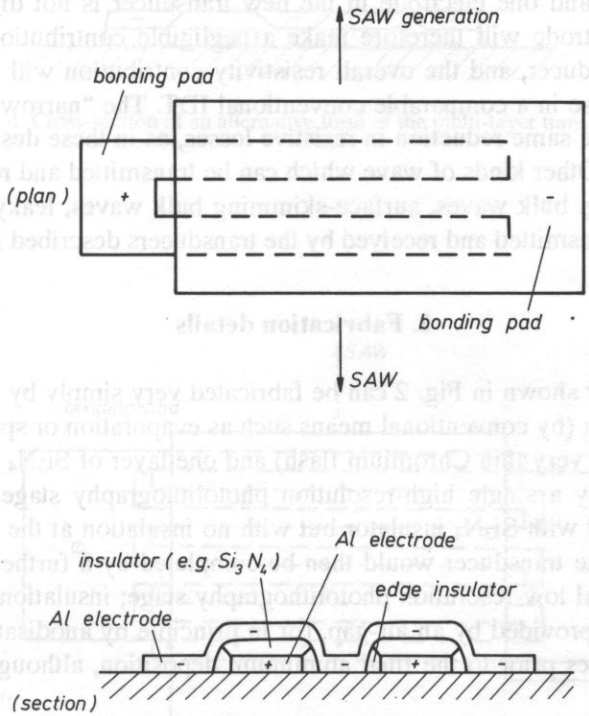

FIG. 2. One form of the multi-layer transducer described in this paper. If the buried electrode is made of aluminium, the edge insulation can be formed by anodisation, or alternatively an air-gap may be used.

the maximum usable frequency; the maximum attainable centre-frequency is $v/2W = 2f_0$.

The transducers described in this paper have the basic construction illustrated in Fig. 2; for this type of structure the required standard of photolithography is lower than for the conventional IDT or the "narrow gap" transducer [2] (i.e. the achievable smallest linewidth can be greater) because in the present devices "bridging" shorts between adjacent "fingers" do not substantially affect performance, whereas in the conventional device a "bridging" short between adjacent "fingers" immediately destroys the RF electric field which must be set up by the IDT in order for it to function. (A "bridging" short in a "narrow gap" transducer [2] may isolate part of the affected "finger(s)", depending on the mask design, thus giving less immunity from the effects of "bridging" shorts compared to the present structure.) If the linewidth achievable with this relaxed constraint is W', where $W' < W$, then the maximum attainable sampling frequency (or centre-frequency) is $v/2W'$ which is greater than twice f_0.

The "filling factor" of the electrodes contacting the crystal surface for the new type of transducer is different from that of the conventional IDT, and this may modify the minimum obtainable insertion loss. A further difference is that the transducer "fingers" are twice the width of those in the conventional IDT with the same bandwidth and

centre-frequency, and one electrode in the new transducer is not digitated at all; the non-digitated electrode will therefore make a negligible contribution to the resistive losses in the transducer, and the overall resistivity contribution will be approximately one quarter of those in a comparable conventional IDT. The "narrow gap" transducers [2] do not offer the same reduction in resistive losses, as in these designs *both* electrodes are digitated. Other kinds of wave which can be transmitted and received by a conventional IDT (e.g. bulk waves, surface-skimming bulk waves, leaky SAW [3] could, in principle, be transmitted and received by the transducers described in this paper.

2. Fabrication details

The transducer shown in Fig. 2 can be fabricated very simply by deposition of one layer of aluminium (by conventional means such as evaporation or sputtering, and usually preceded by a very thin Chromium flash) and one layer of Si_3N_4 (by plasma deposition) followed by a single high-resolution photolithography stage. This leaves the electrodes covered with Si_3N_4 insulator but with no insulation at the sides of the electrodes (Fig. 3). The transducer would then be completed by a further aluminium evaporation and a final low-resolution photolithography stage; insulation between the two electrodes can be provided by an air-gap, (or in principle by anodisation of the aluminium "finger" edges prior to the final aluminium deposition, although in practice this

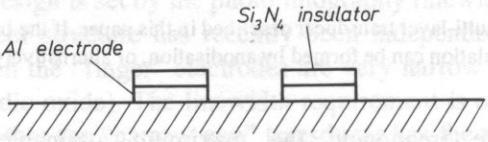

FIG. 3. Cross-section of the device water at an intermediate processing stage during fabrication of the structure shown in Fig. 2.

was found not to be necessary for the designs used in this work). It is an essential feature of the design that only *one* of the photolithography stages is highly critical, and precise alignment between the two stages is not important: the lithography for the digitated electrode and its insulation is "self-aligning".

An alternative structure, shown in Fig. 4, has also been investigated. In this case the initial (high-resolution) photolithography stage is performed only on the first aluminium layer, and the Si_3N_4 insulator and capping aluminium layer only need low-resolution processing; no anodising or other extra insulation is needed for this structure. It is expected that this construction would give increased insertion loss (see section 3).

A possible further variant is shown in Fig. 5, which shows a novel approach to the problem of designing a low-loss unidirectional transducer (UDT). Here the linewidth requirement is $\lambda/3$ (compared with $\lambda/6$ for a conventional UDT) and the design of the electrodes and crossovers is simplified over the conventional case. This type of UDT is the subject of future work.

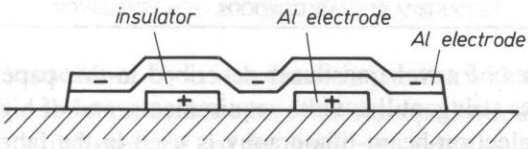

FIG. 4. Cross-section of an alternative form of the multi-layer transducer.

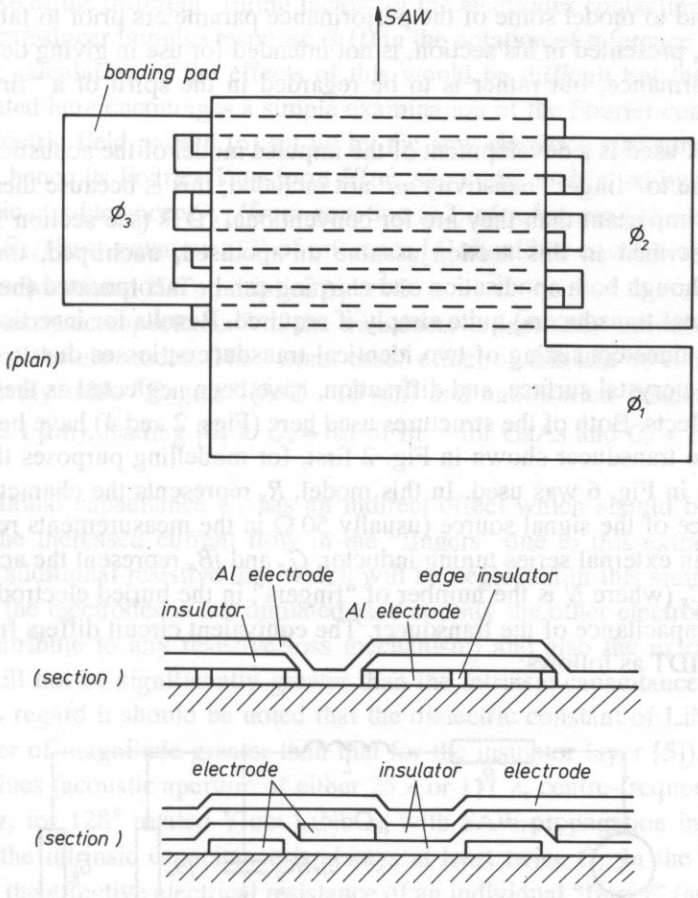

FIG. 5. A novel multi-layer approach to three-phase low-loss UDT design. The electrodes ϕ_1, ϕ_2 and ϕ_3 are driven using a 60° phase shifting circuit. (For simplicity the overlay insulators are not shown on the plan view). Several variants are possible depending on whether the structure is based on Fig. 2 or on Fig. 4 (see the two sectional views).

For all of the types of novel transducer described in this paper, the advantages of lower cost through less stringent linewidth requirements, and of higher frequency capability, still remain if electron-beam-lithography is used in the fabrication process, and in fact are obviously independent of the lithography technology used.

3. Simple model of transducers

An equivalent circuit model of the transducers described here has been developed for the purpose of quantifying some of the most important fundamental properties of the devices and to model some of the performance parameters prior to fabrication; this simple model, presented in his section, is not intended for use in giving detailed predictions of performance, but rather is to be regarded in the spirit of a "first order" approach.

The model used is a development of the impulse model of the acoustic conductance [4]. Losses due to "finger" resistivity are not included; this is because these losses will be much less important than they are for conventional IDTs (see section 1). All the simulations described in this section assume un-apodised, unchirped, transducers for simplicity, although both apodisation and chirping can be incorporated (both in the model and in actual transducers) quite simply if required. Results for insertion loss are given for delay lines consisting of two identical transducers; losses due to SAW attenuation along the crystal surface, and diffraction, have been neglected as these will usually be small effects. Both of the structures used here (Figs. 2 and 4) have been modelled.

Taking the transducer shown in Fig. 2 first, for modelling purposes the equivalent circuit shown in Fig. 6 was used. In this model, R_s represents the characteristic (internal) impedance of the signal source (usually 50 Ω in the measurements reported here), L represents an external series tuning inductor, G_a and jB_a represent the acoustic admittance, and NC_s (where N is the number of "fingers" in the buried electrode) represents the intrinsic capacitance of the transducer. The equivalent circuit differs from that for a conventional IDT as follows:

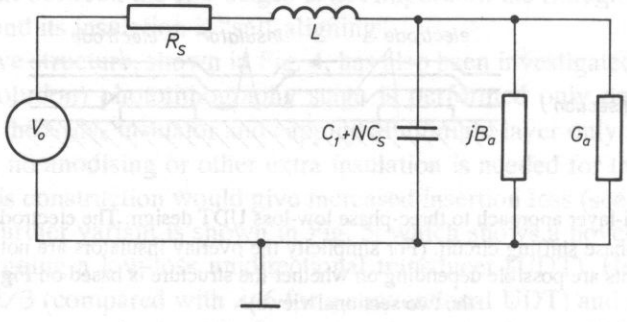

FIG. 6. The equivalent circuit used in this work to model the transducer shown in Fig. 2 (modified from reference [4]).

i. An additional capacitance C_1 is introduced in parallel with the acoustic admittance. This represents the shunt capacitance between the top electrode and the buried electrodes separated by a thickness, d, of insulator. Its value was estimated using the conventional "parallel plate" formula:

$$C_1 = \frac{\varepsilon_r \varepsilon_0 a N \lambda}{2d} \text{ (+ stray capacitance if necessary)} \quad (1)$$

where a is the transducer aperture (in metres), and ε_r is the relative permittivity of the insulator (taken to be 4.2 for Si_3N_4 [5]).

ii. Because of the different "filling factor" of the electrodes contacting the substrate surface, the transducer impulse response ($h(t)$ in the notation of reference [4]) is changed. An exact calculation of the effects of this would be difficult but the spirit of the model presented here encourages a simple examination of the Fourier components present in the electric field pattern [6] set up by the new electrode structure; this implies that $h(t)$, and hence its Fourier Transform $H(\omega)$, should be multiplied by $(\pi\sqrt{2})/4$, and so the acoustic conductance, G_a, (from equation (12) of reference [4] and the acoustic susceptance, B_a, (from equation (13) of reference [4] should be equal to their respective values for a conventional IDT multiplied by $\pi^2/8$.

iii. The "intrinsic capacitance" of the transducer is increased because of the large contact area of the electrodes. The "worst case" effect of this can be estimated by assuming relatively wide "fingers" ($\lambda/2 \sim 10$ μm) and anodisation insulation which is very thin (~ 0.1 μm), leading [6] to $C_s = 6.1\ \text{nF m}^{-1}$ for GaAs and $C_s = 1.8\ \text{nF m}^{-1}$ for $LiNbO_3$.

The additional capacitance C_1 has an indirect effect which should be considered. Because of the increased current flow in the "fingers" due to this extra capacitance, there will be additional resistive loss which will be neglected in this simple model because one of the electrodes is not digitated (and so only the other electrode can be expected to contribute to any resistive loss mechanism) and also the extra capacitance introduced will not be significantly greater than the intrinsic capacitance of the transducer (in this regard it should be noted that the dielectric constant of $LiNbO_3$ is more than one order of magnitude greater than that for the insulator layer [5]). For realistic parameter values (acoustic aperture of either 25 λ or 111 λ, centre-frequency 100 MHz or 1000 MHz, for 128° rotated Y cut $LiNbO_3$, with SAW propagation in the X direction) in fact the intrinsic capacitance is always at least twice C_1. In the first of these design cases, the effective electrical resistance of an individual "finger" (assuming Aluminium metallisation of 0.1 μm thickness, and Si_3N_4 insulator of thickness 0.15 μm) is of the order of 6 Ω but the capacitive reactance per "finger" due to C_1 is approximately 315 Ω; in the second case, "finger" resistance is around 29 Ω and the capacitive reactance per "finger" is 730 Ω.

Application of the theory of electrical networks then leads to the following expression for the insertion loss of each such transducer:

$$\frac{\text{acoustic power out}}{\text{electrical power in}} = \frac{2G_aR_s}{\{1 + R_sG_a - [\omega(C_1 + NC_s) + B_a]\omega L\}^2 + \{\omega LG_a + R_s[\omega(C_1 + NC_s) + B_a]\}^2} \quad (2)$$

Equations (17) and (18) of reference [4] show how to calculate G_a and B_a as functions of k^2 (the piezoelectric coupling constant) and other parameters, enabling analytic calculation of the insertion loss as a function of frequency. An example of the results

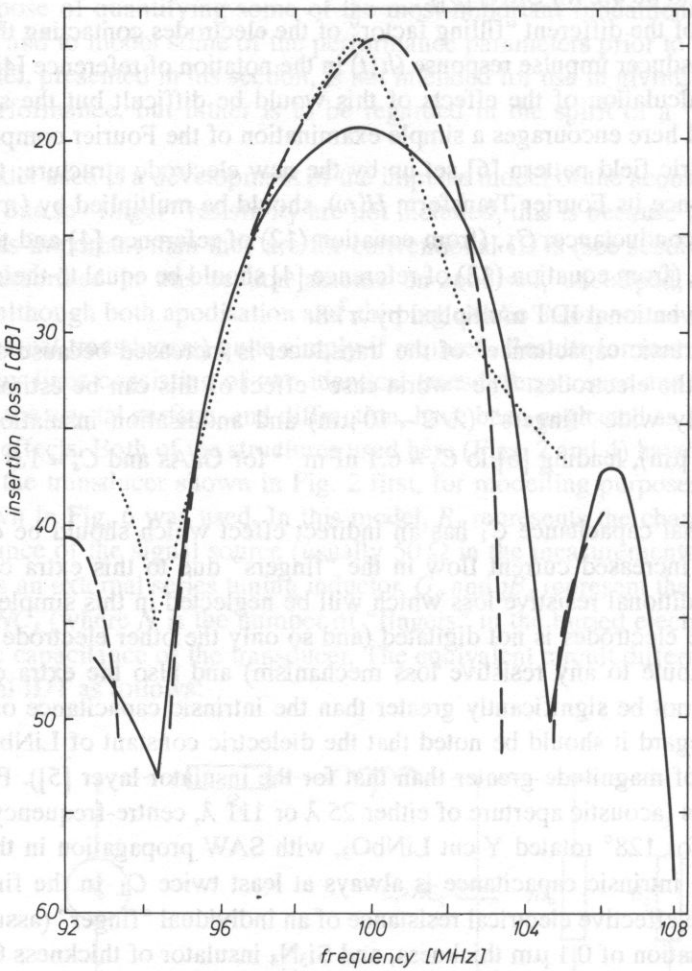

FIG. 7. Insertion loss of a delay line built using the novel transducer shown in Fig. 2: predicted (---) and experimental (···). For simplicity, no impedance-matching components were used. The material was $LiNbO_3$, the synchronous frequency was 99 MHz, transducer aperture $a = 25\ \lambda$, $R_s = 50\ \Omega$, $N = 20$ "fingers" and $d = 0.147\ \mu m$. Also shown (—) is the frequency response of a device of the type shown in Fig. 4, using the same mask and fabricated on 128° rotated Y cut $LiNbO_3$, with SAW propagation in the X direction. Note that the symmetrical response is close to ideal.

from this expression is shown in Fig. 7, compared with some experimental results (see section 4).

Next, taking the transducer shown in Fig. 4, the equivalent circuit of Fig. 8 was used. This is identical to that used above, for the transducer shown in Fig. 2, except that a further capacitance C_1 is introduced *in series* with the acoustic admittance. This represents the capacitance between the top electrode and the substrate surface (and for a buried electrode having a 1:1 mark:space ratio, the value of this extra capacitance is equal to that introduced in parallel with the acoustic admittance in paragraph (i) above). The insertion loss per transducer, at centre-frequency, is given by

$$\frac{\text{acoustic power out}}{\text{electrical power in}} = \frac{2R_s G_a \omega^2 C_1^2}{(B - AL)^2 + (D - EL)^2} \tag{3}$$

where

$$A = \omega^2 G_a (2C_1 + NC_s) \tag{4}$$

$$B = G_a - \omega^2 R_s C_1 (C_1 + NC_s) \tag{5}$$

$$D = \omega C_1 + \omega R_s G_a (2C_1 + NC_s) \tag{6}$$

$$E = \omega^3 C_1 (C_1 + NC_s) \tag{7}$$

and the ideal matching inductance is given by

$$L = (AB + DE)/(A^2 + E^2). \tag{8}$$

If the insulator thickness, d, is small, the shunt capacitance is large, diverting current away from the acoustic conductance and thus reducing the acoustic power generated; if d is large, the series capacitance is small so that very little current can flow through the acoustic admittance. Therefore there is an optimal thickness of insulator at which these degrading effects are minimised collectively, giving the smallest insertion loss. Figures 9 and 10 show the centre-frequency insertion loss for delay lines fabricated on GaAs and $LiNbO_3$ substrates respectively, as a function of insulator thickness, for both the "tuned"(i.e. using a matching inductor with value L given by equation (8))

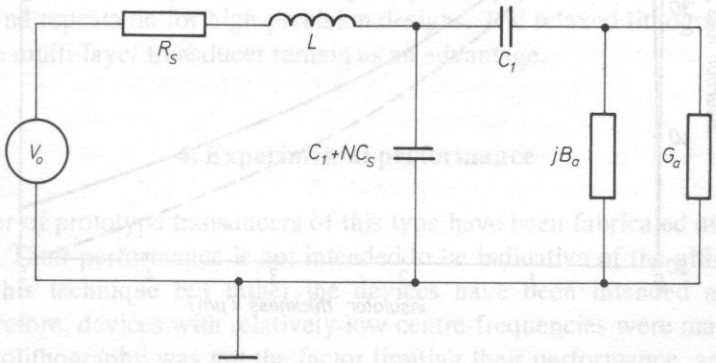

FIG. 8. The equivalent circuit used in this work to model the transducer shown in Fig. 4.

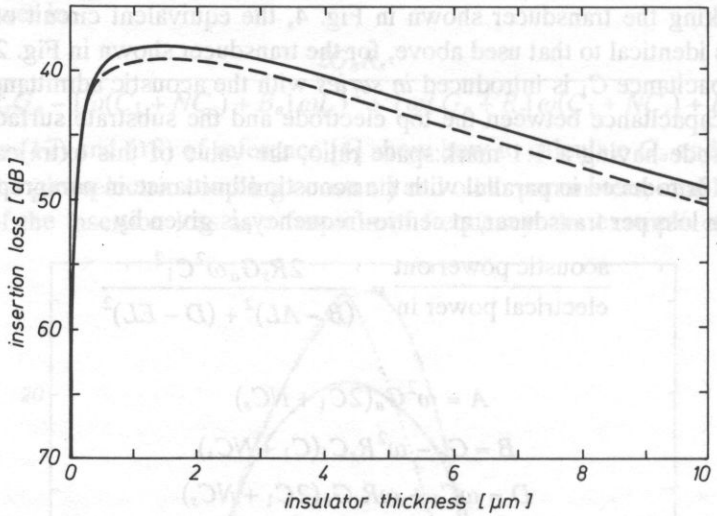

FIG. 9. Predictions of insertion loss of delay lines built using the transducer shown in Fig. 4, plotted against insulator thickness, for both tuned (—) and untuned (----) cases. The substrate is {100} cut GaAs , with SAW propagation in the <011> direction, the centre frequency is 74 MHz, the transducer aperture is 25λ, the source resistance is 50 Ω, and the buried electrode consists of 20 "fingers". Optimising the value of matching inductance L makes little difference to the insertion loss.

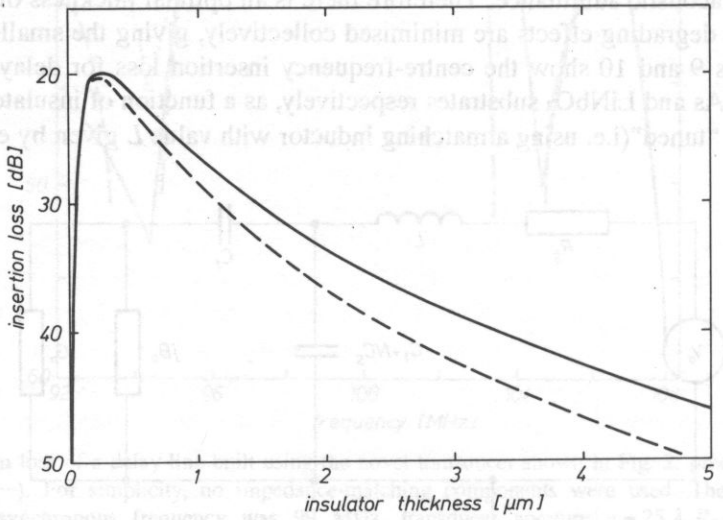

FIG. 10. Predictions of insertion loss of delay lines built using the transducer shown in Fig. 4, plotted against insulator thickness, for both tuned (—) and untuned (----) cases. The substrate is 128° rotated Y cut $LiNbO_3$, with SAW propagation in the X direction, and the centre frequency is 99.7 MHz; other parameters as in Fig. 9.

and "untuned" (i.e. $L = 0$) cases. Material parameters were taken from reference [7]; the centre-frequencies for these examples were chosen to match the typical laboratory trials of the transducer which are reported in section 4. For the device parameters used the acoustic wavelength is 40 μm and the optimum insulator layer thickness is of the order of 1.5 μm for GaAs, and rather less for $LiNbO_3$. Thicknesses of this approximate magnitude are readily achievable using conventional deposition techniques and are small enough (i.e. much less than the acoustic wavelength λ) not to affect SAW propagation significantly [1]. Although at first sight it might appear that the additional capacitances introduced in the equivalent circuits for the novel transducers will significantly degrade their performance compared to conventional IDTs, this is not necessarily correct reasoning as the full network analysis shows, by taking the capacitance values into account quantitatively rather than just qualitatively. The conclusion is that the effect of the additional capacitance is not at all as disastrous as one might initially suppose.

This simple impulse-response model predicts that the performance of the two types of transducer should be similar. Direct comparison with conventional IDTs is not so straightforward but the order-of-magnitude of the insertion losses predicted for the new types of transducer is at worst comparable with that expected from conventional IDTs. (Note that when a conventional IDT is operated at the third or higher harmonic of its fundamental response, as an alternative method of obtaining operation at a higher frequency than would be normal for a given photolithographic linewidth, then its performance is correspondingly degraded). The transducers described here have an extra advantage over conventional IDTs because resistivity loss has not been taken into account in the model presented, and there is a four-fold reduction in this loss mechanism. One other effect not modelled here is that of the mechanical loading introduced by the insulator layer on top of the crystal surface. As the optimum thickness is of the order of $\lambda/20$ (or smaller) this effect will be small [1] and equivalent to that of distributed "mass loading" of the transducer, which will slightly modify the SAW velocity and hence the centre-frequency. For such a small thickness, substantial damping loss would not be expected but in any case the insertion loss may be confirmed experimentally. Similarly, the effect of the thin metal overlay electrode is anticipated to be negligible and limited to a small change in centre-frequency, unimportant in most applications but predictable and repeatable for high-precision designs. The relaxed lithography requirements for the multi-layer transducer remain as an advantage.

4. Experimental performance

A number of prototype transducers of this type have been fabricated as demonstration devices. Their performance is not intended to be indicative of the ultimate obtainable using this technique but rather the devices have been intended as feasibility studies. Therefore, devices with relatively low centre-frequencies were made so that in fact the photolithography was *not* the factor limiting their performance, and other factors could be controlled closely. Substrate crystals of $LiNbO_3$ (128° rotated Y cut)

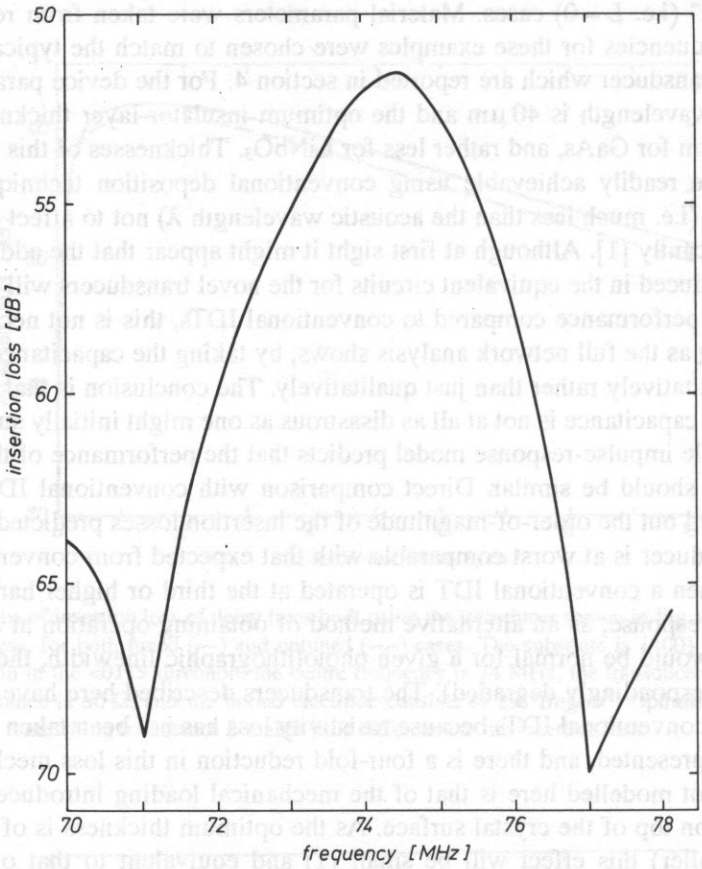

FIG. 11. The frequency response of an experimental device using unweighted transducers, of the type shown in Fig. 4, each having 20 "fingers". This device was fabricated on {100} cut GaAs, accounting for the high insertion loss; this should be compared to Fig. 7.

were used for many devices; in addition, some devices were made using GaAs ({100} cut), in order to demonstrate the fact that the fabrication method can be applied to any substrate material which can support SAW. Higher frequency devices are the subject of future work. Apodisation, in order to tailor the frequency response, has been used in order to establish the feasibility of using simple weighting techniques to produce a desired frequency response; some un-apodised devices have also been produced and tested for the purpose of establishing the fabrication procedures. Devices were tested in a 50 Ω RF system with no external matching or tuning components. Transducers fabricated as depicted in both Fig. 2 and in Fig. 4 have been fabricated and tested.

For the type shown in Fig. 2, the anodisation was omitted but the aluminium layer under the Si_3N_4 was over-etched, leading to an over-hang of the Si_3N_4 layer which was confirmed by microscopy. Then when the continuous electrode was deposited there

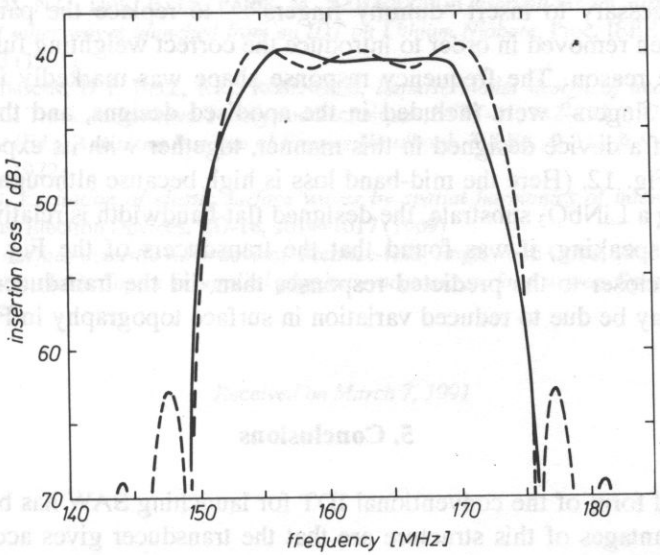

FIG. 12. The frequency response of an experimental device (——) using an apodised transducer of the type shown in Fig. 4, weighted as described in the text proportional to $\sin(2\pi t\Delta f)/t$ truncated sharply at $t = \pm 3/2\Delta f$. This device was fabricated on 128° rotated Y cut $LiNbO_3$, with SAW propagation in the X direction. Also shown is the Fourier Transform (----) of the transducer impulse response.

was an air-gap between the two electrodes so that a solid insulator along the "finger" edges was found to be unnecessary. Experimental results from this device are shown in Fig. 7.

Also shown in Fig. 7, together with Fig. 11, is the performance of a pair of devices of the type shown in Fig. 4 made on $LiNbO_3$ and GaAs substrates respectively; the transducers were all made using the same (un-apodised) mask set. The devices made using GaAs substrate material all showed a high insertion loss at centre-frequency, characteristic of a material like GaAs with a very low piezoelectric coupling constant (k^2) when used for a relatively wideband design, but the un-apodised devices using $LiNbO_3$ show much smaller insertion losses (corresponding to a much greater k^2). In this connection it should be borne in mind that the transducers used in this experimental investigation were operated without series inductors or other matching networks of any kind, and also that as all the transducers made were bidirectional the absolute minimum insertion loss was 6dB.

When apodisation is used for "finger" weighting using conventional IDTs it is normal to include "dummy fingers" across that part of the transducer aperture where the "active finger" has been removed [8]. This is done so that there is phase fidelity over the entire transducer aperture (absence of metallisation would lead to phase distortion of wavefronts travelling at the edges of the IDT aperture compared to wavefronts at the centre of the IDT aperture). Similarly, when apodising the multi-layer transducers, it

was found necessary to insert "dummy fingers" – to replace the parts of "fingers" which have been removed in order to introduce the correct weighting function – for exactly the same reason. The frequency response shape was markedly improved when such "dummy fingers" were included in the apodised designs, and the experimental performance of a device designed in this manner, together with its expected response, are shown in Fig. 12. (Here the mid-band loss is high because although this delay-line was built using a $LiNbO_3$ substrate, the designed flat-bandwidth is relatively large).

Generally speaking, it was found that the transducers of the Fig. 4 pattern performed rather closer to the predicted responses than did the transducers of the Fig. 2 pattern; this may be due to reduced variation in surface topography in Fig. 4 compared to Fig. 2.

5. Conclusions

A modified form of the conventional IDT for launching SAW has been developed. The main advantages of this structure are that the transducer gives access to SAW at higher frequencies than are possible using the conventional IDT, or alternatively a lower standard of photolithography may be used for a given device specification so that device cost is reduced. Electrical resistivity loss is less than with existing types of transducer. Some prototype devices have been fabricated and tested, and show encouraging performance. Delay-lines using apodised transducers on $LiNbO_3$ have proved the viability of apodisation as a technique for weighting the "fingers" when designing this type of transducer. It is not clear at the moment what effect lack of linewidth repeatability (at the resolution limit of photolithography) will have on the performance of these devices and so the evaluation of high frequency devices, on a statistical basis, will be a particularly valuable part of subsequent work. (It would be valuable, for example, to design a set of devices, all having the same low centre-frequency, but with the widths of the "fingers" varying in a known and controlled manner in order to simulate this effect). More complex designs such as unidirectional transducers appear to be feasible as well and will form the basis of future work.

Acknowledgements

It is a pleasure to acknowledge assistance with processing from Dr. G. HILL, Mr. G. PHILLIPS, Mr. I. SIMPSON, Mr. A. WALKER, Miss S.A. WHITE, and Miss E.S. WINDERS.

References

[1] J.D. MAINES, E.G.S. PAIGE, *Surface-acoustic-wave components, devices and applications*, Proc. IEE, **120**, 1078–1110 (1973)

[2] K. YAMANOUCHI, T. MEGURO, K. MATSUMOTO, *Surface-acoustic-wave unidirectional transducers using anodic oxidation technology and low-loss filters*, Elect. Lett., **25**, 958–960 (1989)

[3] P.D. BLOCH, N.G. DOE, E.G.S. PAIGE, M. YAMAGUCHI, *Observations on surface skimming bulk waves and other waves launched from an IDT on Lithium Niobate*, Proc. IEEE Ultrasonics Symp., 1, 268–273 (1981)

[4] C.S. HARTMANN, D.T. BELL, R.C. ROSENFELD, *Impulse model design of acoustic surface-wave filters*, IEEE Trans. Microwave Theory and Techniques, **MTT-21**, 162–175 (1973)

[5] D.E. GRAY (Ed.), *American Institute of Physics Handbook*, 3rd Ed., 9–111 & 9–122. McGraw-Hill, New York, 1972

[6] H. ENGAN, *Excitation of elastic surface waves by spatial harmonics of interdigital transducers*, IEEE Trans. Electron Devices, **ED-16**, 1014–1017 (1969)

[7] S. DATTA, *Surface acoustic wave devices*. Prentice-Hall, Englewood Cliffs, 1986

[8] A.A. OLINER (Ed.), *Topics in applied physics – acoustic surface waves*. Springer-Verlag, Berlin, 1978

Received on March 7, 1991

ARCHIVES OF ACOUSTICS
17, 1, 167–171 (1992)

RIGOROUS *P*-MATRIX FOR UNIFORM NSPUDT

E. DANICKI

Institute of Fundamental Technological Research Polish Academy of Sciences
(00-049 Warszawa ul. Świętokrzyska 21)

A rigorous scattering matrix in mixed representation (*P*-Matrix) is presented for natural single-phase unidirectional transducer (NSPUDT) of surface acoustic wave (SAW). It results from spectral theory of propagation of SAW in periodic system of elastic metal strips on arbitrary anisotropic piezoelectrics.

1. Introduction

Uniform (unapodized) interdigital transducers find many applications in SAW devices. Typically, one or more such IDTs are included in SAW filters, delay lines or SAW resonators. It is then evident that the calculation of frequency response of uniform IDT is frequently required when designing SAW devices.

An useful $\sin x/x$ formula for IDT frequency response has been derived without taking account of SAW reflection from transducer electrodes (neither $\Delta v/v$ nor mechanical) and without admitting peculiar property of piezoelectric anisotropic substrate that may lead to a transducer natural unidirectionality [1]. The above effects, as well as element factor [2] may cause considerable distortion of the above-mentioned simple description of the transducer property.

Below, a corresponding rigorous formula is presented for IDT frequency response that results from spectral theory of propagation and generation of SAW in periodic metal strips on general anisotropic piezoelectric substrate, including possible effect of natural unidirectionality. The theory is a generalization of that presented in [3] to a case of Rayleigh wave.

2. Description of uniform IDT

We consider uniform IDT having N (even number) equally spaced metal strips (periods Λ, strip width $\Lambda/2$, strip thickness $H << \Lambda$, and IDT aperture width W). The strips are perfectly conducting and their mechanical properties are described by mass density ρ and Lamé constants μ and λ.

The mechanical interaction of strips with a plane harmonic wave

$$\exp(j\omega t - jrx)$$

of particle displacement on the piezoelectric substrate surface supporting strips is characterized by a diagonal matrix with diagonal elements g_i

$$-h\begin{bmatrix} \rho\omega^2 - 4\mu\dfrac{\lambda+\mu}{2\mu+\lambda}r(r-K) & 0 & 0 \\ 0 & \rho\omega^2 & 0 \\ 0 & 0 & \rho\omega^2 - \mu r(r-K) \end{bmatrix} \tag{1}$$

resulting from perturbation theory, where $K = 2\pi/\Lambda$ ($K > r > 0$ assumed here), ω – angular frequency, r-wave-number, and $h = H/\pi$ for strips with rectangular cross-section, otherwise h can have comples value.

What concerns electric interaction, we assume that the strips are ideal, thin conductors shielding electric field on the substrate surface. Electric potential of strips can be either $-U/2$ or $U/2$, as the every second strip is connected to either lower, or upper IDT bus. Due to the transducer symmetry, the current I flowing to the IDT upper bus is exactly opposite to that flowing to the lower one. In this paper we assume for simplicity, that the element factor is the same for each transducer fingers, even for the edge ones.

3. Characterization of piezoelectric substrate

Here, we entirely neglect bulk waves, and assume that the transducer works at frequency close to its fundamental frequency. That results in $K - r \approx r$ in (1) and enables us to apply approximated relations between complex amplitudes of electric potential φ, particle displacement vector components u_n, stress components t_{yn} ($n = 1, 2, 3$ corresponding to x, y, z) and electric charge d at the substrate surface $y = 0$ in form

$$u_n = z_n \frac{\sqrt{\varepsilon_e}}{\kappa}\left(-\varphi + \frac{1+\kappa^2}{r\varepsilon_e}d\right) \tag{2}$$

$$(r - k_v)r\varphi - (r - k_0)\frac{d}{\varepsilon_e} = r\frac{\kappa}{\sqrt{\varepsilon_e}}\sum_n z_n^* t_{yn}$$

where ε_e – effective surface permittivity, k_v, k_0 – SAW wave-number for free or metallized substrate surface, and

$$\kappa^2 = k_0/k_v - 1 = \Delta u/v$$

$$z_n = -\frac{\kappa}{\sqrt{\varepsilon_e}}\frac{U_n^{(v)}}{\Phi^{(v)}} = \kappa k_v\sqrt{\varepsilon_e}\frac{U_n^{(0)}}{D^{(0)}} \tag{3}$$

where capital letters denote normalized SAW amplitudes for free (index v), or metallized (index 0) substrate surface [4].

These relations result from approximation of corresponding Green's function in spectral representation, taken at $r \approx k_v$. Equation (2) holds for weak piezoelectrics when $\Delta v/v$ is small, and generally when Eq. (3) are not contradicting, particularly if

$$\varepsilon_e = -\frac{U_n^{(v)}}{k_v \Phi^{(v)}} \frac{D^{(0)}}{U_n^{(0)}} \text{ and } \kappa^2 \approx -\frac{1}{4}\frac{\omega}{k_v} \Phi^{(v)} D^{(0)*}$$

for every n. Otherwise, for our purpose we may apply Eqs. (2) instead of so-called "equivalent isotropic" substrate description. If necessary, we can suitably change parameters characterizing SAW modes in (3) to take account of average loading of the substrate surface by the strips [4].

4. *P*-Matrix for IDT

An useful representation for scattering matrix of IDT is P – Matrix which describes scattering property of IDT at acoustic ports, and admittance of IDT at its electric port, that is

$$[a_L^-, a_R^+, I]^T = [P]\,[a_L^+, a_R^-, U]^T \tag{4}$$

where a – SAW amplitude by definition related to SAW Poynting vector, $\Pi = \frac{1}{2}|a|^2$ (full energy carried by SAW is ΠW). Upper and lower indices mark waves on left (L) or right (R) side of IDT, and propagating in left (–) or right (+) direction. Phases of these complex amplitudes are related to lines which are $N\Lambda/2$ distant from transducer center. I is the transducer current and U is voltage applied to it.

The above-mentioned spectral theory yields

$$r_0 = \frac{K}{2} + Q\,,\ \chi = \sum_{i=1}^{3} g_i (z_i^*)^2\,,\ X = \frac{K}{2} - \frac{k_v + k_0}{2}$$

$$Q = \pm\sqrt{X^2 - |\chi|^2 - \kappa^2 K \frac{\sin \pi r_0/K}{\pi [P_{-r_0/K}(0)]^2}(X - \mathrm{Re}\{\chi\})}$$

$$\gamma^+ = \frac{X + Q - \chi^*}{X - Q - \chi}\,,\ \gamma^- = \frac{X + Q - \chi}{X - Q - \chi^*}$$

$$P_{11} = -\gamma^+ \frac{1 - e^{-jr_0 2N\Lambda}}{1 - \gamma^+\gamma^- e^{-jr_0 2N\Lambda}}$$

$$P_{12} = \frac{1 - \gamma^+\gamma^-}{1 - \gamma^+\gamma^- e^{-jr_0 2N\Lambda}} e^{-jr_0 2N\Lambda}$$

$$P_{13} = \kappa \sqrt{\frac{1}{2}\varepsilon_e \omega} \frac{\sin \pi r_0/K}{P_{-r_0/K}(0)} \frac{\sin N \dfrac{r_0 \Lambda - \pi}{2}}{\sin \dfrac{r_0 \Lambda - \pi}{2}} e^{j\pi \frac{N+1}{2}} e^{-jr_0 N\Lambda/2} \times$$

$$\times \frac{1 - \gamma^+ \gamma^- e^{-jr_0 N\Lambda} + \gamma^+ (1 - e^{-jr_0 N\Lambda})}{1 - \gamma^+ \gamma^- e^{-jr_0 2N\Lambda}} \tag{5}$$

$$P_{3n} = 2WP_{n3}, \; n = 1, 2$$

$$P_{33} = j\omega C_T + W\kappa^2 \varepsilon_e \omega \frac{\sin \pi r_0/K}{P_{-r_0/K}(0)} \frac{(1+\gamma^+)(1+\gamma^-)}{1 - \gamma^+ \gamma^-} \times$$

$$\left[j \frac{\sin N(r_0 \Lambda - \pi) - N \sin (r_0 \Lambda - \pi)}{2 \sin^2 \dfrac{r_0 \Lambda - \pi}{2}} + \left(\frac{\sin N \dfrac{r_0 \Lambda - \pi}{2}}{\sin \dfrac{r_0 \Lambda - \pi}{2}} \right)^2 \times \right.$$

$$\left. \times \frac{1 - \left(\dfrac{1+\gamma^+}{1+\gamma^-} \gamma^- + \dfrac{1+\gamma^-}{1+\gamma^+} \gamma^+ \right) e^{-jr_0 N\Lambda} + \gamma^+ \gamma^- e^{-jr_0 2N\Lambda}}{1 - \gamma^+ \gamma^- e^{-jr_0 2N\Lambda}} \right]. \tag{5}$$

C_T is static capacitance of the transducer and $r_0\Lambda - \pi = Q\Lambda$. The rule for sign of Q is that $\mathrm{Im}\{r_0\} < 0$ or that $r_0 \approx k_0$ To obtain P_{2n}, one should apply relation for P_{1n} with substitutions $\gamma^+ \Leftrightarrow \gamma^-$ and $\exp\left[j\pi \dfrac{(N+1)}{2} \right] \Rightarrow \exp\left[-j\pi \dfrac{(N+1)}{2} \right]$.

5. Comments

As it is seen in (5), there is an asymmetry in the transducer property as concern left, or right propagating SAW detection and generation by IDT, if only γ^+ differs from γ^-. One may then be interested in interpretation of these quantities. In theory they appear in solution for waves in periodic system of short-circuited strips, namely the wave propagating right is composed of forward-propagating wave and backward propagating wave as follows: $a^+(1 + \gamma^+ e^{jKx}) e^{-jr_0 x}$, similarly the wave propagating left: $a^-(1 + \gamma^- e^{-jKx}) e^{jr_0 x}$, r_0 is wave-number of SAW that can take complex value in stop-band. Thus we can interpret γ^+ and γ^- as reflection coefficients of SAW from half-infinite system of periodic strips, from the left, or the right bound of the system (see P_{11} in (5) above).

For typical piezoelectric substrates $\gamma^+ = \gamma^-$ and Eqs. (5) describes a typical two-directional IDT, however accounting for mechanical property of the transducer fingers. For further discussion of the above relations and possible application in analysis of apodized transducers-see [3] and [5].

References

[1] P.V. WRIGHT, *The natural single-phase unidirectional transducers, a new low-loss SAW transducer*, IEEE Ultras. Symp. Proc., pp. 58–63, 1985.

[2] D.P. MORGAN, *Surface, wave devices for signal processing*, Elsevier, Amsterdam 1985.

[3] E. DANICKI, *Spectral theory of natural unidirectionality of SPUDT for B-G wave*, IEEE Ultras. Symp. Proc., pp. 113–116, 1990.

[4] B.A. AULD, *Acoustic fields and waves in solids*, vol. 2, Wiley, New York 1973.

[5] E. DANICKI, *Unified theory of interdigital transducers and SAW reflectors*, J. Tech. Phys., **21**, 387–403 1980.

Received on September 5, 1990

ARCHIVES OF ACOUSTICS
17, 1, 173–176 (1992)

A METHOD FOR MEASURING PHOTOPYROELECTRIC SPECTRA OF DYES IN A POLYMER PYROELECTRIC MATRIX

S. ŁĘTOWSKI and A. SIKORSKA

Institute of Experimental Physics, University of Gdańsk
(80-952 Gdańsk, Wita Stwosza 57)

A method for measuring pyroelectric spectra of a dye admixed to a pyroelectric matrix has been described. Spectra obtained in the visible range by photopyroelectric and photoacoustic methods have been compared for rhodamine B in the pyroelectric PVDF matrix.

1. Introduction

In recent years many steady-state methods for measuring radiationless transitions in dyes embedded in polymer matrices have been developed [1]. The temperature changes occurring in samples due to absorption of light with modulated intensity can, among others things, be detected by the investigation of the photoacoustic effect or by using a pyroelectric transducer attached to the sample. Another method of measuring the radiationless transitions mentioned above has been described hereunder for rhodamine B introduced into the PVDF matrix. The investigations of the spectral characteristics of radiationless transitions were carried out using the technique outlined in the present paper and the photoacoustic method.

2. Measurement method

In our previous report [2] a model of a pyroelectric transducer with a volumetrically admixed dye was presented. The model considered therein consists of a luminophore containing a pyroelectric layer with thickness of l and of light-transmitting electrodes adjoining both its sides. It has been assumed that light can only be absorbed by a dye with a nonzero coefficient of radiationless transitions, and that the matrix is transparent for light in the spectral region where the dye absorbs. The transfer of energy absorbed by the dye to the matrix results in the heating of the latter. Hence an electric potential

difference is created between the electrodes due to the pyroelectric properties of the matrix.

Basing on this method, the measurements of the pyroelectric response were carried out for the pyroelectric PVDF matrix with rhodamine B. A dyed pyrofilm was placed between the electrodes which transmitted light in the optical range and illuminated with monochromatic light of modulated sinusoidal intensity.

3. Samples

The samples of films with rhodamine B were prepared using the method of casting in the Research Branch of the Nitrogen Works in Tarnów. The films, with a rhodamine B concentration of 10^{-4}mol/kg, were subjected to mechanical and electrical treatment under the following conditions: stretching at 80°C, hardening at 120°C, and polarization in the electric field with intensity ≥ 500 kV/cm at 80°C.

4. Measuring apparatus

Photopyroelectric spectra were examined by means of a photoacoustic measuring system built in the Institute of Experimental Physics by A. SIKORSKA and J. SZURKOWSKI, with a suitably changed measuring cell. The transverse cross-section of the cell used in photopyroelectric measurements is shown schematically in Fig. 1. The dyed PVDF pyrofilm was placed between glass plates coated with optically transparent electrodes. The measuring cell was insulated electrically and acoustically from the environment by placing it in an earthed casing with a window for the illuminating beam. The sample investigated was illuminated with a rectangular light beam with dimensions 0.5 cm × 1.0 cm. The block diagram of the system used to measure photopyroelectric spectra is shown in Fig. 2. Similarly as in photoacoustic measurements, a classical optical system with a continuous light source with intensity modulated electromechanically at a frequency of 8 Hz was employed. An 150 W XHP xenon

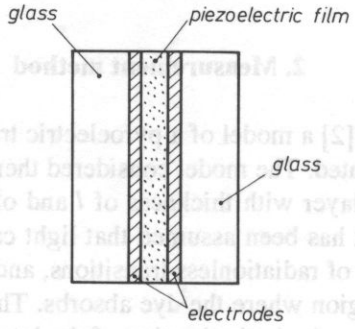

FIG. 1. Construction of the photopyroelectric cell.

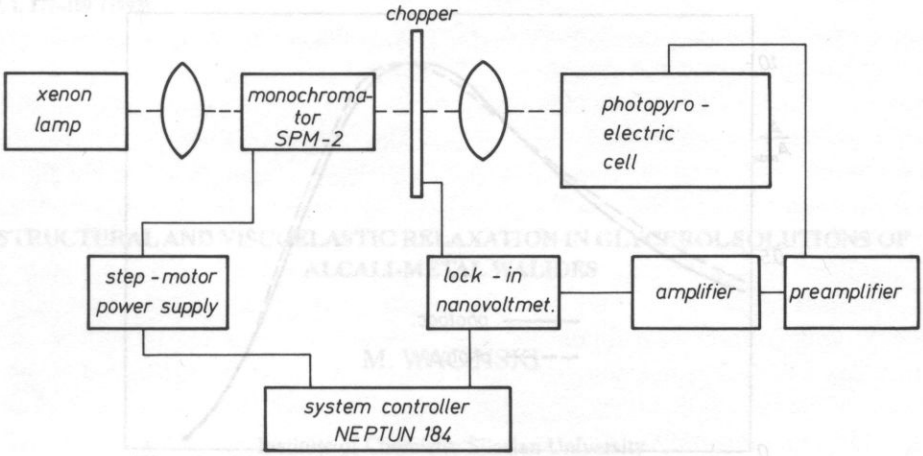

FIG. 2. Block scheme of the experimental set-up.

lamp was used as light source. Following the illumination of the sample with light with selected wavelength and modulated intensity, the obtained pyroelectric signal was fed supplied to a B and K type 2625 transducer, measured by a lock-in nanovoltmeter and, finally recorded on a microcomputer disk in a digital form. The whole measurement was computer-controlled. This enabled the current response of the pyroelectric transducer to be measured automatically as a function of the light wavelength. The photoacoustic signal was received using a B and K condenser microphone.

5. Results and discussion

Photopyroelectric and photoacoustic spectra were measured in the range varying from 400 to 700 nm for the sample films dyed with rhodamine B and treated mechanically and electrically. The electric response obtained as a function of the illumination spectrum from photopyroelectric and photoacoustic measurements were corrected by dividing the values obtained from measurements by the spectral lamp characteristics recorded upon the light transmission through the optical system. The examples of photopyroelectric and photoacoustic spectra of rhodamine B in the pyroelectric PVDF matrix, corrected and normalized to the maximum value, are shown in Fig. 3. The comparison of both spectra implies that similar spectral characteristics are obtained by the two methods employed. Slight differences between photopyroelectric and photoacoustic spectra might be attributed to the volumetric effects, e.g., inhomogeneous distribution of the pyroelectric coefficient throughout the film thickness. Such pyroelectric coefficient distribution has already been observed for PVDF film [3].

Bearing in mind the above results and considerations, the conclusion can be drawn that for dyes embedded in pyropolymer films the photopyroelectric method can, on the

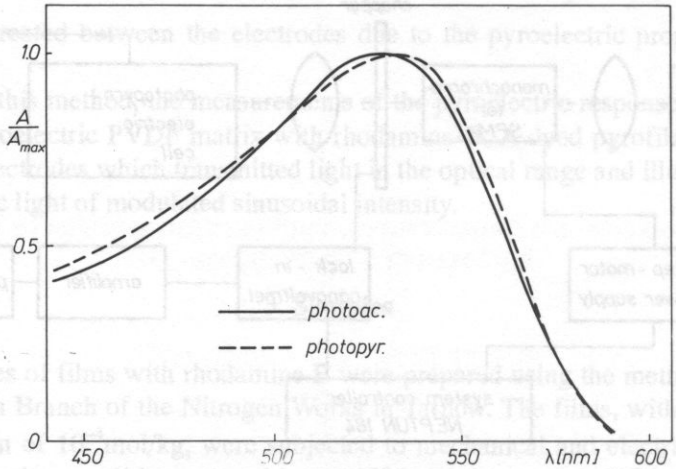

FIG. 3. Photoacoustic and photopyroelectric spectra of rhodamine B in the PVDF pyrofilm.

one hand, be employed, similarly as the photoacoustic method, for the investigation of spectroscopic properties of dyes, and, on the other hand, for the investigation of thermal and electrical properties of the matrix itself.

Acknowledgements

The authors wish to thank U. BAJORSKA from the Nitrogen Works in Tarnów for the preparation of dyed PVDF films. The preparation of pyrofilms by M. BLUKIS from the Institute of Experimental Physics at the University of Gdańsk is greatly appreciated. We would also like to acknowledge the help of J. SZURKOWSKI, PhD. Eng, in putting at our disposal the computer programme to control the measuring system and for the cell used in the photoacoustic measurements.

Carried out under Problem CPBP 02.03.2.14.

References

[1] H. VARGAS, L.C.M. MIRANDA, *Photoacoustic and related photothermal techniques*, Physics Reports 161, 2 (1988).

[2] S. ŁĘTOWSKI, A. ŚLIWIŃSKI, C. LEWA, *Analiza odpowiedzi prądowej przetwornika piroelektrycznego z PVDF domieszkowanego barwnikiem*, Proc. Open Sem. Acoust. 1988 p. 112–117.

[3] R.L. PETERSON, G.W. DAY, P.M. GRUZENSKY, R.J. PHELAN, *Analysis of response of pyroelectric optical detector*, J. Appl. Phys. 45, 8, p. 3296–3303 (1974).

Received on November 15, 1990

ARCHIVES OF ACOUSTICS
17, 1, 177–189 (1992)

STRUCTURAL AND VISCOELASTIC RELAXATION IN GLYCEROL SOLUTIONS OF ALCALI-METAL WALIDES

M. WACIŃSKI

Institute of Chemistry Silesian University
(40-005 Katowice, ul. Szkolna 9)

R. PŁOWIEC

Institute of Fundamental Technological Research
Polish Academy of Sciences
(00-049 Warszawa, ul. Świętokrzyska 21)

This paper presents the results of density, static viscosity and mechanical impedance measurements of glycerol solutions of electrolytes: LiBr, KBr, NaBr, KCl, RbCl, SeCl, NaF, LiF. The following quantities were calculated: limiting shear moduli, relaxation times, viscous flow activation energy and distribution parameters of viscoelastic relaxation times. Distribution parameters of viscoelastic relaxation times were determined on the basis of the Maxwell's model and the B-E-L model supercooled liquids. The occurrence of a wide spectrum of relaxation times was explained on the basis of the McDuffie's and Litovitz's cluster model and the mechanism proposed by Miles and Hammamoto. On the grounds of the achieved parameters of the relaxation time distribution width it was proved that long-range interactions (structural solvation) caused by the influence of the solvated anion decisively influence structural processes in the analysed solutions.

1. Introduction

Rheologic investigations are of great importance to the cognizance of the structure of liquids and nature of intermolecular forces. Measuring methods based on simple shearing i.e. independent density and temperature changes were applied in these investigations.

Structural rearrangements in liquids due to external shearing forces are of cooperative chamber according to the McDuffie and LITOVIZ [1, 2], because they include the entire group of molecules influenced by the short-range molecular order. Rearrangements are relaxation processes related with the structural relaxation time. The

cooperativity of such rearrangements is reflected in the viscosity of non-Arrhenius liquids which viscosity is not proportional to exp $(-E/RT)$, where E is the activation energy of a viscous flow. The inconformily of the temperature dependence to Eyring's theory can be explained by the fact that it neglects the participation of other molecules in the viscous flow processes and includes only position changes between the molecule and free space neighbouring and the probability of achieving the energy necessary to surmount the potential barrier related with the transition of a single molecule.

The effect of a wide spectrum of dielectric relaxation times in associated liquids was explained on the basis of the described above cluster model if the orientation of a molecule with a permanent dipole moment depends neighbouring molecules, dipole polarization will decays in a nonexponential manner, what can be interpreted as the distribution of characteristic times. Thus, the width of the spectrum should depend on the cluster size; a cooperative process of dislocation and then reconstruction of the molecular order takes place within the cluster.

The cluster model was used to interpret the relaxation of mechanical stresses, i.e. it was accepted that the distribution of structural and viscoelastic relaxation times in caused by the cooperative character of structural changes occurring during volume and shear strains.

The mechanism proposed by MILES and HAMMAMOTO [3] is another mechanism which can be applied to explain the occurrence of a wide spectrum of viscoelastic relaxation time. The occurrence of a wide spectrum is a result of a lack of long-range order in the liquid and of the mutual occurrence of ordered regions with various sizes.

2. Ultrasonic relaxation in glycerol solutions of electrolytes

Previous measurements, performed in multi-hydroxide-alcohol electrolyte solutions have proved that ultrasonic relaxation maintains the same structural character as in pure solvents. All characteristic features of structural relaxation were determined from measurements [4, 5]:

a) within the relaxation region a considerable dispersion of the acoustic wave propagation velocity specific for structural processes was observed.

b) outside the relaxation region ($\omega\tau << 1$) – the relaxation of the absorption coefficient (α) and its classical value (α_{kl}) does not exceed 3, while it can achieve values of several thousands in the case of thermal relaxation.

c) in the non-dispersive region α has a negative temperature coefficient-characteristic of structural processes, while the α/α_{kl} ratio can be accepted as independent of temperature. On the basis of equation

$$\frac{\alpha}{\alpha_{kl}} = 1 + \frac{3}{4}\frac{\eta_v}{\eta_s} \tag{1}$$

where η_v – volume viscosity, η_s – shear viscosity.

We can state that both viscositics are characterized by a more or less identical tempera-

ture dependence (similar activation energy for volume and shear strain). This means that they have similar molecular mechanisms i.e. with an identical structural character of observed relaxation.

d) at law temperatures the absorption coefficient-classical absorption ratio does not exceed 1 what indicates relaxation of the shear viscosity.

Shear impedance measurements in glycerol solutions of electrolytes have confirmed the occurrence of viscoelastic relaxation in the same frequency range in which structural relaxation takes place. Also a shift of the relaxation range towards higher temperatures than in pure glycerol was observed.

3. Viscoelastic relaxation

The interpretation of shear impedance measurements reaction of the investigated solutions to shearing vibrations was based on the relaxation theory as it was done previously in papers [6, 7].

A model created by summing Maxwell elements was used to describe the achieved results. This way the relaxation curve could be described with a continuous spectrum of relaxation times. According to the Maxwell's model the real and imaginary parts of the shear modulus (G' and G'') can be presented of the in a reduced form. Shear impedance components (R_l and x_l) can be presented similarly

$$\frac{G'}{G_\infty} = \int_0^\infty \frac{g_{(x)}\omega^2\tau_{s,0}^2x^2}{1+\omega^2\tau_{s,0}^2x^2}\,dx \tag{2}$$

$$\frac{G''}{G_\infty} = \int_0^\infty \frac{g_{(x)}\omega\tau_{s,0}x}{1+\omega^2\tau_{s,0}^2x^2}\,dx \tag{3}$$

where: $g_{(x)}$ – distribution of relaxation times τ_s standarized with respect to an arbitrary intermediate value $\tau_{s,0}$, $x = \tau_s/\tau_{s,0}$

$$\frac{R_L}{(\rho G_\infty)^{\frac{1}{2}}} = \left\{\frac{\omega^2\tau_{s,0}^2}{2}\int_0^\infty \frac{g_{(x)}x^2}{1+\omega^2\tau_{s,0}^2x^2}\,dx\left\{1+\left[1+\left(\frac{\int_0^\infty \frac{g_{(x)}x}{1+\omega^2\tau_{s,0}^2x^2}\,dx}{\omega\tau_{s,0}\int_0^\infty \frac{g_{(x)}x^2}{1+\omega^2\tau_{s,0}^2x^2}\,dx}\right)^2\right]^{\frac{1}{2}}\right\}^{\frac{1}{2}}\right\} \tag{4}$$

$$\frac{X_L}{(\rho G_\infty)^{\frac{1}{2}}} = \left\{\frac{\omega^2\tau_{s,0}^2}{2}\int_0^\infty \frac{g_{(x)}x^2}{1+\omega^2\tau_{s,0}^2x^2}\,dx\left\{1+\left[\left(\frac{\int_0^\infty \frac{g_{(x)}x}{1+\omega^2\tau_{s,0}^2x^2}\,dx}{\omega\tau_{s,0}\int_0^\infty \frac{g_{(x)}x^2}{1+\omega^2\tau_{s,0}^2x^2}\,dx}\right)^2-1\right]^{\frac{1}{2}}\right\}^{\frac{1}{2}}\right\} \tag{5}$$

In order to calculate the relaxation curve from these equations, distribution functions of relaxation times must be chosen. The Gaussian distribution function was chosen on the basis of LITOVITZ'S and PICCIRELLI'S paper [8]

$$g(\frac{\tau_s}{\tau_s'}) = \frac{b}{\pi^{1/2}} \cdot \frac{\tau_s'}{\tau_s} \exp -[b \ln \frac{\tau_s}{\tau_s'}], \quad 0 < \tau_s < \infty \tag{6}$$

It has maximum for $\tau_s = \tau_s'$. Relaxation curves can be calculated from equations (4) and (5) by substituting τ_s' with $\tau_{s,0}$. The parameter b, which defines the width of the distribution, was determined by comparing resistance curves, calculated from equation (4), with experimental resistance values standarized with respect to the resistance of a solid for investigated liquid $Z = (\rho G_\infty)^{\frac{1}{2}}$ and plotted beginning from frequencies standarized with respect to the Maxwell relaxation time $\omega\eta_s/G_\infty$, where ω – circular frequency $(2\pi f)$, η_s/G_∞ – Maxwell relaxation time. In order to match the relaxation time calculated from equation (4) with experimental points, the theoretical coefficient $\exp(-1/4b^2)$, relating the main time of the Gaussian distribution $\tau_{s,0}$ with the Maxwell relaxation time $\bar{\tau}_s = \frac{\eta_s}{G_\infty}$, i.e. $\tau_{s,0} = \frac{\eta_s}{G_\infty} \exp(1 - \frac{1}{4b^2})$, has to be substitutied by an experimental coefficient a, i.e. $\tau_{s,0} = \frac{\eta_s}{G_\infty} \cdot a$. Discrepancies in relaxation times were stated for many associated liquids. Authors of papers [8, 9] have attributed them to unsatisfactory accuracy of G_∞ determination and to the approximate character of the Gaussian distribution.

In order to become independent of such distribution function of relaxation times and to achieve a better description of viscoelastic relaxation, the precoded liquid model according to A.J. BARLOW, A. ERGINSAV and J. LAMBA [10] was applied. This [B–E–L] model is a combination of mechanical impedance of a Newtonian fluid (Z_N) and a perfectly elastic solid body (Z_s)

$$Z_N = R_N + ix_N = (1 + i)(\pi f \rho \eta_s)^{\frac{1}{2}}, \tag{7}$$

$$Z_s = R_s = (\rho G_\infty)^{\frac{1}{2}} \tag{8}$$

$$\frac{1}{Z_l} = \frac{1}{Z_N} + \frac{1}{Z_s}. \tag{9}$$

Thus we obtain the expression for the complex shear compliance:

$$J^* = J_\infty [\, 1 + \frac{1}{i\omega\tau_s} + \frac{2}{(i\omega\tau_s)^{1/2}} \,] \tag{10}$$

where τ_s is the Maxwell relaxation time $\tau_s = \frac{\eta}{G_\infty}$ and $J_\infty = \frac{1}{G_\infty}$, what satisfactorily describes the behaviour of simple liquids.

The model described above has to be modified in order to use it to describe vis-

coelastic relaxation in complex molecular liquids. This is done by introducing one additional parameter K or two adjustable parameters K and β. When $K = 1$ and $\beta = 0.5$, then the real and imaginary parts of mechanical shear compliance are reduced to the original B-E-L model (equation (10)) and to the Maxwell model with a single relaxation time $K = 0$ ($J' = 1/G_\infty$ and $J'' = 1/(\omega\eta_s)$). The values of parameters K and β were determined with the application of a computer programme, which matches the reduced values of mechanical shear impedance to experimental points:

$$\frac{R_l}{(\rho G_\infty)^{1/2}} = \mathrm{Re}\left[1 + \frac{1}{i\omega\tau_s} + \frac{2K}{(i\omega\tau_s)^\beta}\right]^{-1/2} \tag{11}$$

Calculated values are presented in Tables 5 and 6 and in diagrams.

4. Results of measurements

The following quantities were measured: density, static viscosity, mechanical shear impedance. Methods and apparatus were described in earlier papers [4, 5, 7] and presented at the Winter Schools on Molecular and Quantum Acoustics (1990). Limiting shear modules, relaxation times, activation energy of a viscous flow and distribution parameters of viscoelastic relaxation times were calculated.

Results of density and viscosity measurements are presented in Table 1. Measurements were performed within the temperature range 263–323 K with an accuracy of ± 0.05 K. For lower temperatures density was extrapolated from equation $\rho = A - BT$ and viscosity was calculated from equation $\lg\eta_s = C + DT^{-3}$, where A, B, C and D are constant parameters and T denotes temperature. Achieved density and viscosity values are higher in tested solutions than in pure glycerol. Temperature coefficients standing next to T for density measurements have very similar values. The density in serieses of chlorides and bromides (taking similar concentrations into account) increases in a linear manner in the following sequence: glycerol < KCl < RbCl < CsCl and glycerol < KBr < NaBr < LiBr.

In spite of similar temperature coefficients accompanying T^{-3}, analogic changes of temperature dependence of static viscosities occur in the bromide series only. Such viscosity changes are reflected by activation energies of the viscous flow, which are collected in Table 2. Solutions with similar concentrations are presented in the Table.

Table 3 presents values of the limiting shear modulus G_∞, which is considered to be a characteristic quantity describing the liquids molecular structure. Achieved results indicate a minimum influence of electrolytes on the rheological properties of glycerol in the elastic region. The convergence of moduli lies within the measuring error accepted as ± 10%. Static viscosity and limiting shear modulus changes determine changes of the Maxwell relaxation time. Its values are gathered in Table 4.

Mechanical shear impedance measurements were performed in the temperature range 223–303 K and frequency range 0.5–500 MHz. Parameters of the distribution width of viscoelastic relaxation times (b), as well as theoretical and experimental ratio

Table 1

Investigated system		Density (ρ) [kg · m^{-3}]		Static viscosity (lg η_s) [N · s · m^{-2}]	
		A	B	C	D
Glycerol		$1.4360 \cdot 10^3$	$-6.012 \cdot 10^{-1}T$	−3.6344	$+9.3908 \cdot 10^7R^{-3}$
Glycerol – KCl	(0.6023)	$1.4388 \cdot 10^3$	$-5.184 \cdot 10^{-1}T$	−3.8099	$+1.0044 \cdot 10^8T^{-3}$
Glycerol – RbCl	(0.5512)	$1.4707 \cdot 10^3$	$-5.955 \cdot 10^{-1}T$	−3.8567	$+1.0001 \cdot 10^8T^{-3}$
Glycerol – CsCl	(0.3474)	$1.4725 \cdot 10^3$	$-5.937 \cdot 10^{-1}T$	−3.6850	$+9.9849 \cdot 10^7T^{-3}$
Glycerol – LiBr	(0.3742 · 10)	$1.6064 \cdot 10^3$	$-5.917 \cdot 10^{-1}T$	−3.4182	$+1.1145 \cdot 10^8T^{-3}$
	(0.1350 · 10)	$1.4850 \cdot 10^3$	$-5.984 \cdot 10^{-1}T$	−3.6836	$+1.0175 \cdot 10^8T^{-3}$
	(0.1199 · 10)	$1.4773 \cdot 10^3$	$-5.959 \cdot 10^{-1}T$	−3.6908	$+1.0125 \cdot 10^8T^{-3}$
Glycerol – NaBr	(0.1191 · 10)	$1.5860 \cdot 10^3$	$-7.147 \cdot 10^{-1}T$	−3.5426	$+1.0354 \cdot 10^8T^{-3}$
	(0.5791)	$1.5027 \cdot 10^3$	$-6.349 \cdot 10^{-1}T$	−3.6706	$+1.0085 \cdot 10^8T^{-3}$
Glycerol – KBr	(0.1786 · 10)	$1.5408 \cdot 10^3$	$-5.814 \cdot 10^{-1}T$	−3.7340	$+9.6825 \cdot 10^7T^{-3}$
	(0.8638)	$1.4893 \cdot 10^3$	$-6.029 \cdot 10^{-1}T$	−3.7097	$+9.5124 \cdot 10^7T^{-3}$
Glycerol – LiF	(0.2833)	$1.4021 \cdot 10^3$	$-5.723 \cdot 10^{-1}T$	−3.7688	$+9.9166 \cdot 10^7T^{-3}$
Glycerol – NaF	(0.09864)	$1.4345 \cdot 10^3$	$-5.982 \cdot 10^{-1}T$	−3.7636	$+9.4946 \cdot 10^7T^{-3}$
Glycerol – $FeCl_3$	(0.06715)	$1.4284 \cdot 10^3$	$-5.460 \cdot 10^{-1}T$	−3.4155	$+9{,}2424 \cdot 10^7T^{-3}$
	(0.1069)	$1.4404 \cdot 10^3$	$-5.702 \cdot 10^{-1}T$	3.3328	$+9.1404 \cdot 10^7T^{-3}$
	(0.1693)	$1.4438 \cdot 10^3$	$-5.614 \cdot 10^{-1}T$	−3.2573	$+9.1768 \cdot 10^7T^{-3}$
	(0.3058	$1.4707 \cdot 10^3$	$-5.919 \cdot 10^{-1}T$	−3.3343	$+9.9207 \cdot 10^7T^{-3}$
	(0.4015)	$1.4904 \cdot 10^3$	$-6.157 \cdot 10^{-1}T$	−3.6218	$+1.1342 \cdot 10^8T^{-3}$

Concentration of the dissolved substance, i.e. mole per kg of solvent (glycerol) is given in brackets

of the main time of the Gaussian distribution to the Maxwell time have been calculated on the basis of these measurements. They are presented in Table 5.

In order to make the interpretation of results independent of the accepted relaxation time distribution function and in order to achieve better matching (especially for $FeCl_3$ solutions) of measurements and theoretical relaxation curves, the B-E-L supercooled liquid model was applied. Calculated values of the parameter K (matching with one parameter), as well as K and β (matching with two parameters) are collected in Table 6 and presented in a graphical form.

From the achieved results we can draw a conclusions that glycerol solutions of chlorides and fluorides widen the spectrum of viscoelastic relaxation times with respect

Table 2

Activation energy (E_a)
[K J · mol^{-1}]

Temperature	Glycerol	KCl	RbCl	CsCl	LiBr	NaBr	KBr	LiF	NaF
303—293	60.6	64.7	62.9	63.5	64.6	65.1	61.4	63.7	62.5
293—283	66.9	69.1	69.1	69.2	69.3	69.3	66.9	67.9	67.2
283—273	71.8	74.0	74.8	74.2	76.4	77.4	71.8	74.8	72.8
273—263	77.2	80.4	80.1	79.7	80.8	78.5	77.4	79.1	78.3
263—253	83.4	86.5	86.1	86.5	86.9	86.8	83.5	84.8	84.1
253—243	89.9	90.1	93.5	93.2	96.5	95.9	90.3	95.0	92.9
243—223	199.6	211.2	212.2	212.1	212.6	211.4	205.3	208.1	207.1

Table 3

Limiting shear modulus (G_∞)
[Nm^{-2}] · 10^9

Investigated system		Temperature K					
		218	223	228	233	238	243
Glycerol		3.77	3.65	3.52	3.40	3.28	3.16
Glycerol-KCl	(0.6023)	3.73	3.60	3.48	3.38	3.25	3.12
Glycerol-RbCl	(0.5512)	3.74	3.65	3.56	3.47	3.38	3.26
Glycerol-CsCl	(0.3474)	3.76	3.67	3.58	3.49	3.40	3.28
Glycerol-LiBr	(3.742)	3.77	3.65	3.56	3.48	3.39	3.31
	(1.350)	3.76	3.66	3.57	3.48	3.40	3.31
	(1.199)	3.76	3.67	3.58	3.48	3.40	3.29
Glycerol-NaBr	(1.191)	3.79	3.68	3.57	3.47	3.39	3.27
	(0.5791)	3.73	3.60	3.48	3.38	3.25	3.12
Glycerol-KBr	(1.786)	3.74	3.65	3.56	3.48	3.39	3.30
	(0.8638)	3.76	3.67	3.58	3.49	3.40	3.30
Glycerol-LiF	(0.2833)	3.74	3.64	3.57	3.46	3.39	3.29
Glycerol-NaF	(0.09864)	3.75	3.66	3.57	3.48	3.39	3.29

Table 4

Maxwell's relaxation time (τ_s) [s]

Investigated system		Temperature K 223.15	243.15	274.15	293.15
Glycerol		$1.78 \cdot 10^{-5}$	$2.51 \cdot 10^{-7}$	$3.40 \cdot 10^{-9}$	$5.10 \cdot 10^{-10}$
Glycerol-KCl	(0.6023)	$4.59 \cdot 10^{-5}$	$4.10 \cdot 10^{-7}$	$4.74 \cdot 10^{-9}$	$6.17 \cdot 10^{-10}$
Glycerol-RbCl	(0.5512)	$3.84 \cdot 10^{-5}$	$3.85 \cdot 10^{-7}$	$4.05 \cdot 10^{-9}$	$5.35 \cdot 10^{-10}$
Glycerol-CsCl	(0.3474)	$5.52 \cdot 10^{-5}$	$5.57 \cdot 10^{-7}$	$5.93 \cdot 10^{-9}$	$7.82 \cdot 10^{-10}$
Glycerol-LiBr	(1.120)	$7.13 \cdot 10^{-5}$	$7.09 \cdot 10^{-7}$	$6.91 \cdot 10^{-9}$	$8.76 \cdot 10^{-10}$
Glycerol-NaBr	(0.5791)	$6.88 \cdot 10^{-5}$	$7.03 \cdot 10^{-7}$	$7.09 \cdot 10^{-9}$	$8.55 \cdot 10^{-10}$
Glycerol-KBr	(0.8638)	$2.62 \cdot 10^{-5}$	$3.06 \cdot 10^{-7}$	$3.76 \cdot 10^{-9}$	$5.31 \cdot 10^{-10}$
Glycerol-LiF	(0.2833)	$3.87 \cdot 10^{-5}$	$4.25 \cdot 10^{-7}$	$4.56 \cdot 10^{-9}$	$6.05 \cdot 10^{-10}$
Glycerol-NaF	(0.09864)	$3.57 \cdot 10^{-5}$	$3.95 \cdot 10^{-7}$	$4.16 \cdot 10^{-9}$	$5.65 \cdot 10^{-10}$

Concentrations of dissolved substances in moles per kg of solvent

Table 5

Investigated system		b	$\exp -\frac{1}{4b^2}$	a
Glycerol		0.40	0.21	0.19
Glycerol-LiF	($m = 0.2833$)	0.30	0.06	0.14
Glycerol-NaF	($m = 0.09864$)	0.38	0.18	0.14
Glycerol-KCl	($m = 0.6023$)	0.38	0.18	0.12
Glycerol-RbCl	($m = 0.5512$)	0.39	0.19	0.12
Glycerol-CsCl	($m = 0.3474$)	0.39	0.19	0.12
Glycerol-$FeCl_3$	($m = 0.06715$)	0.33	0.10	0.11
	($m = 0.1069$)	0.33	0.10	0.11
	($m = 0.1693$)	0.32	0.09	0.11
	($m = 0.3058$)	0.30	0.06	0.07
	($m = 0.4015$)	0.30	0.06	0.07
Glycerol-LiBr	($m = 1.199$)	0.45	0.29	0.18
	($m = 1.350$)	0.45	0.29	0.18
	($m = 3.742$)	0.50	0.37	0.02
Glycerol-NaBr	($m = 0.5791$)	0.45	0.29	0.22
	($m = 1.191$)	0.45	0.29	0.21
Glycerol-KBr	($m = 0.8638$)	0.42	0.24	0.24
	($m = 1.786$)	0.44	0.27	0.26

Table 6

Investigated system		K	matching	K	β	matching
Glycerol		0.95	0.99954	1.00	0.56	0.99991
Glycerol-LiF	(m = 0.2833)	1.87	0.98860	1.98	0.56	0.99732
Glycerol-NaF	(m = 0.09864)	1.38	0.99990	1.46	0.54	0.99972
Glycerol-KCl	(m = 0.6023)	1.38	0.99792	1.46	0.56	0.99942
Glycerol-RbCl	(m = 0.5512)	1.22	0.99935	1.46	0.60	0.99995
Glycerol-CsCl	(m = 0.3474)	1.22	0.99943	1.45	0.58	0.99998,
Glycerol-$FeCl_3$	(m = 0.06715)	1.38	0.99946	1.28	0.44	0.99996
	(m = 0.1069)	1.31	0.99383	1.20	0.42	0.99876
	(m = 0.1693)	1.47	0.99870	1.34	0.44	0.99956
	(m = 0.3058)	1.70	0.99699	1.58	0.44	0.99919
	(m = 0.4015)	1.87	0.99094	1.56	0.40	0.99870
Glycerol-LiBr	(m = 1.199)	0.74	0.99990	0.88	0.45	0.99999
	(m = 1.350)	0.72	0.99906	0.88	0.46	0.99993,
Glycerol-LiBr	(m = 3.742)	0.52	0.99934	0.54	0.48	0.99990
Glycerol-NaBr	(m = 0.5791)	0.84	0.99895	0.88	0.60	0.99996
	(m = 1.191)	0.92	0.99762	0.98	0.60	0.99992
Glycerol-KBr	(m = 0.8638)	0.83	0.99861	0.88	0.48	0.99985
	(m = 1.786)	0.85	0.99962	0.90	0.56	0.99996

Values of parameter K determined with accuracy of 0.01

to the solvent-glycerol. For LiF b = 0.30, for NaF, KCl, RbCl, CsCl parameter b = 0.39, while for $FeCl_3$ solutions the parameter of distribution width is contained within the range 0.30–0.33.

An opposite effect is observed for bromide solutions. They limit the relaxation time spectrum in comparison to pure glycerol which has parameter b equal to 0.40. For LiBr and NaBr solutions b = 0.45 (excluding the concentrated LiBr solution, where b achieves a value of 0.50). As for KBr solutions parameter b is equal to 0.42.

In accordance with the cluster interpretation of the relaxation time distribution, the cooperativity of structural processes is of greater importance in chloride and fluoride solutions than in pure glycerol, while in bromide solutions it is of less importance. Cooperativity causes a non-exponential stress decay what is expressed by a wide distribution the of time spectra. Hence we can infer that cooperativity increase results in an increase of the width of the relaxation time distribution. On the other hand applying the

model proposed by Miles and Hammamoto we can conclude that the increase of the spectrum width with respect to the spectrum for glycerol suggests that clusters for chlorides and fluorides are more developed, and for bromide solutions there is an opposite effect.

Research concerning the dissolution entropy of water solutions of electrolytes [11] indicated that changes in water structure exceed the first coordination sphere. Values achieved for electrolytes differ from the obtained from value the effect of particle freezing and the ordering effect of the ions electric field. This difference will be characteristic of the structural contribution of individual ions. For halide anions (except F^-) negative values were obtained:

$$S = F^- (+3.5), Cl^- (-10.2), Br^- (-13.9), J^- (-17.9).$$

These values may indicate that the closest layer of water molecules freezes, while the large radius and electric field of the ion cause such a change in the orientation of water particles that they are less ordered in the second layer than in pure water. The introduction of an ion gives rise to two competitive effects: formation of intramolecular hydrogen bands or ion-dipole interaction, and the effect of water structure distruction. The destructive action of an ion increases when the ion's radius increases. According to Pauling radii of ions are equal to values given in A:

cations - Li^+ (0.60), Na^+ (0.95), K^+ (1.33), Rb^+ (1.48), Cs^+ 1.69),

anions - F^- (1.36), Cl^- (1.81), Br^- (1.95), J^- (2.16).

The F^- ion with a radius and polarizability only slightly differing from the respective values of oxygen in water can cause the ordering of particles resembling the order in water.

SAMOJŁOW [12] reached a similar conclusion on the basis of considerations concerning ion hydratation. He defines hydratation as the reaction of an ion to the translational motion of water molecules. The time a H_2O molecule stays (in equilibrium state) near an ion with respect to the time a H_2O molecule stays (in equilibrium state) in pure water in the hydratation measure. If $t_1 > t_0$, then the effect of positive hydratation takes place; while, if $t_1 < t_0$, then negative hydratation occurs. It results from presented calculations that F^- ions correspond to positive hydratation, while K^+, Cl^-, Br^-, J^- correspond to negative hydratation.

It results from our measurements that in glycerol solutions not only F^- ions but also Cl^- ions introduce an order in the solvents structure while larger Br^- anions have a disturbing effect as it happens in aqueous solutions.

Furthermore, a comparison of the obtained results indicates a lack of a distinctive cation effect. The anion has a prevailing influence on the width of the distribution of relaxation times. Parameter b accepts the value of 0.45 for LiBr (except for the highly concentrated solution, $m = 3.742$), NaBr and KBr solutions.

On the basis of the achieved results we can see that structural processes are affected not by direct ion-dipole or ion-induced dipole interaction (i.e. Coulomb solvation), but

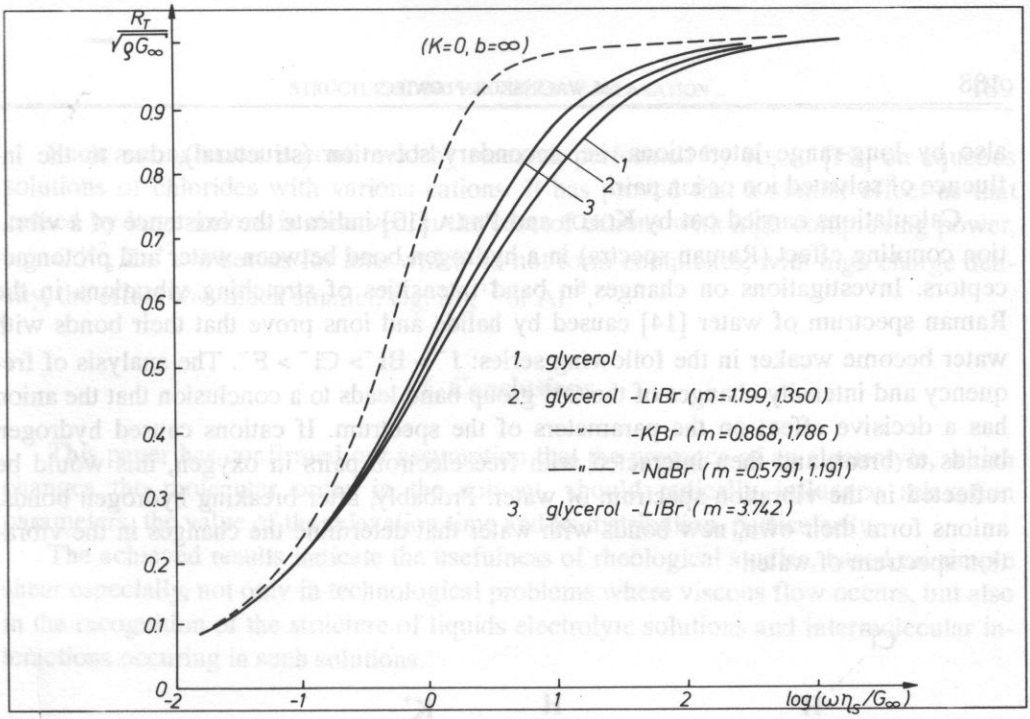
$\frac{R_T}{\sqrt{\rho G_\infty}}$
(K=0, b=∞)
1. glycerol
2. glycerol - LiBr (m=1.199, 1.350)
—"— - KBr (m=0.868, 1.786)
—"— - NaBr (m=0.5791, 1.191)
3. glycerol - LiBr (m=3.742)
$\log(\omega\eta_s/G_\infty)$

FIG. 1

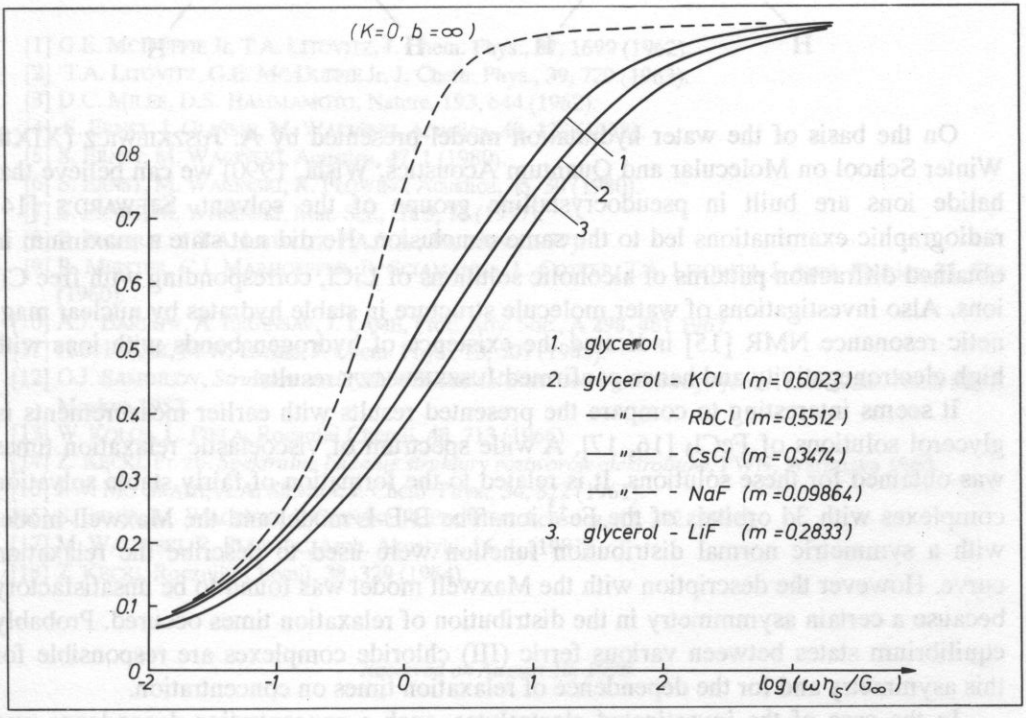
(K=0, b=∞)
1. glycerol
2. glycerol - KCl (m=0.6023)
—"— - RbCl (m=0.5512)
—"— - CsCl (m=0.3474)
—"— - NaF (m=0.09864)
3. glycerol - LiF (m=0.2833)
$\log(\omega\eta_s/G_\infty)$

FIG. 2

also by long-range interactions, i.e. secondary solvation (structural), due to the influence of solvated ion or ion pair.

Calculations carried out by KOŁOS and PIELA [13] indicate the existence of a vibration coupling effect (Raman spectra) in a hydrogen bond between water and proton acceptors. Investigations on changes in band intensities of stretching vibrations in the Raman spectrum of water [14] caused by halide and ions prove that their bonds with water become weaker in the following series: $J^- > Br^- > Cl^- > F^-$. The analysis of frequency and intensity changes of the OH group band leads to a conclusion that the anion has a decisive effect on the parameters of the spectrum. If cations caused hydrogen bands to break and then interacted with free electron pairs in oxygen, this would be reflected in the vibration spectrum of water. Probably, after breaking hydrogen bonds, anions form their own, new bonds with water that determine the changes in the vibration spectrum of water.

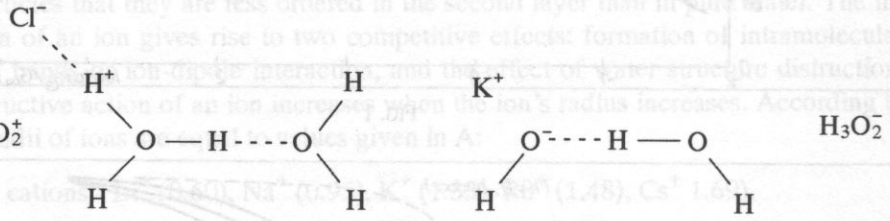

On the basis of the water hydratation model presented by A. JUSZKIEWICZ (XIXth Winter School on Molecular and Quantum Acoustics, Wisła, 1990) we can believe that halide ions are built in pseudocrystalline groups of the solvent. STEWARD'S [14] radiographic examinations led to the same conclusion. He did not state a maximum in obtained diffraction patterns of alcoholic solutions of LiCl, corresponding with free Cl^- ions. Also investigations of water molecule structure in stable hydrates by nuclear magnetic resonance NMR [15] indicated the existence of hydrogen bonds with ions with high electronegativity and hence confirmed JUSZKIEWICZ'S results.

It seems interesting to compare the presented results with earlier measurements in glycerol solutions of $FeCl_3$ [16, 17]. A wide spectrum of viscoelastic relaxation times was obtained for these solutions. It is related to the formation of fairly stable solvation complexes with 3d orbitals of the Fe^{+3} ion. The B-E-L model and the Maxwell model with a symmetric normal distribution function were used to describe the relaxation curve. However the description with the Maxwell model was found to be unsatisfactory because a certain asymmmetry in the distribution of relaxation times occured. Probably equilibrium states between various ferric (III) chloride complexes are responsible for this asymmetry and for the dependence of relaxation times on concentration.

In the case of the investigated electrolytes, such a concentration-dependence was observed for the most concentrated LiBr solution ($m = 3.742$ only). This may lead to a conclusion that a cation effect can take place for ions with great complexing power.

Such a conclusion is confirmed by research performed by KĘCKI [18] on aqueous solutions of chlorides with various cations. It has proved that a similar effect as that caused by large anions is observed in the case of cations with high complexing power, e.g. Cd^{+2}, Zn^{+2}. Whereas for ions which do not form complexes, with high charge density, the effect was much smaller, e.g. Mg^{+2} or Al^{+3}.

5. Conclusions

This paper has confirmed our assumption that the presence of an electrolyte, which changes the molecular order in the solvent, should radically influence relaxation parameters, the value of the relaxation time and its distribution, particularily.

The achieved results indicate the usefulness of rheological studies, based on simple shear especially, not only in technological problems where viscous flow occurs, but also in the recognition of the structure of liquids electrolyte solutions and intermolecular interactions occuring in such solutions.

References

[1] G.E. MCDUFFIE Jr, T.A. LITOVITZ, J. Chem. Phys., **37**, 1699 (1962).
[2] T.A. LITOVITZ, G.E. MC DUFFIE Jr, J. Chem. Phys., **39**, 729 (1963).
[3] D.C. MILES, D.S. HAMMAMOTO, Nature, **193**, 644 (1962).
[4] S. ERNST, J. GLIŃSKI, M. WACIŃSKI, Acustica, **40**, 128 (1978).
[5] S. ERNST, M. WACIŃSKI, Acustica, **47**, 1 (1980).
[6] S. ERNST, M. WACIŃSKI, R. PŁOWIEC, Acustica, **45**, 30 (1980).
[7] S. ERNST, M. WACIŃSKI, Mat. Sci., **III 3**, 75 (1977).
[8] R. PICCIRELLI, T.A. LITOVITZ, J.A.S.A., **29**, 1009 (1957).
[9] R. MEISTER, C.J. MARHOEFFER, R. SCIAMANDA, L. COTTER, T.A. LITOVITZ, J. Appl. Physics, **31**, 854 (1960).
[10] A.J. BARLOW, A. ERGINSAV, J. LAMB, Proc. Roy. Soc., **A 298**, 481 1967.
[11] H.S. FRANK, M.W. EVANS, J. Chem. Phys., **13**, 507 (1945).
[12] O.J. SAMOJLOV, *Struktura vodnych roztvorov elektrolitov i gidratacija jonov*, Izd. Akad. Nauk SSSR Moskva 1957.
[13] W. KOŁOS, L. PIELA, Roczniki Chemii, **40**, 713 (1966).
[14] Z. KĘCKI, Pr. zb. *Spektralne badanie struktury roztworów elektrolitów*, PWN, Warszawa 1969.
[15] J.W. MC GRATH, A.A. SILVADI, J. Chem. Phys., **34**, 322 (1961).
[16] S. ERNST, M. WACIŃSKI, J. GLIŃSKI, R. PŁOWIEC, Acustica, **47**, 292 (1981).
[17] M. WACIŃSKI, R. PŁOWIEC, Arch. Akustyki, **16**, 1, (1981).
[18] Z. KĘCKI, Roczniki Chemii, **38**, 329 (1964).

Received on August 10, 1990

ARCHIVES OF ACOUSTICS
17, 1, 191–198 (1992)

ACOUSTIC EMISSION ACCOMPANYING STABILITY LOSS OF COMPRESSED RODS

Z. KOWAL and J. SENDKOWSKI

Technological University of Kielce

1. Introduction

In metal rod structures more than 90% of failures are caused by different forms of stability loss of elements. From the point of view of effects of stability loss, rod structures can be divided into two groups:

Group 1, in which the stability loss of a single element in the system causes a stability loss of the system. This concerns rod frame systems and grids which contain rods compressed in minimal critical sets of size 1 [1], and therefore it also concerns all statically determinable structures.

Group 2, in which a stability loss of single elements (or local stability loss in surface structures) does not cause exhaustion of the structure load bearing capacity. This concerns a considerable number of statically indeterminable structures known from load bearing capacity reserves in extracritical state. In such cases, a new statical form of the structure equilibrium occurs after stability loss which gives an opportunity to save it. A particular significance of protection against overload occurs in large excavators [2].

In real rods classical stability loss does not occur due to geometrical imperfections which decrease the critical load bearing capacity of rods (and also shells). The more geometrical imperfections are in the rod, smaller is its load bearing capacity, and acoustic signals are to be expected under a smaller load.

In the same rod systems imperfections of fixing and fixing through friction occur, as well as change in conditions of fixing throughout loading which is accompanied by a change of static friction into kinematic.

It should be added that friction has a considerable influence on the critical load bearing capacity of compressed rods fixed in joints [5, 6].

A stability loss of single rods in the elastic area in the elastic-plastic area is qualitatively different, and therefore a change in characteristics of acoustic emission is to be expected together with a change in the slenderness of the investigated rods.

From the initial investigation it is possible to predict on the basis of EA the degree of the danger of a structure caused by a stability loss, and also it is possible to estimate the history of the structure load.

The above premises and experience from projects for industry [1] prompted the present authors to carry out an AE investigation which accompanies a stability loss of rods of different slenderness.

This paper presents the results of the investigation of acoustic emission which accompanies a stability loss of compressed rods of different slenderness made of low carbon steel of the group ST3S.

2. Experimental

Compact rods of a rectangular intersection 10 × 20 mm were investigated. Intersections were obtained by machining (milling and grinding) from steel flat bars made of low-carbon steel of the group ST3S with a long plastical stop.

The characteristic of steel obtained from the present authors' own investigation is as follows: Young's modulus $E = 209$ GPa, upper boundary of plasticity $R_e^g = 350.43$ MPa, lower boundary of plasticity $R_e^d = 329.6$ MPa, elastic strain boundary $\varepsilon_s = 1.600\%$, plastic strain boundary $\varepsilon_{pl} = 1.875\%$ corresponding to the upper plasticity boundary, Poisson's elastic coefficient $\nu = 0.292$.

An inventory of the geometry of the investigated rods was made. Deviations from the straight line axis of the rod was measured. It was described by the terms from Fourier's series [5]. Rods of nominal slenderness 50, 75, 100, 150 three pieces of each range of slenderness, were tested.

Rods were fixed in the hydraulic gripping jaws of the testing machine MTS, the investigated models of rods being rigidly fixed.

The testing machine controlled by a computer made it possible to carry out the tests when the rod ends were mutually displaced longitudinally by the computer (axial shortening Δl). The displacement rate was 0.05 mm/s for slender rods ($\lambda = 50$, 75)and 0.025 mm/s for slender rods ($\lambda = 100$ and 150), and it approached the lower limit of possible rates of displacement in order to obtain quasi-static load.

The hydropulsating testing machine manufactures by the MTS Company (ASSY system No.921.06–01) is a PDP–11/04 computer-controlled machine with an operating memory of 16kb with the attached soft-disc station (8") and a copier.

In the analog part controlled by the machine, it is possible 1) to choose the control factor (force, displacement or strain), 2) to choose the length interval of a given factor, e.g., the smallest range 0–25 kN, or the greatest range 0–250 kN for force, 3) to introduce the value limits of the factor in order to protect the tested element from destruction. The theoretical accuracy of the machine is 0.024 mm for displacement in the range 0–50 mm. On account of the level of electronic noises in the control system, the actual accuracy is estimated to be 2/2047 of the maximum value of a chosen range. The parameters of acoustic emission were measured with an analyzer of acoustic emission

EA-3 produced by IPPT in Warsaw, which was coupled an IBM computer by an interface. The density of AE countings and the momentary values of the RMS parameter of the acoustic emission signal were measured. A piezoelectric transducer of a resonance frequency of 500 kHz and counting range 0.1 s was used.

One free channel of the acoustic emission analyzer was used in order to make a simultaneous measurement of the longitudinal force acting on the investigated rod. The axial force which corresponds to the controlled mutual shortening of the length between the rod ends was automatically digitally recorded during the tests.

A set of procedures written with the help of a TURBO PASCAL compiler version 4 was used for recording and processing of measurement data.

The program PIZAZZ of the Application Techniques Inc. was used to transfer the graphs to the printer. The above-mentioned procedures and programs were developed and tested by Z. RANACHOWSKI of IPPT in Warsaw [4].

3. Results

Using the procedures [4] of visualization of the experimental data, the results of the investigation for the particular tests from no.3 to no.15 are graphically presented. For example, Fig. 1 shows the course of counting density in the function of time s, elongation Δl and static equilibrium path $F(\Delta l)$ for test no.4 ($\lambda = 50$). Plot $F(\Delta l)$ was recorded by the testing machine which controlled displacement Δl. Figure 2 shows analogously the course of the power parameter RMS in the function s and Δl for test 4 ($\lambda = 50$), on which the plot $F(\Delta l)$ was also superimposed. Figure 3 shows the counting density with summing in the function s and Δl for test 4 ($\lambda = 50$). Figure 4 shows the course of a power parameter RMS with summing in the function s and Δl for test no.4 ($\lambda = 50$). In Figs. 3 and 4 we see a synchronized plot of force $F(\Delta l)$ – SEP. Some coordinates of the static equilibrium path SEP and characteristics AE have an essential significance for the signalization of the loss of load carring capacity of structural elements.

Tables 1 through 4 contain the maximal coordinates (s, n), (s, P), (s, RMS), $(s, \max \Sigma N)$ of the investigated rods denoted * in Fig. 1 through 4.

4. Discussion of the investigation results

It follows from an analysis of the coordinates contained in Tables 1 through 4 that there occurs displacement between the coordinates of maxima of the static equilibrium path SRS and maxima of the AE characteristics. Displacement of the maxima of AE characteristics in relation to the coordinates of limit load bearing capacity of a rod calculated from the formula (1) is shown in Table 5

$$\Delta \bar{S} = \bar{S}_i - \bar{S}_{gr} \tag{1}$$

It follows from an analysis of the results contained in Table 5 that there occurs a delay in peaks in the course of counting density and in the course of RMS, and also in

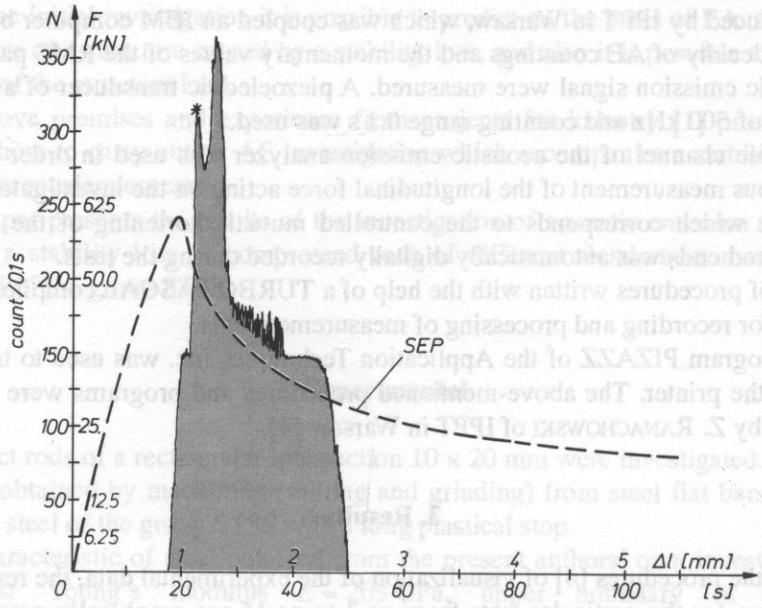

FIG. 1. Course of counting density for test 4 ($\lambda = 50$).

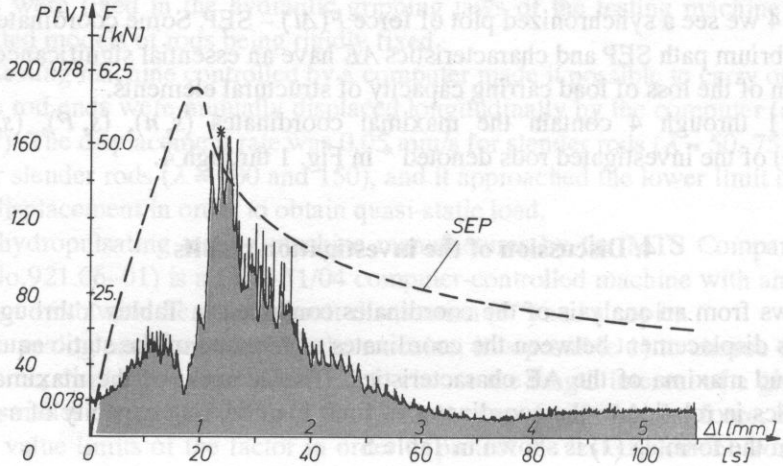

FIG. 2. Course of the power parameter RMS for test 4 ($\lambda = 50$).

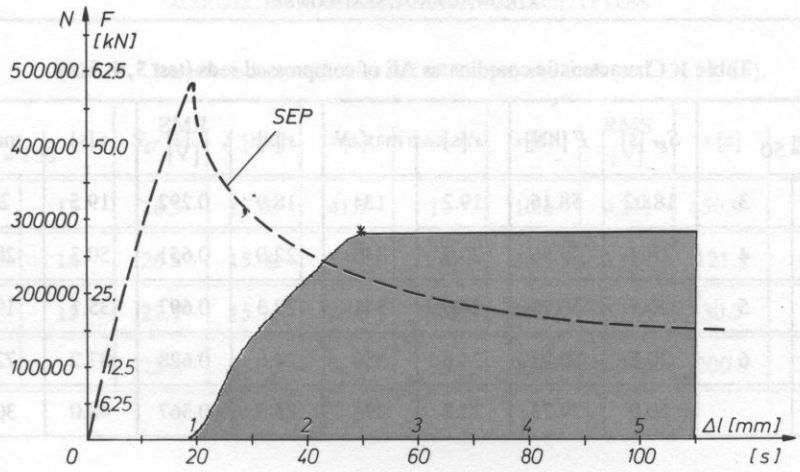

FIG. 3. Course of counting density for test 4 ($\lambda = 50$).

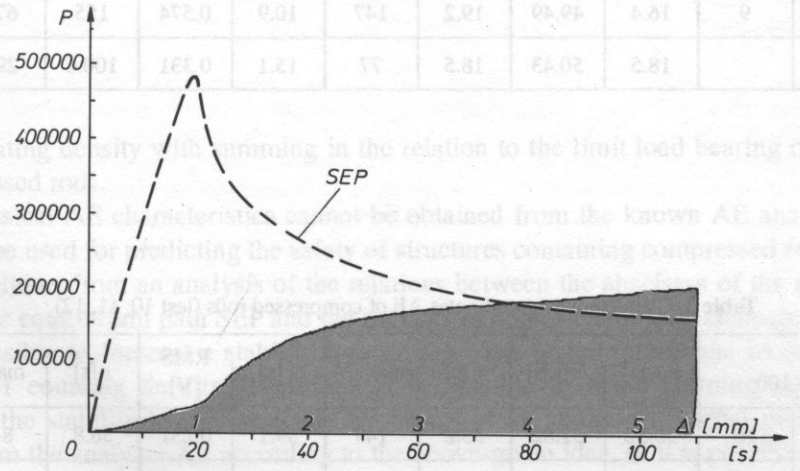

FIG. 4. Course of the power parameter RMS with summing for test 4 ($\lambda = 50$).

Table 1. Characteristic coordinates AE of compressed rods (test 3, 4, 5, 6).

$\lambda = 50$		S_{gr} [s]	F [kN]	s [s]	max. N	s [s]	RMS [V]	s [s]	max ΣN
test	3	18.02	58.16	19.2	134	18.9	0.292	19.5	21000
	4	18.4	59.66	20.4	340	22.0	0.651	50.3	282000
	5	20.7	60.10	24.6	341	28.3	0.697	35.1	198000
	6	20.7	60.98	24.6	350	24.6	0.628	87.2	721000
mid.		20.0	59.73	22.2	291	23.5	0.567	48.0	305500

Table 2. Characteristic coordinates AE of compressed rods (test 7, 8, 9).

$\lambda = 75$		S_{gr} [s]	F [kN]	s [s]	max. N	s [s]	RMS [V]	s [s]	max ΣN
test	7	17.8	48.61	14.4	3	15.1	0.199	24.8	206800
	8	21.2	53.20	21.9	82	19.2	0.220	21.9	2100
	9	16.4	49.49	19.2	147	10.9	0.574	155	678000
mid.		18.5	50.43	18.5	77	15.1	0.331	100.6	296000

Table 3. Characteristic coordinates AE of compressed rods (test 10, 11, 12).

$\lambda = 100$		S_{gr} [s]	F [kN]	s [s]	max. N	s [s]	RMS [V]	s [s]	max ΣN
	10	30.82	31.82	33.2	149	39.1	0.231	56.8	84800
	11	49.74	37.10	56.4	6	46.4	0.165	401.2	710000
	12	33.22	28.90	33.2	3	28.4	0.094	158.7	310000
mid.		37.99	32.60	40.9	53	38.0	0.163	123.4	368000

Table 4. Characteristic coordinates AE of compressed rods (test 13, 14, 15).

$\lambda = 150$		S_{gr} [s]	F [kN]	s [s]	max. N	s [s]	RMS [V]	s [s]	max ΣN
test	13	26.5	15.03	41.7	10	10.6	0.211	450.9	710000
	14	26.5	15.02	27.7	136	11.4	0.187	121.3	160000
	15	22.7	15.91	26.5	122	15.2	0.196	30.3	20000
mid.		25.2	15.32	32.0	93	12.4	0.198	200.8	330000

Table 5. Displacement of the maximum of average counting densities and RMS in relation to limit load bearing capacity.

	$\bar{S}_{gr}$ [s]	$\bar{F}$ [kN]	$\bar{S}_i$ (N)	$\bar{S}_i$ (RMS)	$\Delta\bar{S} = \bar{S}_i(N) - \bar{S}_{gr}$	$\Delta\bar{S} = \bar{S}_1(RMS) - \bar{S}_{gr}$
$\lambda = 50$	20.0	59.73	22.2	23.5	2.2	3.5
$\lambda = 75$	18.5	49.49	18.5	15.1	0.0	-3.4
$\lambda = 100$	37.9	32.60	40.9	38.0	3.0	0.1
$\lambda = 150$	25.2	15.32	32.0	12.4	6.8	-12.8

the counting density with summing in the relation to the limit load bearing capacity of compressed rods.

Classical AE characteristics cannot be obtained from the known AE analyzers and cannot be used for predicting the safety of structures containing compressed rods.

It follows from an analysis of the relations between the abscissas of the maxima of the static equilibrium path SEP and the maxima of acoustic emission characteristics that it is possible to forecast a stability loss on the basis of the rate of the increase in the peaks of counting density. Therefore, it is possible to make warning signalization against the stability loss of structure by means of an additional, digital processing of data from the analyzer AE according to the above-given idea, or it is possible to build a special analyzer to accomplish this purpose.

A more precise analysis requires the development and implementation of analytic programs based on a correlational spectrum analysis, nonstationary stochastic process, or to build new analyzers. The investigation aimed at advances techniques of measurement and processing of signals AE is carried out by the present authors.

5. General conclusion

Exhaustion of the load bearing capacity of compressed rods is accompanied by a change in the value of AE characteristics.

The investigation results obtained indicate that there is a possibility of using AE in practice to monitor the hazard of structures susceptible to buckling and which gives an opportunity to save the structure. It requires the introduction of additional AE characteristics. It will be the subject of a separate publication.

References

[1] Z. KOWAL, *Zuverlässigkeit von Konstruktionssystemen*, Wissenschaftliche Zeitschrift der TU Dresden, **25** 1/2 (1976).

[2] Z. KOWAL, J. SENDKOWSKI, *Ocena stanu technicznego wysięgnika koparki urabiającej Rsch-900 w kopalni węgla brunatnego Józefów w Koninie*, Sprawozdanie z prac badawczych, Politechnika Świętokrzyska, Wydział Budownictwa Lądowego, KBMiTK, 1983.

[3] S. PILECKI, *Wykorzystanie emisji akustycznej w badaniach właściwości mechanicznych i pękania ciał stałych*, Arch. Akustyki, **21**, 1, 109–134 (1986).

[4] J. RANACHOWSKI, E. ADAMCZYK, *Aparatura do pomiarów emisji akustycznej w elementach betonowych i do zastosowań w chemii przemysłowej*, Sprawozdanie z wykonania celu wdrożeniowego Nr 64 w CPBP 12.2, IPPT PAN, Warszawa 1988.

[5] J. SENDKOWSKI, *Trwała nośność graniczna ustrojów kratowych*, praca doktorska, Politechnika Warszawska 1989.

[6] Z. KOWAL, J. SENDKOWSKI, *Emisja akustyczna towarzysząca utracie stateczności prętów ściskanych o różnej smukłości*, praca wykonana na zlecenie IPPT w ramach CPBP 02.03 temat 1.19/1.89 Warszawa 1989.

Received on August 15, 1990